The Pennsylvania State University

The Graduate School

College of Engineering

STUDY OF CONDENSED PHASE REACTIONS BETWEEN HYPERGOLIC PROPELLANTS USING MICROREACTORS

A Dissertation in

Mechanical Engineering

by

Pulkit Saksena

Submitted in Partial Fulfillment
of the Requirements
for the Degree of

Doctor of Philosophy

August 2014

The dissertation of Pulkit Saksena was reviewed and approved* by the following members:

Richard A. Yetter
Professor of Mechanical Engineering
Dissertation Co-Advisor, Co-Chair of Committee

Srinivas Tadigadapa
Professor of Electrical Engineering
Dissertation Co-Advisor, Co-Chair of Committee

Stefan T. Thynell
Professor of Mechanical Engineering

Donghai Wang
Associate Professor of Mechanical Engineering

Siyang Zheng
Assistant Professor of Biomedical Engineering

Karen A. Thole
Professor of Mechanical Engineering
Head of the Department of Mechanical and Nuclear Engineering

*Signatures are on file in the Graduate School

ABSTRACT

The testing of hypergolic propellants has been carried out for decades and the use of hypergolic propellants at a systems level is very well understood. Extensive testing has provided the design and construction of rocket engines which have been very reliable. Safety procedures have been developed for the handling and storage for hypergolic propellants, which all too often are highly toxic. But the condensed phase chemistry for these hypergolic propellants is not very well understood. The models in place for ignition and combustion do not handle the coming together of two liquid streams of these hypergols and the two-phase aspects that are expected once the reactions occur. Moreover, it is not clear what makes a fuel and oxidizer pair hypergolic in nature.

The coupling of physical and chemical factors that control the ignition of hypergolic propellants makes the direct study of the transient ignition process difficult. The current study presents a novel method to study hypergolic propellants (very fast liquid reactions) using microreactors instead of conventional drop tests, modified versions thereof or impinging jet tests. Planar counterflow microreactors are used to isolate liquid-phase reactions from secondary gas phase reactions that occur later during the ignition process and thus provide valuable insight in to the pre-ignition mechanism.

The microreactor fabrication, flow field characterization, reactivity results from experiments performed using a variety of fuels and nitric acid as the oxidizer and numerical simulation results of reactive flow in the microreactor are presented in this study. Particle image velocimetry measurements and numerical simulations were conducted to characterize the laminar velocity flow-field in the microreactor and strain rates at the stagnation point along the centerline of the microreactor. Temperature measurements at the stagnation zone, the exit and positions along the length of the microreactor were used as a measure for the extent of the reaction or the heat released from the reaction. For the hypergols, an increase in reactant flow (or equivalently strain rate at the

stagnation point) was found to initially increase temperatures at both the stagnation zone as well as along the length of the reactor, but eventually resulted in a decrease in temperature, revealing a maxima in temperature and reactivity. The trends indicated a reaction that was initially diffusion or heat loss controlled, which transitioned towards kinetic control at higher strain (flow) rates. Numerical simulations of the reactive flow in the microreactor stagnation zone were also carried out in which the reaction zone in the microreactor was treated similar to the reaction zone occurring in a counter-flow diffusion flame. These simulations showed that the flow rates at which the peak in temperature occurred was dependent on the rate of the reaction occurring between the hypergol pairs. The numerical simulations also show that heat loss from the top and bottom surfaces can play a role on the temperature trends seen in the microreactor. This study details the first comprehensive measurements and analysis of the condensed phase interfacial reactions occurring between hypergols.

TABLE OF CONTENTS

LIST OF FIGURES

LIST OF TABLES

ACKNOWLEDGEMENTS

This journey has been much tougher than I had ever imagined it to be when I first started graduate school, and I have numerous people to thank for their help and patience over the past few years. I am immensely indebted to both my advisors for their support and I certainly could not have completed this journey without their guidance. I am grateful to Dr. Richard A. Yetter for introducing me to experimental combustion research and to Dr. Srinivas Tadigadapa for his invaluable help in teaching me how to fabricate on the micron scale. Their rigorous and meticulous approach to science has made me a better researcher. I would also like to thank my committee members, Dr. Thynell, Dr. Wang and Dr. Zheng for their invaluable inputs to this dissertation. In particular, I am thankful to Dr. Thynell for sharing his insight on hypergolic propellant chemistry and for helping me carry out drop-test experiments in his laboratory.

As a member of two research groups that have vastly differing research interests, I have benefited from the diverse perspectives offered by my many labmates. Their input, feedback and assistance over the years have helped me improve my experimental research skills. In particular, I would like to thank Dr. Marcelo Pisani who helped me get started with fabrication in the cleanroom; Dr. Jongguen Lee and Dr. Michael Weismiller for their guidance on the design of my early experiments; Bo-Han Kuo and Amanda Baker for their advice on developing a process for LTCC fabrication of microreactors; Terrence Connell for support with experimental design as well as for always being there in case I needed something fabricated in a hurry; Dr. Shiqing Wang for his assistance in setting up the drop-test experiments; Larry Horner for sharing his machining expertise; and Mary Newby for helping me get through all the paperwork and bureaucratic hassles. I would especially like to thank my partner-in-crime, Sharat, who like me, has been a member of both the

Yetter and Tadigadapa research groups and has so often helped me both inside and outside the lab, irrespective of the time of the day.

My stay here at Penn State has been all the more enjoyable thanks to a large group of friends (both here and back home) who helped make small town life more livable. So, thank you Madame Zhao, for the coffees and conversations and also a huge thank you for being there and lending an ear through all the lows. Thank you to Kuni-san, for introducing me to wonderful Japanese whiskey and for always being up for joy-riding in new sports cars; to Raja and Githin for the fun evenings and the long conversations; and to Arnab for providing a warm home and helping me settle down in a new country with such ease. I am extremely grateful to Surdy, Tushar, Hardy, Nakul and Wonder Girl for always being available to listen, especially when I was down and ready to give up – your support has meant the world to me and has helped me steer through the roughest of times.

To conclude, I would like to express my immense gratitude to my family. To Mom, for always being in my corner, for being able to read my thoughts so well, and for her patience and understanding even when I was too caught up to have a proper conversation. I now wish I had called home more often, if for nothing else but to put a smile on your face. To Dad, for being so solid and dependable; your silent support and unwavering faith in me have inspired me to try to be more like you. To Priyasha, for an unending stream of Rakhi gifts which never failed to light up my day. I still think it is the crowning glory of my life that I have convinced you to do the gift giving on Rakhi. And finally to Tejas, for being my rock and keeping me sane over the past few years. Your calm voice has helped me through more often than you believe.

"Basic research is what I am doing when I do not know what I am doing."

– Wernher von Braun

Chapter 1

Introduction

1.1 Chemical Rocket Propulsion

Given that a major part of this study focusses on chemical rocket propellants, it is natural to first define what chemical propulsion is and how it is classified into various categories. Propulsion is the act of changing a body's motion through the production of thrust. There are many different types of propulsion mechanisms that are used depending on the intended application. Jet propulsion is a type of propulsion where a body is propelled due to the reaction force that results from the momentum of expelled matter. Jet propulsion is in turn categorized under two different headings. The first kind of jet propulsion is termed as duct propulsion or air-breathing propulsion and consists of systems that combine oxygen in the atmosphere with fuel in the engine to form a combusting reactive mixture that releases thermal energy and creates high-momentum gases that can be used to create thrust. Systems which do not use atmospheric oxygen and rather rely on oxidizers carried on board with the fuels are classified under rocket propulsion[1].

As air is freely available while traveling within the earth's atmosphere, rocket propulsion is more suited for applications dealing with space travel but has been used for missiles (for launching weaponry at a target) as well. Table 1-1 shows different propulsion devices, along with their level of development with different energy sources [1]. There are a large number of energy sources that have been shown to be applicable for the purpose of rocket propulsion. And although nuclear energy may be a viable option in the future, at present, most the energy is derived by means of an exothermic chemical reaction and this may be the case for many years to come [1]. These systems which use a chemical reaction as the main source of energy are categorized under chemical rocket propulsion. Chemical rocket propulsion can, in-turn, be classified under different categories based on the type of

propellants used to derive the energy for propulsion. The three broad categories are: liquid propellant, solid propellant, and hybrid. The following section will review these three classifications.

Table 1-1: Propulsion concepts and their level of development [1].

Propulsion Device	Energy Source[a]			Propellant or Working Fluid
	Chemical	Nuclear	Solar	
Turbojet	D/P	TFD		Fuel + air
Turbofan	D/P	TFD		Fuel + air
Turbo–ramjet	TFD			Fuel + air
Ramjet (hydrocarbon fuel)	D/P	TFD		Fuel + air
Ramjet (H_2 cooled)	TFD			Hydrogen + air
Rocket (chemical)	D/P	TFD		Stored propellant
Ducted rocket	TFD			Stored solid fuel + surrounding air
Ducted underwater rocket	TFD			Propellant + water
Air turborocket	TFD			Stored + surrounding air
Electric rocket	D/P	TFD	D/P	Stored propellant
Nuclear fission rocket		TFD		Stored H_2
Nuclear fusion rocket		TFND		Stored H_2
Solar heated rocket			TFD	Stored propellant
Photon rocket		TFND		Photon ejection (no stored propellant)
Solar sail			TFD	Photon absorption (no stored propellant)

[a] D/P, developed and/or considered practical; TFD, technical feasibility has been demonstrated, but development is incomplete; TFND, technical feasibility has not yet been demonstrated.

1.1.1 Liquid Propellant Rockets

As the name suggests, liquid propellant rockets make use of injecting propellant in its liquid form into a rocket thrust chamber, subsequently combusting the propellant and accelerating the hot product gases through a nozzle to create thrust. A variety of propellants can be used in the case of the liquid propellant rockets to create suitable chemical reaction. A bi-propellant system has two separate liquid propellants, namely the liquid oxidizer (often liquid oxygen) and the liquid fuel (usually rocket-grade kerosene or liquid hydrogen). The two liquid propellants are stored separately and are only

injected into the thrust chamber during the combustion process. This injection is usually done under high pressure. A schematic of a pressure fed bi-propellant liquid rocket engine is shown in the Figure 1-1. Monopropellant systems (hydrazine, nitromethane, hydrogen peroxide), on the other hand, consists of an oxidizing agent and the combustible matter combined in one single substance. These propellants are stable at storage conditions, but decompose and yield hot combustion gases under the action of external heat or the presence of a catalyst.

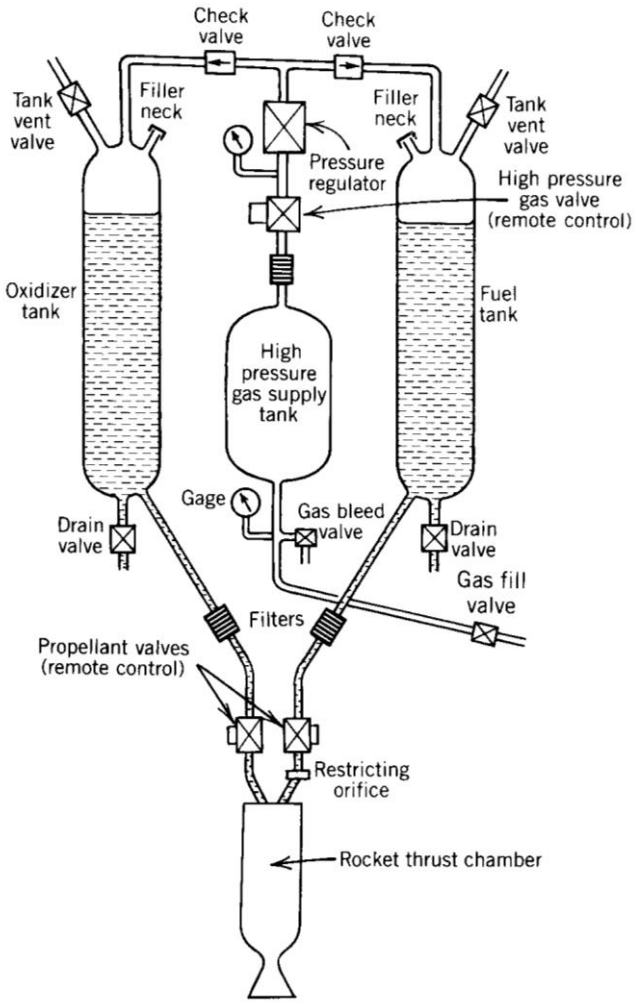

Figure 1-1: Schematic of pressure fed bi-propellant liquid rocket engine (taken from [1]).

As liquid bi-propellants usually have higher specific impulse than other forms of chemical propulsion, there has been considerable research in the field of liquid propulsion leading to liquid propulsion systems being highly dependable and proven means of propulsion [2]. Liquid rocket engines were by far the most popular means of rocket propulsion in the early stages of US development. Although conceived over a hundred years ago, Robert Goddard launched the first liquid bi-propellant sounding rocket, fueled with gasoline and liquid oxygen, in 1926. Early US tactical and ballistic missiles were propelled with liquid rocket engines, and the F-1 engine, which made up the first stage of the Saturn V rockets of the Apollo program, was a liquid bi-propellant rocket running on RP-1 and LOX. The more recent J-2 engine, which made up the second stage of the Saturn V, and the now discontinued space shuttle main engines (SSME) also used liquid bi-propellants to power themselves with the fuel being liquid hydrogen (LH_2) while the oxidizer being liquid oxygen (LOX). It should be noted that although the LH_2 – LOX combination has many disadvantages when it comes to storage and handling, it does have a very high specific impulse (420s) and is thus a very popular propellant combination.

An important advantage of liquid propellant rocket engines is the fact that it is possible to throttle the propellant as well as reliably terminate the thrust produced; something which is not possible with solid propellant rockets. This becomes particularly advantageous when it comes to aborting a launch and in general for other safety reasons when the thrust power from the engines would need to be switched off. This throttling capability also allows the engine to be restarted as well as be pulsed quickly to account for quick altitude and velocity changes [3].

1.1.2 Solid Propellant Rockets

Solid propellant rocket motors usually have no moving parts and unlike liquid propulsion system, the solid propellant rockets do not require any complex injection system or high pressure

storage tanks. This makes the solid propellants rocket system operationally very simple and reliable. The solid propellant rockets usually consist of the solid propellant grain that is contained within the combustion chamber, an igniter is positioned appropriately, and a nozzle is used to accelerate the hot combustion gases and create thrust. A simple schematic of a solid rocket motor, which has a center-perforated grain in a star configuration to allow for neutral burning (in which the burning rate remains constant with time), is shown in Figure 1-2. Once ignited, the combustion of the solid propellant continues at a predetermined rate until all the propellant is consumed. Thus solid propellant rockets usually lack a mechanism in which the combustion can be stopped and then restarted when needed. Also, due to the lack of feed valves and other control mechanism, the thrust produced cannot be changed after the start of the combustion by throttling.

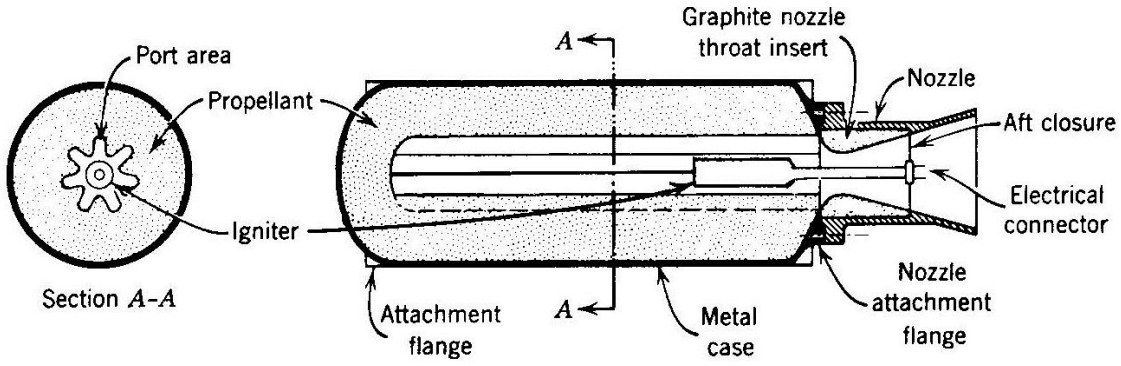

Figure 1-2: Schematic of solid rocket motor (taken from [1]).

Owing to the system being so simple and easy to understand and fabricate, solid propellant rockets are the oldest rockets of all. The first solid rockets were developed by Chinese alchemists, who were experimenting with mixing various chemicals which were known to be 'flame-producing'. There have been reports that they mixed chemicals such as charcoal, sulfur, and potassium nitrate to form black powder, the first solid propellant. The initial use of solid propellants was in fireworks, and the applications were mostly peaceful except for a few instances in which they were used by the Chinese as 'fire arrows'. But solid propellants are now more ingrained in the imaginations of the

people in the form of black powder used in guns and other explosives when they became popular in Europe in the 19th century. Unlike other forms of propulsion, whether it is chemical or otherwise, since solid rockets are so simple, the course of their development is mostly concerned with the development of the propellant itself. A detailed discussion on this development has been given by Davenas [4].

Modern solid rocket motors are able to offer high impulse density and combine that aspect with a relatively simple design. They are thus the cheapest and least complex method to generate the high thrust needed for lift-off. Also, in cases where the major part of the propulsion for a vehicle comes from liquid propellants, solid propellants have often been used to act as booster rockets for increased performance during intensive tasks such as lift-off [4]. This, along with good aging characteristics and excellent storage properties of the propellants, has made solid rocket motors the most widely used propulsion system for current tactical and ballistic missile designs with a bright future for military and space applications.

1.1.3 Hybrid Propellant Rockets

Hybrid propellant rockets have the two propellant components stored separately with one being in the liquid phase while the other is stored in the solid state. The concept of the hybrid rocket engine was developed in the 1930s and it has received considerable interest owing to the fact that it has a number of advantages when compared to liquid and solid propellants as it combines the advantages of both these types of propellants. The main advantage of using hybrid propellants comes down to safety. Unlike solid propellants, hybrid propellants are stored separately and are thus less prone to accidents while in storage or while loading. More importantly the flow of the propellants can be stopped or modulated in case of a malfunction. The fuels are more inert than those compared to

other propulsion systems and they are also less prone to cracking like solid propellants and are thus safer to handle.

A classical hybrid motor has the fuel in a solid form (Hydroxyl-terminated polybutadiene (HTPB) or other hydrocarbon polymer) along with the oxidizer being in the liquid form (LOX, N_2O) [5], although the inverse of this configuration has also been studied. A simplified schematic of a typical hybrid rocket motor is shown in Figure 1-3.

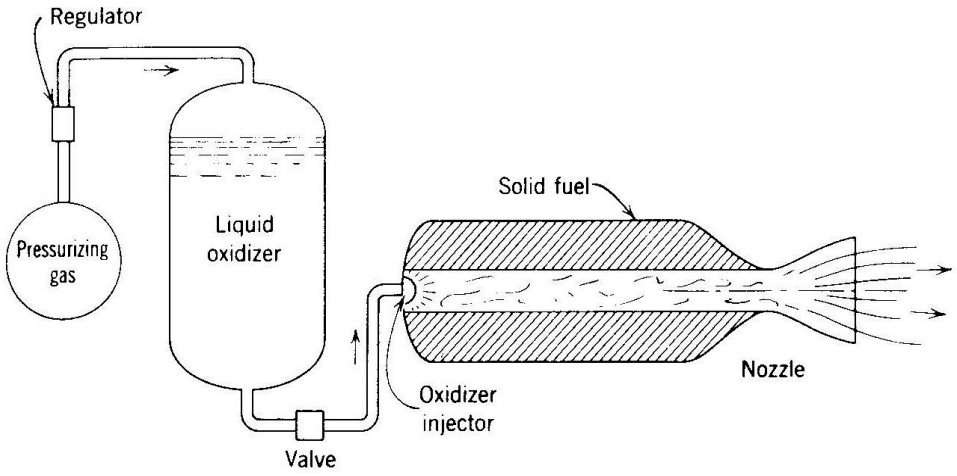

Figure 1-3: Simplified schematic of hybrid rocket motor (taken from [1]).

Apart from being safer than the other propulsion systems, hybrid rocket engines also have relatively low cost and complexity of construction when compared to liquid propellant systems. Hybrid propellants also have higher specific impulse and thrust modification abilities when compared to solid propellants. These advantages have spurred research in the field of hybrid propellants in the past and especially in the 1960's considering that the advantages of hybrid propellants made them very well suited for manned space flights. The history of hybrid rocket development has been well discussed by Risha [6] and can be referred to for more information.

The primary disadvantage of the hybrid configuration that has stopped it being a commercial success is the fact that there is insufficient knowledge when it comes to many aspects of hybrid

propulsion. Some of these aspects include efficiency, burning rate, controlling of the oxidizer to fuel ratio. Other disadvantages of this technology include the relatively low mass-burning rate of the solid fuels (thus requiring a large burn surface), high combustion temperatures, complex and delayed ignition, complex injector designs, prone to large-amplitude, low-frequency pressure fluctuations and a serious difficulty in scaling up of laboratory hybrid engines [1], [7].

1.1.4 Hypergolic Propellant Rockets

Hypergolic bipropellants are a special variety of liquid propellants and are defined as fuel and oxidizer pairs which are able to spontaneously ignite when they come in contact with each other. This spontaneous ignition negated the employment of complex ignition systems and a hypergolic engine can be properly controlled using just two valves (one for each of the two fluid propellants) [8]. But although the ignition systems may be simpler, the ignition process itself involves a complex interrelation between physical and chemical phenomena which is poorly understood. The discovery of hypergolicity occurred in Germany around 1937 and there has been widespread research on hypergolic propellants, especially since the 1950s. Hypergolic propellants have proven to be an attractive energy source for propulsion due to the fact that they have high density, long term storage ability and high performance [9]. These propellants have been used for a variety of applications such as spacecrafts and certain tactical missiles that use multiple small thrusters for vehicle control because they provide a very simple and reliable design. However as these fuels are usually very toxic and in some cases carcinogenic, there is a need to identify new less toxic fuels. To develop these fuels, we need a better understanding of the processes leading to ignition (e.g. condensed-phase and gas phase kinetics, molecular and turbulent mixing, etc.) during hypergolic combustion.

A popular fuel-oxidizer combination for use in hypergolic rocket motors has been monomethylhydrazine (MMH) with red fuming nitric acid (RFNA) due to their short ignition times

and high specific impulse [10]. Other hydrazine based fuels such as unsymmetrical dimethylhydrazine (UDMH) have also been used with nitrogen based oxidizers such as dinitrogen tetroxide (NTO). However hydrazine based fuels are shown to be highly toxic and carcinogenic in animal testing, and while the same results have not been detailed in humans, it is expected that these fuels pose a health risk to the personnel handling them [2]. To reduce these risks there has been active research to find less toxic hypergolic alternatives, and a group of tertiary amines and azides has been identified [11]–[23]. The most promising of the proposed replacements are dimethylaminoethylazide (DMAZ) and tetramethylethylenediamine (TMEDA). And although TMEDA and DMAZ are not expected to surpass the performance of MMH, they have been shown to be less toxic [24]. It should be noted though that a mixture of TMEDA and DMAZ has been reported to have ignition characteristics as the MMH-IRFNA systems [15] and the mixture could be a viable option in the shift to less toxic hypergols.

1.2 Dissertation Overview

The following sections of this dissertation are intended to provide the reader with a deeper understanding into hypergolic propellants and the methods used to study them – both conventional and the newer ones proposed in the present study. First, in Chapter 2, a comprehensive overview is provided, which includes methods conventionally used to study hypergols and the popular hypergols currently being researched. The chapter also provides reasoning into why newer methods of studying hypergols are needed. Chapter 3 provides an introduction to physics at the micron-scale and explains how the current study aims to use microfluidics to address some of the issues encountered in the conventional methods used to study hypergols. Chapter 4 discusses, in detail, the fabrication processes used to fabricate the microreactors for the present study. Chapter 5 describes the cold-flow characterization of the fabricated microreactors using Particle Image Velocimetry (PIV) techniques as

well as numerical simulations. Chapter 6 explains the experiments carried out using conventional methods as well as the fabricated microreactors with reactive hypergolic propellant pairs. And Chapter 7 carries forward the study of these reactive propellants by discussing the numerical simulations of reactive flow in the microreactors. Finally, Chapter 8 draws up the conclusions from the present study and suggests future work that can be performed to continue the work carried out in the present study.

Chapter 2

Literature Review on Hypergolic Propellants

As a complex ignition system is not needed for hypergolic propellants, these propellants are able to have better restart reliabilities than other types of propellants and thus are ideal for space missions and spacecraft maneuvering systems [8]. The Titan, Gemini and Apollo missions all used hypergolic bipropellants and the service module that first orbited the moon and later returned the astronauts to earth used a single hypergolic engine. The lunar excursion module that landed the astronauts on the moon used separate hypergolic engines for both the descent to the surface of the moon as well as the return journey back to the service module. The use of hypergolic propellants is still very popular with the Ariane, Long March, the Space Shuttle and the International Space Station programs all using hypergolic propellants [25].

A major issue with the hypergols currently in use is that the reactants are usually extremely toxic in nature. There is thus an urgent need to develop hypergolic fuels that are less toxic to humans and the environment. But the only way to develop such fuels is if we can better understand the chemical kinetic mechanisms taking place during hypergolic combustion. If a better understanding of the chemical kinetics and the free radical generation exists for the toxic, but popular hypergolic systems, these mechanisms can be eventually used to develop alternate organics or mixtures of organics that produce similar or even better performance when compared to the current hypergolic propellants but at reduced toxicity levels.

2.1 Approaches to the Study of Ignition in Hypergolic Propellants

"Hypergolic ignition is said to rely on exothermic low-temperature liquid-vapor chemical reactions that initiate combustion throughout the chamber. The vaporization of the propellants in the confined space of the chamber and the initial rise in the chamber pressure are critical to the ignition and the ensuing chemical reactions cause pressure and temperature rises which further accelerate the reaction rate, leading to thermal runaway or ignition [26]. Important physical and chemical processes involved in the ignition of a hypergolic propellant engine include the response of the propellant feed system, the manner in which atomization of the spray occurs, the mixing between the propellants, the vaporization of the droplets formed after atomization, the evaporative cooling of the droplets formed, condensation of preignition products on the chamber walls, flashing, the reactions between the liquid and the gas phases of the propellants, thermal ignition and transient combustion. Thus, the study of ignition and combustion using hypergolic propellants can be a complex endeavor. Numerous studies have tried to simplify these aspects to understand the fundamentals of the ignition processes in hypergols.

An important measure of hypergolic activity is based upon ignition delay times. Ignition delay time can be defined as the temporal delay from the contact of the fuel and oxidizer to full combustion. A long ignition delay is considered to be unfavorable as it allows the explosive intermediate species and unburned propellants to accumulate in the combustion chamber and may lead to detonation upon ignition [2]. The ignition delay as described earlier contains both the chemical delay and the physical delay times. The chemical delay is governed by the chemical reactions occurring between the propellants while the physical delay deals with the physical properties of the propellants or the experimental technique used. These physical properties may include properties of the propellant such as viscosity, surface tension and miscibility or be dependent on the manner of injection of the propellants into the chamber. Thus a comparison of chemical delay times gives a more accurate comparison of the chemical performance of the hypergolic propellants

than using just the ignition time delay as the chemical delay times will be independent of the mixing technique used. There are a number of techniques that are used to measure the ignition delay of hypergolic propellants.

2.1.1 Liquid Drop Tests

Drop tests usually consist of an experimental setup wherein one reactant is dropped from a set height into a stationary quantity of the second reactant. The original drop test was standardized by Broatch [27] and had a crucible with a fuel into which droplets of various sizes of the oxidizer were dropped. A beam of light was focused onto the crucible, with a photocell placed a set distance away. The stream of oxidizer droplets broke the light beam as they fell into the crucible triggering the start of the measurement and the photocell ended the measurement when it sensed the appearance of a flame. A schematic of the Broatch drop test is provided in Figure 2-1.

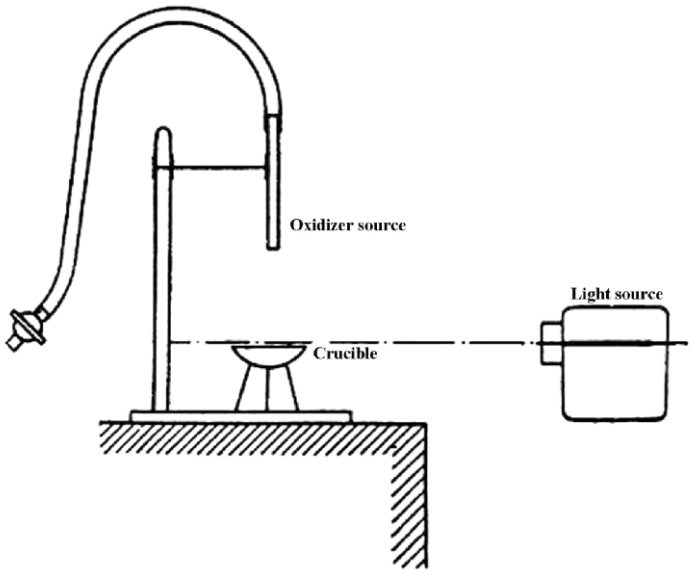

Figure 2-1: Schematic of Broatch's liquid drop test (taken from [27]).

Since the size of the droplets could not be controlled and the fuel to oxidizer ratio could not be accurately computed, the delay time suffered from variabilities inherent to the experimental setup. Moreover the photodiode used was a simple one and was not able to gauge the strength of the reaction.

Gunn [28] made changes to the setup such that the droplet sizes could be much better controlled and the triggering mechanism for recording the delay time was improved. Recent studies by Hampton et al. [25] and Alfano et al. [29] have used high power lasers and two photodiodes instead of the original one used by Broatch. These photodiodes, unlike the earlier one, are also able to calculate the strength of the reaction, apart from just gauging the time delay in the reaction. The use of two photodiodes enables the setup to distinguish between when the droplet hits the reactant in the crucible and when the reaction starts (in the form of a vapor trail). This gives the setup the added advantage of being able to isolate the chemical delay time from the overall ignition delay time. Although much progress has been made in drop tests, these tests are very prone to variabilities that are inherent to the experiment and even with the use of two photodiodes these experiments only yield qualitative results. Despite these variabilities, due to their ease of setup, drop tests are often used to measure ignition delays and are used as screening tools to determine if a propellant combination is hypergolic.

2.1.2 Mixing Tests

Modified forms of drop tests that usually enhance mixing between the reactants are usually referred to as mixing tests. Instead of just using droplets like in the drop test, Pino [30] used injectors to actually inject the oxidizer into a stationary fuel. This pressurized injection helped in better mixing of the two reactants than what could be achieved using the simplistic drop tests. Again, the measurement for the delay time was made using a photodiode. Kilpatrick and Baker [31] pressurized

the injection of both the fuel and oxidizer into a separate test chamber with the ignition delay measurement being made by sensing the change in pressure in the test chamber. This method of measurement was plagued with inaccuracies as a lot of vapor is usually generated locally by the bipropellants just before actual ignition and thus the delay times would be incorrect if just relying on a rise in pressure. Moreover, the change in pressure could occur anywhere in the chamber and thus would affect the response time for the change in pressure. Instead of using pressurized mixing, Ladanyi and Miller [32] used a small glass ampoule containing a fuel which was submerged under a few milliliters of the oxidizer. The ampoule was then crushed to release the fuel and mix with the stationary oxidizer. The ignition delay was measured by sensing an appearance of the flame with the initial time being the time at which the ampoule was crushed. The mixing rates varied from test to test as the ampoules differed from one another and also as mixing of the fluids could not be well quantified. This in turn had an effect on the calculated ignition delay times.

2.1.3 Impinging Jet Tests

Impinging jet techniques rely on the impact of liquid streams to mix and atomize the propellants under study. The streams or jets are created by forcing the liquid propellants through small orifices in injectors. The injectors usually have a length that is much greater than the orifice diameter. A circular cross-section is the most popular configuration for the orifice, although square and rectangular cross-sections have also been studied. As two cylindrical liquid jets impinge, a liquid sheet is formed in a plane perpendicular to the plane of the two jets. The perpendicularity of the two planes is dependent on the location of the point of the impingement of the jets relative to the centerline of the jets. This alignment affects the mixing between the two liquid jets and thus the atomization of the spray produced after impingement. Other major factors that influence the mixing are usually orifice

diameter ratio, impingement angle, properties of the liquid, jet momentum ratio and the overall quality of the jet produced.

Saad and Goldwasser [33] used the impinging jet technique for their experiments with hypergolic propellants. The measurement for the time delay was started at the time the valves for the injectors were released and a photodiode measurement of the appearance of a flame was used to end the measurement. As the time measurement did not start when the two propellants came in contact with each other, the time recorded in their studies was not the ignition delay as usually defined in literature.

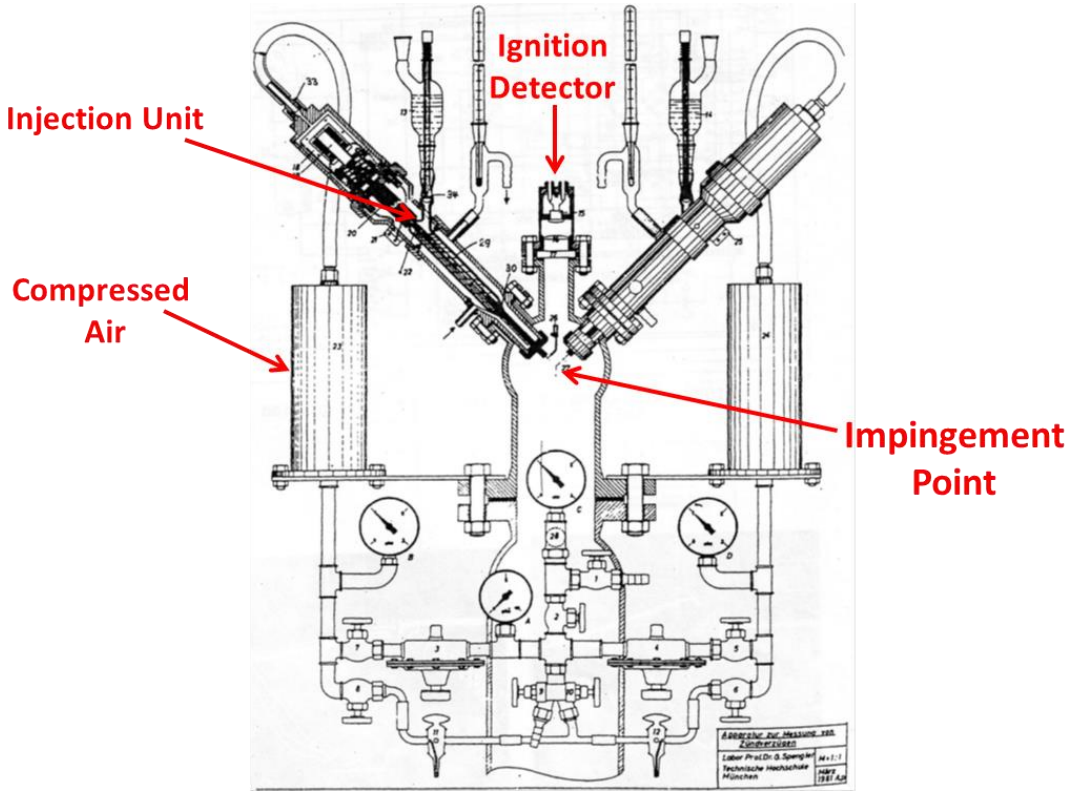

Figure 2-2: Impinging jet apparatus using two jets for measuring ignition delay of hypergols by Spengler and Bauer (taken from [34]).

Spengler and Bauer [34] (Figure 2-2) on the other hand, conducted impinging jet experiments in which the measurement of the time delay was started when the two jets impinged on each other and

thus gave a far more accurate value for ignition delay times. It should be noted that just like the droplet and mixing tests, the impinging jet technique is highly dependent on the transport and mixing of the propellants under study. Thus the information gathered from these tests is rudimentary at best. The impinging tests are mostly used to simulate actual rocket engine injectors in ignition experiments.

2.2 Hypergolic Reactants

Considering that there has been widespread research into hypergolic reactants over the past few decades, there exist a large numbers of hypergolic fuels and oxidizers. Although there is a large variety in terms of numbers of hypergolic reagents available, these reagents are usually limited to certain groups of chemicals. The oxidizers usually are from among nitric acid, oxides of nitrogen and other strong oxidizers such as hydrogen peroxide and fluorine. Some examples of oxidizers include pure nitric acid, white fuming nitric acid (WFNA), red fuming nitric acid (RFNA), nitrogen tetroxide (NTO) and hydrogen peroxide. Fuels on the other hand include organic compounds including amines, polyatomic phenols, heterocyclic compounds and even some alcohols. Usually used examples of fuels include hydrazine, monomethylhydrazine (MMH), unsymmetrical dimethylhydrazine (UDMH), furfuryl alcohol, and aerozine-50 (a mixture of 50% hydrazine and 50% UDMH). The most popular combination of these propellants is MMH with NTO as the ignition delay times are small and there is also a large specific impulse available [35].

2.2.1 Monomethylhydrazine (MMH)

Monomethylhydrazine (MMH) is a hydrazine derivative formed by replacing one of the H-atoms with a methyl (CH3-) group. A schematic of the chemical structure of MMH is shown by Figure 2-3. It is a clear, colorless, volatile liquid and has a sharp, fishy ammonia-like smell which is

typical of organic amines. It has a melting point of -52˚C and a boiling point of 87˚C. MMH is known to be a highly reactive reducing agent and contact with oxides of copper or iron and with lead, manganese, copper or their alloys can lead to fires or explosions. Monomethylhydrazine is considered to be a potential human carcinogen [36] and the current permissible exposure limit for MMH as recommended by the Occupational Safety and Health Administration (OSHA) is 0.2 parts of MMH per million parts of air (ppm).

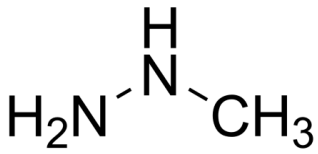

Figure 2-3: Chemical structure of monomethylhydrazine (MMH).

MMH has been a popular hypergolic propellant in the past few years and the research on its properties and its hypergolic properties have been extensive. These studies have included in-depth analysis of its thermal decomposition, its hypergolic behavior with nitric acid, with nitrogen tetroxide (NTO), as well as studies of its behavior with other oxidizers.

Thermal decomposition studies of MMH have helped provide an understanding into its thermal stability and storability, but more importantly these studies have also helped in understanding pre-combustion reactions as well as help in formulating full mechanisms for combustion. A full mechanism would consist of both the condensed-phase and gas-phase reactions in both the combustion as well as at the preignition stages and would be extremely helpful in modeling a rocket motor. Early studies were carried out for thermal decomposition of MMH by using flow reactors at elevated temperatures at atmospheric and low pressures [37], [38] and it was found that H_2, NH_3, HCN, CH_2NH and CH_3NNH were the major products. Numerous shock tube measurements [39]–[41] of the decomposition of MMH have been carried out over a large range of temperature and pressure to calculate the pressure dependence of reaction rates. A number of mechanisms for the

decomposition of MMH have been suggested over the years with Sun and Law [42] recently proposing one which had 160 reactions involving 43 species based on the quantum Rice-Ramsperger-Kassel (QRRK) theory. At atmospheric conditions, the reactions involving N-N and C-N bond scission were found to be the major reaction pathways.

MMH is known to be extremely reactive with NTO and thus a number of studies have detailed the preignition behavior [43] as well as ignition characteristics between the two at different pressures and mixture ratios. These tests were carried out using simple drop tests [44] as well as impingement tests [45]. It was found that the ignition delay was highly dependent on droplet size and impact velocities. These tests have led to the development of reaction mechanisms as well as combustion models. Saad et al. [46] analyzed the products of condensed-phase MMH/NTO reactions under non-ignition conditions at -20°C in CCl_4 solution. Their results showed the major pre-ignition products included methylhydrazinium nitrate ($MMH \cdot HNO_3$), N-methylformamide (CH_3NHCHO), CH_3NH_2, $(CH_3)_2NH$, CH_3OH, CH_3NHNO, $(CH_3)_2NNO$, H_2O, N_2, and oxides of carbon and nitrogen. Meanwhile, Catorie et al. [47]studied the gas phase reactions to create a mechanism for gas-phase preignition reactions that indicated a series of HONO elimination reactions. More recently studies [48] have developed a reaction mechanism for MMH and MON (mixture of NTO and NO) which has also been used to model a vortex engine.

As NTO is known to be extremely toxic and corrosive to even aerospace-grade materials, more recent research on MMH hypergolicity has concentrated on its combustion with nitric acid and its variants such as white fuming nitric acid (WFNA) and red fuming nitric acid (RFNA). Numerous drop and impinging jet tests have been done using RFNA as the oxidizer [44], [49]. But actual experimental studies of the chemical reactions between MMH and nitric acid are very scarce. A recent study [50] has used chemical pathways similar to those in their MMH-MON mechanism to formulate a mechanism for the MMH-nitric acid reactions. This mechanism though only concentrates on the gas-phase aspect of the interaction. More recently Wang et al. [51] have conducted drop tests

as well as conducted spectroscopy of the products of the reactions using MMH and various forms of nitric acid. This study identified both gas-phase and liquid phase reactions leading up to ignition and proposed a mechanism for the reactions. The experimental study proposed that MMH, on interaction with nitric acid, first gets neutralized to monomethylhydrazinium nitrate ($MMH.HNO_3$) which is then oxidized to methyl nitrate (CH_3ONO_2).The nitrate is usually the salt seen at the end of the reaction as well the cause of the aerosol cloud in the gas-phase reactions.

2.2.2 N,N,N',N' – Tetramethylethylenediamine (TMEDA)

As mentioned earlier, although hydrazine-based fuels such as MMH are the industry norm and are heavily used as hypergolic propellants due to their high performance, they are highly toxic and carcinogenic. Thus the development of environment-friendly propellants is of extremely high interest.

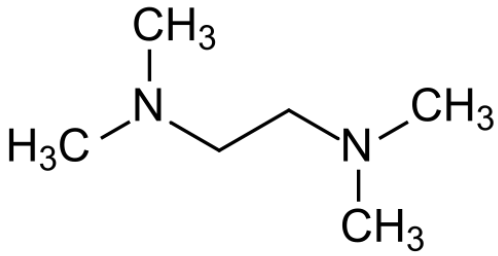

Figure 2-4: Chemical structure of N,N,N′,N′ - Tetramethylethylenediamine (TMEDA).

Alkyl mutiamines have been suggested as candidates to replace toxic hydrazine derivatives and a series of tertiary amines have recently been developed and tested as alternative fuels [12], [15], [17]. Among the various alkylamines proposed, Tetramethylethylenediamine (TMEDA) is considered to be one of the most promising because of its short ignition delay when reacting with white fuming nitric acid (WFNA). WFNA consists of pure HNO_3 with no more than 2% water and less than 0.5%

dissolved nitrogen dioxide or nitrogen tetroxide. Although the reaction of TMEDA with RFNA shows larger ignition delays than the corresponding reaction of MMH, the fact that TMEDA is believed to be far less toxic [24], makes it quite an attractive alternative. A schematic of the chemical structure of the TMEDA molecule is shown in Figure 2-4.

A literature survey for the uses of TMEDA shows that before it was proposed as an alternative hypergolic fuel, its main application was as an industrial ligand. After being suggested as a fuel, the army has carried out research on the viability of using TMEDA as a fuel. Chen et al. [52] have developed a mechanism for TMEDA/RFNA based on the much better understood MMH/RFNA mechanism. This research concentrated on the gas phase reactions between TMEDA and NO_2 (an important constituent of RFNA) and did not focus on the liquid phase reactions at all. The mechanism consisted of over 400 species and 1400 reactions, with the important early steps involving the H-atom abstraction from TMEDA by NO_2 and the formations of nitro and nitrite intermediates. These intermediates then dissociated to yield aldehydes and nitrosamines.

Simple drop tests have been conducted to calculate ignition delay and specific impulse between TMEDA and RFNA [15], [17]. More detailed studies of liquid phase reactions have been carried out by Wang et al. [53] between TMEDA and 90% nitric acid. These studies included analysis of the gaseous species from condensed and gas phase reactions between the two reactants using Fourier transform infrared (FTIR) spectroscopy and analysis of the salt formed by the liquid phase reactions using confined rapid thermolysis (CRT) coupled with FTIR spectroscopy. The hypothesis presented by the study was that the initiation reaction in the liquid phase between TMEDA and 90% nitric acid was an exothermic Lewis-type acid-base reaction which resulted in the formation of TMEDA-dinitrate (TMEDADN).

$$TMEDA + 2\,HNO_3 \rightarrow TMEDADN$$

These types of acid-base reactions usually have relatively low activation energies and thus the salt formation reaction is the dominant reaction and is also very rapid. This initial condensed phase salt formation reaction has been shown, through quantum mechanical calculations, to have a heat of reaction of -30 kcal/mol by Wang et al. [53] while Liu et al. [54] have estimated the heat of reaction to be -45 kcal/mol. The exothermic salt formation reaction then offers the heat needed to evaporate the other reactants, decompose the nitric acid as well as cause more reactions between TMEDA and the nitric acid to occur. In the gas phase, TMEDA and the nitric acid reacted to form either a complex or an ion that condensed to form a solid particulate cloud. This cloud was very noticeable during drop tests where it would form even before the droplet hit the surface of the reactant in the cuvette thus implying a purely gas-phase reaction.

2.2.3 2-Dimethylaminoethylazide (DMAZ)

Recently various 2-azidoethanamines have been synthesized and evaluated as potential non-carcinogenic hypergolic fuels [14] and 2-dimethylaminoethylazide (DMAZ) has been identified to be the best candidate amongst the class of 2-azidoethanamines. DMAZ is a liquid with physical properties comparable to MMH and it has been found to support hypergolic ignition with NTO-based oxidizers. But more importantly, considering the interest in finding safer alternatives to MMH, DMAZ, like TMEDA, DMAZ has proven to be less toxic and much safer [24]. A schematic of the chemical structure of the DMAZ molecule is shown in Figure 2-5.

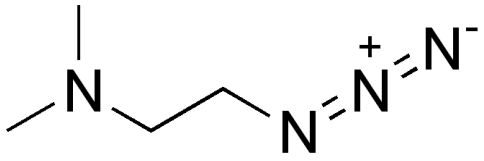

Figure 2-5: Chemical structure of 2-Dimethylaminoethylazide (DMAZ).

A literature survey found very few references to DMAZ and in most cases, before it was identified as a propellant, DMAZ was used as a pre-cursor reactant in academic chemistry. This interest in DMAZ as a propellant replacement has spurred research with numerous studies now concentrating on the thermal decomposition [55] of DMAZ as well as its hypergolic behavior with various forms of nitric acid [52], [56], [57].

DMAZ yields performance comparable to aerozine-50 in IRFNA oxidized experimental systems. However DMAZ-IRFNA systems still do not meet the higher performance standards set by the MMH-IRFNA systems, with the main stumbling block being a longer ignition delay. Stevenson [15] has recently claimed that the addition of TMEDA to DMAZ helps in reducing the ignition delay times and it was suggested that a mixture of 66.7% TMEDA and 33.3% DMAZ was capable of having minimum ignition delay times as low as 9ms for a drop test and dropping further to 4ms in an engine test.

Preliminary studies have been carried out using density functional theory (DFT) analysis to concentrate on the interaction of DMAZ with nitric acid [58]. These studies have shown that upon contact with nitric acid, a condensed phase DMAZ-nitrate is formed along with a large release of heat which occurs due to proton-transfer reactions from nitric acid to the nitrogen lone pairs on DMAZ. Studies have also been able to model the full mechanism for DMAZ/RFNA as well, based on the much more understood mechanism for MMH/RFNA and modeled the impinging stream vortex engine using these mechanisms [52]. The early steps for the DMAZ/RFNA reaction proposed by the simulation of the mechanism included (i) simple scissions of C-H, C-N, C-C bonds, (ii) N-N bond fissions via either a concerted reaction or a stepwise reaction, (iii) HN_3 molecular elimination with the formation of dimethylaminoethylene, and (iv) N_2 elimination with cyclization to form molecules with three or four member heterocyclic rings. Although there has been quite a lot of numerical studies carried out to study the hypergolicity of DMAZ and how effective a propellant it will be, very few experimental studies have been carried out to prove the same.

2.3 Current status of the field and contribution of present study

Current methods used to test and study hypergolic interactions (such as drop tests and impinging jet tests) can be stochastic in nature owing to the complexities of the number of processes that take place during hypergolic ignition. Figure 2-6 is a schematic that shows the interaction of a fuel droplet with an oxidizer pool in a cuvette. The schematic also shows the variety of processes that usually occur in a simple drop test experiment. The interaction between the droplet and the oxidizer pool usually begins with the initial mixing of the reagents in their condensed form. The mixing of the reagents is usually due to the impact of the droplet with the pool in the cuvette and it leads to the condensed phase reactions that in-turn produce heat. The heat from these condensed phase reactions causes the vaporization of both the initial reagents (the fuel and the oxidizer) as well as the products that are formed from the condensed phase and heterogeneous reactions. The fuel and oxidizer, now in the vapor phase, as well as the evaporated condensed phase reaction products now interact with each other and lead to the gas phase reactions. The gas phase reactions cause a large heat release which ultimately leads to an ignition of the vapors in the upper part of the cuvette.

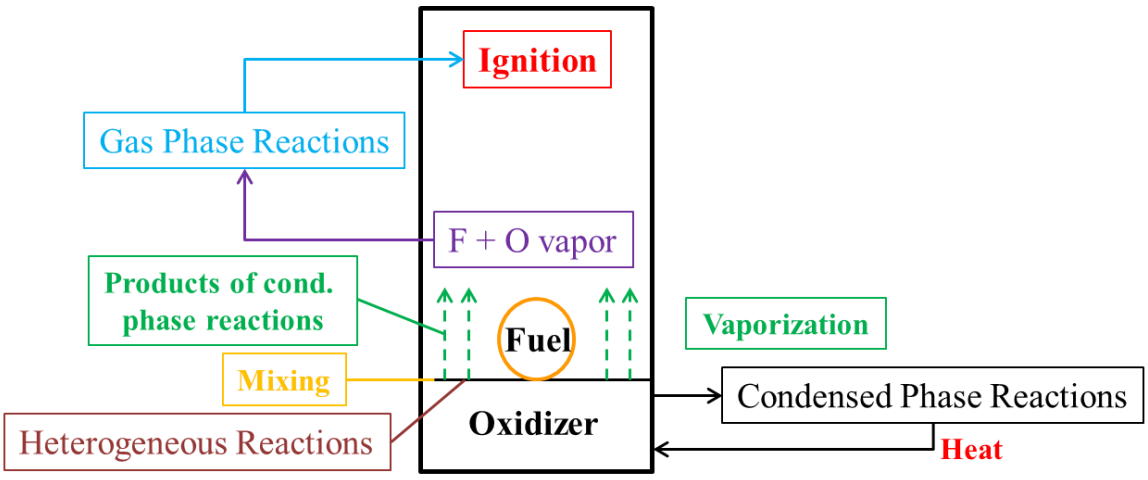

Figure 2-6: Processes involved in a hypergolic drop test.

Impinging jet tests in a similar manner involve a number of processes: impinging of the jets, mixing of the reagents from the jets, condensed phase reactions, vaporization of reagents and products, gas phase reactions and then ignition of the gases. Thus the overall process of ignition can be said to be a complex interaction between physical and chemical processes making the study of hypergols in-turn, quite complex.

The present study aims to take a new approach to studying hypergolic interactions and avoid the variabilities that arise in previous experimental studies such as drop tests and impinging jet tests (usually these variabilities are caused by variabilities in drop size and the lack of quantification of mixing between the reagents). Moreover, it has been very hard to isolate the early chemistry in previously used experimental methods. Previously used experimental techniques allow the system to transition to ignition and thus take into account both the condensed phase and gas phase chemistry. This study aims to concentrate on only the early condensed phase chemistry between hypergolic reagents and never allowing the system to transition towards ignition. Considering that most mechanisms currently in place for hypergolic reactions do not account for the condensed phase reactions at all, it is hoped that the present study with its emphasis on condensed-phase interactions will provide a much needed insight into the pre-ignition reactions and will help in creating better models for simulation of combustion and fluid dynamics of these hypergols in rocket engines.

Chapter 3

Microfluidics and Microreactors to Study Hypergolic Reactions

Although there has been widespread research conducted with regard to testing of hypergolic propellants in the manner of drop tests, mixing tests, and impinging jet tests, these studies have always been plagued by variabilities that are inherent to the test system. These variabilities in the experiment are usually caused by droplet size, the manner in which the droplet impacts the other reactant, the manner in which the two reactants impinge on each other in impinging jet tests and the most important of all factors, how the two reactants mix with one another. To control the mixing, and the environment in which the reactions occur, as well to concentrate only on the condensed phase reactions occurring between hypergols, this study aims on using microreactors rather than conduct tests on a macroscale, as has usually been done.

3.1 Microfluidics

The term fluidics was introduced as being analogous to "electronics" and is a general term that encompasses mainly hydraulic and pneumatic control systems and employs fluids (both gases and liquids) instead of electrons for signal transfer, processing or manipulation [59]. Over time the term became wider in its definition and is now used to refer to the handling of fluid flows. This handling of the flow can involve generation of the flow via pumps, guiding it through channels or conduits, storing it in vessels and most importantly, controlling the flow of the fluids. Microfluidics, similarly, is the science and technology that deals with systems capable of handling and manipulating

small amounts (10^{-9} to 10^{-18} liters) of fluids, through the use of channels with dimensions ranging from tens to hundreds of micrometers [60].

Ever since Richard Feynman [61] delivered his lecture on miniaturization at the 1959 meeting of the American Physical Society at Caltech, there has been a large spread of research in the pursuit of making things smaller, particularly electronic devices. Microelectronics became the most significant technology of the last century with the level of miniaturization getting better and better. To keep pace with the level of miniaturization in the microelectronics world, researchers are pushing the boundaries of photolithography techniques as the current dimensions of fabrication are smaller than the wavelength of light used in the fabrication processes. The development of the miniaturization of non-electronic devices though has not been at the same blistering pace as that of microelectronics. It was only in the late 1970's that fabrication techniques used in the world of microelectronics were adapted to make mechanical devices on the smaller scale. The miniaturized mechanical devices, later integrated mechanical and electrical components on a common substrate, became to be known as microelctromechanical systems or MEMS. These simple mechanical devices have improved with time and now include complex systems that are even able to mimic human muscle movement using polymers [62] and the flapping of the wings as seen in insects and small birds [63]. A natural progression of developing miniaturized mechanical devices was adding optics and fluid handling capabilities to them.

Unlike microelectronics, where the emphasis has always been on making devices smaller and smaller, microfluidics is more interested in making the volume of the fluid handled by the device smaller and smaller, irrespective of the overall size of the device. Microfluidics has thus been more intent on making more complex systems of channels with better fluid-handling capabilities by utilizing scaling laws for better performance and new effects. The early stages of microfluidics devices concentrated on the fabrication of fluid handling devices, similar to those seen in macroscopic fluid flows. Thus most of the research work in the 1980's concentrated on designing and perfecting

micropumps, microvalves and microflow sensors. The research area took a major turn in direction in the late 1980's when papers [64] were published that indicated that these microfluidic devices could be used for biological and chemical analysis. Both these fields require the ability to manipulate small quantities of fluids at very small length scales as well as have cheap and reliable diagnostic tools. Microfluidic devices can carry out various tasks using very small amounts of samples or reagents, with high resolution and sensitivity, at low cost and with a small footprint, making them very attractive for a wide range of applications.

Although most of the microfluidic applications have been in the world of chemical [65]–[67] and biological sciences [68]–[71], with an extension into medicine [72], there are also applications of microfluidics in other spheres of science. The technology has a long history of being used to develop fluid based control system, for heat management [73], display technology [74] and energy generation [75]. Fuel cell research [76] has now started to concentrate on using microfluidic principles and applications to look at flow of fluids through materials and solving their 'plumbing' issues. Microfluidic applications have not just been relevant in the world of academic research but have also made a viable impact on consumer products such as inkjet printers, where orifices less than 100μm in diameter are used to create droplets of ink, and also in liquid crystal displays. Microfluidic devices are now so advanced and improved in their function that they are now available commercially for a variety of applications.

3.2 Fluid Physics at the Micron-Scale

To design complex systems for fluid handling, it is but natural to better understand the behavior of fluids in microchannels. The understanding of fluid physics is particularly important on the micron scale, as fluidic systems can, very quickly, reach length scales where the miniaturization affects fundamental fluid mechanics rather drastically [77].

A number of physical phenomena occur in microchannels and the essential aspect of fluid physics is dictated by the competition between these physical phenomena. Dimensionless numbers have often been used to quantify this completion by expressing as a ratio, the various physical phenomena. Thus these dimensionless numbers can help qualify where a system is placed in a fluidic parameter space. The most important dimensionless numbers pertaining to microfluidics are, the Reynolds number Re (relates inertial forces to viscous forces), the Péclet number (relates convective effects to diffusion effect in the flow), the Grashof number (relates inertial forces to viscous forces in buoyant flow) and the Rayleigh number (relates convective effects to diffusion effect in buoyant flow). We will concentrate on just the Reynolds number and the Péclet number in this study as they are the most relevant to the processes of mixing in microfluidic devices.

Before a discussion into how the two dimensionless numbers affect flow in the microchannels, it is important to study basic fluid properties and the dimensional parameters that characterize them. Fluids, even at the very small scale usually used in microfluidics, can be considered to be continuous. The conservation laws of mass, momentum and energy still apply and continuous fields such as density (ρ) and force density ($\boldsymbol{f}$) are used instead of the discrete quantities like mass and force. The velocity field for a Newtonian fluid can be expressed by the Navier-Stokes equations which equate the inertial acceleration to the forces acting on the fluid body. This can be expressed as:

$$\rho\left(\frac{\partial \boldsymbol{u}}{\partial t} + \boldsymbol{u}.\nabla\boldsymbol{u}\right) = \nabla.\boldsymbol{\sigma} + \boldsymbol{f} = -\nabla p + \mu\nabla^2\boldsymbol{u} + \boldsymbol{f}$$

In the equation, $\boldsymbol{f}$ represents the body force acting on the fluid, $\boldsymbol{\sigma}$ are the fluid stresses (forces per unit area) exerted on the fluid element, $\boldsymbol{u}$ is the velocity of the fluid elements, μ is the viscosity of the fluid and p is the external pressure acting on the fluid element. When the inertial forces are small

as compared to the viscous forces, the non-linear term in the Navier-Stokes equation can be neglected and the equation reduces to what is known as the Stokes equation:

$$\rho \frac{\partial \boldsymbol{u}}{\partial t} = \nabla . \boldsymbol{\sigma} + \boldsymbol{f} = -\nabla p + \mu \nabla^2 \boldsymbol{u} + \boldsymbol{f}$$

As the conservation of mass applies for both the Navier-Stokes and the Stokes equation, the incompressible flow condition requires that $\nabla \cdot \boldsymbol{u} = 0$ for fluids such as liquids.

3.2.1 The Reynolds Number (*Re*)

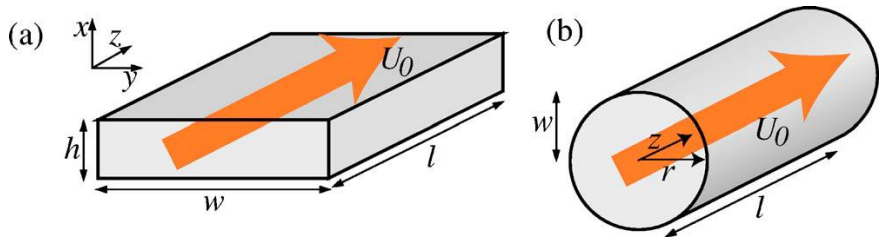

Figure 3-1: Fluid flow with characteristic velocity scale U_o through (a) rectangular and (b) circular microchannels (taken from [77]).

The Reynolds number is the most important and most cited of the dimensionless numbers when it comes to the science behind microfluidics [77]. It gives a measure of the ratio between the inertial forces and the viscous forces acting on a fluid body. The Reynolds number thus quantifies the relative importance between the two forces for a given set of flow conditions. Figure 3-1 shows a schematic of fluid flow in microchannels and denotes the characteristic velocity (U_0) as well as the coordinate system.

Viscosity is the measure of the internal resistance of a fluid which is being deformed by either shear or tensile stresses and it produces a tendency for fluid to move in parallel layers usually

referred to as laminar flow. Viscous force densities develop due to gradients in viscous force stresses and thus they tend to scale as:

$$f_v \sim \frac{\mu U_0}{(L_0)^2}$$

where, μ is the viscosity of the fluid, U_0 is the fluid velocity and L_0 is the characteristic length scale. Inertia on the other hand, is the resistance of any physical body to a change in its state of motion or rest. Inertia is based on the first law given by Newton and inertial force densities scale according to it. Thus, inertial force densities will depend on a change of velocity with time as:

$$f_i \sim \rho \frac{\partial u}{\partial t} \sim \rho U_0 \frac{\partial u}{\partial z} \sim \frac{\rho U_0^2}{L_0}$$

As the Reynolds number is a ratio between the inertial force density and the viscous force density, it can be defined as:

$$Re \equiv \frac{f_i}{f_v} = \frac{\rho U_o L_0}{\mu}$$

Thus a reduction in the length scales, as seen with miniaturization in microfluidics, results in a drastic reduction in the Reynolds number of the flow associated with it. These low values of Reynolds number in the devices mean that the inertial forces acting on the fluid are usually negligibly small when compared to the viscous. When the Reynolds number is very small, the non-linear terms from the earlier expressed Navier-Stokes equation can be neglected and the fluid flow is said to be linear in nature [77]. As the non-linear terms are neglected, the Stokes equation can be applied to

fluid flow on the micron-scale. As the Reynolds number increases, the inertial affects become more apparent and compete with viscous effects. As the Reynolds number increases further (typically $Re>10^3$), the non-linear inertial terms in the equations start to dominate over the viscous forces in the fluid. These non-linear terms can eventually lead to destabilization of the flow and causing the flow regime to transition to turbulent flow. Turbulent flow is usually characterized by the chaotic changes in properties.

Given the length scales associated with microfluidics, the Reynolds number of the flow is usually under 100 and it is safe to assume that inertial forces rarely, if ever, play a role in microfluidics. Thus, in devices with simple geometries, the flow, without the inertial non-linearity, is regular and deterministic. This makes the study of fluid flow much simpler than in the macroscopic world, where turbulence causes chaos and unpredictability.

3.2.2 The Péclet Number (*Pe*)

The Péclet number is a dimensionless number that is usually employed in the study of transport phenomena in fluids and it compares the diffusive forces acting on the fluid to the convective forces. Diffusion is defined as the random thermal motion of molecules within the environment while convection is defined as the transport of molecules as a result of the bulk motion of the fluid. Thus the Péclet number gives a measure of mixing in fluid flows and compares the relative importance of mixing via pure diffusion to mixing due to convection.

The mixing process can be better explained by taking an example in which two fluids (*A* and *B*) are flowing side by side inside a channel as shown in Figure 3-2. As the two fluids flow alongside each other, a diffusion front develops in a steady situation. This diffusion front progresses to develop in the transverse direction of the flow as one moves downstream in the channel [78], [79].

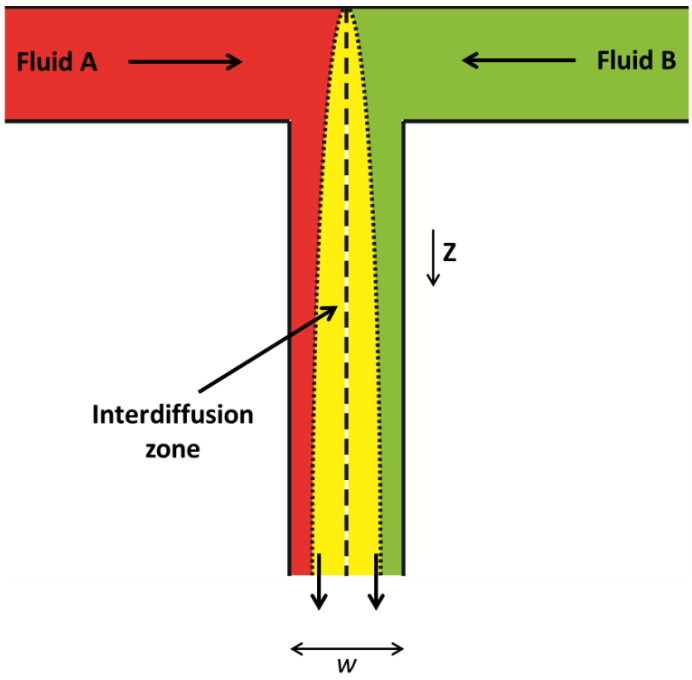

Figure 3-2: Flow and diffusion of fluids flowing in a microchannel.

If we denote molecular diffusivity of the particles as $\boldsymbol{D}$, then the time taken for the molecules to diffuse across the width of the channel would be given as $\boldsymbol{\tau_D \sim w^2/D}$. Where $\boldsymbol{w}$ is the width of the channel and thus the characteristic length for the situation. But at the same time as the diffusion is occurring, the two fluids are moving further downstream. The distance that the fluid moves in the same time can be given as $\boldsymbol{Z \sim U_o \tau_D \sim U_o w^2/D}$. A comparison of the convective flow in the fluid to the diffusive power can be calculated by comparing the number of channel widths it would take for complete diffusive mixing to take place. This comparison is the dimensionless number known as the Péclet number and is given as:

$$Pe \equiv \frac{Z}{w} = \frac{U_o w}{D}$$

Péclet numbers in general engineering applications are very large because in the macroscopic world, convection dominates over the diffusion of molecules. A major reason for this is that most macroscopic flow-fields usually have high Reynolds numbers, where random eddies churn the fluids around us, thus leading to chaotic turbulent mixing with small mixing time scales. On the other hand, due to the low Reynolds number flows in microfluidics, this turbulent characteristic of the flow is missing. The flows are orderly, deterministic and laminar. These laminar flows prevent the convection mixing to dominate and thus most, if not all, mixing in microfluidics is due to diffusion alone [77].

3.2.3 Using microfluidic physics to study reactions

Most chemical and biological applications require different solutions to be brought together and mixed rapidly to form the resultant solutions. A high degree of mixing is thus required for these chemical or biological reactions to occur quickly. For this purpose, a large part of microfluidic research has been dedicated to improving mixing and reducing the length scales over which mixing can occur so that the overall footprint of the devices can be reduced. A number of passive and active techniques [80] have been developed for this purpose and there is considerable research still ongoing in this field of microfluidics.

The opposite requirement is demanded by applications requiring the sorting of particles or analysis of chemical reactions. Here we want there to be as little mixing as possible between the fluidic streams and microfluidics is able to offer this. The laminar flow in microchannels ensures that the mixing between two streams of fluids is through diffusion only. If conditions are made to exist (either by the design of the device or the flow conditions) that the Péclet number is high, then the mixing will be negligible [81]. Thus by adjusting parameters such as fluid flow rate, contact time and

size of the microfluidic device, even the interfaces between miscible fluids can be sharply defined with very little diffusional mixing occurring between the fluid streams.

Microfluidics, thus allows us to study the interaction between reacting fluids without letting the fluid flow conditions and the mechanics of the flow affect the chemistry at the interface. Moreover, as the reagents used are very small, the study is cost effective as well as relatively safer than running tests in the macroscopic world. This is particularly true if the reagents used or the intermediates and the products formed from the reactions are toxic or unstable. Due to the excellent heat transfer characteristics of the microreactors, owing to their small volume of reactants, they are particularly useful when studying highly exothermic reactions. The high rate of heat transfer allows one to control the heat extraction from the microreactors very well and even allows reactions to occur at near isothermal conditions, something which is not possible if the tests are run on a larger scale. Thus, theoretically, microreactors make the perfect systems to test and analyze the reactions that occur when the typically highly toxic hypergolic propellants react with one another giving out a large amount of heat.

Chapter 4

Fabrication Methods for Microfluidic Devices

Methods used to fabricate microfluidic devices have long followed the fabrication techniques used in the microelectronics industry. And although there have been new techniques used to fabricate devices from polymers, the much used and perfected techniques originating from the microelectronics field still persist and are heavily used to make the fluidic devices. These microfabricated devices are usually not free standing and are usually fabricated on a substrate. The substrate most popular with the microelectronics industry is silicon, given its semi-conducting properties. Thus microfluidic devices often use silicon as the main substrate for the fabrication of devices as well. These silicon based devices have also been supplemented with devices made out of glass or quartz when optical access to the devices is required.

To fabricate microdevices, numerous processes need to be performed and more often than not, these processes need to be repeated multiple times. The level of complexity in the design of the device makes the fabrication usually more complex too and thus the repetitions only increase. Microfabrication processes often include steps in which the design is transferred from a master pattern on to the substrate (lithography), removal of material from the substrate to form structures (etching) and deposition of material or thin films (evaporation, oxidation or doping) if needed to make the surface of the devices more suitable for the final applications [82]. Modern microelectronics fabrication processes, given their level of complexity, often go through up to 30 steps of lithography and 20 steps of selective etching. These steps are often accompanied with multiple oxidation and doping steps interspersed between the lithography and etching processes. Although fabrication of microfluidic devices has not reached this level of complexity, the principles of fabrication remain the same and will be discussed in more detail in the following section.

Fabrication using silicon or glass substrates, due to the highly accurate processes used by the semi-conductor industry, is very precise and elegant. But the devices made on these substrates are usually very fragile and more often than not, very expensive. As microfluidic devices are now most often used in biological research, these silicon based devices are often unnecessary and not the best suited either. Silicon, as it is opaque to visible and ultra-violet light, cannot be used with conventional optical methods of detection and neither glass nor silicon, have properties that are required to work with living mammalian cells (such as permeability to gases). Considering it is easier and cheaper to fabricate devices that are used for microanalytical purposes using elastomers than rigid materials, most of the microfluidic devices are now not fabricated using silicon or glass.

Much of the exploratory work in microfluidic devices is now carried out in systems made from polydimethylsiloxane (PDMS), an elastomer with properties very dissimilar to silicon [83]. PDMS is optically transparent, less fragile due to its flexibility and much less expensive to work with than silicon and glass. Instead of using the usual microfabrication techniques involved with silicon, PDMS fabrication techniques are based on replication and often involve casting, embossing or injection molding [84]. Thus PDMS devices have a quick turn-around time and are very effective in a research environment where changes to the device design are frequent. Apart from PDMS, a number of other polymers such as polycarbonate and polyolefin have also been used to make microfluidic devices [85].

The use of silicon and glass is still popular in areas of research where the rigidity of the walls is an important issue. PDMS, being a flexible polymer, tends to not be very rigid and also has an especially high thermal expansion. Another disadvantage of using PDMS is that it has a high level of hydrophobicity and it is prone to absorbing non-specific hydrophobic compounds on its surface during use which leads to problems in protein analysis. Also, some applications use reagents that are not compatible with PDMS (PDMS readily swells when used with non-polar solvents such as toluene and hexane) and thus silicon and glass substrates are best suited for those applications [86]. PDMS is

also known to have low thermal and electrical conductivity which may hamper some applications. In the case of the present study, the use of highly oxidizing agents such as nitric acid warrants the use of silicon and glass channels instead of the much easier to fabricate PDMS channels.

4.1.1 Photolithography

Lithography is usually the first step in microelectronic fabrication as well as micromachining. It is the technique used to transfer copies of the master pattern onto the substrate (usually glass or silicon). The word lithography comes from the Greek words *lithos*, meaning 'stone' and *graphein*, meaning 'to write' and is used to describe the process developed in the late 1700's [82]. This process used stones that were inked and treated with chemicals to transfer images onto paper. Lithography techniques can be subdivided into different categories depending on the type of energy beam used to transfer the pattern from the master to the substrate. These techniques usually are photolithography, X-ray lithography, ion lithography and electron lithography.

The principle behind photolithography is simple enough. A schematic of the process usually used is shown in Figure 4-1 and the overall process can be covered under the following steps:

- Spinning or spreading uniformly a light sensitive photoresist (a layer that can 'resist' the etching process to be used later on) onto the substrate.
- Selectively exposing the photoresist by illuminating the substrate through a photo-mask that contains the master pattern on it.
- Developing the exposed photoresist on the substrate and completing the pattern transfer from the mask onto the substrate.

The master pattern which is transferred onto the substrates is done via use of a quartz plate called a photo-mask. This quartz plate is transparent to the incident light that is used for the photography process and the pattern is printed onto it usually in the form of a thin chromium layer.

Thus during the exposure of the photoresist, the incident light is only able to reach the selectively exposed areas through the mask.

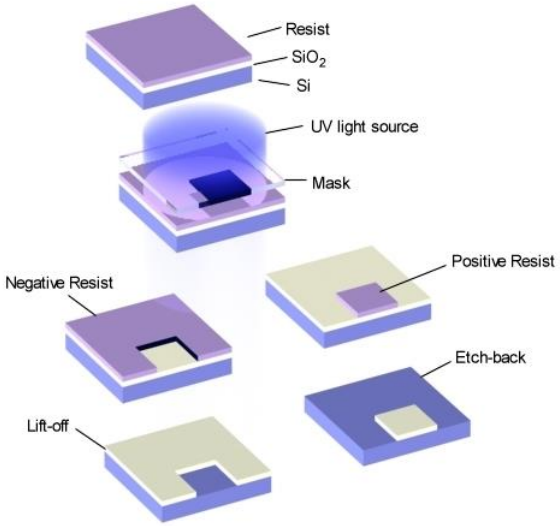

Figure 4-1: Photolithography process to etch away a thin film of silicon dioxide showing use of both a positive and a negative resist.

One of the most important aspects of photolithography is the photoresists that are used. These are materials which are designed to change their properties when exposed to incident light. When these materials absorb light, the energy from the photons in the light, breaks the original bonds present in the resist and then the resist restructures itself to form new bonds. The two kind of resists used in the photolithography process can be broadly classified as positive and negative resists. Positive photoresists are those which become more soluble in the developer after exposure to the incident light, while negative resists are those that become less soluble. Thus if a positive resist is used, the exposed regions from the mask are washed away after the developing step while in the case of the negative resist, the exposed regions are the only ones left after developing. This action is also shown in Figure 4-1.

Coating the photoresist on the substrate uniformly is an important step in the process and is usually done by spinning the resist (which is usually in the form of a viscous solution of the photosensitive polymer) onto the wafer at a high speed. At these high speeds, the centrifugal forces cause the solution to flow to the edge of the wafer from where it is expelled once the surface tension is exceeded. Thus the thickness of the resulting photoresist on the substrate is a function of solution viscosity and spin speed. The quality of the spin process affects all future steps of the fabrication on the substrate and thus is usually very precisely controlled. After spinning the photoresist on the wafer, the substrate is usually baked at an elevated temperature in a step that is called *soft baking*. The process of soft baking helps remove any solvents that were present in the initial photoresist solution and also promotes better adhesion of the photoresist layer onto the substrate.

After the soft bake, the substrate coated with the photoresist is selectively exposed through the photo-mask to an incident light. In photolithography, the wavelength of the light sources usually used range from the deep UV (150 nm) to the near UV (500 nm), with the most popular ones being the *g-line* (436 nm) and the *i-line* (365 nm) of a mercury lamp. The wavelength of the light used for exposure affects, among other things, the resolution of the lithography process [82]. It is thus closely monitored for uniformity over the entire substrate. The substrate is often again baked at an elevated temperature in a step called the *post-exposure bake*. The main purpose of the post-exposure bake is to quicken the reactions that occur in the photoresist at the time of exposure.

After the post-exposure bake, the substrate is ready for the development of the exposed photoresist. The development step converts the latent image that is formed on the resist during exposure into an actual relief image that can be used as a mask for the substrate during further steps which may include etching or deposition. Developing usually involves a solvent selectively dissolve away the resist to leave behind a pattern on the substrate, thus completing the pattern transfer from the original mask onto the substrate. The solvents sometime cause a slight swelling of the photoresist as well as a loss of adhesion between the resist and the substrate. Thus another bake step is added

onto the process after the development step. This is called the *hard bake* and it helps remove the residual developing solvents as well as improves the adhesion of the resist layer onto the substrate.

Thus, although photolithography is based on a simple concept and has been done for decades, the actual implementation is still very complex and thus also expensive. This is because there are many steps that go into completing the process and each step comes with its own set of parameters that need to be addressed in order to ensure resolution, accuracy, and batch output as demanded by the design.

4.1.2 Etching

A photolithography step is usually followed by an additive process such as thin film deposition or a subtractive process like etching. Depending on the environment in which the etching occurs, it can be divided into two categories, namely "wet etching" and "dry etching". Wet etching requires the wafer to be submerged into liquid etchant solutions and the exposed material is etched mostly by chemical processes. Dry etching on the other hand, involves etchants in the gas-phase from a plasma etching away the exposed material. The etching in the dry etching environment occurs via both physical and chemical processes [87].

Wet etching is the easiest and the least expensive method owing to the fact that it requires only the etching solution and containers to hold the wafers as they are safely submerged into the etchants. Moreover wet etching provides higher etch rates and better etch selectivity than that is offered by the dry etching methods. The main downside to using wet etching for microfabrication purposes is that it is relatively difficult to control the etching process while using wet etching methods. Moreover, wet etching being a purely chemical process, etches the silicon in a purely isotropic manner. That is, the etching of silicon takes place at the same rate in all directions. Due to the isotropic nature of wet etching, the silicon is usually etched even under the masks on top of the

wafer and the side walls in the channel are usually curved. Special wet anisotropic etchants do exist, but these only etch the silicon anisotropically along certain crystal planes. Thus the walls are usually aligned along only those crystal planes. This etching behavior for both the isotropic and the anisotropic etch using wet etching is shown in a schematic in Figure 4-2.

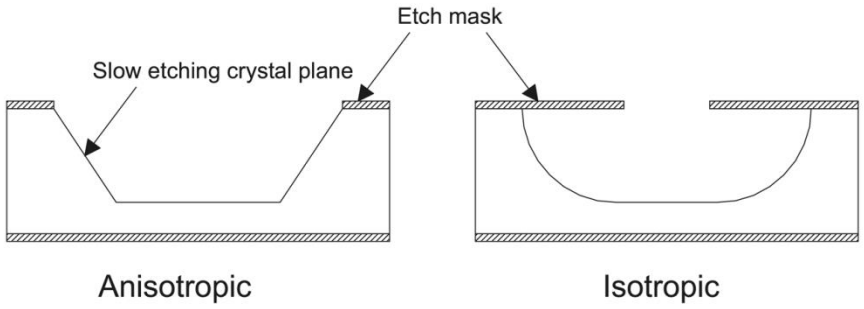

Figure 4-2: Silicon profiles after wet etching.

Dry etching is the generalized term that covers methods of etching a substrate using a gas phase by either physically bombarding the surface with ions, by a chemical reaction with a reactive species present in the gas phase or by a combination of both such that the surface of the substrate is bombarded with ions that are able to cause physical damage as well as react chemically. Physical dry etching suffers from the problem of low selectivity as the physical action of the ions cannot choose between etching away the mask on top of the substrate or the substrate itself, hence etching both at the same rate. Purely chemical dry etching is highly selective but much like wet etching, it is isotropic in nature and is thus not able to form straight side walls. A combination of this physical and chemical etching hopes to combine the advantages of both methods giving high selectivity as well as better anisotropy of the etch. This technique is called reactive ion etching (RIE) and consists of exciting the reactive gases to ions and then using low pressures and high electrical fields to bombard these ions onto the surface of the substrate almost perpendicularly. The reactive gas usually used is SF_6 or CF_4, which provides the fluorine which reacts readily with silicon to form volatile products that can be easily removed from the etch-trench.

A common problem faced even with RIE is that the side walls are not exactly straight. The top of the trench is exposed to the etching plasma and the reactive ions for a much longer time than the bottom of the trench. Thus the trench ends up being wider at the top than at the bottom and the slope in the wall only gets worse with higher aspect ratio of the trench..

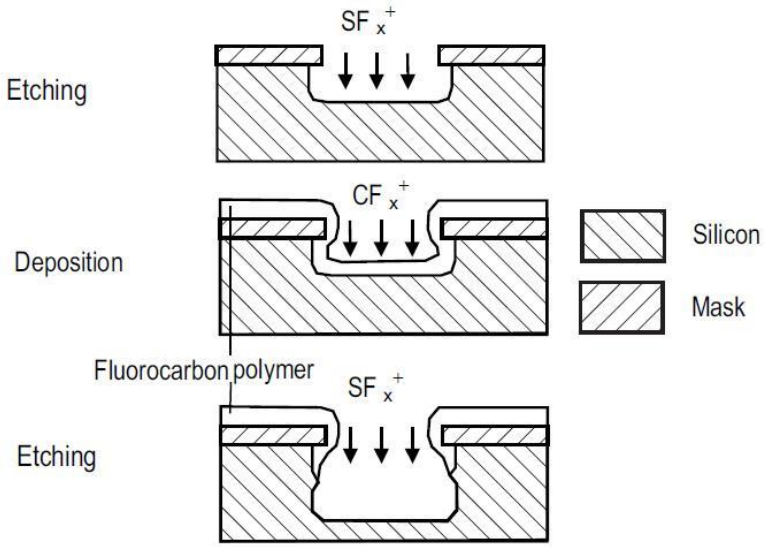

Figure 4-3: Schematic of the Bosch process (DRIE) used to improve anisotropy of RIE (taken from [88]**).**

To solve this problem, the side-walls need to be protected from the etching and a method to do just that was created by Robert Bosch GmbH, Germany [89] and is thus called the *Bosch process* and is often called deep reactive ion etching (DRIE). In this process silicon is etched using SF_6 which is switched on for about 3-10 seconds and this leads to the etching of the trench. This is followed by a deposition step in which a Teflon like layer is applied to the trench including the side walls using a gas like C_4F_8. This deposition step is again followed by an etching step in which the deposited layer at the bottom of the trench is removed by the bombardment of ions and further etching of the silicon at the bottom of the trench occurs while the layer on the side walls is left intact. Thus the side walls are

protected during the etching steps and remain straight even at large aspect ratios for the trench. A schematic of the DRIE process is shown in Figure 4-3

4.1.3 Anodic Bonding

Anodic bonding, also known as field-assisted bonding or electrostatic bonding, is a wafer bonding procedure that uses no intermediate layers between the bonded wafers. It is mostly used to bond silicon or metals to glass through the use of electric fields. A major advantage of this bonding process, compared to just plain thermal bonding, is that the process is carried out at a relatively lower temperature and thus the materials being bonded have lower residual stresses. Since both the silicon and the glass remain rigid during the process, it is possible to bond the silicon to the glass while preserving the etched features in both the silicon and the glass wafers. An important criterion while bonding wafers is the relative thermal expansion of both materials. It is desired that the thermal expansion for both materials be as close to each other as possible such that the generation of thermal stresses from the process is reduced to a minimum. Generally glass wafers with sodium in them are used for bonding purposes as the sodium addition to the glass makes its thermal expansion similar to that of silicon. The bonding between the wafers depends on surface roughness and clean surfaces. Extra care is taken to clean both the wafers before the bonding process to ensure that the bonding is more efficient.

A schematic of the anodic bonding process is shown in Figure 4-4. The chuck on which the wafer stack is placed acts as an anode while the top tool acts as the cathode. Typical voltages applied during the anodic process range between 400-1000 V. Both the tool and the chuck are typically capable of being heated and help raise the temperature of the wafer stack. This elevated temperature, usually in the range of 200-450 ˚C, helps in achieving better mobility of the ions in the glass wafer.

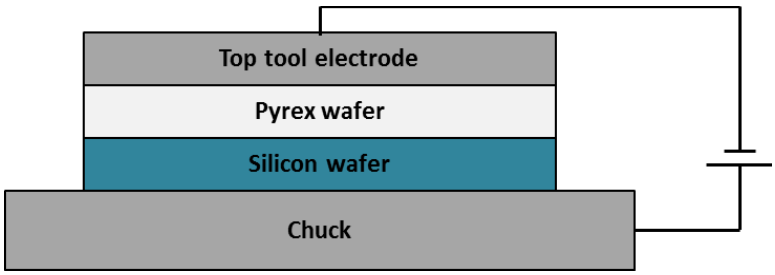

Figure 4-4: Schematic of anodic bonding process.

The anodic bonding mechanism is not yet fully understood and there are many assumptions in the process. Electrochemical, electrostatic, thermal mechanisms as well as a combination thereof have been put forward to explain the anodic bond process, but the dominant mechanism has still not been clearly defined [82]. The most accepted explanation that exists suggests that at elevated temperatures, the glass begins to act like a conductive solid electrolyte and the bonding results through the migration of the sodium ions in the glass towards the cathode. As these ions move towards the cathode, they leave a space charge (bound negative charges) in the region of the silicon-glass interface. Most of the high voltage that is applied across the wafer stack drop across this space charge region and the small width of the region results in a very high electric field across the silicon-glass interface. This high electric field generates a large electrostatic force that binds the glass and silicon wafers closer to each other. The elevated temperature of the wafer stack now results in the covalent bonding of the surface atoms at the interface of the silicon and glass wafers. During the bonding process, the temperature and the voltage are kept constant. As soon as the voltage is switched on, a large peak in current is observed, which indicates a drift of sodium ions to the cathode as well as the buildup of the space charge region. This large peak in the current is noticed to decay exponentially with time while the voltage across the wafer stack is kept constant.

4.2 Fabrication of silicon-glass microreactors for present study

As mentioned earlier, owing to the use of extremely corrosive reagents used in the present study, it is not possible to use microfluidic devices made out of polymers like PDMS as the rest of the biological and chemical research world has begun to. Instead the microreactors fabricated for this study have been made using etched silicon bonded to glass. The use of silicon is open to the questions of material compatibility between it and the various propellants that are being used. But coating the silicon substrates with an appropriate coating of either silicon nitride or another suitable metal may be easily carried out to avoid the material compatibility issues with silicon. It should be noted that there was no noticeable change in the surface of the reactors with the reagents used in the study and neither was there any surface reaction that was noticed.

In the case of PDMS devices used for biological purposes, the process of introducing the reagents into the device and the fixing of the tubing to the device hardly ever plays an issue with the device design. In PDMS devices, the inlet tubing is generally introduced into the device using vertical holes made into the polymer itself via conventional machining. The tubing is then fixed to the device using a commercially available curable adhesive. For the present reactors, the introduction of the reagents played a role into the design of the reactors too. As the top layer of the reactor was made from glass instead of a polymer, introducing tubing through the top by making holes through the glass would be difficult as well as tedious. Thus the reactors were designed to sit on a manifold where they would be held in place with a compression seal with the inlet and the exhaust ports being etched into the silicon from underneath.

To etch both sides of the silicon, a double side polished wafer was used to begin with rather than the more conventional single side polished wafers. As no electrical devices are being fabricated onto the silicon reactor, the resistivity of the wafers used was not an important parameter. But for the sake of uniformity, all the reactors for the study have been created using 4” wide n-type silicon wafers with a resistivity between 2 to 5 Ω-cm.

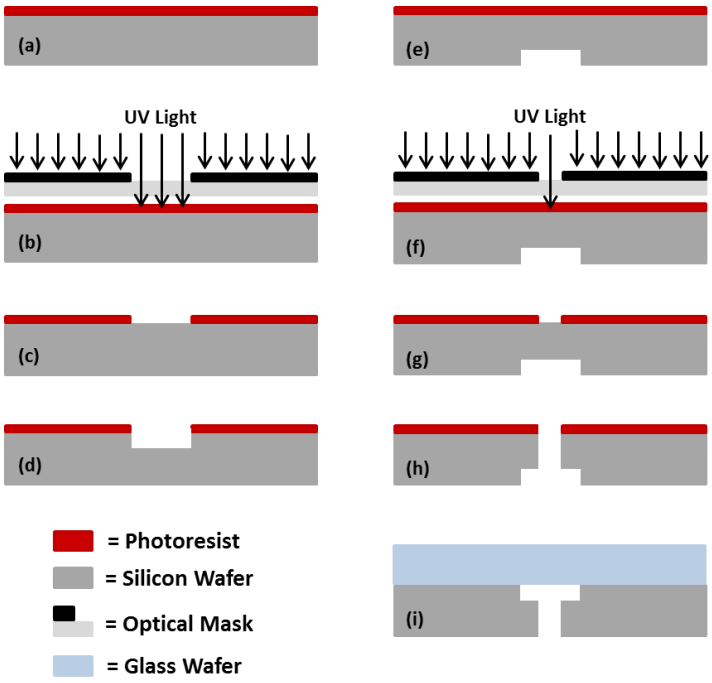

Figure 4-5: Schematic of fabrication process for the microreactors. Steps (a), (b) and (c) illustrate the photolithography process for one side of the double side polished silicon wafer. Step (d) shows the deep reactive ion etching (DRIE) of the silicon wafer to create the reactor channels. Steps (e), (f) and (g) illustrate the photolithography process for the back side of the etched silicon wafer. Step (h) shows the DRIE process for the back side of the wafer to create the inlet and outlet ports. Step (i) illustrates the anodic bonding of the etched silicon wafer to a borosilicate glass wafer.

The photolithography for the pattern transfer on to the silicon substrate was carried out using the MicroChem® KMPR. KMPR is a chemically enhanced high contrast epoxy based i-line photoresist. It was chosen over the more traditionally used photoresists such as (1810 and 1827) due to the fact that it has better adhesion to silicon as well as better resistance to chemical and plasma etchants. The pattern on the silicon wafer was etched using a deep reactive ion etching (DRIE) process where the silicon was etched anisotropically using a Bosch process [89]. The same process was repeated for etching the inlet and exhaust through-holes on the back-side of the silicon wafer. Once the etching of the wafer was complete, the silicon wafer was thoroughly cleaned using a piranha

clean solution (50% concentrated sulphuric acid and 50% hydrogen peroxide) and then bonded to a borosilicate glass wafer using anodic bonding.

The last step of the fabrication was dicing of the bonded wafer to obtain individual reactors. This was done using a conventional dicing saw (ADT 7100). A detailed description of the photolithography, etching and bonding processes used to fabricate the microreactors is given in the following section while a schematic of the entire process is shown in Figure 4-5.

Two sets of microreactors were fabricated for the study (Figure 4-6), with one mimicking the impinging jets experiment widely used to test hypergolic propellants while the other microreactor provided a stagnation flow within the channel. Each of the reactors had a main channel with a width of 240µm, a total length of 1cm and a depth of 55-60µm. The width of the inlets to the main-channel for the reactors was varied between 120µm and 240µm to study various strain rates in the main channel.

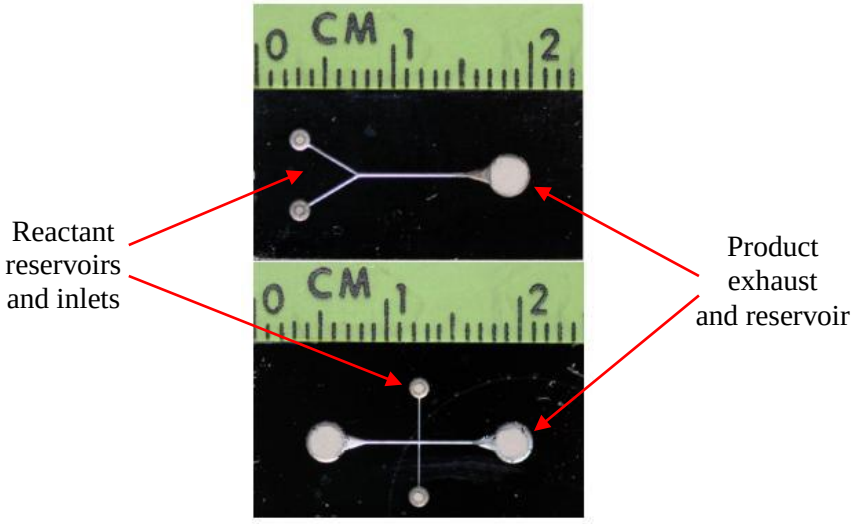

Figure 4-6: Fabricated Microreactors. Top microreactor mimics the impinging jets experiment while microreactor on the bottom is the stagnation flow microreactor.

Although two sets of microreactors were fabricated for the study, all the experiments were carried out only using the stagnation flow reactor. This was because it was noticed that the

microreactor that mimicked the impinging jet experiment always had a solid wall (of the silicon from the microreactor) interact with the fluids when the fluids first contacted each other. Moreover it was noticed that this side wall could influence the flow of the fluids down the long main channel. Any slight perturbation caused due to an imperfection in the fabrication of the microreactor would cause instabilities in the flow down the main channel. The stagnation reactor was thus preferred so as to isolate the point of contact between the fluids from the side walls of the microreactor .

4.2.1 Photolithography Procedure using KMPR

Before the actual photolithography process the silicon wafer is first cleaned by washing it with acetone and isopropyl alcohol to remove any organic contaminants and particulates from the surface of the wafer. The wafer is then washed with deionized water to remove any traces of the solvents and then dried using a stream of nitrogen. The wafer is now baked at 125˚C for at least 30 minutes to get rid of any water that may have not been removed under the nitrogen stream. The wafer is taken off the hotplate and put onto the photoresist spinner. Before the photoresist is spun on the wafer, the wafer surface is prepared by coating it with hexamethyldisilazane (HMDS). HMDS is used so as to improve the adhesion of the photoresist onto the wafer and is spun onto the wafer in a process that is similar to spinning on the photoresist. After the HMDS is spun onto the wafer, the wafer is taken off the spinner and baked on the hot plate at a temperature of 115˚C for at least 3 minutes. This baking helps get rid of all the solvent from the HMDS solution. Now the wafer is taken off the hotplate and placed on the spinner again. About 4 ml of KMPR is carefully poured onto the wafer so as to cover most parts of the wafer. Unlike regular resists like 1810 or 1827, KMPR is very viscous and it needs to be applied carefully so as to prevent non-uniformity of the resist after the spinning process. The wafer is now spun at 3000 rpm for 30 seconds to get a uniform coating of the photoresist on the wafer.

The wafer is now soft baked at 100˚C for 6 minutes and then the photoresist on the wafer is ready to be exposed. The wafer is taken off the hot-plate and cooled on some wipes until it reaches room temperature. The wafer is then transferred to the aligner (EVG-620) for its exposure. The aligner, as the same suggest, helps align the mask with the silicon wafer. The aligner is particularly useful when multiple photolithography steps are needed for a wafer. The correct exposure for KMPR is 500mJ/cm^2 and the exposure time is calculated depending on the power of the mercury lamp being used. As the development of the photoresist is especially dependent on the exposure time, much effort is spent on making sure that the incident light is uniform over the entire wafer and that the power of the lamp is correctly calibrated. The total exposure time is divided into a number of segments so as not to expose the wafer all at once. This is particularly helpful in a chemically activated resist as the time gap in between the exposure segments gives the much needed time for all the catalytic reactions to complete in the resist layer. For the current process with KMPR the calculated exposure time was segmented into 4 equal parts with equal time gaps in between each exposure.

The wafer is now transferred back on to the hot-plate for its post exposure bake which is carried out at 100˚C for 3 minutes. It should be noted that, if the exposure has been correct, the image from the mask will clearly be visible on the photoresist after the post exposure bake. No visible latent image on the photoresist usually means that the exposure time was insufficient or that the temperature of the post exposure bake was too low. After this post exposure bake, the wafer is again cooled on wipes till it reaches room temperature. The wafer is now ready for the last step in the photolithography process which is the development of the exposed photoresist. KMPR is designed to develop in 2.38% tetramethylammonium hydroxide (TMAH) aqueous alkaline developer. And CD-26, a commercially available developer from Microposit, is used to develop the wafers. The wafer is immersed into the CD-26 solution and agitated a little so as to improve the mixing of the developer solution. The development of the exposed photoresist usually takes between 4 to 6 minutes and is stopped when the bare silicon under the design of the microreactors is clearly visible on the wafer. No

hard bake of the KMPR is done for the current fabrication process as it is noticed that the hard bake causes the resist to become extremely resistant to chemicals and it becomes very hard to remove the resist even after the etch processes are complete.

It should be noted that this is the process for the first lithography step. To make the pattern for the inlet and exhaust ports, another lithography step is required. The process for this step is the same as the first one just with the added parameter of having to align the mask of the 2^{nd} pattern with the pattern already etched on the front side of the silicon wafer. This alignment is done using alignment marks that were made on the first pattern that were thus etched into the front side of the silicon wafer and a corresponding pair of alignment marks on the second mask. The alignment is of utmost importance and is achieved using the aligner system (EVG-620).

4.2.2 Etching of the microreactors using DRIE

The photolithography step is followed by the etching of the exposed silicon on the wafer. To achieve an anisotropic etch, the silicon wafer was etched using deep reactive ion etching (DRIE) using a standard Bosch process [89]. The process was carried out on an Alcatel Speeder 100 and used sulfur hexafluoride (SF_6) as the gas to generate the plasma to attack the silicon, while using octafluorocyclobutane (C_4F_8) as the source gas to generate the chemically inert passivation layer which helps in etching vertical side-walls as well as a achieve a high aspect ratio for the etch. For every cycle of the DRIE process, the SF_6 was flowed for 3 seconds at 300 sccm while the C_4F_8 was flowed for 1.5 seconds at 300 sccm. Oxygen (O_2) gas was also flowed into the chamber between the SF_6 and C_4F_8 pulses at 100 sccm for 1 second.

An LF generator was used for the process initially but it was noticed that the bottom of the etched reactor was not flat and instead had a deep ridge in the middle (Figure 4-7 (a)). The etch process was then modified to use an RF generator instead of the LF generator, while keeping the rest

of the process parameters the same. The etch resulted in perfectly flat bottom in the etched channels (Figure 4-7 (b)) and thus ensured the flow in the reactors was deterministic by having a uniform rectangular cross-section throughout the length of the reactor.

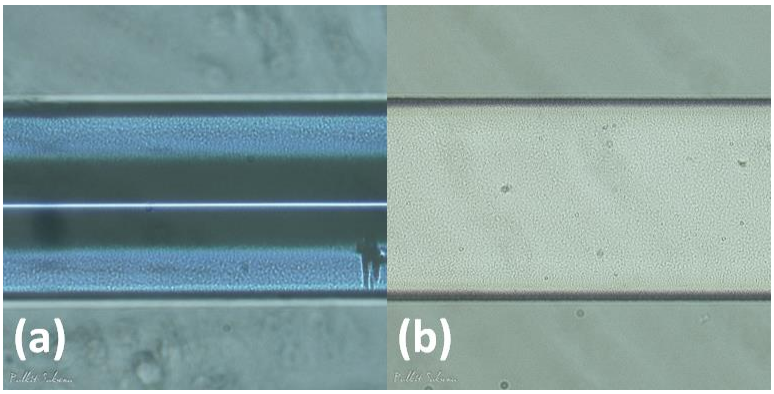

Figure 4-7: Top-view of etched main channel using (a) LF generator and (b) RF generator for the DRIE

The overall etch rate for the process was approximately 6µm/minutes with relatively straight side-walls being formed as shown in the SEM image of the cross-section as seen in Figure 4-8. A 60µm deep main-channel of the microreactor could be etched using a 10 minute etch while the back-side etch to make the inlet and exhaust ports usually took between 55 and 60 minutes of etching using the same process.

KMPR is designed to be removed using MicroChem® Remover PG and after the etching process, the wafer is immersed in a bath of Remover PG that has been heated to 80˚C. The entire layer of resist dethatches from the surface of the wafer and lifts off as a sheet in about 10-15 minutes. In case of difficulty in removal of the resist, the wafer can be put into a sonicated bath containing Remover PG.

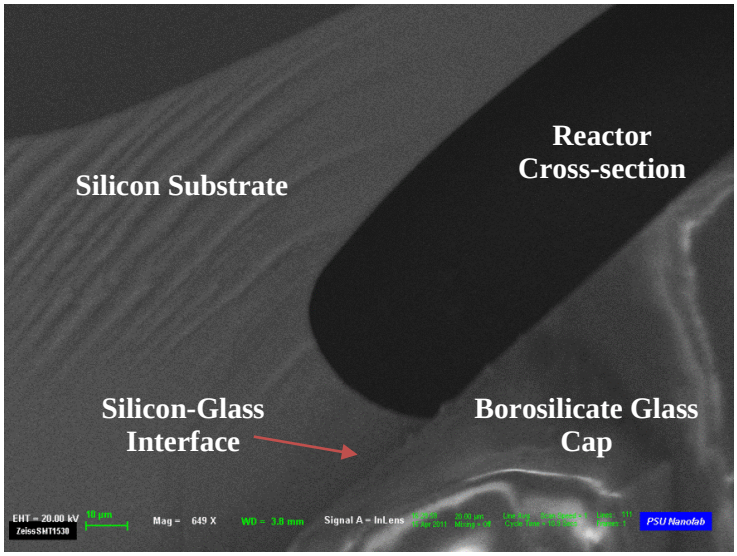

Figure 4-8: SEM image of microreactor cross-section.

4.2.3 Anodic bonding of silicon wafer to borosilicate glass wafer

Once the silicon wafer is etched on both sides as required by the design, the wafer is ready to be bonded to a borosilicate glass wafer. A major requirement of anodic bonding is that the wafers need to be free or any dust particles or organic residue. To facilitate this, both the silicon and the borosilicate glass wafers are cleaned using a Piranha clean. A Piranha clean consists of a 1:1 solution of concentrated sulphuric acid in hydrogen peroxide. Care should be taken while mixing the two as the sulphuric acid is very corrosive and the reaction between the sulphuric acid and the hydrogen peroxide is extremely exothermic. Each of the wafers is dipped into the solution for a minimum of 10 minutes and is then washed carefully but thoroughly with deionized water. The wafers are now dried under a stream of nitrogen gas and then baked at about 125˚C to get rid of any residual water from the cleaning process.

After the baking, the wafers are stacked on top of the bond chuck with the silicon wafer at the bottom. The stacking of the wafers can either be done manually or by using the aligner which was used for the lithography step, if more precision is desired. The top graphite electrode is added onto the

stack and the entire assembly is transferred into the bonder (EVG-501). The bonder is then sealed and the vacuum is switched on. The top and bottom heaters are turned on once the vacuum inside the chamber reaches a value of 10^{-5}mbar. The temperature of both the top tool and the bottom chuck are set to 400˚C and a couple of minutes are given after this temperature is reached for the temperature of the wafer stack to stabilize.

Once the required temperature is reached, a 50N force is applied onto the wafer stack to bring them in contact. A voltage of 500V is now applied to the wafer stack. Upon the application of the voltage, a large spike in current is seen signifying the displacement of the ions inside the glass and the occurrence of the bonding process. Once the current values have returned back to a low enough value, the voltage is momentarily turned off and then reapplied at a higher value of 700V. Again the current is seen to rise, only to a lesser peak value than before. The voltage is once again turned off when the current value drops off and the process is once again repeated for a voltage of 1000V. The wafer stack is now cooled back to room temperature upon which the bonded wafers are then extracted for inspection. The actual bond process, excluding the time needed for heating cooling and attaining the appropriate vacuum in the chamber, can be carried out in only takes a few minutes.

4.3 Fabrication of microreactors with through optical access

Although all of the studies with reactive hypergols were carried out with the reactors that were etched to a depth of 60 µm, another set of microreactors was fabricated which allowed for through optical access. For these microreactors the silicon wafers were etched all the way through and thus the depth of the microreactors was the thickness of the silicon wafer (500 µm). After through etching the silicon wafer, the wafer was then bonded to two borosilicate glass wafers so as to form a ‘cap’ on both sides. The process of fabricating these microreactors is very similar to the process

detailed in 4.2. The same process is used to transfer the master pattern onto the silicon wafers and a similar DRIE etching recipe is used to etch the silicon wafers after the pattern transfer.

The only difference being that as the Alcatel Speeder 100 is does not allow for through etching a wafer (as the machine is setup to make sure there are no gaps between the clamping chuck and wafer that allow for the leakage of gases), thus the wafers that were to be through etched were mounted onto a dummy wafer. These dummy wafers thus acted as a base wafer which would not be etched and thus the wafer on the top could be etched all the way through. The mounting was achieved by heat-sensitive double sided sticky tape. After the etching process the wafers were heated so as to release the etched wafer.

A common problem that was faced was that there was no etch-stop and thus once the wafer on the top was through etched, the plasma would leak to the back of the wafer and start blanket-etching the back-side of the wafer. To stop this from occurring, the wafer was coated with photo-resist (which was blanket-exposed and developed) on the back-side. This resist coating on the back side helped in protecting the back side of the wafer from any etching caused by the leakage of the plasma in the DRIE process once the wafer was through-etched. Considering that the back-side of the wafer was now protected from the etching, the DRIE process did not need to be timed perfectly and the entire process of through etching the wafer usually took between 90-100 minutes.

Once the etching was completed and the photoresist was stripped (using the method detailed in 4.2.2), and the first of the two borosilicate glass wafers was anodically bonded to the etched silicon wafer (using the process detailed in4.2.3). Once the wafers were bonded to each other, a micro-drill with a diamond-tip drill bit (0.03” diameter), was used to make inlet and outlet via-holes in the borosilicate glass wafer. Drilling the glass was chosen instead of etching the borosilicate glass wafer owing to the very slow etch rates that can be achieved while etching glass using the DRIE. The bonded wafers were then cleaned to remove any debris generated from the drilling and were then again immersed in a Piranha clean solution to prepare the silicon to be bonded on the other side. As

anodic bonding requires electrical contact with the silicon wafer from the bottom chuck (as shown in Figure 4-4), thus thin strips of Aluminum foil were used to connect the silicon wafer to the chuck of the anodic bonder. The wafer stack for the anodic bonding of the second borosilicate glass wafer to the other side of the silicon wafer is shown in Figure 4-10.

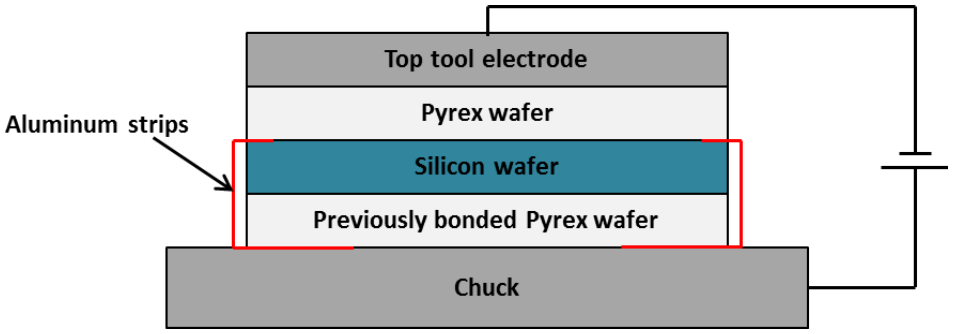

Figure 4-9: Schematic of wafer stack for anodic bonding of borosilicate glass wafers on both sides of the silicon wafer.

The actual process for bonding the wafers (after the creation of the wafer stack) now is exactly the same as that which is followed for the first bonding. As with the previous set of microreactors these reactors were also diced into individual reacrors using the ADT 7100 dicing saw.

4.4 Fabrication of microreactors using LTCC

To study the effect of reactor materials on the reaction occurring in the microreactor, as well as try out more number of reactor designs than that were possible with the silicon-glass microreactors, stagnation flow reactors were also fabricated using Low Temperature Co-fired Ceramics (LTCC). These ceramics were in the form of commercially available green tape (Dupont 951) and were originally developed as a multilayer ceramic technology. The tapes were used for microelectronic packaging primarily in telecommunication systems because LTCC had superior microwave performance as well as good thermal and mechanical properties [93]. These tapes are glass-ceramic

composite materials with the ceramic usually being alumina (Al_2O_3). A third component is the organic binder which is usually added to help bind and provide viscosity control to the tape before sintering [90]. The physical properties of the ceramic can be adjusted by adjusting the combination of materials. Commercially available tapes usually have a thickness varying from 100-400 μm and tapes of larger thicknesses can be fabricated by laminating multiple tapes together. These tapes are flexible in the green tape stage and all the machining required for the microfabrication design is done at the green tape stage.

The main advantage of using microreactors fabricated from LTCC instead of designing and fabricating new microreactors using silicon and glass is that the development process is far faster and cheaper with LTCC. Thus newer designs of the microreactors with minor changes, to account for newer thermocouples or aspect-ratio of the main channels, could be created with a relatively short turnaround time. LTCC tapes have recently been used to fabricate integrated microfluidic devices [90]–[92] and are known to be resistant to corrosive oxidizers thus making them perfect to be used with the propellants in the current study.

Figure 4-10 shows a schematic of a typical process that is used while fabricating using green ceramic tapes. The tapes are often shipped in the form of rolls and thus need to be preconditioned and blanked into flat sheets. Each of the sheets (green tape) is processed separately in its unfired stage. Desired designs and configurations (channels, vias and cavities) can be made into each sheet by cutting out the shapes in each sheet. This may be done by either punching, CNC machining or by using a laser.

These flat sheets can now be used to create three-dimensional structures by laminating multiple sheets together (to form a single structure) and then sintering/firing the structure. Lamination of the sheets is usually done by assembling the sheets on a platform with alignment pins and a subsequent application of pressure (≈ 3000 psi) and heat (≈ 70 °C) to the assembled structure. The application of pressure is usually done with the help of an isostatic press, and the sheet assembly is

usually held (at the peak temperature) for about 3-10 minutes so that the assembly can reach a homogeneous temperature.

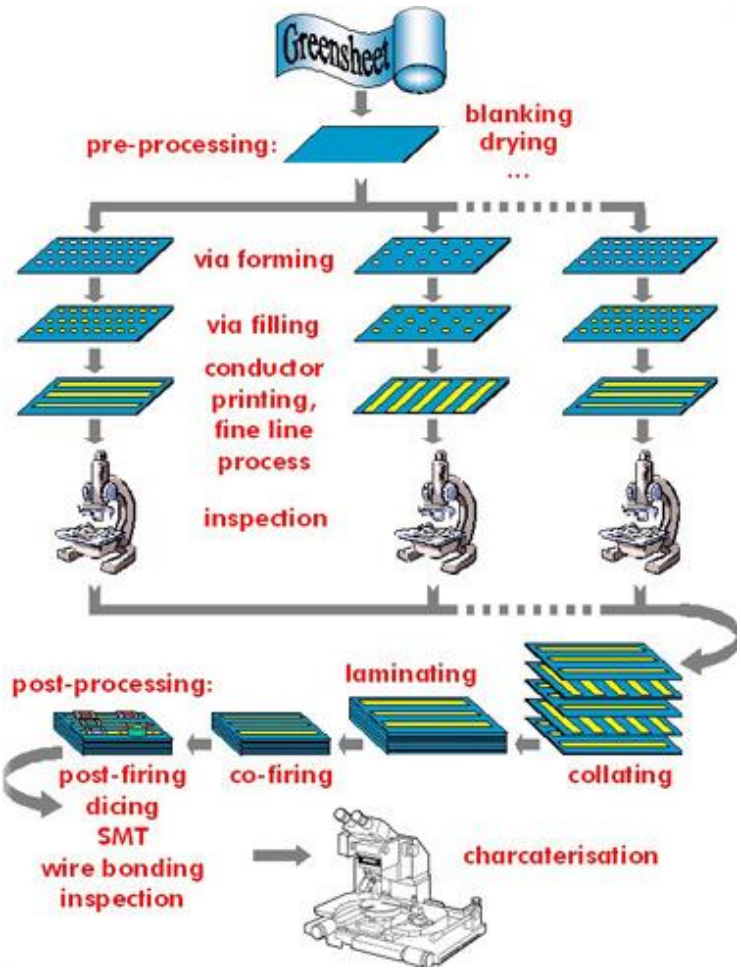

Figure 4-10: Typical process flow for LTCC fabrication (taken from [93]).

. In the sintering/firing process, the laminated sheet assembly is place in an oven with a ramped temperature profile. A typical profile starts off with a temperature ramp of 2-5 °C till a temperature of about 500 °C is reached. The assembly is held at this temperature for about two hours and the organic binder in the sheet evaporates during this step. The temperature is then raised to about 850-900 °C which is usually the sintering temperature for LTCC. The assembly is held at the sintering temperature for a duration ranging between 10 and 15 minutes and then the entire assembly

is cooled to room temperature. Dupont 951 sheets were used for the fabrication of the LTCC microreactors. The mechanical and thermal properties of the LTCC green tape used for the fabrication process are given in Table 4-1.

Table 4-1: Mechanical and thermal properties for Dupont 951 green tape.

Property	Reported Values
X and Y shrinkage (%)	12.7 ± 0.3
Z Shrinkage (%)	15 ± 0.5
Density (g/cm^3)	3.1
Thermal coefficient of expansion (ppm/°C)	5.8
Thermal conductivity (W/m-K)	3.3
Max operating temperature (K)	~ 1200
Flexural strength (MPa)	320
Young's modulus (GPa)	120

For the fabrication of the microreactors using LTCC, the design for each layer of the microreactor was cut into the green sheet using a CO_2 laser. The laser had a beam width of about 50 µm and thus all designs for the reactor had to account for the widening caused due to the beam width. The number of sheets that were used to make the reactor depended upon the aspect ratio of the main-channel that was required. Unlike the silicon-glass microreactors making new designs and changing the aspect ratio was relatively simple and quick when fabricating the LTCC microreactors.

The sheets were then aligned using a simple jig and the LTCC stack was assembled to form the three dimensional structure of the microreactors. Given the small dimensions of the inlet and outlet channels, care had to be taken while laminating the sheet assembly as a large application of force using the isostatic press caused warping or collapse of the channels. Instead a viscous organic fluid (85 wt% honey mixed with 15 wt% water) was used to bind the sheets together into an assembly. The assembly was then enclosed in a plastic bag and a vacuum was pulled onto the bag in order to spread the binding honey-water mixture evenly across interfaces of the sheets in the stack.

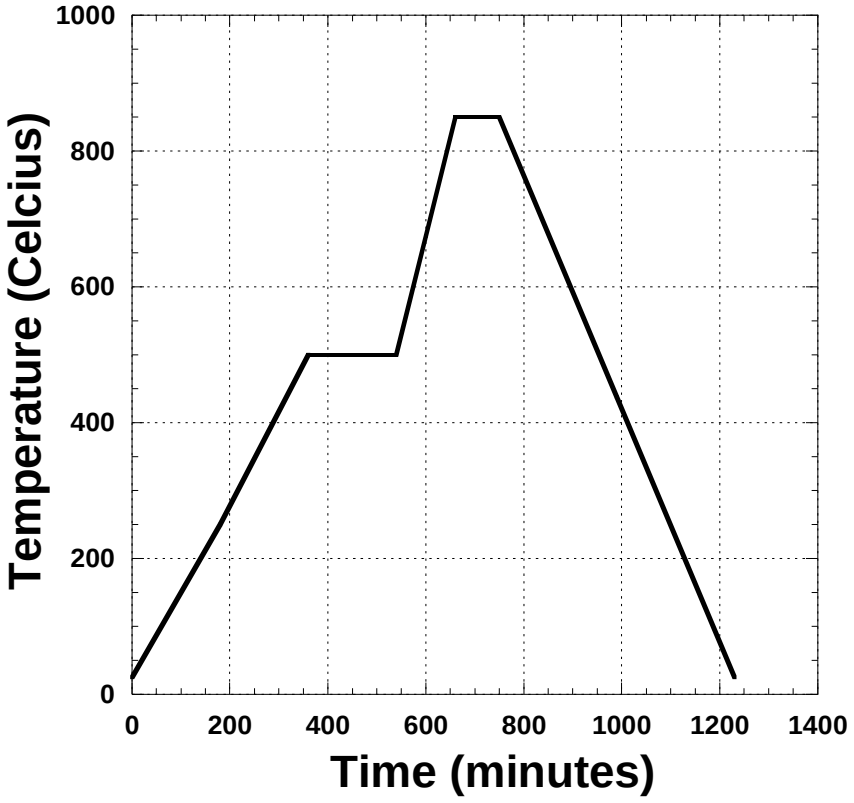

Figure 4-11: Temperature profile followed for the sintering of the LTCC microreactors.

After successfully laminating the sheets to form a three dimensional structure, the sheet assembly was diced into individual reactors. The individual reactors were now ready to be sintered and they were placed on a ceramic block inside a box furnace (Lindberg/Blue M BF51894C-1). The

temperature profile that was followed for the sintering process is shown in Figure 4-11, with the entire sintering process taking between 22-24 hours to complete.

Chapter 5

Cold-flow Characterization of the Microreactors

Before the microreactors were used to study actual reactive flow within them, the flow fields were characterized both experimentally and numerically using non-reactive liquids (cold-flow). This The non-reactive liquids used for these tests were distilled water and acetone. The experimental method employed to visualize the velocity flow-field in the microreactor was Particle Image Velocimetry (PIV), while the numerical simulations of the microreactor were carried out using the commercial software, FLUENT (version 14.0) [94].

5.1 Particle Image Velocimetry (PIV)

Particle Image Velocimetry is an optical flow visualization method in which the fluid is made visible by adding small particles that trace the flow-streams. From the positions of these tracer particles at two instances of time, it is possible to calculate the displacement of the particles and thus the velocity flow-field. The illumination of the particles at these two time instances is provided by a planar light source and it is assumed that the particles move with the local flow velocity between the two illuminations. To evaluate the flow-field, the entire frame is divided into smaller sections called "interrogation areas" [95] and the local displacement vectors are calculated for each of these areas using statistical methods (either using cross- or auto-correlation). It is assumed that between the illuminations at the two time instances, the particles in each interrogation area move homogeneously. Due to the planar nature of the illumination of the particles in the flow-field, usually a PIV system can only determine two (in plane) components of the velocity vector. It should be noted that newer methods of PIV measurement, such as stereo-techniques and dual-plane PIV, are able to calculate

even the third component of the vector field. PIV methods of flow visualization are able to provide vector fields with high spatial resolution [96] and with the advent of improved high-speed cameras and femtosecond lasers, the technique now also provides a high temporal resolution.

PIV is a non-intrusive method to measure velocity of the fluid and does not use probes such as hot wires or Pitot-static tubes. PIV can thus be used in high speed flows with shocks and in the boundary layers close to the wall where the use of probes will affect the flow-field. Also, unlike other usual flow measurement techniques such LDV, which are point measurement techniques, PIV as a technique, is able to record large parts of the flow-field and can then extract the velocity flow-fields from the entire frame. PIV measurements can thus give a better picture of the underlying flow patterns which are missing when using single point measurement techniques.

5.1.1 Components of a typical PIV system

A typical PIV system is shown in Figure 5-1 and usually consists of four basic components: (1) A light source to illuminate the particles; (2) Recording hardware usually in the form of a CCD camera to capture the images from the particles; (3) An optically accessible test section with the flow-field under study seeded with tracer particles; (4) A computer software that controls the timing (using a synchronizer) of the light source and the CCD camera, collects the images from the camera and then analyses the data to extract velocity vectors for the flow-field.

Lasers are the most commonly used light source in PIV systems due to their ability to emit high energy density, monochromatic light which can be converted into thin sheets. These properties help in illuminating and imaging the seeded flow particles without any chromatic aberrations. Solid state lasers are quite popular lasers due to their compact size and Neyodym-YAG lasers (Nd:YAG) are the most commonly used lasers for PIV purposes and produce monochromatic beams of light at a wavelength of 1064 nm. The beam is generated by Nd^{3+} ions which can be incorporated in various

host materials and in this case are incorporated inYAG (yttrium-aluminum-garnet) crystals for lasing applications. The triply ionized neodymium, Nd(III), typically replaces a small fraction of the yttrium ions in the host crystal structure of the YAG crystal, since the two ions are of similar size. Nd:YAG lasers have high amplification, good thermal, and mechanical properties and optical pumping, which provides the excitation for the laser to function, can be provided by white light.

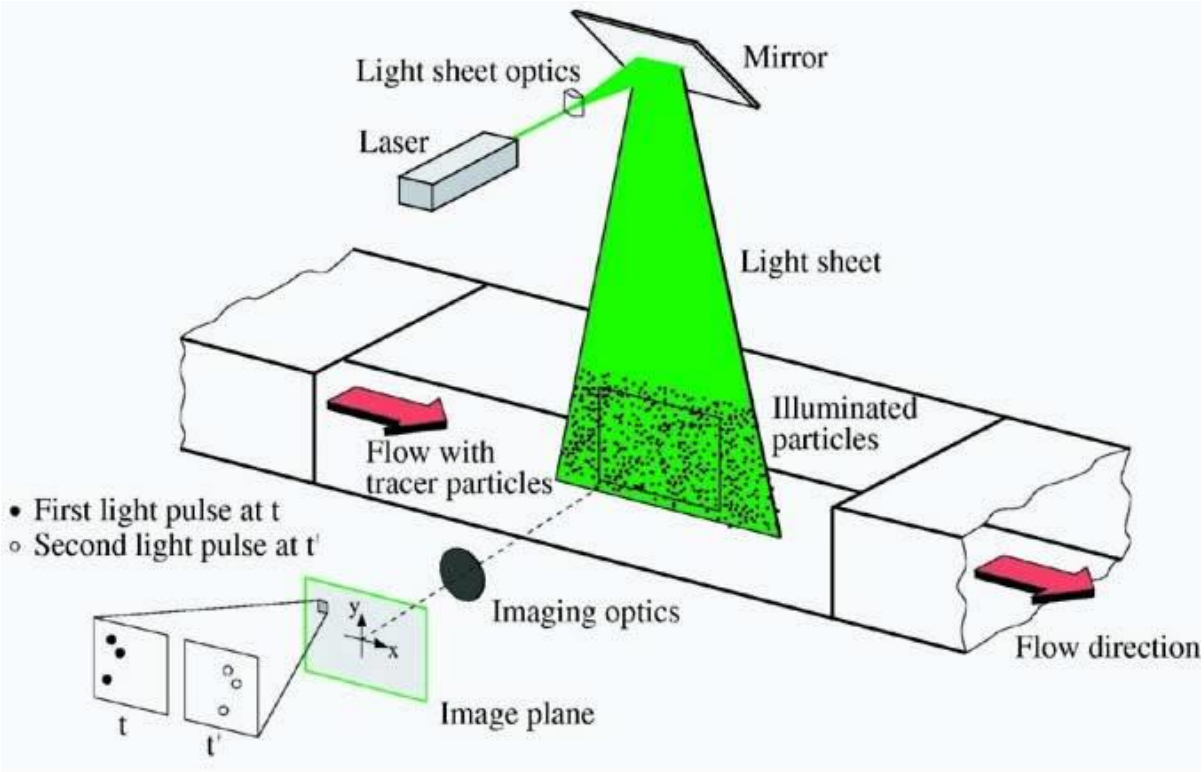

Figure 5-1: Basic PIV system (taken from [95]).

For PIV applications, the fundamental wavelength of a Nd:YAG laser (1064 nm) is frequency doubled using crystals and after separation, the light energy is available at a wavelength of 532 nm. The beam of the laser is converted into a light sheet, thus providing a planar field of view that allows the in-focus particles, which are illuminated, to be seperated from the out-of-focus particles outside the light sheet. Nd:YAG lasers can be operated in continuous or pulsed modes. By including a quality

switch (Q-switch) the laser can be operated in a triggered mode. Q-switching allows the production of light pulses at extremely high peak power, much higher than that achieved during a continuous wave operation. Although Q-switching can be made to generate more than one pulse out of a resonator, PIV lasers are usually designed with double oscillator systems [97]. A double oscillator system allows for the adjusting of the separation time between the pulses.

The duration of the pulse as well as the separation time between pulses is very important for PIV measurements. The duration of the laser pulse should be short enough so that the particles seeding the fluid flow are 'frozen' and there is no blurring or streaking of the image. Meanwhile the separation time between pulses should be short enough to avoid particles with an out-of-plane velocity component leaving the light sheet between successive illuminations but at the same time the time gap should be long enough to be able to calculate the displacement of the tracer particles from one image frame to another.

Image collection and recording is usually provided by an electronic image sensor with charge coupled devices (CCD) and complementary metal-oxide-semiconductor (CMOS) devices being the most common. A CCD is a sensor that converts light into electrical charge and is comprised of an array of many individual CCDs arranged either in the form of a line or a rectangular array. Each CCD element (usually on the order of $10 \times 10\ \mu m^2$) forming the array is called a pixel. When a photon of the appropriate wavelength enters the junction of the semiconductor, an electron-hole pair is created (photoelectric effect) and thus the electric charge created is proportional to the intensity of light falling on the sensor. A charge amplifier converts the electric charge into voltage and an array of voltage information can be digitally processed to form an image. At the time when the laser sheet is pulsed each particle in the plane of the laser sheet forms an in-focus spot on the camera image plane. With the second pulse of the laser another set of images is formed. These images can now be correlated to calculate displacement of the particles and their local velocities.

The exposure for a CCD camera is determined by the duration of the incident light pulse as it is usually much smaller than the shutter time of the camera. The process for pixelization is fast but the determining factor for speed in the entire process is the transfer of all the digitized data off the chip, which is usually quite slow (~ 10 ms). Thus standard video cameras cannot record two separate frames between the time-step of the two pulses and instead record the two images on a single frame. This is called single-frame double-pulsed recording. Special PIV cameras have been developed that transfer the charge created by the first exposure from each pixel to an adjacent storage well (in effect storing the pixelized image) while recording the second image. This transfer of charge is a fast process (~ 1 μs) and both the images for the two pulses can now be transferred off the chip in a quick manner. This is called two-frame single-pulsed recording and is usually the most popular method of recording PIV images [97].

In order to visualize the flow, the flow-field needs to be seeded with tracer particles. These particles have to be small enough to follow the fluid streamlines without disturbing the flow but at the same time they have to be large enough to scatter enough light to form clear and bright images. Spherical particles are best suited to be used for seeding the flow as the images produced by them are independent of particle rotation and the centroid of the particle image usually corresponds to the centre of mass of the particle. Another important factor in selecting the tracer particles is that their densities are not too different from the density of the fluid, thus making sure that the gravitational forces do not play a large role in the velocity field measurement. Unfortunately most materials with a specific gravity close to one (in order to track water flow) also have a refractive index similar to that of water, making these materials weak at scattering the incident illumination from the laser. If a tracer particle scatters illumination weakly, then more powerful lasers or more sensitive cameras are needed, thus making the PIV system more expensive. Care should be taken to ensure that the particle sizes are similar as even small differences in particle diameters can cause large difference in the scattered-light

energy and thus the exposure of the image. Thus if the particles are not monodisperse to a high accuracy, there will be differences in the images that are recorded by the camera.

The disadvantage of using particles to trace the streamlines in the fluid flow is that they must slip with respect to the fluid in order to generate the drag force that is needed to follow the acceleration of the fluid. Based on the acceleration of the flow-field, the proper seeding can be selected so that the slip velocity can be kept within acceptable limits. The ability of the particles to follow accelerations of the flow increases in inverse proportion to the square of the particle diameter. Thus accurate measurements of the flow-field in all but very slow moving gas flows are done using very small particles and a high-powered illumination source like a laser.

5.1.2 Image Processing and Image Interrogation in a PIV System

Image processing is the step which involves the enhancement in quality of the images collected by the CCD camera. This usually involves making the images less noisy and the particles more visible. One of the most commonly followed steps for image processing is background subtraction. Images from the background and the flow boundaries are usually recorded without any particles in it and these images are subtracted from the tracer-particle seeded flows, in turn only leaving the particles visible in each image.

Another common method for background subtraction is collecting a large number of images with the seeded flow and then averaging them. Due to the fact that the particles move quickly and are randomly distributed in every frame the particles will disappear in the averaged image, and the background image will be one in which only the illumination from the background and the flow boundaries is present (as these do not move from one frame to another) [98]. Background subtraction can lead to erroneous results if there is unequal illumination between the two frames as the extraction process will result in a double-frame image. This situation can be avoided by either applying a gray-

scale equalization before the background extraction process (in essence equalizing the unequal peak intensities between the two frames) or by averaging out each frame of the image frame separately and finally arriving at two background images which can be subtracted from each frame of the image-pair.

An important feature of a PIV system is that the measurement can be easily quantified and automated such that the displacement of the particles can be measured over the entire field of view in a rapid manner. This step of image analysis is called image interrogation. After the interrogation of the image, the displacement field is validated by placing statistical constraints designed to identify invalid displacement vectors [97].

Interrogation of images is often carried out by space-time cross-correlation of the particles within small regions of the image which are referred to as interrogation spots. Thus the entire image is now divided into a grid of interrogation spots in the *X*-*Y* plane of the image which have an area of $A_I = D_{Ix} \times D_{Iy}$ and centers at a set of points $\{X_I\}$ (Figure 5-2). The corresponding spot in the object plane is located at x_I with the dimensions $d_{Ix} \times d_{Iy}$. The spatial resolution of a PIV system is dependent on the statistical correlation of the image-pairs and thus the quality of the correlation is vital to the process.

The division of the images into smaller interrogation spots should be performed with care as a balance between the statistical number of tracer particles in each spot and the relative displacement of the particles from one image to the other has to be maintained. If an image is divided into interrogation spots that are too small then far too few tracer particles will exist within the spots for an accurate statistical correlation to take place. On the other hand, if the interrogation spots are too large, then the displacement of the particles from one image to the other in the image-pair can be greater than the image diameter of the particles. This situation results in an increase in noise as the displacements of individual particle correlation peaks are too large to add to the net correlation signal

[99]. Interrogation spots are generally square but do not need to be and a typical grid size is 64×64 pixels or 32×32 pixels.

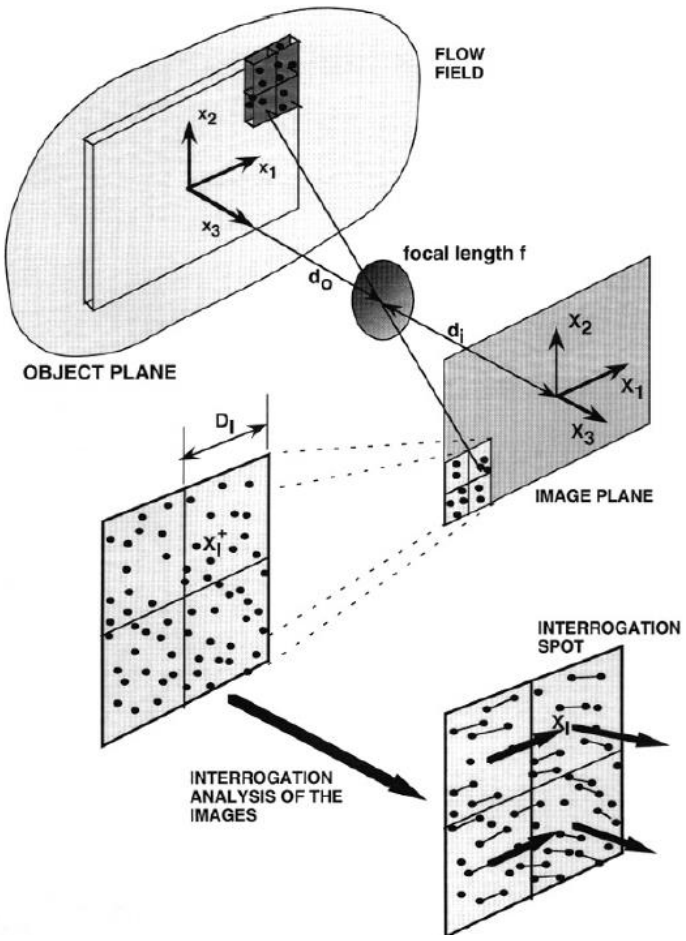

Figure 5-2: Interrogation analysis of images using interrogation spots on the pixel array centred at $\{X_I\}$ (taken from [100]).

If the first light pulse and image is recorded at a time t and is followed by another pulse of light and image at a time $t + \Delta t$, then the image intensities for the two images can be defined as:

$$I_1(X) = I(X, t) = \int J(z)\tau_0[X - F(x)]g\big[x - x_p(t)\big]dx$$

$$I_2(X) = I(X, t + \Delta t) = \int J(z)\tau_0[X - F(x)]g\big[x - x_p(t + \Delta t)\big]dx$$

where, $J(z)$ is the illuminating beam intensity, $\tau_0(X)$ is the exposure of a particle image per unit illuminating beam intensity, and $g(x,t)$ is the position of all the particles in the interrogation spot. The two images contain random patterns of particles that can be used to uniquely identify the particles. Correlation methods can be used to calculate the instantaneous vector fields by cross-correlating the intensities I_1 and I_2. The cross-correlation estimator between the two images, at a spot labeled W_1, can be expressed as:

$$R(s) = \int_{W_1} I_1(X) I_2(X+s) dX$$

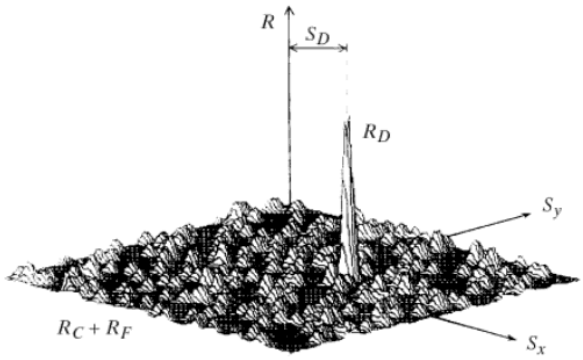

Figure 5-3: Correlations of a single-pulse, double-frame images (taken from [99]).

The cross-correlation function will have a peak in the *s*-plane and will be located at the displacement between the recorded images (ΔX_p). Thus locating the sharp peak of $R(s)$ determines the displacement of the particles between the two images (Figure 5-3). If all the particles in the interrogation spot do not move with the same velocity then the displacement calculated using the correlation function is an average value for all the particles. As can be seen from Figure 5-3, the cross-correlation function also has a number of false correlation peaks which are usually caused due

to the images from different particles overlapping at the various *s* locations. These minor peaks are usually referred to as noise. If an interrogation spot contains *N* particles in both the frames of an image-pair, then the displacement peak due to correlation should be *N* times higher than the peak of a single-particle overlap (which is causing the noise in the image). Thus the signal-to-noise ratio of the correlations between the two images can be increased by having more particles in every interrogation spot, that is, by increasing the overall seeding concentration of the flow [97].

5.1.3 Micro-PIV

Over the past few years particle image velocimetry has been successfully adapted to measure flow-fields at a micron-scale resolution in microfluidic devices. Due to both physical limitations as well as practical implementation difficulties, at the small length scales associated with micron-scale flow, PIV measurements are slightly different from the PIV methods used in macro-scale flow. Unlike macro-PIV, where a light sheet is used to illuminate the seed particles, in micro-PIV systems it is quite difficult to form a sheet which is only a few micrometers thick. Volumetric illumination is thus used instead to illuminate the seed particles in the flow-field. Volumetric illumination (Figure 5-4) illuminates the entire test section with a volume of light and then depends on the depth of field of the lens to define the in-plane and out-of-plane thicknesses. All the particles illuminated by the cone of light scatter the light but only those particles within the measurement plane (defined by the depth of field) are sufficiently focused and thus are involved in the correlation process.

The depth of field of a standard microscope objective can be defined as:

$$\delta_z = \frac{n\lambda_o}{NA^2} + \frac{ne}{NA \cdot M}$$

where n is the refractive index of the fluid between the objective and the microfluidic device, λ_o is the wavelength of the light being imaged by the optical system, NA is the numerical aperture of the lens, e is the smallest distance that can be resolved by the detector (in most cases the CCD sensor and thus e is the spacing between the pixels), and M is the total magnification of the system.

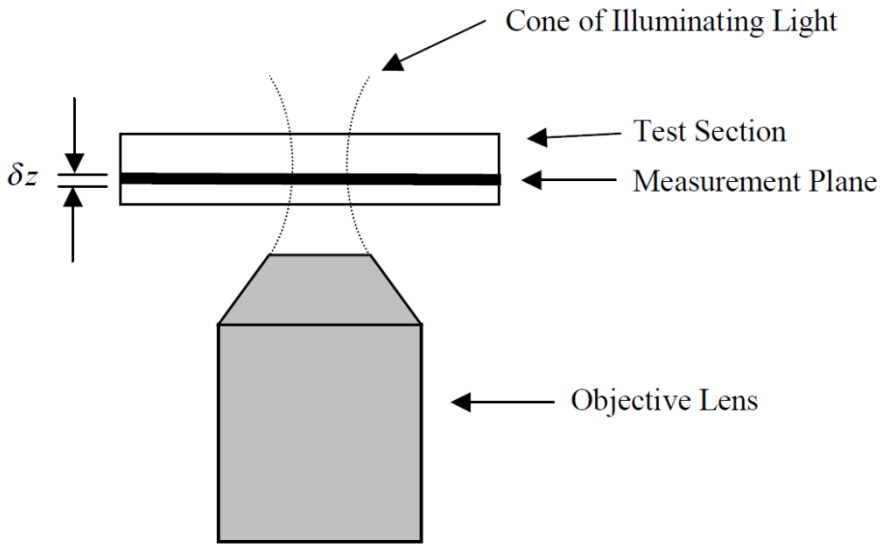

Figure 5-4: Volumetric illumination via an objective lens (taken from [101]).

The light sheet used in macro-PIV systems is particularly useful as it helps in minimizing the background noise caused by the out-of-focus particles and thus ensures that all the particles visible to the camera are well focused. Due to volumetric illumination in micro-PIV systems, there is a presence of background light scattered from the test section surfaces as well as the out-of-focus particles. The background light due to the test surface can be removed by using fluorescence techniques that filter out light at the same wavelength as that of the illumination (elastically scattered light) while leaving light of a longer wavelength without any attenuation [96]. Background light emitted from the out-of-focus particles is not so easy to remove as it occurs at the same wavelength as the signal from the in-focus particles.

The visibility of an in-focus particle (V) can be given by an equation derived by Olsen and Adrian [102]:

$$V = \frac{4M^2\beta^2(s_o - a)(s_o - a + L)}{\pi C L s_o^2 \left\{M^2 d_p^2 + 1.49(M+1)^2\lambda^2 \left[\left(\left(\frac{n}{NA}\right)^2\right) - 1\right]\right\}}$$

where M is the magnification of the system, β is the parameter chosen to determine the cutoff level that defines the edge of the particle image, s_o is the object distance, a is the depth at which the measurement takes place in the microfluidic device, L is the test section thickness, C is the number of particles per unit volume of the fluid, d_p is the diameter of the particles, n is the refractive index of the fluid between the microscope objective and the microfluidic device, and NA is the numerical aperture of the objective used. It can be seen that the visibility of the particles in-focus can be improved by either decreasing the particle concentration (C) or by decreasing the test section thickness (L). Care must thus be taken while seeding the flow in a microfluidic device. Too high a seeding concentration will result in a large number of out-of-focus particles, while too low a seeding will result in not enough in-focus particles for a high quality correlation, which in turn will result in a less accurate velocity field.

In many micro-PIV applications the particles used are much smaller than the wavelength of light used to image them, but can range typically between 200 nm and 2 μm. Often oil or water immersion lenses with a high numerical aperture are used to have a good visibility of such small particles. Another aspect of using such small tracer particles is that their motion in the fluid is affected by a large degree by Brownian motion. The Brownian motion of these particles can result in random noise and thus make it more difficult to have accurate velocity fields. This source of error has been quantified by Santiago et al. [96] and can be defined as:

$$\varepsilon_B = \frac{(S^2)^{1/2}}{\Delta x} = \frac{1}{u}\sqrt{\frac{2D}{\Delta t}}$$

where ε_B is the error caused due to Brownian motion, S^2 is the random-mean-square particle displacement, Δx is the displacement in the x direction, u is the local fluid velocity, D is the diffusivity of the spherical particles and Δt is the time step between the recording of the two image frames. The error due to Brownian motion thus places a limit on how small Δt can be for an experiment as well as on the particle diameter (d_p) which affects the diffusivity of the particles as:

$$D = \frac{k_B T}{3\pi\mu d_p}$$

where k_B is the Boltzmann's constant, T is the absolute fluid temperature, and μ is the dynamic viscosity of the fluid. Thus, error due to Brownian motion can be seen to decrease if the time-delay between the two exposures increases or if the size of the particles becomes larger. Brownian motion is generally seen to affect PIV measurements when the size of the particles ranges between 50nm and 500nm as well as for flow velocities less than 1 mm-s^{-1}.

Given that the particle image density in a micro-PIV system is not very high, thus special processing methods are required to process the micro-PIV recordings. These low image density (LID) recordings are usually evaluated using particle-tracking algorithms. In this technique the velocity vector is calculated using only one particle and thus the accuracy is limited [98]. In addition, owing to the low density of particles present in every frame, an interpolation procedure is required to attain velocity vectors at the desired grid locations (adding more uncertainties to the final velocity field). Special methods have been developed to improve these algorithms and they often rely on the periodic

or quasi-steady nature of micro-scale fluid flow (given that these flows are usually laminar and have low Reynolds numbers).

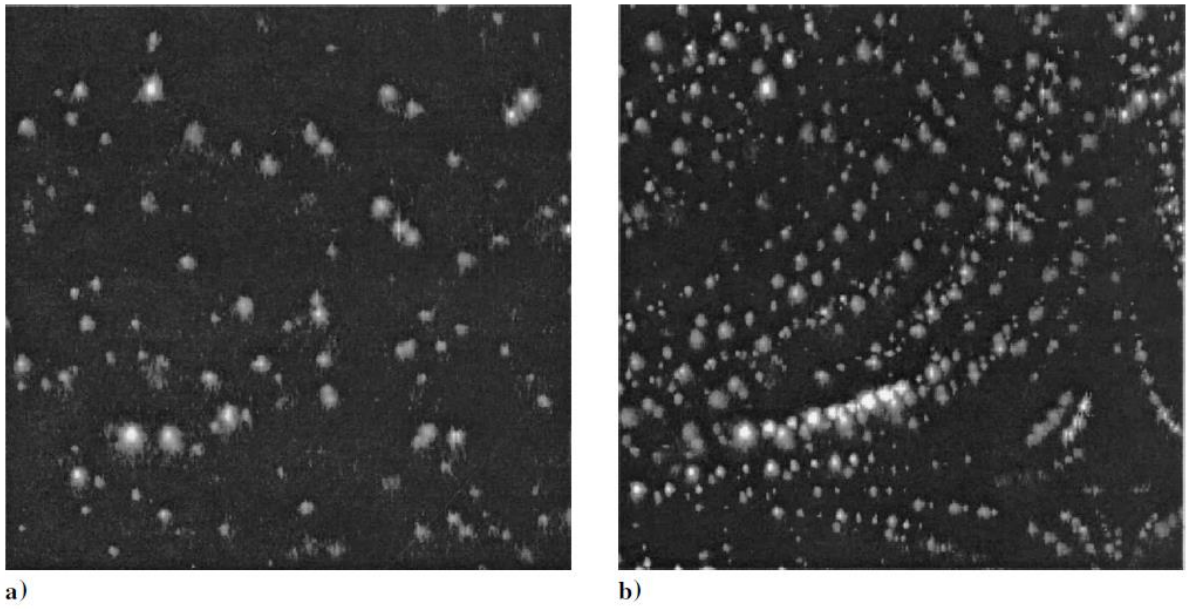

Figure 5-5: Example of LID overlapping: a) one LID-PIVC image and b) result of 9 overlapped LID-PIV images (taken from [98]).

One of the earliest methods to improve the particle tracking algorithm was superimposing multiple LID-PIV recordings on one frame. This helped increase the particle density of each frame and thus made the tracking of particles and the interpolation between the different velocity vectors far more reliable. The effect of overlapping multiple images on a single frame is shown in Figure 5-5 and the process can be mathematically represented as [98]:

$$g_0(x\,,y) = max\{g_k\,(x\,,y)\,, K = 1, 2, 3, \dots, N\}$$

where $g_k\,(x\,,y)$ is the gray value distribution of the LID-PIV recordings with a total number of N images and $g_0(x\,,y)$ is the value for the overlapped recording. The resulting image improves

the particle tracking algorithm and the velocity vectors are now denser and more regularly spaced than with just a single LID-PIV image. The effect can be seen in Figure 5-6 where the velocity fields from the images shown in Figure 5-5 are calculated.

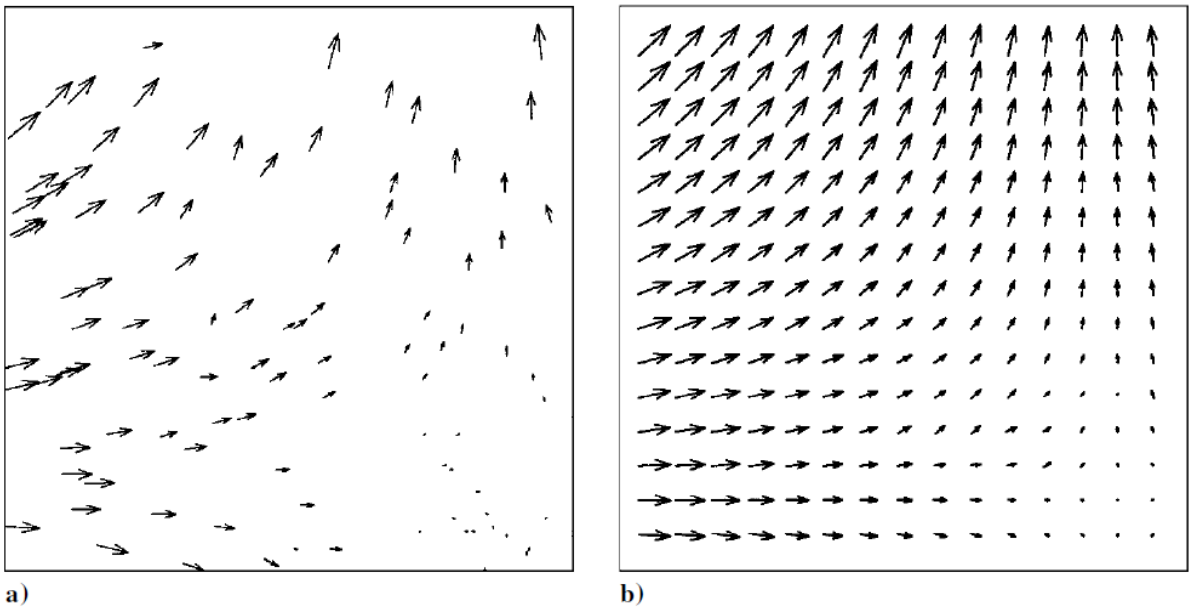

Figure 5-6: Velocity fields calculated using a) single LID-PIV image and b) using overlapped LID-PIV images (taken from [98]).

Another popular method used to improve PIV measurements is ensemble correlation or correlation averaging. This method was originally developed to reduce the errors caused due to Brownian motion of the particles but has been adapted to improve on low-quality images as well as flows which have low particle concentration. In this technique an ensemble of image-pairs is collected over a specified period and the entire set of images is spatially correlated. The resulting correlation functions for the same interrogation regions are then ensemble averaged to obtain an averaged correlation function.

This averaged correlation function has been proven to be a more reliable estimate of the mean particle displacement than the displacement calculated by standard correlation functions from a single

image-pair. The major drawback for this method is that as a large number of images are ensemble-averaged to obtain the final velocity flow-field, all information about the instantaneous flow-field is lost. Moreover, this method cannot be used for flows which are not steady and laminar.

In general the correlation function of an interrogation spot (Φ_k) can be represented as [98]:

$$\Phi_k(m\,,n) = \sum_{j=1}^{q}\sum_{i=1}^{p} f_k(i\,,j)\cdot g_k(i+m\,,j+n)$$

where, $f_k(i\,,j)$ and $g_k(i\,,j)$ are the gray value distributions of the first and second exposures respectively, in the k^{th} image-pair at a certain interrogation spot with a size of $p \times q$ pixels. The correlation function from a single image-pair will form a peak at the position of the particle displacement and this should be the highest peak amongst all the peaks of Φ_k. The other peaks, which will be smaller than the displacement peak, will be caused due to noise or the wrong correlation between different particles. If the interrogation spot is small or does not contain enough particles to create a good correlation, the noise level will be high and the main peak (caused by particle displacement) will become weaker in comparison (and in some cases become even lower than the other peaks in the interrogation spot). This results in the calculated velocity flow-field to not being as reliable.

When the flows are laminar and the velocity flow-field is independent of time thus image-pairs taken over a period of time should show similar particle displacements. Thus the main peak of Φ_k is always at the same position but the sub-peaks (due to their random nature) will appear at different positions and with different intensities for different image-pairs. Thus, if Φ_k is averaged over a large number of image-pairs (N), the main peak will remain at the same position in each Φ_k while the random sub-peaks will be averaged to zero. The averaged (ensemble) correlation function ($\Phi_{\mathrm{ens}}(\mathrm{m}\,,\mathrm{n})$) can be given as [98]:

$$\Phi_{ens}(m,n) = \frac{1}{N}\sum_{k=1}^{N}\Phi_k(m,n)$$

Figure 5-7 shows the effect of ensemble correlation on the correlation function by averaging 101 image-pairs. As can be seen from the graphs, the averaging leads to a reduction in the overall noise in the image and makes the displacement peak clearly stand out (with the sub-peaks hardly noticeable), thus making for a better signal. Much like the overlapping for LID-PIV images, the ensemble correlation technique can only be used for steady flows which can be averaged without changing the displacement vector. But unlike the overlapping of LID-PIV images, the ensemble correlation method is not limited to a small number of images.

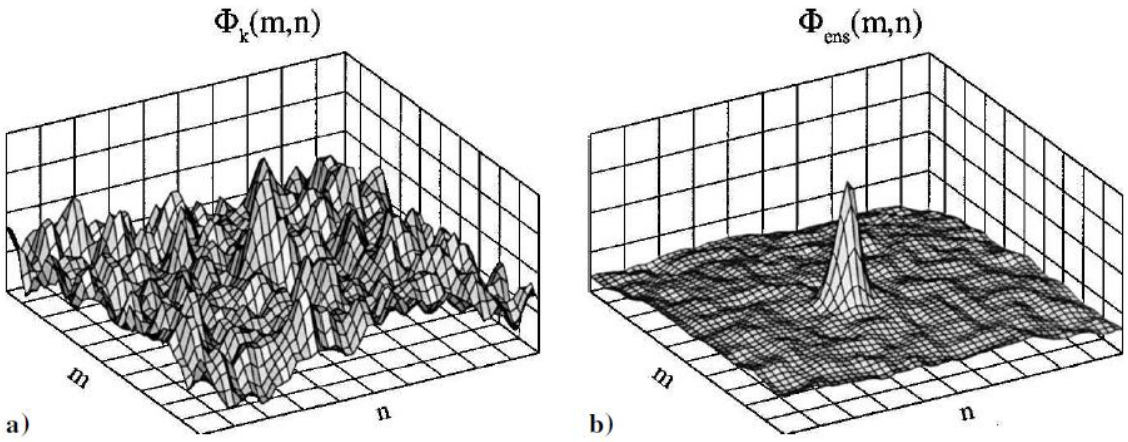

Figure 5-7: Demonstration of ensemble correlation with a) showing the correlation function from a single image-pair and b) showing the correlation function from 101 ensemble correlated image-pairs (taken from [98]**).**

5.1.4 Experimental Micro-PIV Setup

Manifolds (Figure 5-8) were fabricated for the microreactors using SS 316 which helped in providing a suitable way to pump the seeded flow or propellants into the reactors without causing too much of a pressure drop, which is known to be a problem when using hypodermic tubing. Moreover, the manifolds helped in providing a safe and secure way of collecting the exhaust fumes and residual salt produced from the reaction between the reagents. The inlets and outlets of the manifold to the reactor were sealed using Kalrez o-rings to prevent any leakage of the chemicals. A pressure driven flow was used to create the fluid flow in the microreactors with a positive pressure being applied at the inlets while keeping the exhaust open to atmospheric pressure. The fluids were introduced into the manifold using Teflon tubing connected to high pressure stainless steel syringes. These syringes were controlled by a high pressure syringe pump (Harvard Apparatus PHD4400), giving a high degree of control on the flow rates.

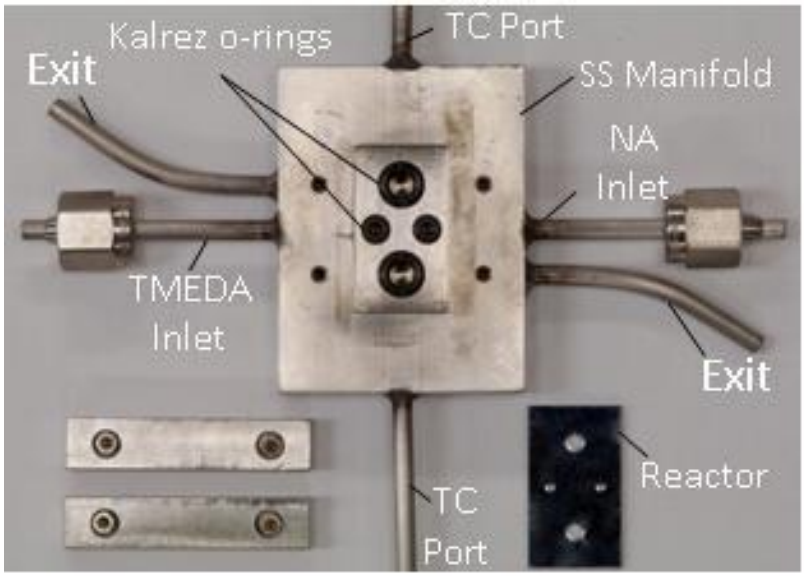

Figure 5-8: Stagnation flow microreactor with manifold assembly.

A schematic of the micro-PIV system used in the study is given in Figure 5-9. The reactor and manifold assembly were placed under an inverted microscope (Nikon Eclipse TE2000-U) and a 10x objective (Nikon Plan Flour NA = 0.3) was used to magnify the image. The illumination for the PIV was provided by a double pulsed Nd:YAG laser (λ = 532 nm, New Wave Research – Solo III) which provided the two pulses of 50 mJ at a repetition rate of 15 Hz.

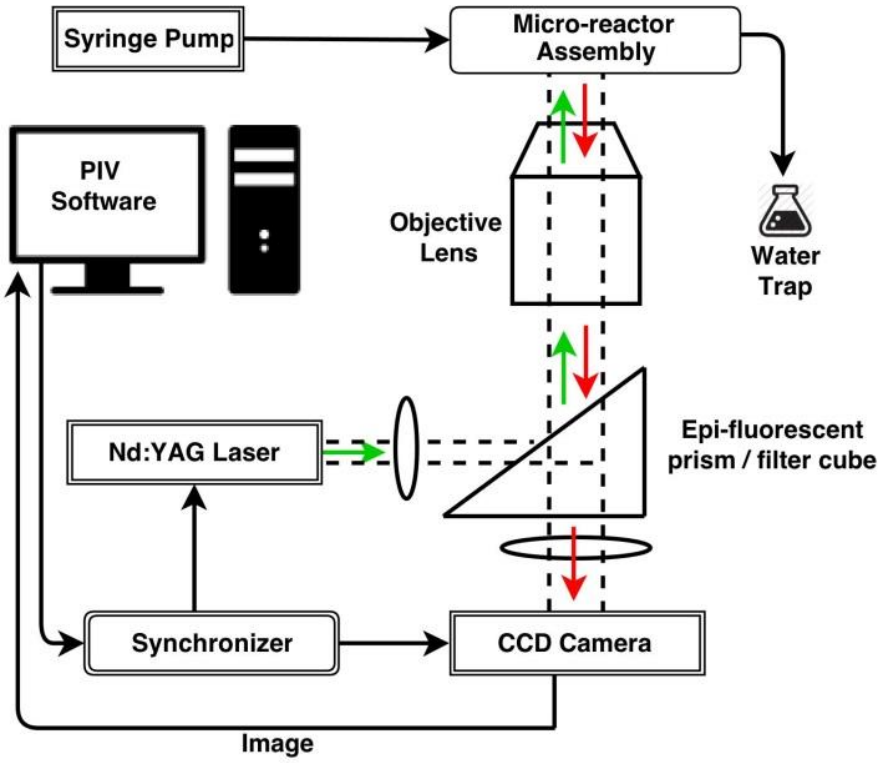

Figure 5-9: Schematic of PIV system showing all the components.

The flow in the microreactor was seeded using 2 μm diameter fluorescent particles (Thermo Scientific Fluoro-Max Red Aqueous Fluorescent Particles) which when excited by the laser have emission peaks of 542/612 nm. The fluorescent emission from the particles passes through a high-pass filter cube in the microscope and is recorded by a 12-bit high resolution (1360 x 1024 pixel) CCD camera (TSI PIVCAM-14-10) which provides the images to the PIV software. The double

pulsed laser and the CCD camera are connected to a workstation via a laser pulse synchronizer (TSI 610034) which controlled the timing of the volumetric illumination from the laser as well as the image acquisition. A scaling factor of 0.35 μm/pixel was used for the present study and thus the observation area was 476 μm × 360 μm. Each pulse from the double pulsed laser was recorded as a separate image (forming an image-pair) and was processed using a PIV software (TSI Insight 6.0) which managed both data acquisition as well as the data analysis.

The laser pulse delay, which is controlled by the synchronizer, varied depending on the flow-rate of the fluid inside the microreactor. It was calculated such that the particles moved at an average of 8 pixels from one frame of the image-pair to the other. The average flow velocity in the channels of the microreactor was used for these calculations. A total of 120 image-pairs were acquired for each experimental run so as to provide a sufficient amount of data for the averaged correlations to be accurate.

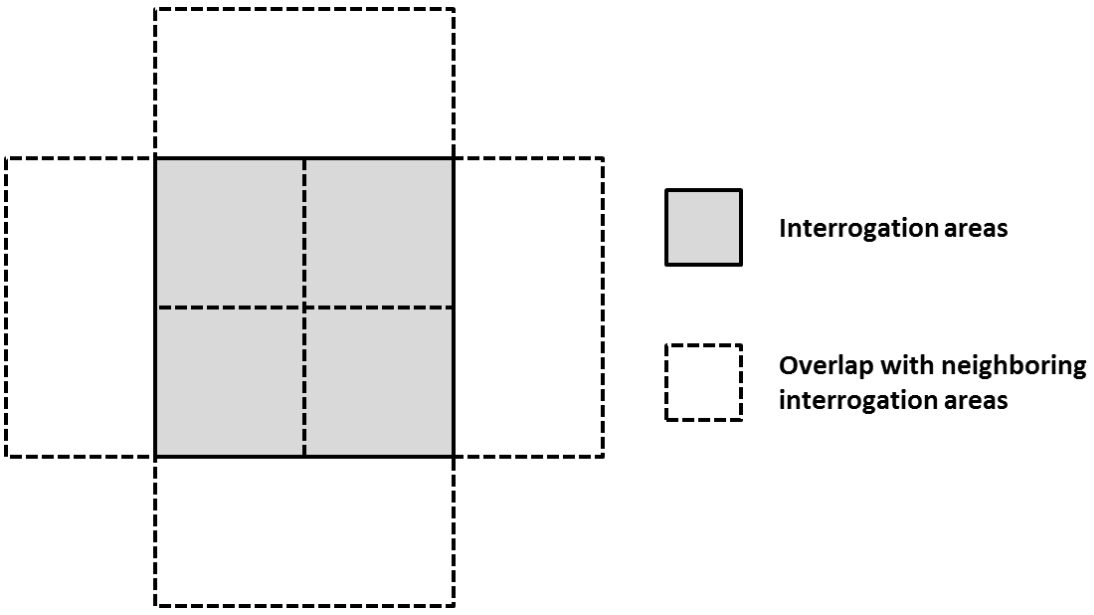

Figure 5-10: Nyquist grid used to process the PIV images.

The images obtained by the PIV software were processed using a Nyquist Grid. The Nyquist Grid (Figure 5-10) sets vectors with the *x*-direction spacing equal to half of the interrogation spot width and the *y*-direction spacing equal to half of the interrogation spot height. No spot offsets are used (which provides an effective overlap of 50% between each image-pair) and the processing only used a single pass.

The correlations were computed with a FFT correlation engine and a Gaussian peak algorithm. An ensemble method of correlation was used which helps in improving signal to noise ratios when there are steady flows under observation [98]. The interrogation window was kept at 48 × 48 pixels to have multiple particles in each window and thus to form better cross-correlations (by increasing the signal to noise ratio) while calculating the displacement of the particles as well as the velocity flow-field. A detailed step-by-step process to carry out the experimental PIV runs, including setting up of the experiment, processing the PIV image pairs, and plotting the vector fields is provided in Appendix A.

5.2 Numerical Modeling of Cold-Flow in the Microreactors

A fluid flow field can usually be modeled using two methods – either by treating the fluid as a collection of molecules or by treating the fluid as a continuum. If the fluid is treated as a collection of molecules then the modeling methods are deterministic (Molecular Dynamics calculations) and probabilistic in nature. On the other hand, with the fluid being treated as a continuum, the velocity, pressure, density etc. are defined at every point in space and time and by following the laws of conservation for mass, energy and momentum a set of governing non-linear partial differential equations can be formed (Euler or Navier-Stokes). The continuum model is easier to solve mathematically when compared to the molecular model and is thus preferred unless conditions make it non-applicable. In macro-scale devices, the fluid can safely be treated as continuum and the flow

field can be modeled using the Navier-Stokes laws but the fluid flow at the micron-scale can differ greatly in its behavior (as seen in section 3.2) and thus one should be careful while choosing the method to model the fluid behavior at the micron-scale.

The Navier-Stokes equations which are usually used to model fluid flow on the macro scale are valid only when a certain set of conditions are satisfied [103]:

- The continuum approximation – This condition specifies that the fluid can be treated as an indefinitely divisible continuum.
- Thermodynamic equilibrium or quasi-equilibrium – This condition assumes that the macroscopic quantities have enough time to adjust to their changing surroundings.

The continuum approximation treats the fluid as a continuous medium which can be described in terms of variations in density, temperature, pressure and other macroscopic flow quantities. Thus the model provides relatively accurate predictions as long as local properties can be described as averages over elements that are large when compared to the microscopic structure of the fluid, but small enough when compared to the scale of the macroscopic phenomena. In case of gases, the continuum approximation can be related to the mean free path. The mean free path is defined as the average distance travelled by the molecules between collisions. The mean free path ($\mathcal{L}$) is related to the temperature (T) and the pressure (p) as:

$$\mathcal{L} = \frac{kT}{\sqrt{2}\pi p\sigma^2}$$

where, σ is the molecular diameter and k is the Boltzmann constant. The continuum model is only valid when the mean free path is much smaller than the characteristic flow dimension (L). The ratio between the mean free path and the characteristic length is termed as the Knudsen number:

$$\text{Kn} = \frac{\mathcal{L}}{L}$$

In the limit of the Knudsen number being zero, the transport terms in the continuum momentum and energy equations are negligible and the Navier-Stokes equations reduce to the inviscid Euler equations. The standard continuum models can be used to a value of Knudsen number below 0.01 [104]. As the Knudsen number increases, the rarefaction effects in the gas become more important and at a critical stage, the continuum approximation is no longer valid.

As the density of liquids is usually about one-thousand times the density of gases, thus the spacing between the molecules in liquids can be approximated to be ten times smaller than that in gases. Liquid molecules do not have an estimated mean free path as gases do, but the lattice spacing can be used as a similar measure as has been used by Bridgman [105]. The lattice spacing (δ) can be defined as:

$$\delta = \left(\frac{\overline{V}_l}{N_A}\right)^{1/3}$$

where, $\overline{V}_l$ is the molar volume while N_A is the Avogadro's number. For water, the lattice spacing can be calculated to be 0.3 nm and thus for a characteristic length of 1 μm and 100 μm, the equivalent Knudsen number can be calculated to be 3×10^{-4} and 3×10^{-6}. Thus, in both cases, the Knudsen number lies well within the limits for the continuum model to be applied. Thus, in the case of fluid flow on the micron-scale, the continuum model only seems to fail when the characteristic length is on the order of a few nanometers.

The final condition that needs to be satisfied to apply the Navier-Stokes equations is the condition of thermodynamic equilibrium. In the case of fluids in motion, it is near impossible to have exact equilibrium as there is a constant change in the volume, momentum and energy of the fluid

particles. Thus, in fluid dynamics, a state of quasi-equilibrium is desired. The macroscopic quantities of the flow can revert back to their equilibrium state only if the molecular time scales and length scales are small when compared to the corresponding macroscopic flow scales. In this condition, numerous molecular collisions will occur in a sufficiently short time to equilibrate the fluid particles, leading to little variation in macroscopic properties over distances that are comparable to the molecular length scales. The condition for thermodynamic equilibrium implies that the macroscopic quantities such as velocity and temperature will have nearly linear gradients over molecular distances. The thermodynamic equilibrium condition also leads to the no-slip and no-temperature-jump boundary conditions [106], [107].

The no-slip condition in enforced at the fluid-solid interface, while applying the momentum equation. Similarly the no-temperature-jump condition is enforced while applying the energy equation. The two conditions are enforced so that there are no finite discontinuities of velocity or temperature within the fluid. A discontinuity would mean that there would exist regions, where the temperature and velocity gradients would be infinite leading to infinite viscous stresses and infinite heat fluxes. To have a no-slip condition and the no-temperature-jump condition, the fluid velocity must be zero relative to the surface and the temperature of the fluid should be equal to the temperature of the solid surface. This is only possible when the fluid flow adjacent to the solid surface is in thermodynamic equilibrium. This thermodynamic equilibrium can be achieved only if there are infinite number of collisions between the fluid and solid surface. In reality, the no-slip and no-temperature-jump conditions can be applied as long as the value of Knudsen number is less than 0.001 [108]. When the Knudsen number is raised beyond this value, the number of collisions that occur between the fluid and the solid surface are not high enough for the thermodynamic equilibrium condition to be met.

Recent studies [109], [110] have shown that liquid flows in microchannels can be predicted by using macro-scale continuum theory without large errors. Also, given that the scale of the

dimensions of the microreactor in the present study are large enough to keep the Knudsen number smaller than 1×10^{-4}, thus it is safe to assume that the governing equations used in macro-scale flow can be applied to model the flow of liquid through the microreactors used in the present study.

5.2.1 Governing Equations for Fluid Flow in the Microreactors

As flow in the microreactors satisfies the conditions for the continuum model, the governing equations are similar to the equations used for macro-scale fluid flow. These equations are the conservation of mass and the conservation of momentum which can be represented as:

$$\frac{\partial \rho}{\partial t} + \nabla \cdot (\rho \vec{v}) = S_m$$

and,

$$\frac{\partial}{\partial t}(\rho \vec{v}) + \nabla \cdot (\rho \vec{v} \vec{v}) = -\nabla p + \nabla \cdot (\bar{\bar{\tau}}) + \rho \vec{g} + \vec{F}$$

where, ρ is the density of the fluid, $\vec{v}$ is the velocity of the fluid-flow, t is the time-step involved, S_m is the source term for the mass added to the continuous phase from a dispersed second phase (such as vaporization of liquids) or any user defined sources, $\rho \vec{g}$ is the gravitational force acting on the fluid body, $\vec{F}$ is the external body force on the fluid, and $\bar{\bar{\tau}}$ is the stress tensor which can be defined as:

$$\bar{\bar{\tau}} = \mu \left[(\nabla \vec{v} + \nabla \vec{v}^T) - \frac{2}{3} \nabla \cdot \vec{v} I \right]$$

where μ is the molecular viscosity of the fluid while I is the unity tensor. The second term, on the right hand side of the equation, refers to the effect of volume dilation.

As the fluid-flow problem in the microreactors can also involve heat transfer and reactions between multiple species, additional conservation equations need to be added to the set of governing equations. These equations are the conservation of energy equation and the conservation of species equation which can be represented as:

$$\frac{\partial}{\partial t}(\rho E) + \nabla \cdot \left(\vec{v}(\rho E + p)\right) + \nabla \cdot \left(K_{eff} \nabla T + \sum_j h_j \overrightarrow{J_j} + \left(\bar{\bar{\tau}}_{eff} \cdot \vec{v}\right) \right) + S_h$$

and,

$$\frac{\partial}{\partial t}\left(\rho Y_j\right) + \nabla \cdot \left(\rho \vec{v} Y_j\right) = -\nabla \cdot \overrightarrow{J_j} + R_j + S_j$$

In the equations above, E is the total energy of the volume, h is the sensible enthalpy, K_{eff} is the effective conductivity, $\overrightarrow{J_j}$ is the diffusion of flux of species j, S_h is the source term that account for any heat from a reaction or other volumetric user defined heat sources, Y_j is the local mass-fraction of each species, R_j is the net production of each species due to a chemical reaction, and S_j is the rate of creation of species due to any user defined functions.

5.2.2 Numerical Solution of the Governing Equations

The governing equations form a coupled non-linear set of partial differential equations (PDE) that in most engineering cases cannot be solved analytically. However, the solution to these PDEs can be estimated by computational methods and that is what most CFD packages aim to do. Numerical methods such as CFD replace the continuous domain of a problem with discretized domain using a mesh/grid that is specially generated for each problem. Figure 5-11 shows the discretization of a continuous domain 1D into one that is divided by *N* grid points.

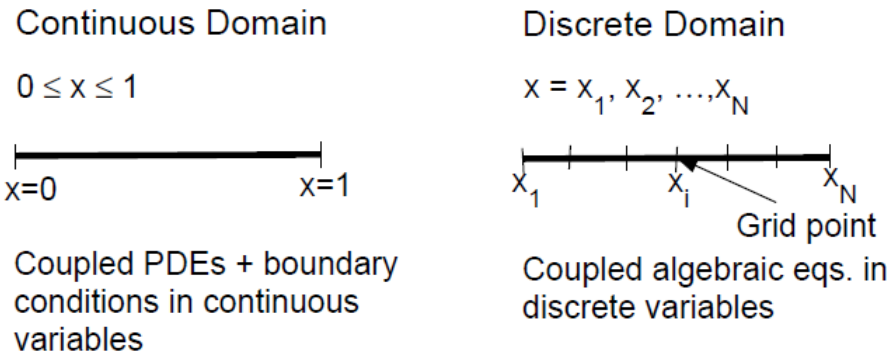

Figure 5-11: Discretization of a continuous domain.

The flow variables in the continuous domain are defined at each point in the domain. Pressure (p) could thus be defined as:

$$p = p(x)\,, \qquad 0 < x\ < 1$$

While in the case of a discretized domain the flow variables are only defined at the grid points and thus the pressure would be defined at only the *N* grid points shown in Figure 5-11 as:

$$p_i = p(x_i), \qquad i = 1, 2, 3, \dots, N$$

A numerical solution using CFD would now only solve the flow variables at the grid points in the discretized domain and the values of the flow variables at other points in the domain would be interpolated from these calculated values. In the continuous domain the governing equations and boundary conditions are defined in terms of continuous variables (p). In a discretized domain the coupled governing equations are defined in terms of discrete variables (p_i). The discretized system with its coupled governing equations can be solved (for the values of the flow variables at the various

grid points) using methods similar to those used to solve matrix inversion problems. The matrix inversion problem requires numerous repetitive calculations (iterations) and is usually handled by a digital computer.

FLUENT was chosen as the software to solve the governing equations for the fluid flow in the microreactor. FLUENT is a commercially available computational fluid dynamics (CFD) solver offered by ANSYS Inc. and can be used to model fluid flow, heat transfer as well as chemical reactions in often complex geometries. FLUENT [94] is able to model flows that are laminar, turbulent as well as compressible and can solve for a steady state solution as well as transient ones. FLUENT uses the finite-volume method, a method popular for solving fluid mechanics problems, for finding the solutions to the flow variables in the governing partial differential equations [111]. "Finite volume" in the method refers to the small volume surrounding each node point on a mesh/grid. The volume integrals in the partial differential equations that contain a divergence term are converted to surface integrals, using the divergence theorem. These terms are then evaluated as fluxes at the surfaces of each finite volume. Because the flux entering a given volume is identical to that leaving the adjacent volume, the flux values, and thus the solutions, are conserved. The method is popular for fluid mechanical problems as it can be easily formulated to allow for unstructured meshes and because it is able to handle large problems without using a lot of computational resources.

5.2.3 Setting up a Fluid-Flow Problem in FLUENT

A typical solution of a fluid mechanical problem in FLUENT requires the following steps:

- Creation of the model geometry and mesh/grid
- Setting up boundary conditions
- Setting up the physical and solver models
- Computing and monitoring the solution

- Analyzing the results and revising model if necessary

The model geometry and the mesh for the fluid problem is usually created using separate meshing software. The most commonly used meshing software for FLUENT is GAMBIT, a commercially available drawing and meshing software. All the geometry is usually created and meshed in GAMBIT before the mesh being imported into FLUENT. GAMBIT allows for complex grids to be formed which allow for the fluid flow to be modeled better as well as have complex interactions when it comes to boundary layer flow.

The through-etched microreactors as well as the shallow etched microreactors that were used for the PIV studies were both modeled for the cold-flow simulations. A 3D geometry mimicking the geometry of the actual reactor was recreated in GAMBIT (Figure 5-12).

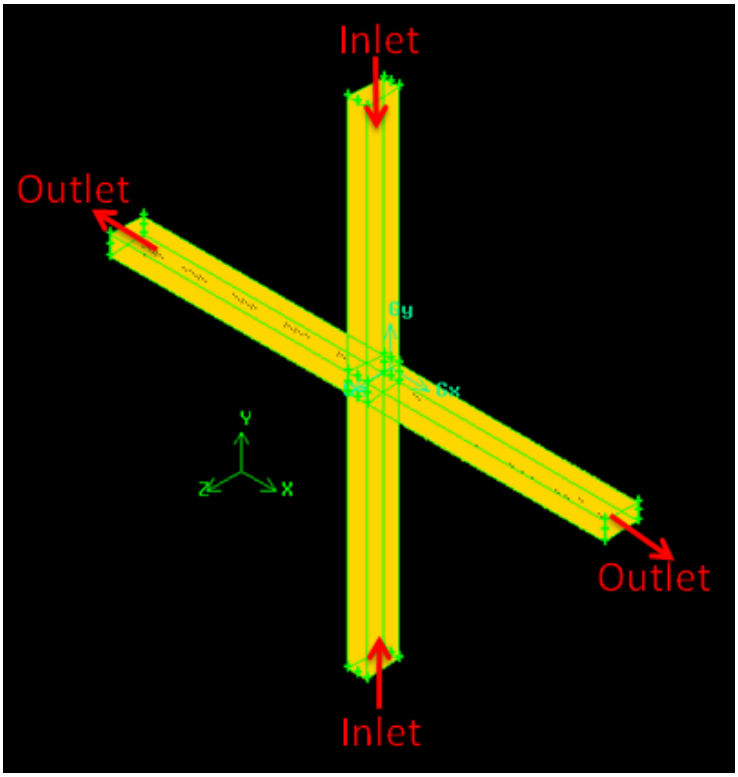

Figure 5-12: Geometry of stagnation-flow microreactor created in GAMBIT.

In order to minimize the computational resources needed for the simulation, the entire length of the inlets and the exits were not modeled but instead the inlets and the outlets were kept at a length of 4 mm each. This allowed for the development of the flow to occur in the microreactor and thus have a simulation that would be truly representative of the actual microreactor. The designation of the boundary conditions for the inlets and the outlets, as well as the walls is also done in GAMBIT before exporting the mesh.

Hexahedral elements were used to form a structured mesh of the microreactor geometry as the accuracy of solutions using hexahedral elements, for the same cell elements, is the highest. Due to the large changes in the velocity field that take place in the stagnation zone, care was taken that the stagnation zone was more densely meshed than the volume along the length of the reactor. A mesh independence study was carried out using FLUENT to make sure that the size and density of the mesh did not affect the solution of the fluid-flow problem. A sample 3D mesh created for use of the cold-flow simulations is shown in Figure 5-13.

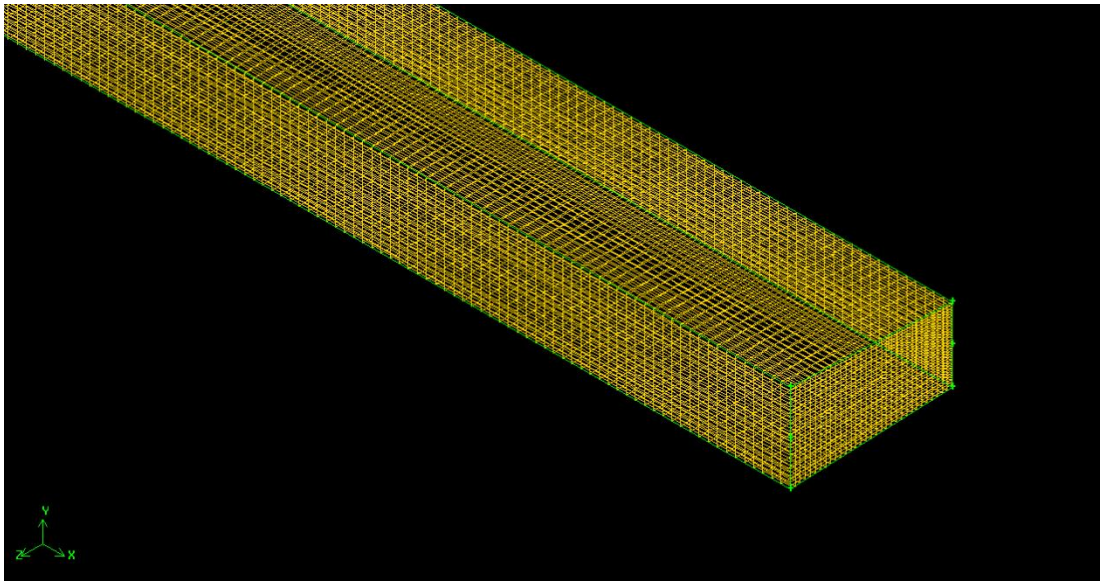

Figure 5-13: Mesh using hexahedral elements created for numerical simulations of the microreactor.

The mesh created in GMABIT was then imported into FLUENT and the solver was setup for a laminar, pressure-based, steady-state solution with the fluid in the microreactor having the same physical properties as liquid water. The inlet velocity of the fluid into the reactor was specified to match the average flow velocity expected for the various flow-rates that were used in the PIV experiments. The outlets were designated as pressure outlets with the outlet exposed to atmospheric pressure. All the walls in the microreactor were designated as stationary walls with a zero-slip shear condition applied. An iterative solution was setup with the iterations continuing till a convergent solution for the flow problem was reached.

As the numerical solution is an interactive process, the values for the fluid flow variables change with each successive iteration. If these changes are significant, then the flow-field predicted by the simulation will not be completely accurate. As every numerical process contains errors in the solution the aim of a successful model is to minimize the errors and keep them at an acceptable level. The acceptable level of error may vary enormously from one flow variable to another and from one case study to another. The absolute error in the solution of a particular variable is represented by solver residual values. On a computer with infinite precision, these residual values will eventually go to zero as the solution is converged. For a normal computer though, these residual values will reach a small value and then stop changing. For single precision computations, as used for the present study, the residuals can drop as much as six orders of magnitude before leveling off. Thus the residual values are monitored to check for a converged solution. For the present study the absolute residual values were set at 10^{-8} for a converged solution to be reached. A stiff convergence criterion was important owing to the small dimensions of the microreactor and the large changes in the velocity flow-field in the stagnation zone.

5.3 Results and Discussion

Figure 5-14 shows the flow of reagents in the stagnation-flow microreactor. A variety of non-reactive fluids such as water, acetone and glycerol were used to test the reactor. The flow in the reactor was visualized using red fluorescent polymeric micro-spheres that are normally used for particle image velocimetry (PIV) measurement and that were 2μm in diameter. These particulate spheres were added to one inlet of the reactor while keeping the other inlet absolutely clear of the particles to be able to visualize the interface between the flows from the two inlets.

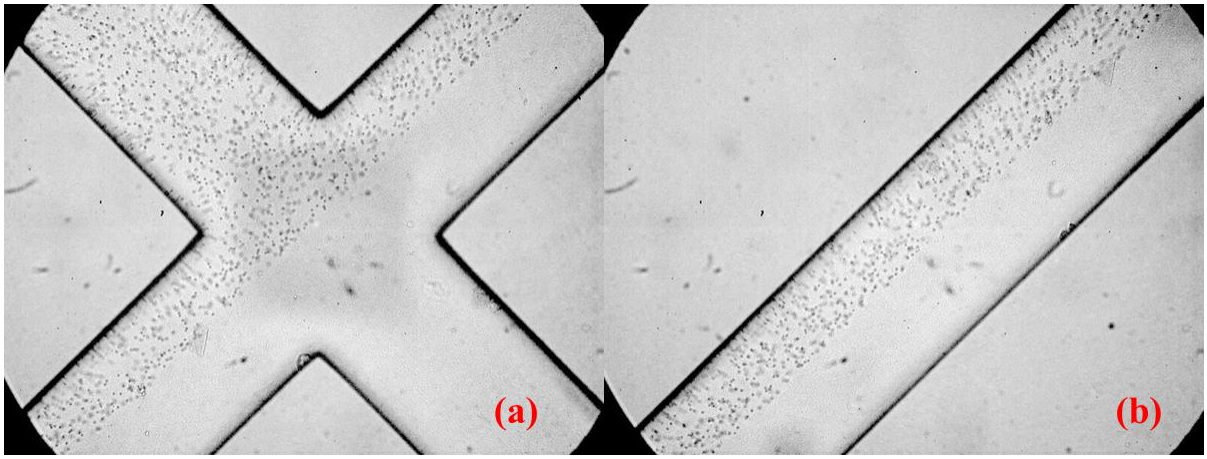

Figure 5-14: (a) Cold flow testing of microreactor using micro-spheres to visualize flow at stagnation zone. (b) Cold flow visualization downstream of the stagnation zone showing very little broadening of diffusion interface.

The flow rates were varied to achieve a range of Reynolds numbers in the reactor and these ranged from 15 to 120. As expected from behavior generally observed in microchannels at low Reynolds numbers, laminar flow was achieved with a clean interface between the flows from the two inlets. The quasi-steady stagnation plane between the two streams in the stagnation reactor (visualized by the fact that only one stream had the particles in it) was observed to be near the center of the reactor channel. The stagnation plane between the two fluid streams at the stagnation zone of the microreactor is seen in Figure 5-14 (a). Also, the particles continued to stay only on one side of the

channel with hardly any transfer to the other side, even downstream of the stagnation zone as can be seen in Figure 5-14 (b). It can now be said that there was hardly any mixing between the two flow streams, thus also affirming that the mixing across the fluid interface in the microreactor was heavily dependent on diffusion rather than convective effects. Previous studies[78], [112] have identified molecular diffusion in microfluidic devices and the broadening of this diffusion zone as the fluid travels along the length of a device. The broadening of the diffusion zone relates to the mixing between the molecules of two streams as the fluid travels downstream and can be related to the velocity of the fluid flow as:

$$\delta(z) = \left(\frac{2Dz}{U_a}\right)^{1/2}$$

where, $\delta(z)$ is the thickness of the interfacial diffusion layer at a distance z along the length of the microfluidic channel. D is the diffusivity of one fluid into the other while $U_a$is the fluid flow velocity. For the present microfluidic device, if we assume D to be on the order of 10^{-9} m^2/s, and the total length of the channel to be approximately 0.5 cm, then the thickness of the interfacial diffusional layer at the end of the main channel, based on the different flow rates used for the experiments, will be between 2.08 µm and 5.88 µm.

Both the PIV experiments as well as the numerical simulations for the stagnation flow microreactor were run for flow-rates at each inlet ranging between 62.5 µl/min and 500 µl/min. Both the shallow etched microreactor (etched to a depth of 60 µm) and the through-etched microreactors (etched to a depth of 500 µm) were used for these studies. As the velocities in the microreactors are dependent on the depth of the reactor etch, the two kinds of stagnation flow microreactors have different velocities for the same flow rates of the reagents. This resulted in the Reynolds number

ranging between 2 and 60 with a residence time between 40 ms and 5 ms per channel width for the fluid in the main channel of the microreactor.

A typical averaged velocity flow-field for the stagnation zone of the microreactor is shown in Figure 5-15. The inlets to the stagnation zone are aligned along the *y*-direction while the outlets from the stagnation zone are aligned along the *x*-direction. The magnitude of the velocities in the flow-field is indicated by the colors of the velocity vectors in the figure. The blue colored vectors indicate a low velocity magnitude while a high velocity magnitude is indicated by the red color of the velocity vectors. The velocity flow-field is seen to be symmetrical about the stagnation point near the centre of the microreactor.

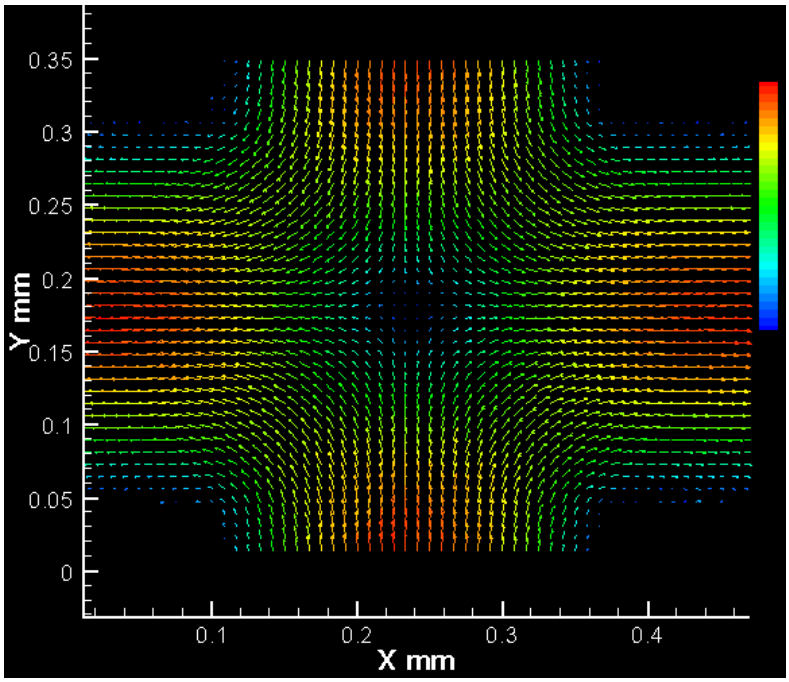

Figure 5-15: Typical average velocity flow-field calculated from PIV measurements. Magnitude of velocity is shown by using colored vectors in the image with blue vectors indicating a low velocity magnitude while red indicates a high velocity magnitude.

A common method for normalizing the velocities in a counter-flow configuration is usually by using the strain-rate instead of flow rates of the reactants. The strain rates at the interface for the

counter-flow setup were approximated as $(U_1 + U_2)/L$, where U_1 and U_2 are the velocities of the fluid from the two inlets respectively, and L is the separation distance between the two inlets. Figure 5-16 shows the deceleration of the fluid velocities from the opposing inlets to the stagnation zone of the microreactor for one of the strain rates studied in the microreactor. The fluid velocities from both the experimental PIV measurements as well as the FLUENT simulation are plotted with the solid line showing the numerical result while the individual points show the experimental data. The flow-field can be seen to be symmetrical about the stagnation point in the microreactor.

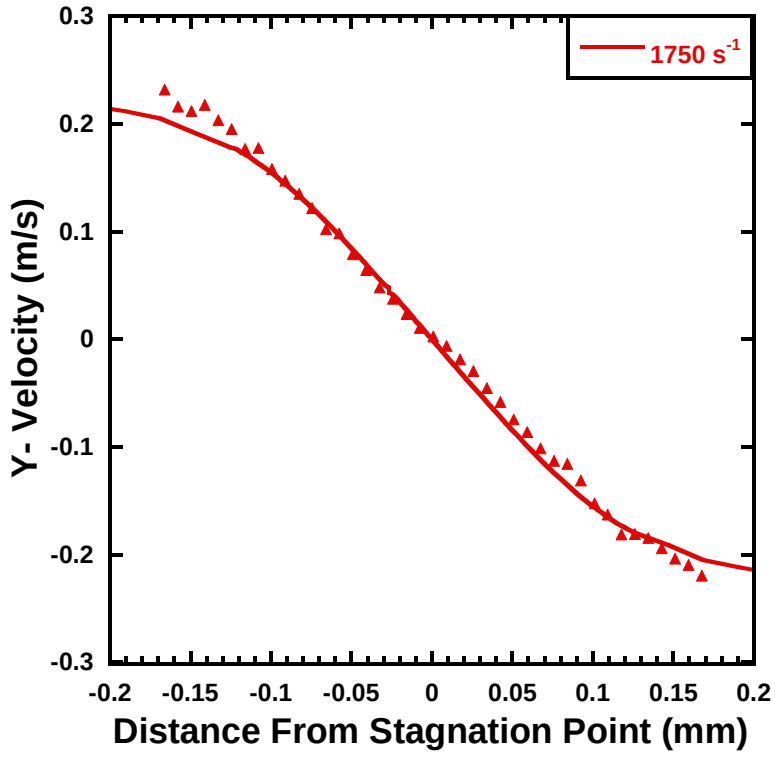

Figure 5-16: Fluid velocity from opposite inlets of the stagnation flow reactor as the flow decelerates towards the stagnation point. Solid line indicates FLUENT simulation results while the points indicate experimental PIV measurements.

Both experimental data from the PIV measurements and the corresponding results from the FLUENT simulations for the various strain rates under study are shown in Figure 5-17. The results shown concentrate on the stagnation zone of the reactor as this is the location where the flow-field

changes the most and show the decelerating velocities only from one inlet of the stagnation flow microreactor owing to the inherent symmetrical nature of the flow. The lines in the plots are the FLUENT simulation results while the points denote the experimental PIV results for corresponding strain rates. The measurements from the PIV system were limited to a strain-rate of 7000 s^{-1} since the PIV camera was not able to collect two full frames of data any faster. The maximum Reynolds number for the flows studied using the PIV was 60

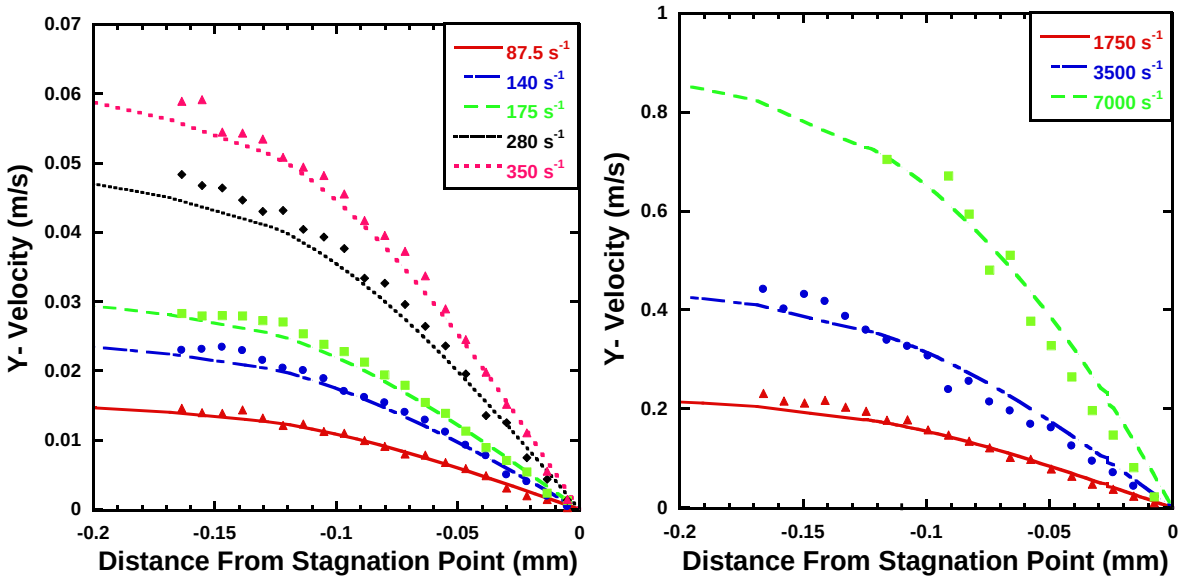

Figure 5-17: Fluid velocity as the flow decelerates towards the stagnation point. Lines indicate FLUENT simulation results while the points indicate experimental PIV measurements.

Figure 5-18 shows the velocity measurements as the flow decelerates towards the stagnation zone but at different depths in the microreactor. As the flow-field is three dimensional in nature, the flow-field will be different near the centre of the microreactor than near the walls. These measurements were made to prove that the flow-field was well understood at all depths in the stagnation zone. In the figure, Z = 0 indicates PIV measurements and FLUENT simulations at a depth which coincides with the centre of the microreactor. As the total depth of the microreactor is 500 µm, thus Z = 125 µm indicates measurements made at a distance halfway between the reactor wall and the

centre-depth of the microreactor. Similarly Z = 187.5 µm indicates measurements made at three quarters the distance between the reactor wall and the centre-depth of the microreactor. As can be seen from Figure 5-18, the FLUENT simulations and the PIV measurements agree very well with each other at almost all points in the domain apart from regions close to the reactor walls.

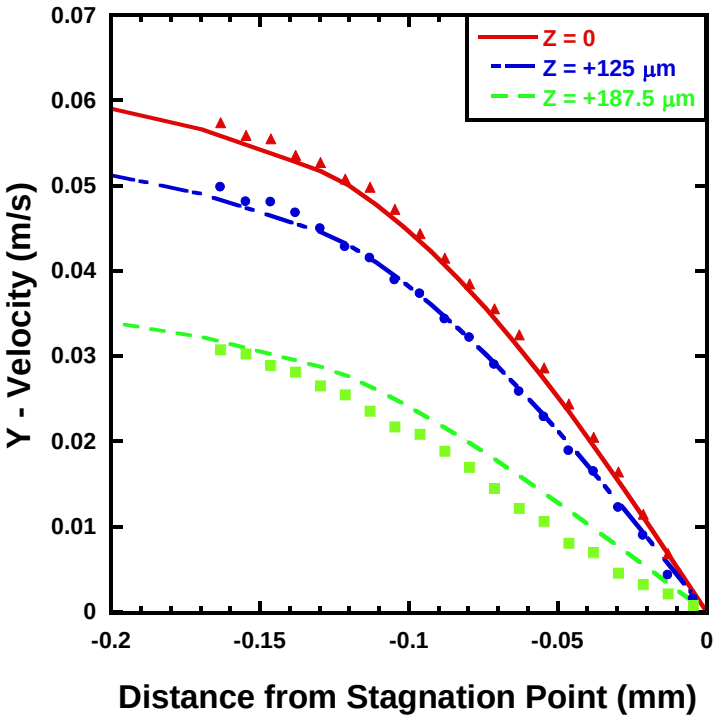

Figure 5-18: PIV measurements and FLUENT simulation results at various heights in the stagnation zone. All measurements and calculations at a strain rate of 280 s^{-1}.

As the present study is carried out with a stagnation flow reactor, it is important to quantify the velocity profiles of the fluids entering and exiting the stagnations zone. Thus Figure 5-19 shows the comparison of the FLUENT simulation results to the PIV experimental data by plotting the velocity profiles at the entrance and outlet to the main stagnation zone. Again, the lines indicate the simulation results while the points on the graphs indicate the experimental results for the various strain-rates. As can be seen from the plots, the numerical simulations agree very well with the experimental PIV results apart from very close to the wall. The reason for this discrepancy could be

because of the relative large size of the microparticles that have been used to track the flow. The relative large size of the particles (2μm) could be responsible for the poor resolution of the details in the flow-field close to the walls. But overall, the PIV measurements of the flow-field in the microreactors are in very good agreement with the predictions made by the numerical models. Thus the simulations can be used to correlate distance with reaction time and evaluate local strain rates as well as mixing rates.

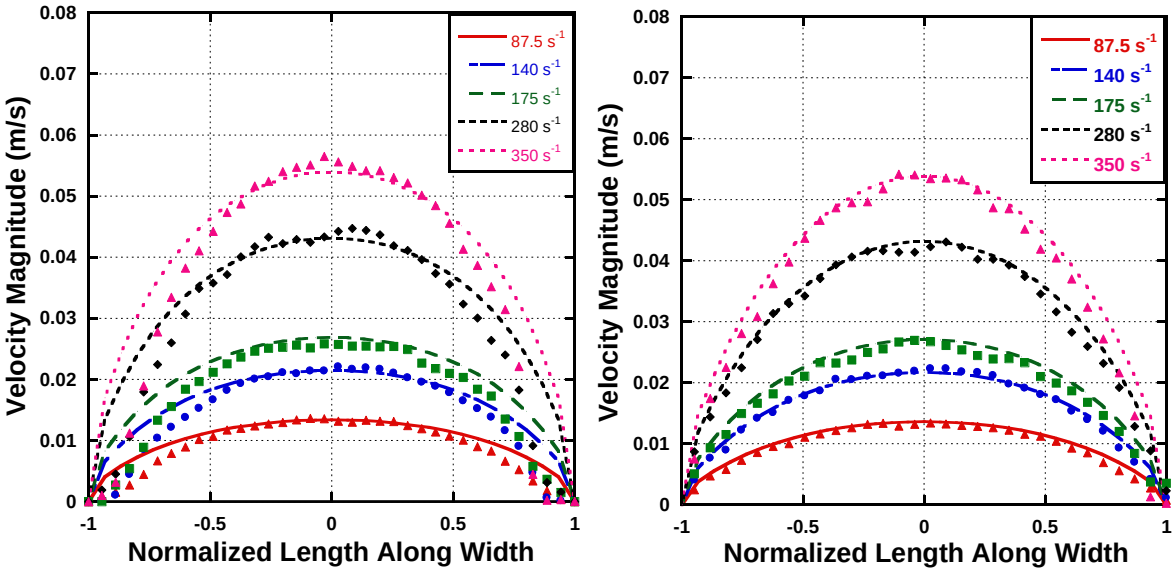

Figure 5-19: Velocity profiles at (a) inlet to stagnation zone and (b) outlet to stagnation zone.

5.4 Instabilities at High Flow Rates

Although very good agreements between the PIV measurements and the FLUENT simulations were observed over a range of low to moderate flow rates of the reagents into the microreactor, instabilities were seen to occur when the flow rates were raised to a critical high value. At low flow rates the flow-field is seen to be symmetric about the centre of the microreactor stagnation zone as shown in Figure 5-15 but when the flow rate is raised above a critical value the flow-field is no longer symmetric but instead the stagnation plane shifts towards one inlet or the other

which varies with depth. The flow-field when this shift in the stagnation plane occurs is visualized in Figure 5-20. The direction in which the stagnation plane shifts is purely stochastic in nature and cannot be predicted. A number of experiments were conducted and it was found that there was equal probability of the stagnation plane to move towards one inlet or the other.

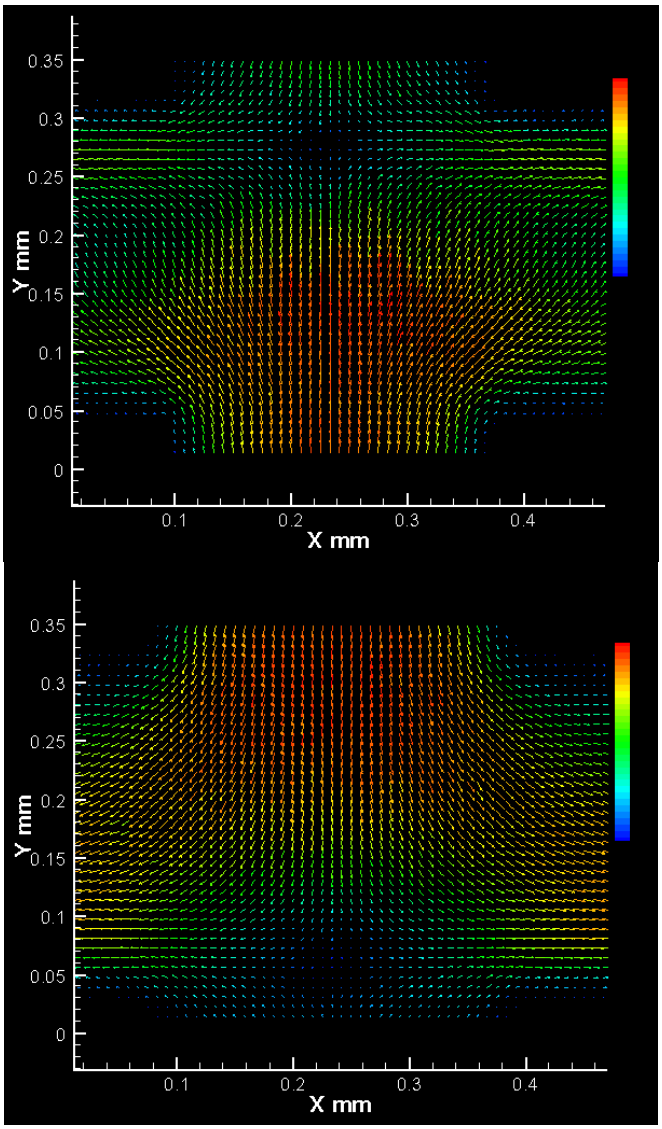

Figure 5-20: Shifting of the stagnation plane from the centre of the microreactor towards one inlet or the other.

Measurements were made at various heights along the width of the reactor to find the position of the stagnation plane at these various heights. Figure 5-21 shows the relative position of the stagnation plane at various heights for a number of experimental runs. As can be seen from the graph, the position of the stagnation plane is no longer vertical along the height of the microreactor (as would be expected in stagnation flow reactor) but instead shifts rapidly from one side of the microreactor to the other with very little change in the vertical direction.

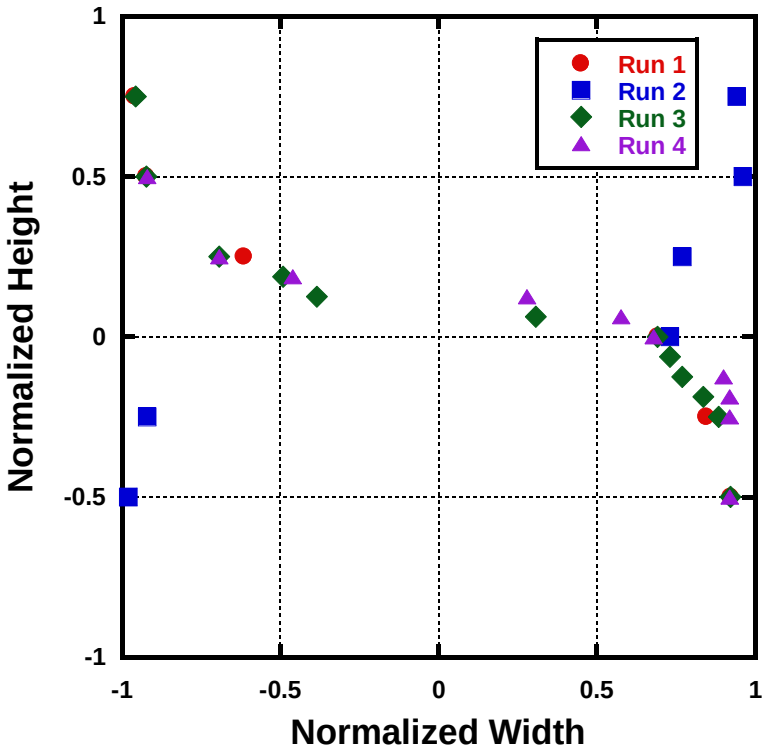

Figure 5-21: Position of stagnation plane at various heights in the deep-etched microreactor.

This shift in the stagnation plane is caused by the fact that the two fluids 'slip' over one another instead of coming to rest at the stagnation plane. Figure 5-22(a) shows a schematic of the cross-sectional view of the stagnation zone of the microreactor in the case of low flow rates of the fluids into the microreactor. The stagnation plane between the fluids entering the reactor is shown by the red line and is seen to be stable and vertical. When the flow rates are increased over a critical

value the stagnation plane is seen to shift and can be represented by the schematic in Figure 5-22(b). It should be noted that multiple runs made with the same flow conditions in the microreactor resulted in the stagnation plane that would shift towards either one inlet to the other, with the direction of the shift not being predictable.

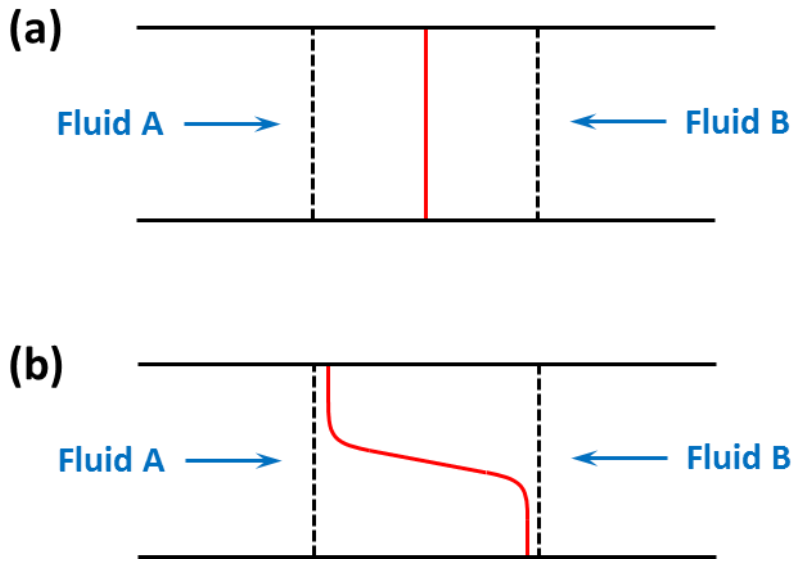

Figure 5-22: Schematic of the cross-sectional view of the stagnation zone of the microreactor showing the stagnation plane (red line) between the two fluid flows. (a) shows a stable stagnation plane between the two fluids at low flow rates and (b) shows the unstable stagnation plane at high flow rates in which the plane shifts towards one inlet or the other.

Similar bifurcation instability has also been seen in macroscopic experiments involving stagnation flows formed between opposing jets of gases [113]. The experiments from the study show that at low Reynolds number and with equal jet velocities, the flow remains symmetric about a plane between the two nozzle exits and the stagnation plane is located midway between the nozzles. When the flows from the jets were increased past a critical Reynolds number then the flow remained symmetrical no longer and stagnation plane was observed to shift away from the midway plane. Figure 5-23 shows the velocity flow-field from PIV measurements done in the study. As can be seen from the visualization of the flow-field, the stagnation plane, instead of being symmetrically in the

centre, shifts towards one inlet or the other. Also noticeable from the images, is the fact that the shift in the stagnation plane is not always in the same direction, even though the flow conditions otherwise remaining unchanged. This 'pitchfork bifurcation' instability is very similar to that observed in the present microreactor.

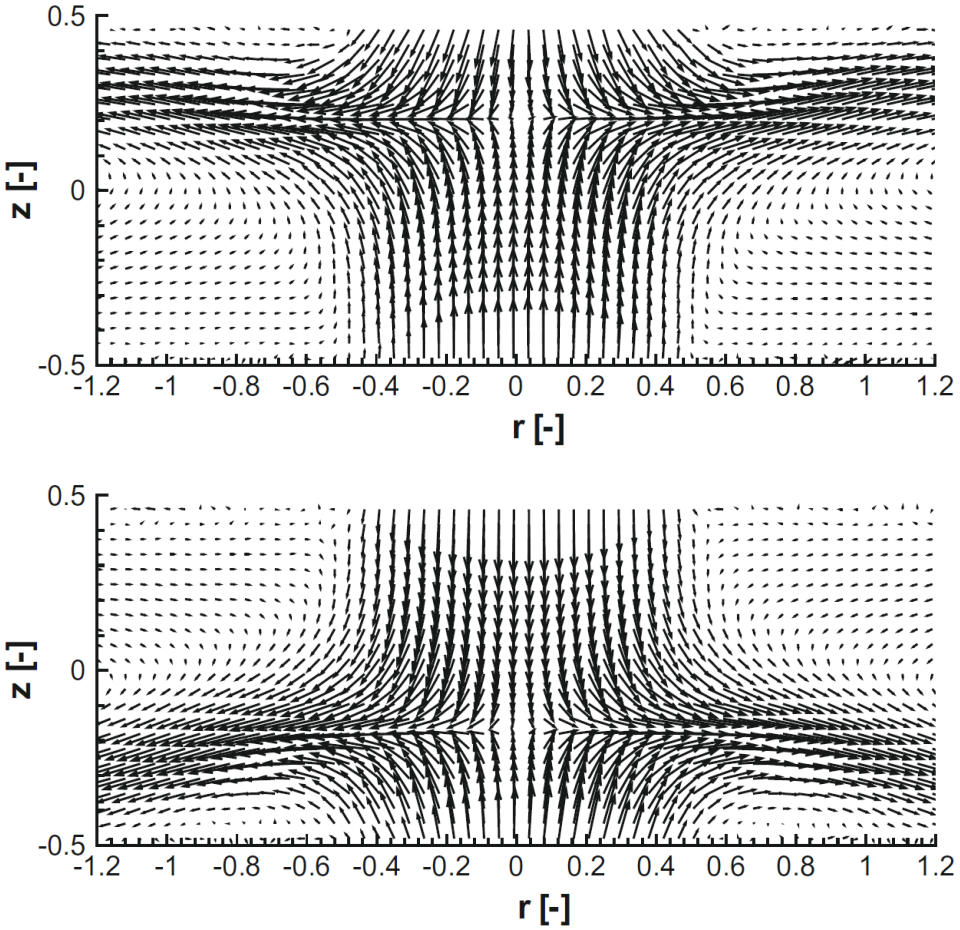

Figure 5-23: Velocity flow-fields from PIV measurements between two opposing jets. Both cases were at a flow velocity of 24.5 cm/s and Reynolds number of 153.7 (taken from [113]).

Instabilities have also been noticed at higher Reynolds number flows in microfluidic devices. A number of studies [114]–[120] in the past have shown that when the fluid velocities are increased, the flow in microfluidic devices do not remain laminar in nature. Most of these studies have concentrated on the mixing efficiency in *t*-type micromixers. As the mixing in the microreactors is

based on diffusional mixing alone, thus one method of increasing the mixing efficiency is by changing the flow regime from a simple laminar one to a more chaotic one.

Studies [114], [115] have found that three kinds of laminar regimes exist in the mixing channel. At very low Reynolds numbers, the flow between two fluids is stratified in nature and the mixing occurs only due to molecular diffusion. When the Reynolds numbers are increased then the flow regimes change slightly to a more chaotic regime resulting in more mixing between the fluids. This regime is referred to as the vortex flow regime. When the Reynolds numbers are increased even further then the flow shifts to a regime called the engulfment flow regime. Engulfment flow is characterized by the creation of secondary flows and the separation of the boundary layers due to the sharp edges of the corners at the junction of the micromixer.

Figure 5-24 visually shows the pathlines generated using numerical simulations of a t-type micromixer. It can be clearly seen that as the Reynolds number is increased from a low number (12) to one that is significantly higher (240), the regime shifts from a simple stratified laminar flow regime to one that is chaotic in nature. It is believed that the instabilities seen in the present study at high Reynolds number flows are similar in nature to the engulfment flow regime. The shifting of the stagnation plane can now be explained by the creation of secondary flows in the stagnation zone.

The study of the stagnation flow between two opposed jets by Ciani et al. [113] demonstrated that the Reynolds number alone could be used to characterize the flow between two opposing jets. But in the present microreactor, these instabilities set in at different flow rates in the deep etched reactors (500 μm deep) and the shallow etched reactors (60 μm deep). The instabilities occurred when the flow rate of the fluids was increased over 750 μl/min for the deep etched reactors (i.e. a Reynolds number of 24) while they occurred above a flow rate of 2000 μl/min for the shallow etched reactors (i.e. a Reynolds number of 240). As the critical flow rate at which this bifurcation instability occurs is different when the aspect ratio of the reactor is changed, thus it can be stated that the instability depends on both the volume flow rate as well as geometrical parameters of the microreactor. Thus,

Reynolds number alone cannot be used to characterize the flow and another dimensionless number is needed.

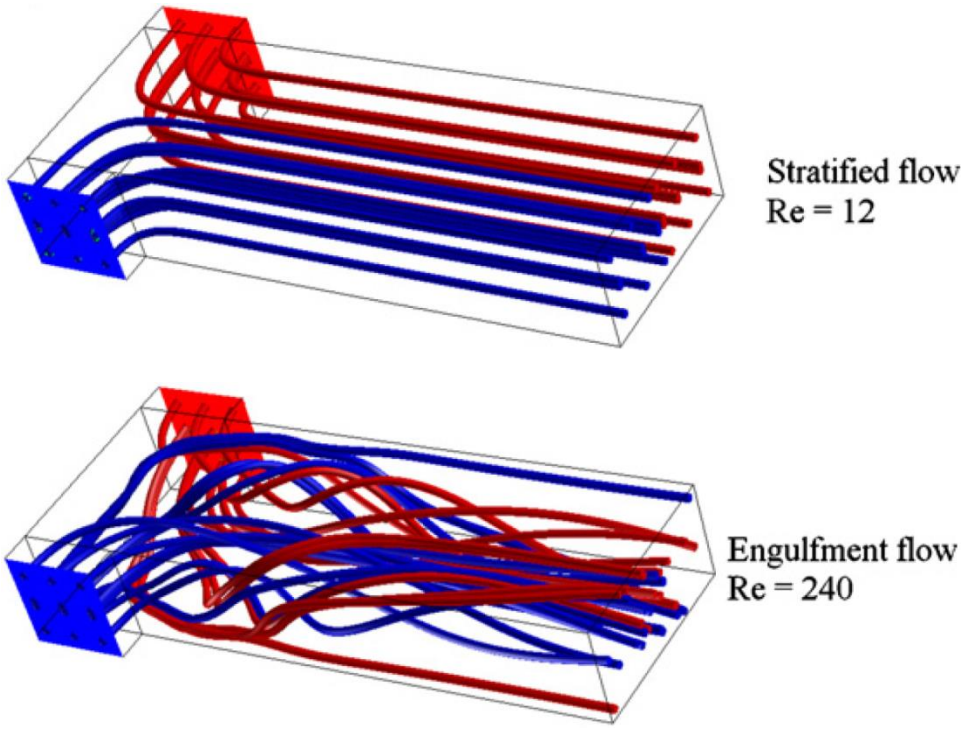

Figure 5-24: Pathlines at the entrance of a microfluidic mixing channel for different flow regimes showing difference between low Reynolds number and high Reynolds number flows (taken from [117]**).**

Such a dimensionless number was suggested by Soleymani et al. [121] and has been used by other studies as well to predict when the engulfment in the flow-field will set in. These studies showed that the transition to the engulfment flow regime is not governed by Reynolds number of the flow alone but is also affected by parameters such as aspect ratio, the width of the inlets and width of the mixing channel. This dimensionless number is referred to as the identification number (K) and can be defined as:

$$K = Re^{0.82}\left(\frac{W}{h}\right)^{-0.79}\left(\frac{D_{h,in}}{D_h}\right)^{-1.5}\left(\frac{w}{h}\right)^{0.15}$$

where, Re is the Reynolds number of the flow at which transition to the engulfment regime occurs, W is the width of the inlet channels, h is the depth of the reactor channels, $D_{h,in}$ is the hydraulic diameter of the inlet channels, D_h is the hydraulic diameter of the mixing channel and w is the width of the mixing channel. It was found by a variety of studies [114], [116]–[118], that the transition to the engulfment flow regime occurs at an identification number close to 100. But a study by Sultan et al. [119], which studied t-type micromixers with headspace, found there to be no correlation between the transition to a chaotic flow regime and the identification number. For the present study, the identification number (as defined by Soleymani et al.) for the shallow-etched reactor was found to be 27 while that for the through-etched reactor was 29. The difference between the present study and the ones before (where transition to the engulfment flow regime was related to the identification number of 100) could be attributed to the fact that the present study does not use t-type micromixers but is instead a study of a planar stagnation flow microreactor.

Considering that instabilities were only found to exist at high Reynolds number flows in the shallow-etched reactor which was to be used for the reactive hypergolic studies, care was taken to conduct the experiments in the regime where the transition to the chaotic regime did not take place.

Chapter 6

Studies with Reactive Hypergols

This chapter discusses the experiments carried out with the hypergolic propellants. The hypergols used in the study were studied using both conventional drop tests as well the microreactors fabricated from LTCC as well as silicon and glass. In addition to the new, promising hypergols mentioned earlier (TMEDA and DMAZ) a number of other fuels were also used to provide a baseline for the results provided by TMEDA and DMAZ with nitric acid. The chosen fuels were triethylamine, dicyclopentadiene and indene as interactions of these fuels with white fuming nitric acid have been previously studied. Schala et al. [122] have demonstrated that triethylamine is hypergolic with WFNA while Trent and Zucrow [123] have studied the interactions of WFNA with dicyclopentadiene and indene in a flow reactor.

6.1 Drop Test for Hypergols

Drop tests have been the most popular method to test for hypergolicity owing to their simplicity and the ease of experimental setup. The tests rely on opto-electrical devices for detecting the initiation of the event and identification of the ignition kernel, and on thermo-electrical devices for recording the temperatures traces in the gas phase above the condensed-phase reaction zone. The drop test experiments performed for this study were performed using a setup identical to the one described by Wang et al. [53] for their studies regarding the interaction between TMEDA and nitric acid. A schematic of the experimental setup is provided in Figure 6-1 and a detailed description is provided in the study by Wang et al.

For the drop test, an excess amount of nitric acid (either 90% nitric acid or WFNA) of approximately 80 µL was placed at the bottom of a square glass cuvette. The cross section of the

cuvette was 10 mm on each side of the square and it was about 45mm tall. The drop of fuel was produced using a plunger attached to a glass syringe which slowly produces a droplet of fuel. This fuel droplet was approximately 7~10 µL in volume and traveled towards the centre of the oxidizer pool in the cuvette. Care was taken that no additional momentum was supplied to the droplet of fuel. A Phantom high speed camera was used to record the process from the actual release of the fuel droplet to the end of the ignition event. . A He-Ne laser, and a corresponding photodiode, placed underneath the syringe triggered the data acquisition system through a reduction in the photodiode signal as the drop of fuel descended and cut across the laser beam.

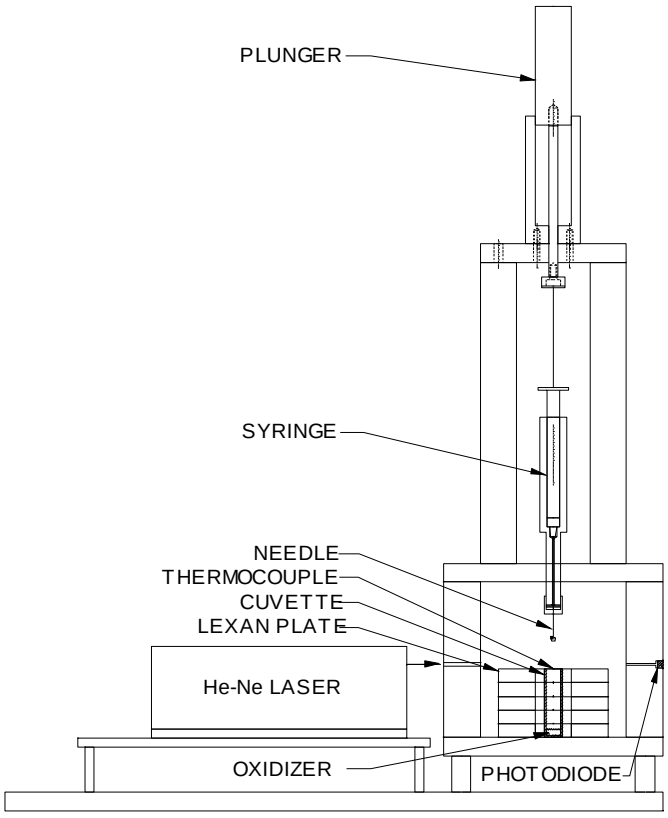

Figure 6-1: Schematic diagram of hypergolic drop-test experiment (taken from [53]**).**

All drop tests were conducted with the Phantom camera set at 2000 fps and with 80 μL of the oxidizer placed at the bottom of the cuvette. Given that the inner dimensions of the cuvette were 9mm x 9mm, this provided for a depth of about 1mm of the oxidizer in the cuvette. The depth of the oxidizer pool in the cuvette did vary with it being higher at the walls of the glass cuvette than at the centre of the cuvette due to the surface tension of the oxidizer. The time notation used for all the tests is such that $t = 0s$ indicates the time at which the fuel droplet just makes contact with the oxidizer pool in the cuvette. Five tests were conducted for each fuel and oxidizer combination and the results presented below are the typical results from any one test.

6.1.1 Drop Tests with TMEDA – WFNA

Drop tests conducted in previous studies [53] have been shown that the reactions that occur during the interaction between TMEDA and nitric acid are extremely energetic and have very low ignition delay times. When the drop tests for the present study were conducted between TMEDA and WFNA, these characteristics were again observed.

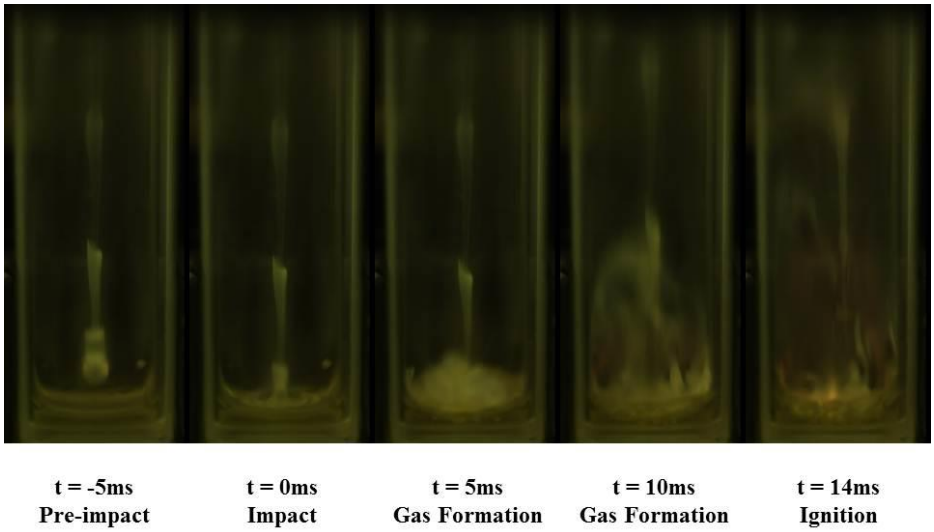

Figure 6-2: Still images from drop-test between TMEDA and WFNA showing ignition in the last frame.

When the TMEDA drop travelled towards the WFNA pool in the cuvette, a particulate wake was noticed behind the droplet (Figure 6-2). The particulate wake was quite dense and it can be safely assumed that it is caused due to the reaction between the TMEDA droplet and the vapors from the oxidizer pool that are trapped within the cuvette. The TMEDA droplet impacts the oxidizer pool and causes enough mixing between the two liquids for the condensed phase reactions to occur. These condensed phase reactions give rise to gas phase products and a particulate cloud is seen to form over the oxidizer pool almost instantaneously. Boiling of the oxidizer pool, caused due to the exothermic condensed phase reactions, is noticed around 10ms with more gas formation and an increase in the particulate cloud over the oxidizer. The boiling of the oxidizer pool continues till ignition is achieved at about 14ms from the time of impact. The ignition occurs very close to the surface of the oxidizer pool as very little time has elapsed since the time of impact and thus the time allowed for the gaseous products to collect higher up in the cuvette is also lower. The flame continues to burn very close to the oxidizer pool until the fuel droplet is completely reacted.

6.1.2 Drop Tests with DMAZ – WFNA

In the case of DMAZ with WFNA, the particulate wake, as the fuel droplet approaches the oxidizer pool, is still present but is fainter (Figure 6-3) than what is seen when TMEDA interacts with WFNA. The initial impact of the droplet into the oxidizer pool causes a splash and mixing of the two liquids together which leads to the initial condensed phase reactions. These condensed phase reactions cause a temperature rise which can be visualized by the boiling of the oxidizer pool.

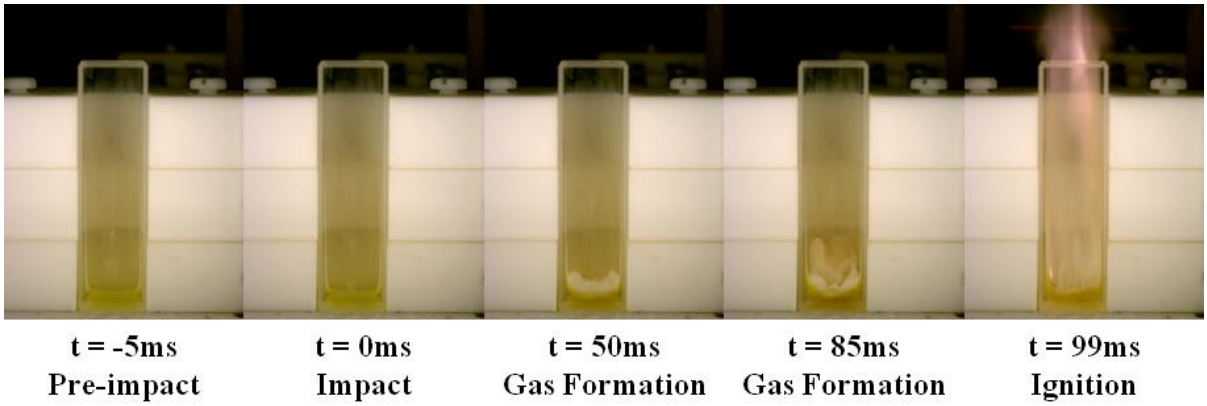

Figure 6-3: Still images from drop-test between DMAZ and WFNA showing ignition in the last frame.

After impact of the fuel with the oxidizer pool, the formation of gas, as well as the dense particulate cloud around the droplet is not instantaneous but rather is a little delayed and takes about 50 ms for the particulate cloud to become really dense. The condensed phase reactions continue and further give rise to more gas formation and the particulate cloud becoming denser continues till ignition is achieved around 99 ms. The ignition is far more violent than that seen for the TMEDA-WFNA case and a sharp popping noise is heard along with the ignition event. The flame rapidly moves upwards in the cuvette and continues to burn, staying close to the oxidizer pool, as long as the unreacted gaseous reactants are present.

6.1.3 Drop Tests with Triethylamine – WFNA

In the test between triethylamine and WFNA, the particulate wake that was seen in the earlier drop tests with the other fuels was again seen to be present, when the fuel droplet approached the oxidizer pool (Figure 6-4). The particulate wake was denser than the one when DMAZ was used as a fuel. The impact of the droplet into the oxidizer pool in this case as well causes a large splash and mixing between the two liquids.

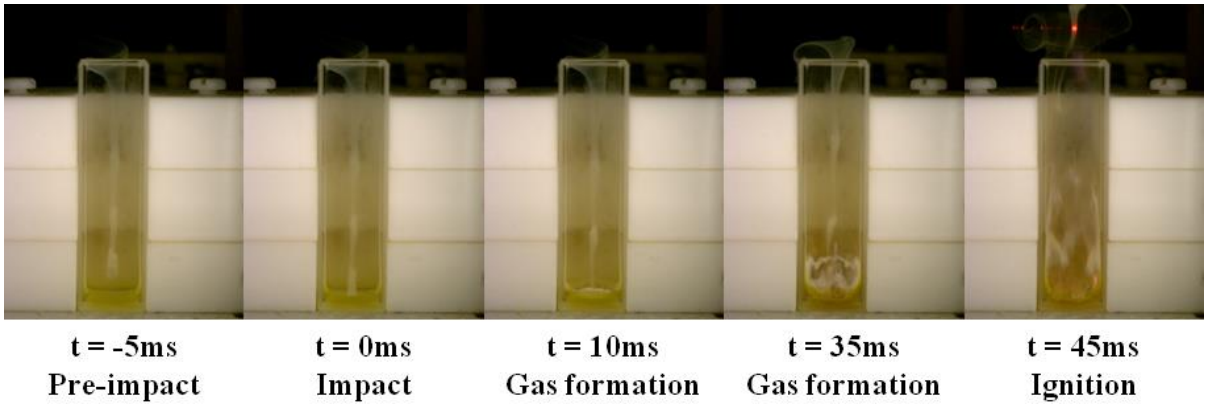

Figure 6-4: Still images from drop-test between triethylamine and WFNA showing ignition in the last frame.

This initial mixing between the reactants causes the condensed phase reactions to occur and the bubbles are seen to form in the oxidizer pool, indicating a rise in temperature and gas evolution. After impact of the fuel droplet into the oxidizer pool, the formation of gases occurs almost instantaneously (Figure 6-4) with the accompanying particulate cloud that forms around the droplet. The condensed phase reactions add more gases to the particulate cloud which grows rapidly (~35 ms from the time of impact). The reactions now begin to occur at a much faster rate due to the elevated temperatures and leads to the ignition of the reactants in the gas phase above the oxidizer pool. The flame rapidly moves upwards in the cuvette to portions where there are still unreacted gaseous reactants left and unlike the case where DMAZ is used as the fuel, the flame does not remain close to the oxidizer pool and seems to be contained in the gas phase in the upper parts of the cuvette. The flame only returns to be concentrated near the surface of the oxidizer pool once all the gas phase reactants have been exhausted and the flame is about to extinguish. The average ignition delay measured for the various drop tests conducted with triethylamine as the fuel was about 45 ms. A sharp popping sound is heard along with the ignition event which can be attributed to the gaseous products being forcefully ejected from the cuvette.

6.1.4 Drop tests with Dicyclopentadiene – WFNA

As in the case of triethylamine, the dicyclopentadiene used in drop tests along with WFNA to recreate the reactants used by Trent and Zucrow [123] to test the behavior of alicyclic hydrocarbons with nitric acid. The drop test for dicyclopentadiene with WFNA showed results which differed from the results seen when the other fuels were used. At the onset, there was almost no formation of a white plume-like wake as seen in the other tests when the droplet travelled towards the oxidizer pool (Figure 6-5 and Figure 6-6). This indicated that the reactions occurring between the nitric acid vapors present within the walls of the cuvette and the fuel droplet were minimal.

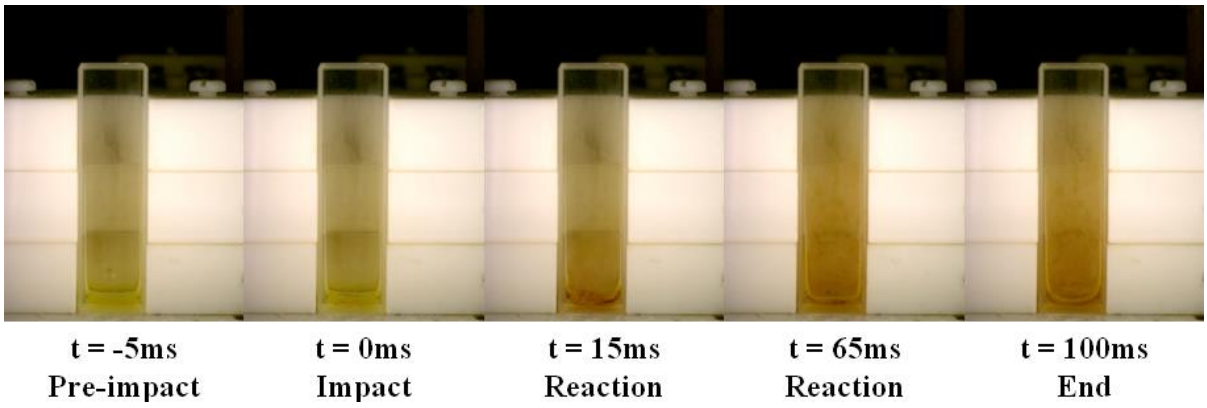

Figure 6-5: Still images from drop-test between dicyclopentadiene and WFNA showing ignition in the last frame.

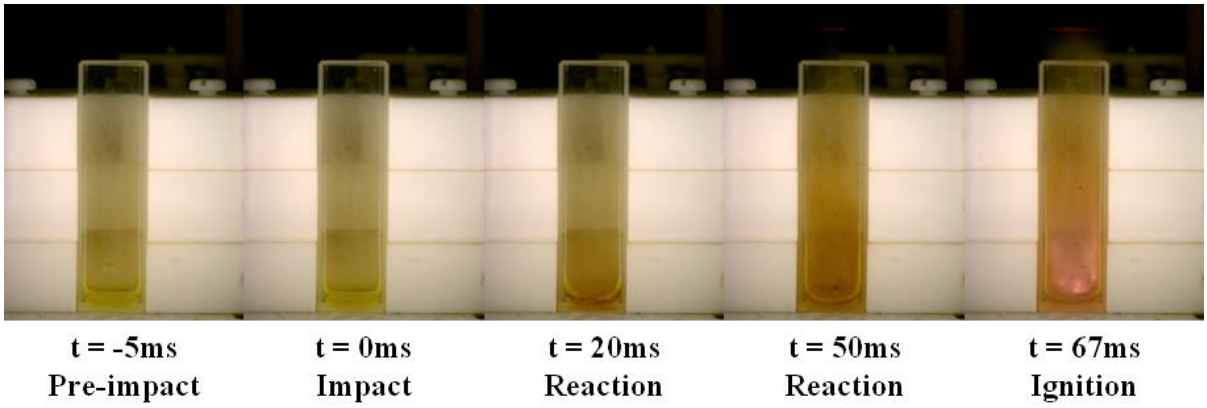

Figure 6-6: Still images from drop-test between dicyclopentadiene and WFNA showing no ignition.

The initial impact caused the mixing of the two fluids and led to reactions in the condensed phase. Two kinds of outcomes were seen during the drop tests between dicyclopentadiene and WFNA: one in which ignition occurred (Figure 6-5) and the other where there was a vigorous reaction and gas formation but no ignition (Figure 6-6). In both these cases the fuel droplet stayed submerged within the oxidizer pool after impact and the initial reactions caused the reactants to be splattered away from the point of impact. In the case of no ignition, a formation of a dark product was seen early on (~15 ms) with the occurrence of a vigorous reaction, which resulted in bubbles being formed in the oxidizer pool, that started about 65 ms from the time of impact. This vigorous reaction was accompanied by an evolution of gases and subsided by about 100 ms from the time of impact. In the case of ignition, the vigorous reaction accompanied with the evolution of gases started much earlier (~50 ms) with ignition itself occurring at about 67 ms. In the case of ignition, the flame produced was extremely bright and more luminous than that seen when the other fuels were used. Also, the flame produced by the ignition event lasted much longer (almost 1s) than when other fuels were used. There was no difference in droplet position or the amount of gas produced between the case where ignition occurred and where it did not. It should be noted that the case of ignition only occurred once and it was not possible to reproduce it in the five drop tests that were conducted between dicyclopentadiene and WFNA.

6.1.5 Drop Tests with Indene – WFNA

The final fuel used for this study was Indene and this was in accordance with the aromatic hydrocarbons used by the study by Trent and Zucrow [123]. The drop test when Indene was used as a fuel with WFNA was similar to the one where dicyclopentadiene was used as the fuel. Almost no plume was noticed when the droplet travelled towards the oxidizer pool (Figure 6-7) as was the case when dicyclopentadiene was used for the drop tests.

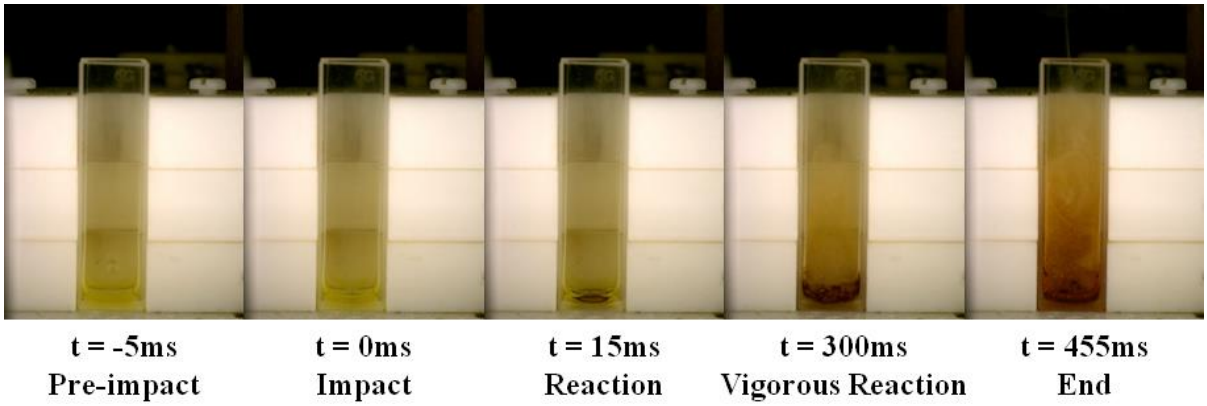

Figure 6-7: Still images from drop-test between indene and WFNA showing no ignition.

When the droplet impacted the oxidizer pool, it stayed submerged in the pool and was not ejected out. The impact of the droplet causes a large splash and a noticeable appearance of a black product which starts to coat the side walls of the cuvette because of the splash. The reaction between the fuel and the oxidizer when the droplet impacted the oxidizer pool, though, was much slower than that noticed for dicyclopentadiene. Although a dark product was noticed quite early in the drop test, there was no vigorous reaction (boiling of the oxidizer pool) or gas formation till about 300 ms from the time of impact. This vigorous reaction then continued till approximately 455 ms but lead to no ignition between the two reactants. The tests were repeated four more times but ignition was not achieved for any of the tests. A dark, viscous and extremely sticky product was left behind after ever drop test that was conducted.

6.2 Experiments with Fabricated Silicon-Glass Microreactors

The experimental setup (Figure 6-8 and Figure 6-9) for reactive flow studies carried out using the microreactors consisted of the manifold-reactor assembly (similar to the one used for the PIV studies), placed under an upright microscope (Nikon Eclipse LV100). A high speed camera (Phantom V 7.3) was mounted onto the upright microscope to optically study the flow in the microreactors. A

pressure driven flow was used to create the fluid flow in the microreactors with a positive pressure being applied at the inlets while keeping the exhaust open to atmospheric pressure. The fuel and oxidizer were introduced into the manifold using Teflon® tubing connected to high pressure stainless steel syringes. These syringes were controlled by two independent high pressure syringe pumps (Harvard Apparatus PHD4400), giving a high degree of control on the flow rates.

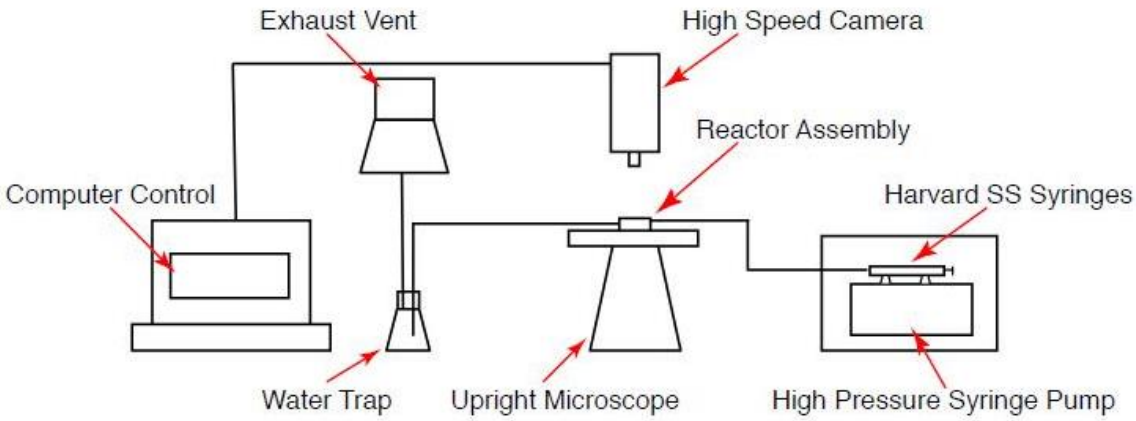

Figure 6-8: Schematic of microreactor experimental setup.

Fine-wire shielded K-type thermocouples were introduced into the exhaust reservoir of the main channels to record the temperature of the exhaust fluids from the microreactor. A rise in temperature at the exit was an indication that an exothermic reaction had occurred inside the reactor. A water trap and high velocity exhaust fan were also attached to the exhaust of the manifold for the safe disposal of the toxic products of the reaction.

All experimental runs in the microreactor were carried out with the oxidizer being diluted with distilled water. Dilution of the oxidizer helped in reducing the available nitric acid in the system and thus made sure that the exothermic reactions inside the microreactor could be properly controlled. This is of particular importance as the reaction between most hypergols is extremely exothermic and

almost instantaneous with the production of large amount of gases and salts. The dilution of the oxidizer thus helped in isolation of the early condensed phase reactions in the system. Moreover the dilution helped in studying a range of conditions within the reactor. The microreactors were tested using flow rates such that the Reynolds number of the flow in the channels ranged between 7 and 112. These flow rates yielded a residence time ranging between 0.432 ms and 27 us per channel width.

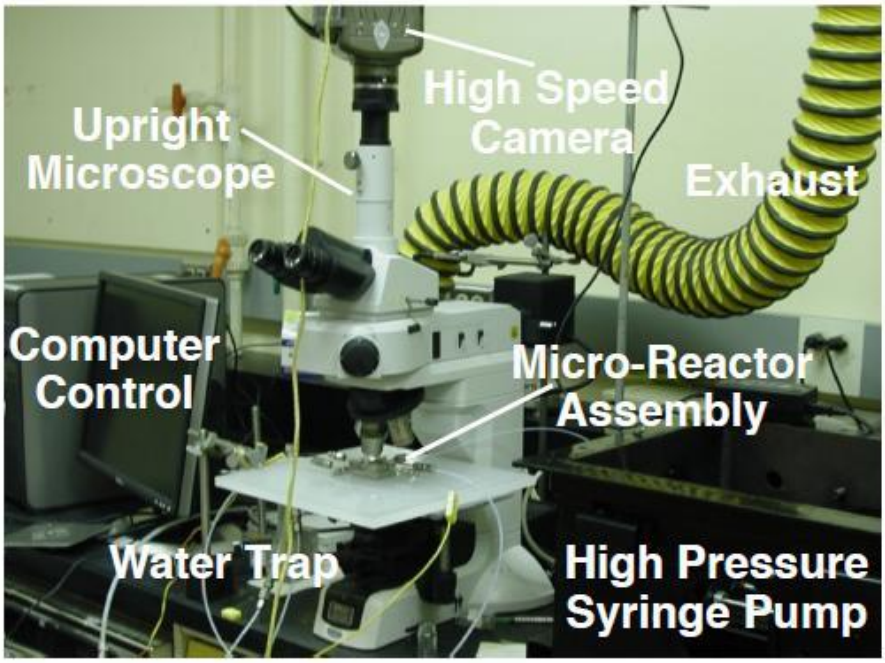

Figure 6-9: Photograph of setup used for reactive hypergols in microreactor experiments.

Figure 6-10 shows still images from high-speed videos of reacting flows between the various fuels and 30% WFNA. All images were taken at 1000 fps with the flow rate of all reactants being 500 µl/min. As can be seen from the images the reaction fronts are very stable with very few perturbations even with a reaction occurring at the interfaces and a laminar flow was achieved using all the fuel and oxidizer combinations. It can be reasoned that due to the reaction being diffusion controlled and very little mixing taking place in the reactor, the system will always remain a liquid-liquid interaction and the reaction zone can be properly controlled to study the interactions in the condensed phase as well

as the impact of diffusion on the reactions. It should be noted from the high speed images of the reaction front that the reaction diffusion zone is extremely thin for the TMEDA – nitric acid case but grows to become quite thick when indene and WFNA were reacted in the microreactor.

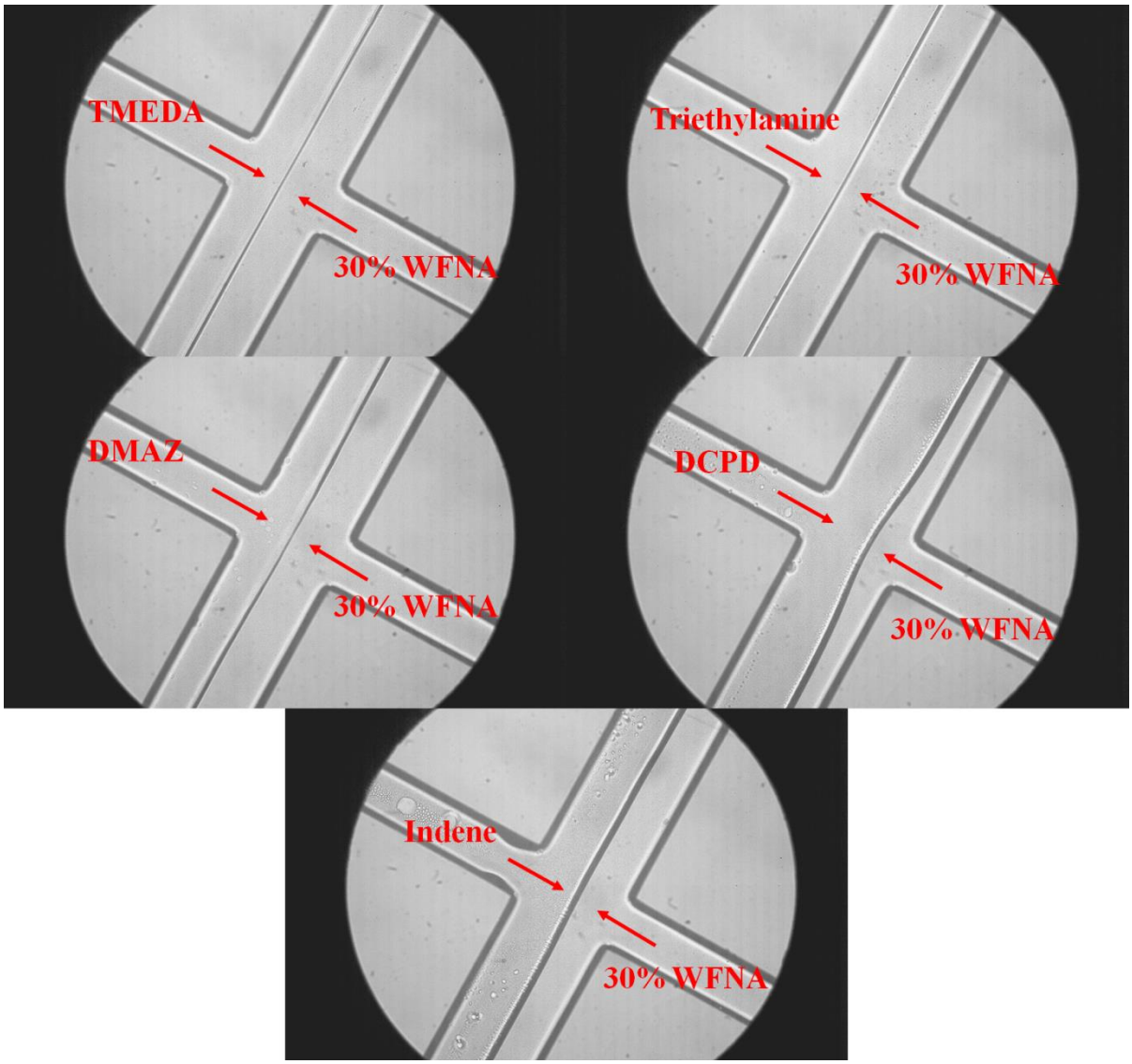

Figure 6-10: Still frames from reactive flow in microreactor using the various fuels with 30% WFNA. All flow rates for the reactants were set at 500 µl/min and the images were captured at 1000 fps.

6.2.1 Microreactor Experiments with TMEDA – Nitric Acid

Care was taken while running TMEDA along with nitric acid in the microreactors as the reaction between the two is extremely exothermic and also instantaneous. As one of the first heat releasing reactions between TMEDA and nitric acid is a salt formation reaction [53], to isolate the early condensed phase reactions, the microreactors were run at very low concentrations of the oxidizer. Exit temperatures were measured using the fine wire thermocouples attached to the stainless steel manifold for a variety of flow rates and oxidizer concentrations.

Figure 6-11 shows the change in exit temperatures with changing flow rates of the reactants as well as changes in oxidizer concentration. As can be seen from the plotted graph, a rise in exit temperature is observed even at very low concentrations of the oxidizer. This can be expected due to the highly exothermic nature of the TMEDA – nitric acid reaction. This rise in exit temperature of the fluids was noticed to increase with an increase in concentration of the oxidizer. The dilution of the oxidizer concentration, which resulted in a drop in the temperature of the products at the exit is because of the lowering in the reaction rates between the reactants that are able to diffuse across the interface and thus cause a reaction to occur. With the dilution of nitric acid, there are lesser reaction-causing nitric acid molecules that are available to diffuse across the interface to interact with the TMEDA molecules. Thus it is natural that the amount of reaction occurring between diluted nitric acid mixtures and TMEDA is far lesser than the reaction that occurs with undiluted nitric acid and TMEDA. When more reactants are available to diffuse across the interface, the reactions that occur see an increase and the temperature of the products at the exit rises accordingly. Also seen in the temperature plot (Figure 6-11), is that rise in exit temperatures is also seen to increase with an increase in flow rates of the reactants into the microreactor. Care was taken to limit the flow rate of each of the reagents into the microreactor to 2000 μL/min so as to ensure that the flow-field in the reactor did not transition into an unstable regime.

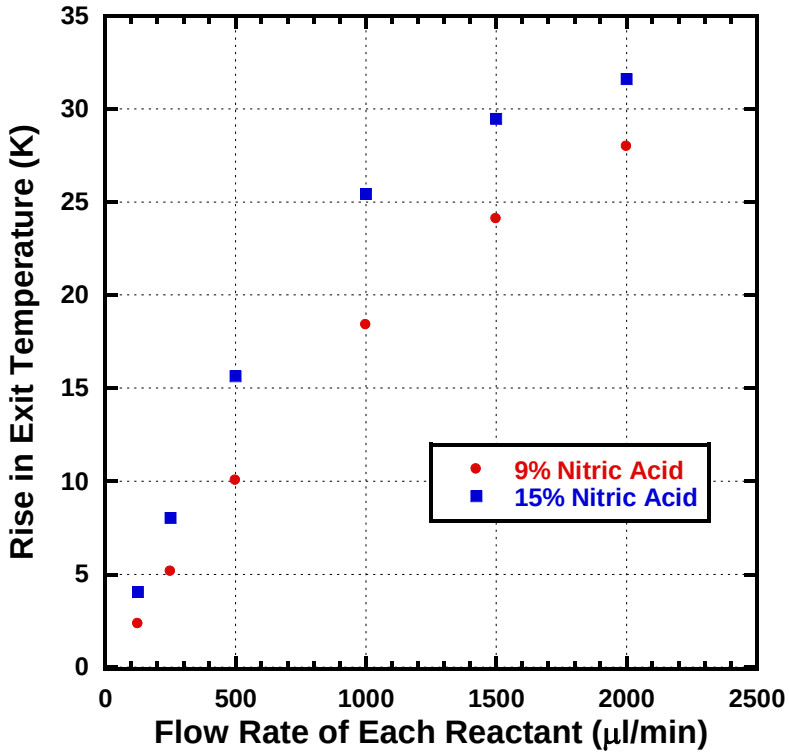

Figure 6-11: Change in exit temperatures for TMEDA and Nitric Acid in the microreactors with increasing flow rates of reactants.

.

It should be noted that the experimental runs for TMEDA and nitric acid using the microreactor were only possible at very low concentrations of the oxidizer. At lower concentrations the amount of salt produced by the reaction between TMEDA and nitric acid was low and the salt stayed in solution without precipitating out. At higher concentrations of the oxidizer, there was a large amount of salt precipitation that occurred in the main channel of the reactor as seen in Figure 6-12 and the system no longer remained a simple condensed phase laminar flow one and gave way to a transient multi-phase system. Given that the early condensed phase chemistry could no longer be isolated in the microreactors with high concentrations of the oxidizer, care was taken to always maintain a low concentration of nitric acid while running it along with TMEDA in the microreactor.

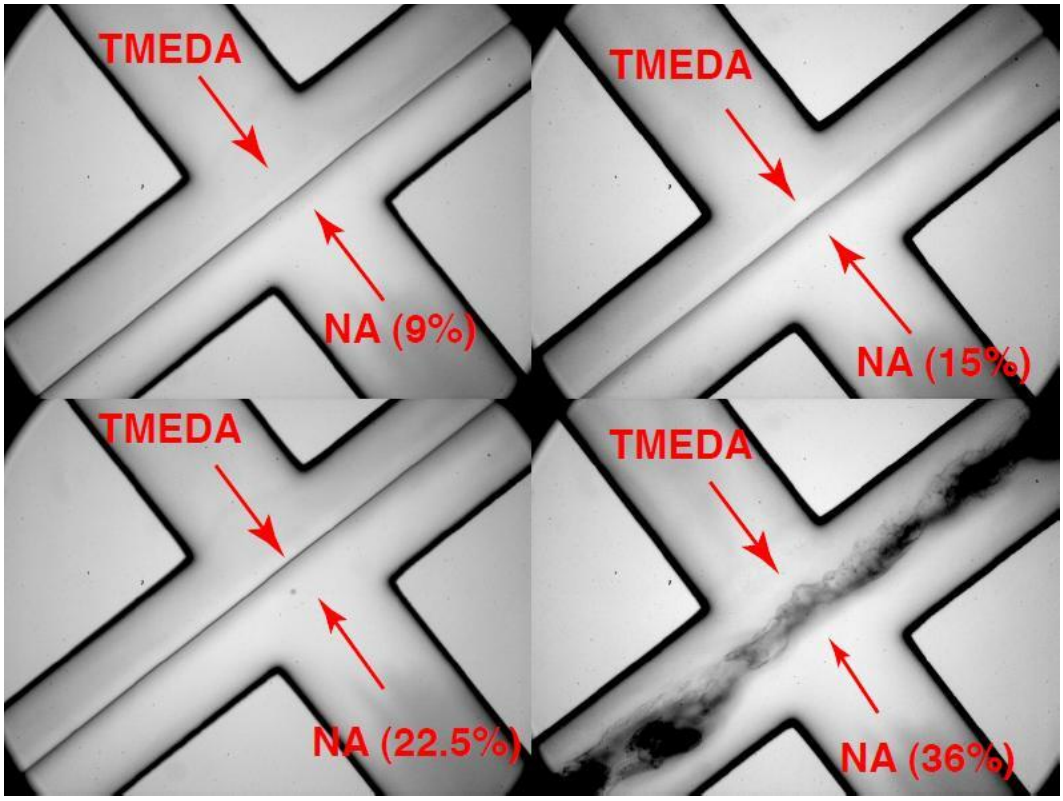

Figure 6-12: Interaction of TMEDA with nitric acid diluted with distilled water along with salt-formation at higher concentrations of nitric acid. The flow rates for all the reactants in each case were set at 500 ul/min and the images were captured at 1000 fps.

6.2.2 Microreactor Experiments with DMAZ – Nitric Acid

With the setup and the environmental conditions being the same as that used for the TMEDA-NA experiments, the experiments for DMAZ with nitric acid were started with a similar concentration of nitric acid. In this case as well it was noticed that the rise temperature observed at the exits increased with an increase in flow rates of the reactants (Figure 6-13). Also as in the case of the TMEDA – nitric acid system, the rise in temperature increased when the concentration of the oxidizer was increased. An interesting point to note when comparing to the TMEDA – nitric acid system is that the rise in exit temperatures for similar concentrations of the oxidizer and the flow rates are much higher for TMEDA than they are for DMAZ. Also when the flow rates were continued to increase the rise in exit temperatures eventually reached a peak value and any further increase in the flow rates of

the reactants caused a drop in the exit temperatures. This peak was usually around 750 µl/min for the DMAZ – nitric acid system and was consistent across multiple runs as well as when the concentration of the nitric acid was changed.

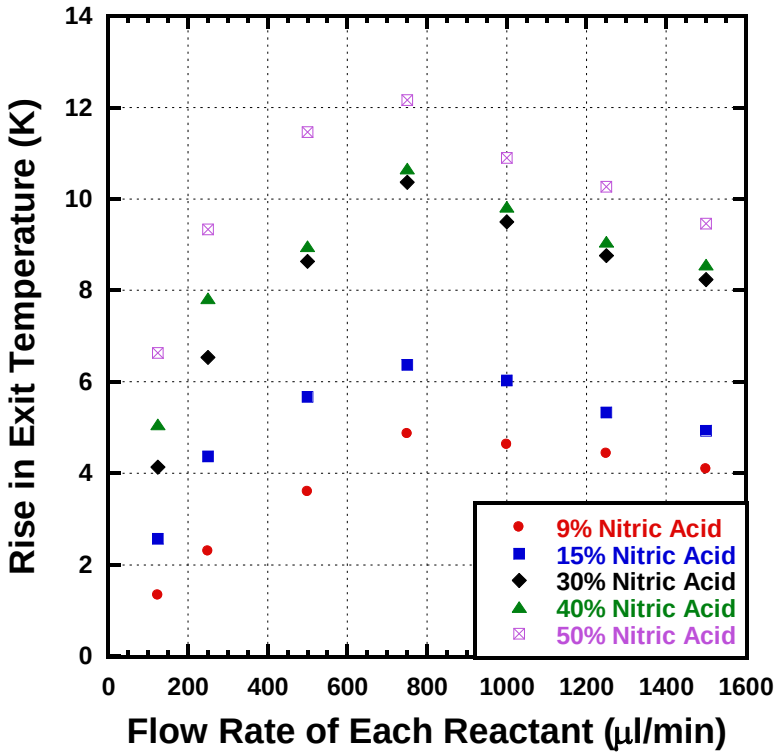

Figure 6-13: Change in exit temperatures for DMAZ and Nitric Acid in the microreactors with increasing flow rates of reactants.

As there was no problem with salt formation when DMAZ was flowed in the microreactor with the nitric acid, thus higher concentrations of the oxidizer could be tested with DMAZ. If the flow rates of the reactants into the microreactor were kept constant, the change in exit temperature was observed to rise monotonically with an approximate linear dependence with concentration of the nitric acid as shown in Figure 6-14. This near linear behavior with a change in oxidizer concentration also proved that the dilution of the oxidizer with distilled water did not have a role to play in the chemistry occurring at the interface of the fluids in the microreactor.

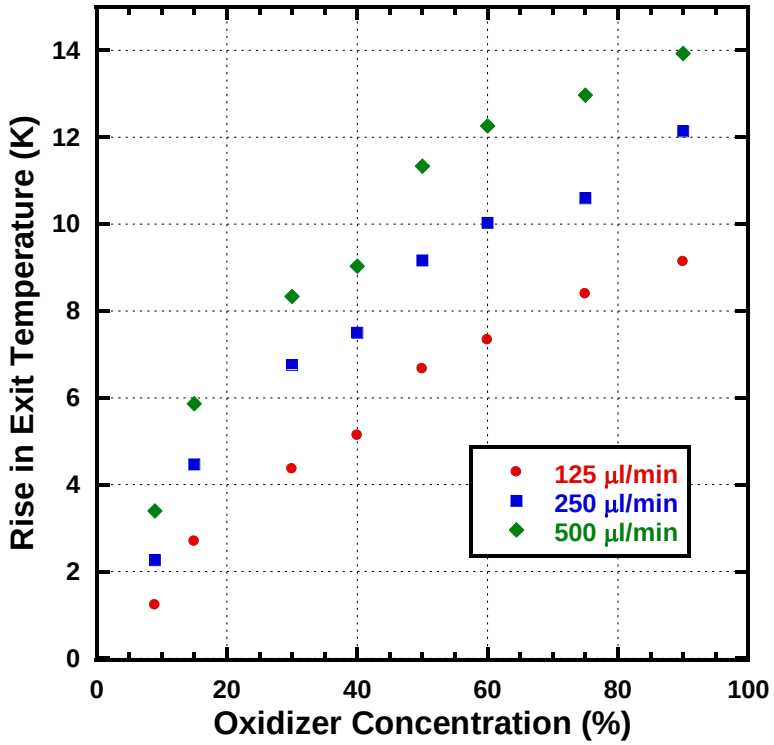

Figure 6-14: Change in exit temperatures for DMAZ and nitric acid in the microreactors with a change in oxidizer concentration.

6.2.3 Microreactor Experiments with Triethylamine – WFNA

As shown in the fuel drop-tests, triethylamine was able to undergo vigorous reaction with the WFNA and actually was able to achieve ignition. This ignition delay, though longer than the TMEDA – WFNA combination, was shorter than the ignition delay of the DMAZ – WFNA combination. To test the triethylamine in the microreactor it was reacted with WFNA to create an system of hypergols similar to the one studied by Schala et al. [122]. Similar to the runs made with TMEDA and DMAZ, with triethylamine too, an exothermic reaction was observed with a very low concentration of the oxidizer (10%). Much like earlier, the rise in exit temperatures rose with an increase in flow rates as well as oxidizer concentrations (Figure 6-15). Interestingly, the amount of heat release observed via the measurement of the exit temperatures showed that the reaction between triethylamine and WFNA

was less exothermic than the liquid-liquid reaction between TMEDA and nitric acid but was more than the one observed between DMAZ and nitric acid.

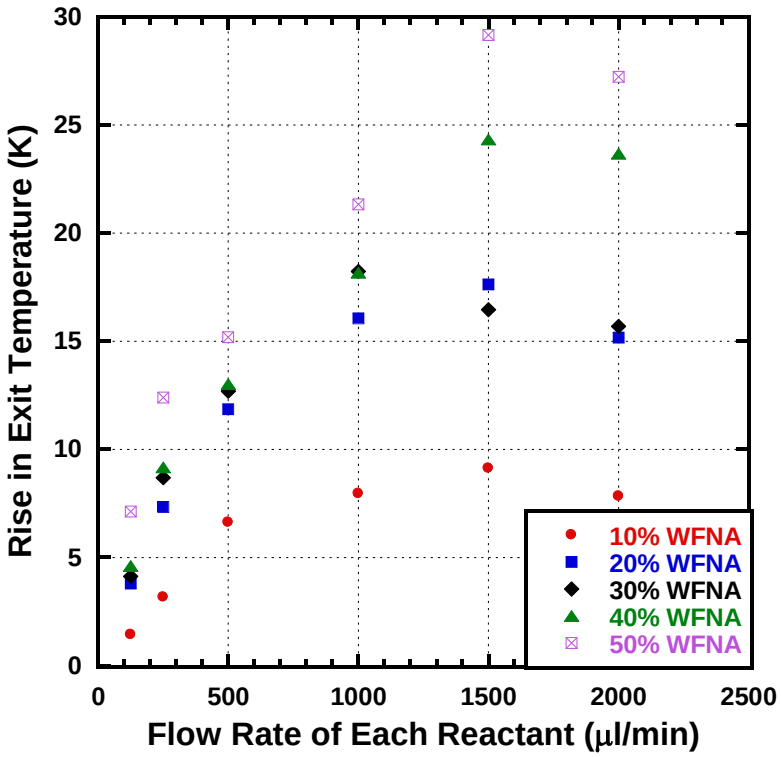

Figure 6-15: Change in exit temperatures for Triethylamine and White Fuming Nitric Acid in the microreactors with increasing flow rates of reactants.

In the case of the triethylamine – WFNA system a peak in exit temperature similar to the one observed in the DMAZ – nitric acid system was observed when the flow rates of the reactants were increases. The flow rate at which this peak in rise of exit temperatures was observed (1500 µl/min) was higher than the flow rate at which the peak was observed in the DMAZ – nitric acid system (750 µl/min). Once again, the flow rates of the reactants into the microreactor were limited to a value of 2000 µl/min to ensure stable laminar flow in the microreactor with no transition to a chaotic flow regime.

6.2.4 Microreactor Experiments with Dicyclopentadiene – WFNA

Drop tests earlier in this study showed that the reaction between dicyclopentaidene with WFNA was quite slow when compared to fuels like TMEDA and triethylamine and ignition was achieved in only one of the drop tests. When the fuel was ran through the microreactor with WFNA the heat release measured using the thermocouples at the exit of the microreactor showed very low temperature rise when compared to the other fuels, with almost no noticeable rise in temperature at low concentrations of the oxidizer. Even when the flow rates of the reactants into the microreactor were increased, the rise in temperatures at the exit remained small.

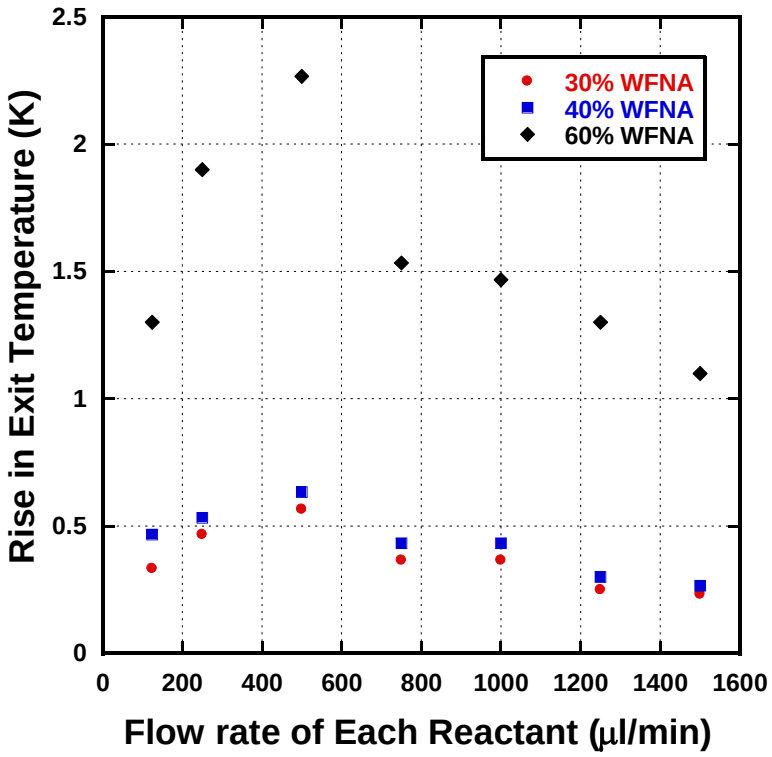

Figure 6-16: Change in exit temperatures for Dicyclopentadiene and White Fuming Nitric Acid in the microreactors with increasing flow rates of reactants.

Though the rise in exit temperatures was very low when compared to the earlier fuels, the trends in temperature with a change in flow rate were very similar. Also the peak value in the

temperature vs. flow rate plot (Figure 6-16) was noticed to be at a much lower value even when compared to the DMAZ – nitric acid combination. In this case the peak was consistently noticed to be at a flow rate of around 500 µl/min.

6.2.5 Microreactor Experiments with Indene – WFNA

Indene was the final fuel used along with WFNA as the oxidizer in the microreactor. Although the temperature trends were similar as to that seen for the other fuels, the rise in exit temperatures were very low with the rise being almost negligible for an oxidizer concentration less than 40% WFNA (Figure 6-17). The peak temperatures as well as the flow rates at which these peaks occurred were lesser than even those observed for the dicyclopentadiene – WFNA combination and occurred at a flow rate of around 400 µl/min.

The reaction between indene and WFNA produces a viscous, sticky black substance as can be seen from the drop tests (Figure 6-7), thus it was not possible to run the microreactor with very high concentrations of WFNA as it was noticed that the sticky substance ended up clogging either the ports in the manifold or the main channel of the microreactor itself. This residue, much like the salt produced by the TMEDA – nitric acid reaction, was tough to remove from the reactor and made it impossible to maintain a purely laminar flow in the main channel. Thus the tests for indene were run at a maximum oxidizer concentration of 60% WFNA to avoid issues of clogging the microreactor.

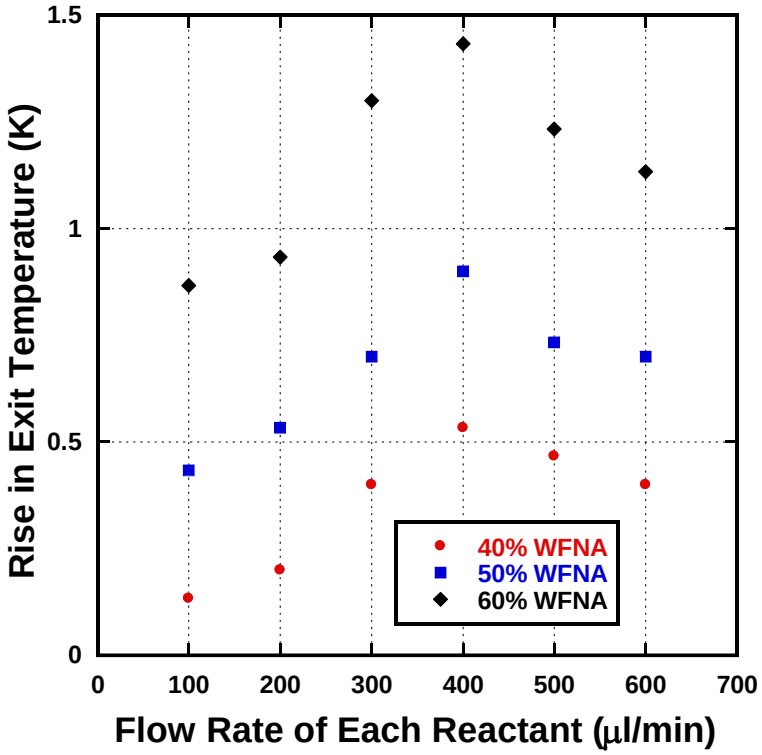

Figure 6-17: Change in exit temperatures for Indene and White Fuming Nitric Acid in the microreactors with increasing flow rates of reactants.

6.2.6 Microreactor Experiments with TMEDA – DMAZ Mixtures and Nitric Acid

In a recent study, Stevenson [15] found that mixtures of hypergolic fuels sometimes perform better than the individual fuels themselves in drop and rocket tests. In particular, the study concentrated on mixing hypergolic tertiary diamines (like TMEDA) with hypergolic amine azides (like DMAZ). In drop tests with inhibited red fuming nitric acid (IRFNA) TMEDA had an ignition delay of 14 ms while DMAZ on itself had an ignition delay of over 26 ms. But when the two fuels were mixed in various proportions the ignition delay seemed to change and in certain cases the ignition delay was found to be lesser than even the ignition delay for pure TMEDA with IRFNA. The results from the study have been re-plotted in Figure 6-18.

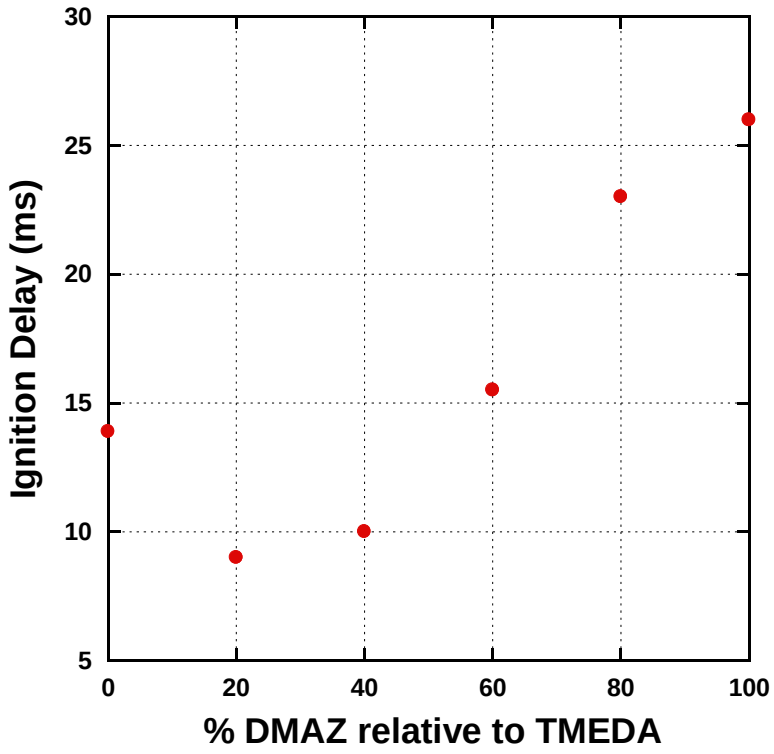

Figure 6-18: Ignition delay results from drop-tests carried out by Stevenson using mixtures of TMEDA and DMAZ as the fuel and Nitric Acid as the oxidizer [15]**.**

As can be seen from the plot, the minimum ignition delay (9ms) was noticed for a mixture which consisted of 66.6% TMEDA and 33.3% DMAZ. A hypothesis proposed by the study was that the ignition delay times were dependent both on the heat released by the hypergolic reaction as well as the ignition temperature of the reactants. The reaction between the tertiary diamine and nitric acid provided a larger heat release than the reaction between the amine azide and nitric acid owing to the higher amine content in the diamine (and thus higher basicity). But the ignition temperature of the amine azide was noticed to be much lower than that of the much heavier tertiary diamine. A combination of the two fuels thus provided for a mixture which provided for a large heat release as well as for a lower ignition temperature thus making the ignition delays much shorter in the case of mixtures. It was also noticed that the mixtures of TMEDA and DMAZ burned in a much cleaner

manner, leaving lesser residues behind, with IRFNA than when pure TMEDA was used. An improvement in ignition delay times as well as having lower residues while burning makes the mixtures of TMEDA and DMAZ an attractive replacement for the more toxic MMH.

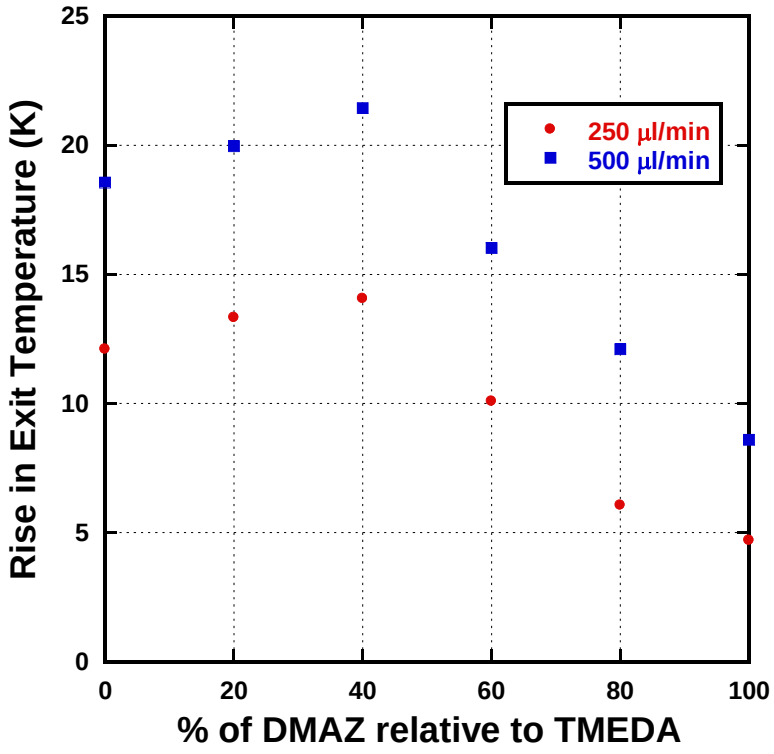

Figure 6-19: Change in exit temperatures for TMEDA-DMAZ mixtures and 30% Nitric Acid in the microreactors with increasing flow rates of reactants.

Mixtures of TMEDA and DMAZ were then created to be tested in the microreactor along with diluted nitric acid. For the tests using these fuel mixtures the concentration of nitric acid was kept at 30% and the tests were run at two flow rates of 250 µl/min and 500 µl/min. The heat released from the reaction between these fuel mixtures and the nitric acid was again related to the rise in temperature at the exit of the microreactor. Temperature trends from these tests (Figure 6-19) seemed to be similar to the trends noticed in the drop tests by Stevenson and were consistent even with a change in flow rate. A maximum heat release was actually seen for a mixture of TMEDA and DMAZ

rather than for pure TMEDA. Moreover the maximum heat release was noticed for a mixture of 60% TMEDA and 40% DMAZ mirroring very closely the drop tests results in the study by Stevenson.

The significance of having a higher heat release in the case of mixtures of TMEDA and DMAZ rather than for one of the fuels separately is that rather than just having TMEDA-NA provide the high heat release and DMAZ provide for the lowering of the ignition temperature, as suggested by Stevenson in his study, the current results indicate that there is a new mechanism present wherein all three reactants, namely TMEDA, DMAZ and nitric acid, react together via new pathways which provide for a higher heat release and thus a shorter ignition delay time. Another hypothesis that could be forwarded for the similar trends found between the drop test and the microreactor experiments for the TMEDA-DMAZ blends could be that the reactions that occur in the liquid phase between the hypergols are very similar to the reactions that occur later on in the gas phase. Thus, the liquid phase reaction will affect the later occurring reactions and will have a large role to play in the ignition of the hypergols. The relative importance of the liquid phase reactions in the reaction between blends of TMEDA and DMAZ with nitric acid has also been shown in a recent study [124] which conducted ignition drop tests at elevated pressures. The study found very little variation in ignition delay times of the TMEDA-DMAZ blend when reacted with nitric acid, leading to the conclusion that the ignition was controlled by the early liquid phase reactions whose rates do not depend on the applied pressure.

6.3 Experiments with Fabricated LTCC Microreactors

Given the time needed to fabricate the silicon-glass microreactors, a quick turnaround method to create microreactors of varying designs was needed. LTCC was chosen as the material to work with to make quick changes to the reactor designs. As no photomasks are required for the fabrication process and the design is directly cut into the LTCC sheets, thus design parameters could be easily changed and new via holes for the introduction of new thermocouples could also be fabricated with

ease. Moreover, these new microreactors also helped check the effect of reactor material on the reaction occurring within the microreactor. A number of experiments were run with these new reactors, primarily with TMEDA and triethylamine as the fuels of choice.

6.3.1 Effect of Microreactor Material

LTCC microreactors were created with the design of the reactor being kept similar to the silicon-glass reactors. These new LTCC microreactors were then mounted on the manifolds that had been used for the previous microreactor studies (with the silicon-glass reactors) to conduct experiments with the hypergols. The new LTCC microreactors were tested using TMEDA and diluted nitric acid in a manner similar to the silicon-glass microreactors. Both concentration of the oxidizer and the flow rate of the reagents into the microreactor were varied for the tests. The temperature trends for the new LTCC reactors (Figure 6-20) were found to be similar to the temperature trends noticed earlier in the silicon reactors. The use of LTCC reactors demonstrated that neither the surface of the silicon-glass reactors nor the surface of the LTCC reactors played a significant enough role in affecting the reaction within the microreactors making it safe to use the reactors to study the interfacial reactions.

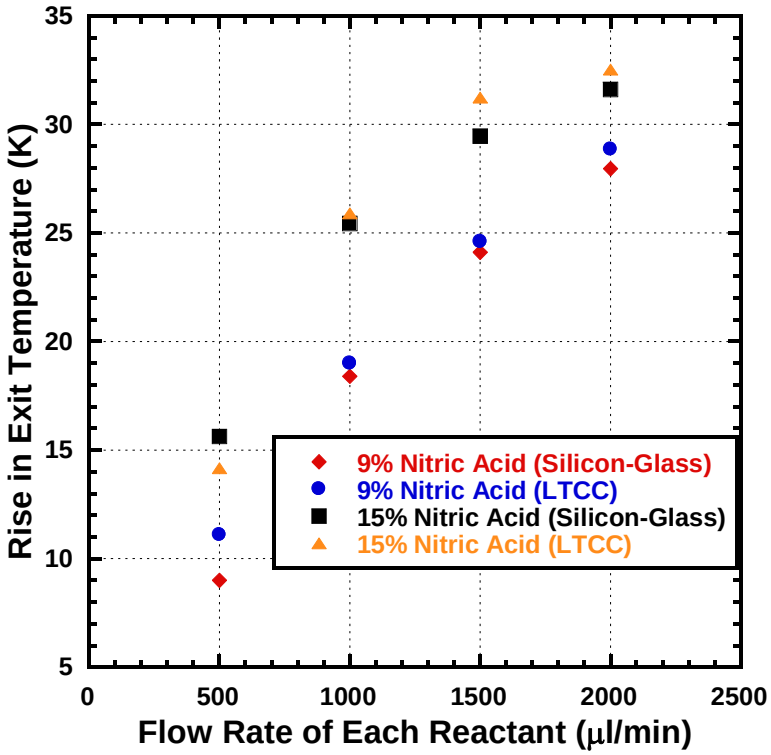

Figure 6-20: Effect of microreactor material on exit temperatures in a TMEDA-nitric acid system.

.

6.3.2 Temperature Trends Along the Length of Main-Channel of Microreactor

As it was relatively easy to introduce new via-holes in the design of the LTCC microreactors, given that etching of the silicon was not required to create them, via-holes could be created along the length of the microreactor main channel. Fine-wire thermocouples could be now introduced into the main-channel (Figure 6-21) with the aim of measuring the temperature trends along the reactor length, without disturbing the flow in the microreactor too much.

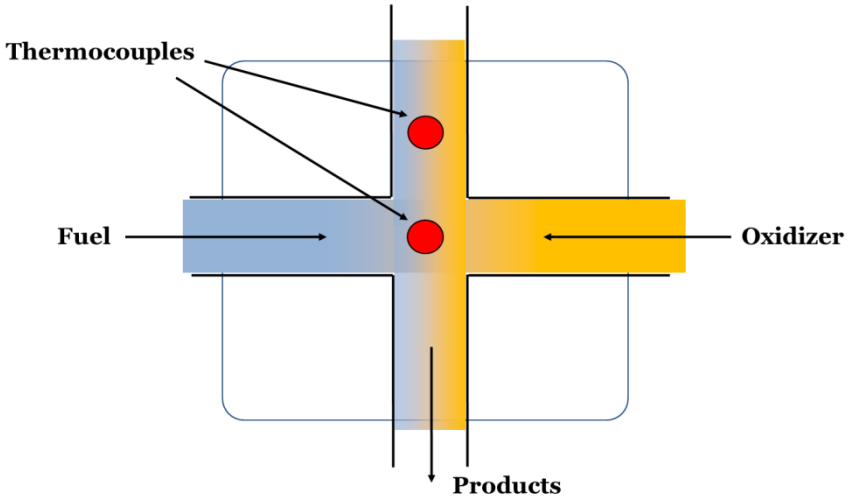

Figure 6-21: Schematic showing position of thermocouple at the stagnation zone of the microreactor.

The via-holes in the microreactors were fabricated so as to accommodate fine-wire thermocouples that measured in 0.008" diameter (Omega Mini-Hypodermic Thermocouple Probe Model HYP-0). The manifolds used earlier were modified so that these new thermocouples could be introduced through the manifolds to the bottom of the microreactors. Multiple new LTCC microreactors were designed so as to accommodate the thermocouples at the stagnation zone of the reactor as well as at one-sixth and half the length of the main-channel. The holes made into the reactor were sealed using a compression seal with nitrile (Buna-N) O-rings (inner diameter of 0.008") against the stainless steel manifold. As these o-rings were not as resistant to the corrosive reagents used in the study as the Kalrez or Viton O-rings, care was taken to check their integrity periodically during the tests. The added thermocouples thus allowed for the measurement of the development of the temperature profile from the stagnation zone, along the length of the main channel, all the way to the exit ports.

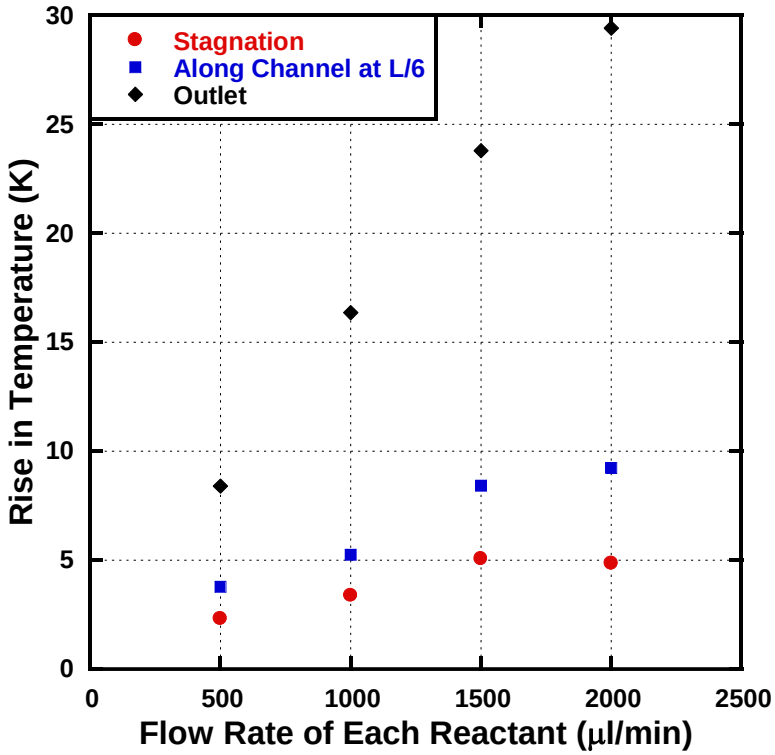

Figure 6-22: Change in temperatures along the length of the microreactor for TMEDA and 9% Nitric Acid in the LTCC microreactors with increasing flow rates of reactants.

Figure 6-22 shows the change in temperature at the various thermocouples placed along the length of the main channel for a TMEDA – nitric acid system. In this case the nitric acid was diluted with distilled water to 9%. The temperature at the stagnation zone as well as at length equivalent to one-sixth the overall length of the main channel, was found to increase with an increase in the flow rate of the reactants into the microreactor. These temperature trends are thus very similar to the temperature trends measured at the exit ports of the microreactor. Also noticeable is the fact that the temperature of the fluid tends to increase as the fluid goes down the main channel. This could possibly be due to the fact that the two reactant streams continue to react with one another as the fluids go down to the exit of the microreactor. But as the temperature trends are similar at different points along the length of the reactor, it can be said that the initial reaction at the stagnation zone will have an effect further downstream.

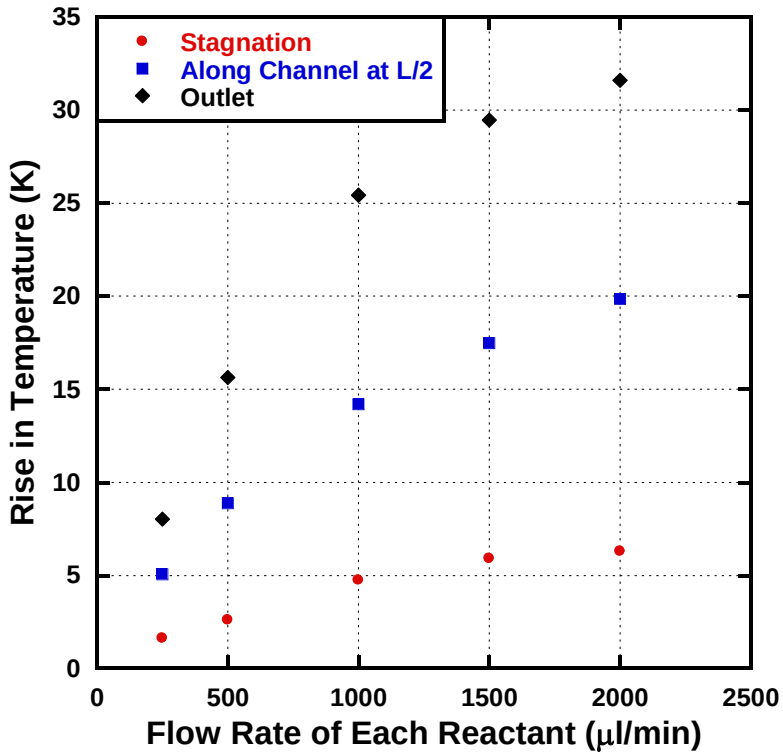

Figure 6-23: Change in temperatures along the length of the microreactor for TMEDA and 15% Nitric Acid in the LTCC microreactors with increasing flow rates of reactants.

Figure 6-23 shows a similar temperature – flow rate plot for the TMEDA – nitric acid system. In this case the nitric acid was diluted to 15% and the temperature was measured at the stagnation zone, the exit port and at half the length between the stagnation zone and the exit port. The temperature trends at both the stagnation zone and at half the length down the main channel were once again similar to those seen at the exit ports. On comparing the temperature values for the stagnation zone between Figure 6-22 and Figure 6-23, it can be clearly seen that the rise in temperature is higher with the higher concentration of nitric acid. This is similar to what is seen when the temperatures are measured at the exit ports.

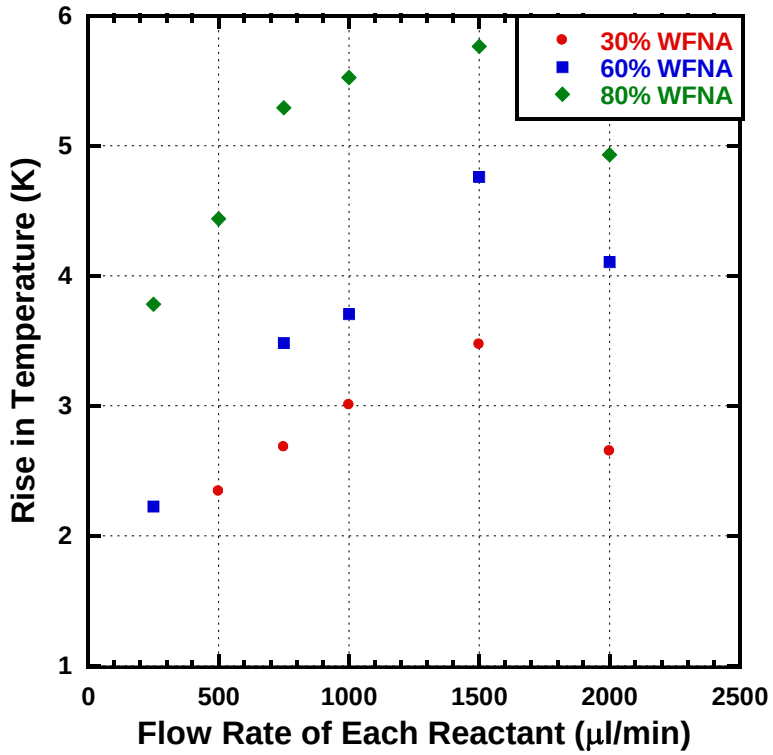

Figure 6-24: Change in temperatures at the stagnation zone of the microreactor for triethylamine and WFNA in the LTCC microreactors with increasing flow rates of reactants.

The experiments with the added thermocouples in LTCC microreactors were also repeated for the triethylamine – WFNA system. Figure 6-24 shows the temperature trends for the triethylamine – WFNA system with the thermocouples placed at the stagnation zone. While Figure 6-25 shows the temperature trends when the temperatures are measured at a length equivalent to L/2 down the length of the main channel of the microreactor. The temperature trends at the stagnation zone and along the length of the microreactor were similar to the temperature trends observed at the exit of the microreactor. The rise in temperatures was found to increase with both flow rates of the reactants as well as concentration of the oxidizer. This rise in temperature was then seen to hit a peak and decrease with a further increase in flow rates.

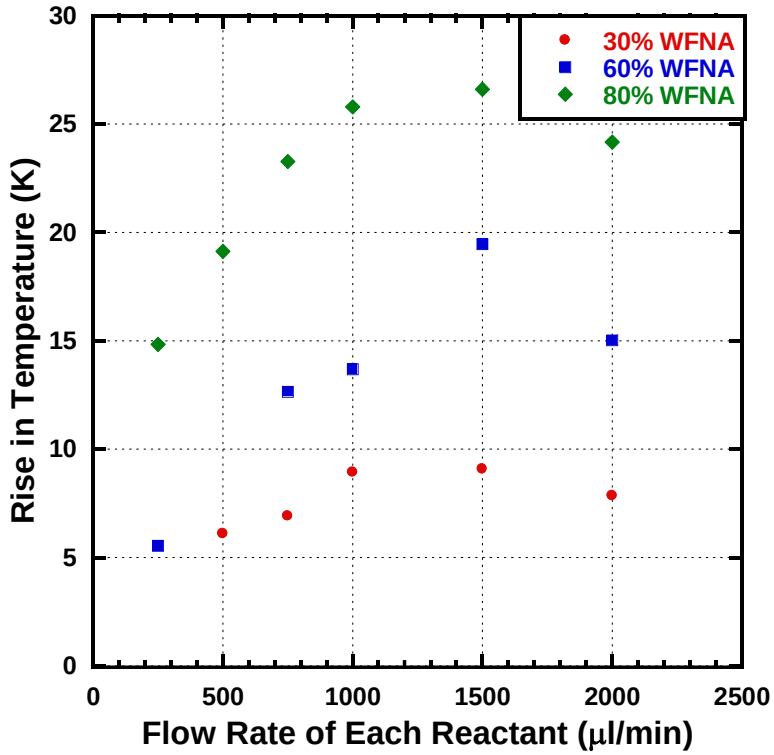

Figure 6-25: Change in temperatures at length L/2 along the length of the main channel in the microreactor for triethylamine and WFNA in the LTCC microreactors with increasing flow rates of reactants

6.4 Discussion based on Experimental Observations

The present study uses microreactors to concentrate solely on the condensed phase reactions that occur at the interface between hypergols. Temperature trends at the exit of the microreactor, as well as along the length of the reactor have been used to correlate the importance of early condensed phase reactions to the overall ignition event between hypergolic pairs. For this purpose, along with reactive studies in microreactors, drop tests were conducted for the various hypergolic fuels. The drop tests were able to measure ignition delay times for each hypergolic pair and thus were able to quantify a delay time which took into account both physical processes (such as mixing and diffusion of the reagents) as well as chemical processes (concerning both condensed phase and gas phase

reactions). The microreactor experiments, on the other hand, concentrated only on the initial condensed phase reactions by limiting the amount of mixing that occurs at the interface between the two reagents.

Exit temperatures in the microreactor experiments were measured simultaneously to the visualization of the flow using the thermocouples placed at the exhausts of the microreactor. There was a rise of temperature at the exit observed for almost all the different runs made at different concentrations of the oxidizer indicating that the reaction between the nitric acid and the various fuels was observable even at very low concentrations of the oxidizer (except in the case of dicyclopentadiene and indene where a higher concentration of oxidizer was needed to show a temperature rise). This rise in exit temperature of the fluids was noticed to increase with an increase in concentration of the oxidizer. The diluting of the oxidizer concentration, which resulted in a drop in the temperature of the products at the exit is because of the lowering in the reaction rates between the reactants that are able to diffuse across the interface and react with each other. With the dilution of nitric acid, there are lesser reaction-causing nitric acid molecules that are available to diffuse across the interface to interact with the fuel molecules. Thus it is but natural that the amount of reaction occurring between diluted nitric acid mixtures and the various fuels is far lesser than the reaction that occurs with undiluted nitric acid and the various fuels. When more reactants are available to diffuse across the interface, the amount of reaction that occurs sees an increase and the temperature of the products at the exit rises accordingly. If the strain rate was kept constant, the change in exit temperature was seen to increase almost linearly with an increase in the concentration of the nitric acid used in the microreactor (Figure 6-14).

The more interesting observation was the increase in temperature at the exit when the flow rates (strain-rates) for the reactants were increased. With further increase of the flow rates the temperatures at the exit attained a peak value and then started decreasing. The reaction is diffusion based and depends on how much of the reactants are able to diffuse across the interface. When the

flow rates are increased, the residence time for the reactants in the main channel is reduced and thus the reactants get lesser and lesser time to diffuse across the interface. It is noted in most studies considering mixing of fluids in microchannels that the mixing can be increased when the residence time of the fluids in the channel is increased and the fluids get more time to diffuse across the interface [78]. But here the reaction seems to be getting better and more exothermic with an increase in flow rates and thus a decrease in residence time. The increase in the temperatures observed with an increase in flow rates could be attributed to either heat loss through the top and bottom of the reactor or if the rate of diffusion of the species across the interface is increasing with an increase in flow rates. The heat loss through the top and bottom surfaces will affect the lower flow rates more than the higher flow rate cases as the thermal diffusion will be higher at lower flow rates than the higher flow rates. The effect of heat loss through the top and bottom surfaces of the microreactor will be discussed in more detail in Chapter 7 wherein a numerical simulation of the reactive flow in the microreactor is carried out. To concentrate on the diffusion of species across the interface the species transport equation for an incompressible fluid can be used [125]:

$$\frac{\partial c}{\partial t} + u_x \frac{\partial c}{\partial x} + u_y \frac{\partial c}{\partial y} + u_z \frac{\partial c}{\partial z} = D\left[\frac{\partial^2 c}{\partial x^2} + \frac{\partial^2 c}{\partial y^2} + \frac{\partial^2 c}{\partial z^2}\right] + R$$

where, c is the species concentration of one of the fluids, u_x, u_y, u_z are the velocities of the fluid in the x, y and z directions respectively, D is the diffusion coefficient and R is the rate of change of concentration due to the chemical reaction. It should be noted that for the present case the x-direction is considered to be along the axis of the main reactor channel while the y-direction is across the width of the reactor channel and the z-direction is along the depth of the main channel. Now assuming a two dimensional, steady state condition in and x and y at the stagnation point, we eliminate the time dependent term as well as the convection of species gradients caused due to the

velocities. This is because at or near the stagnation point of the reactor, the velocities are negligibly small. Also, due to the high Péclet number of the flow we can assume there to be no diffusion of species along the axis of the main channel (in the x direction). Thus near the stagnation zone, the above equation now reduces to:

$$-D\left[\frac{\partial^2 c}{\partial y^2}\right] = R$$

Thus, the rate of change of the concentration due to the reaction is now directly dependent on the diffusion of the species across the interface. As has been shown by previous studies in both t-shaped reactors [112] and stagnation flow reactors [126], the species concentration gradients tend to increase with an increase in the fluid flow rates of the reactants into a microreactor. Thus from the above expression, the increased species gradients in-turn causes an increase in mass-flux of species across the interface. As the reaction occurs in the form of a sheet between the two reactants, the enhancement of the mass flux of the species across the interface causes more of the reaction to occur even though the residence time for the reactants in the main channel has been reduced with higher flow rates.

The peak in temperatures in the trends can be attributed to the flow in the microreactor shifting to a flow regime that is kinetically controlled. In the diffusion controlled regime, the amount of reaction occurring at the interface is affected mostly by the amount of diffusion of reactants across the interface as the reaction occurs so quickly. Whereas, in the kinetically controlled regime, the residence time of the reactants in the reactor plays a far more important role as the residence time is now lower than the time required for the reaction between the products to occur. When the flow rates of the reagents into the microreactor are increased, the residence time of the reagents is reduced. This causes the total reaction occurring in the main-channel of the reactor to reduce and thus, in turn, this causes a lower temperature to be recorded at the exit of the reactor by the thermocouples. The

phenomenon occurring during the shifting of the regime can be explained by the first Damkohler similarity group (D_1) which can be defined as:

$$D_1 = \frac{time\ characterizing\ the\ flow}{time\ characterizing\ the\ chemical\ activity}$$

The time characterizing the flow is usually given by the residence time of the reagents and in this case can be attributed to the strain rate. The time characterizing the chemical activity is usually given by the rate of the reaction occurring at the interface. For a large value of D_1, the flow rates are low and thus the reaction is not affected by the time characterizing the chemical activity and is dependent on the diffusion time of the species. On the other hand, as the flow rates are increased, the time characterizing the flow becomes smaller along with the value of D_1. At a critical D_1 the time characterizing the chemical activity becomes more important than the time taken for diffusion of the species, that is the time taken for the chemical reaction to take place will govern the amount of reaction occurring at the interface. Thus after the critical D_1 any increase in the flow rate will result in the species at the interface having less time to react than the reaction time. This will cause the reagents to be carried downstream from the stagnation zone without being completely reacted.

This phenomenon can be explained analytically if we again refer to the species transport equation at the stagnation point but in this case now assume the velocities to not be negligibly small in the x direction. The equation now reduces to:

$$u_x \frac{\partial c}{\partial x} = D\left[\frac{\partial^2 c}{\partial y^2}\right] + R$$

Thus with a large increase in u_x, the convection term ($u_x \frac{\partial c}{\partial x}$) term dominates over the diffusion term ($D\left[\frac{\partial^2 c}{\partial y^2}\right]$) and the species are convected downstream instead of diffusing across the interface. Thus the reaction occurring at the interface is reduced and there is a drop in temperatures that is observed in the microreactor. Flow rates have also played a role in ignition behavior of hypergols during impingement jet studies. A recent study [10] noted that ignition of monomethylhydrazine (MMH) and red fuming nitric acid (RFNA) could not be achieved until the flow rates of the reactants, through the respective jet inlets, was reduced to a critical value. Again, the reason given for the behavior was that lowering the flow rates of the reactants gave the chemicals enough time to mix and react and thus achieve ignition.

The present scenario, with the stagnation flow microreactors can be thought to be similar to the phenomena occurring in counter-flow stagnation diffusion flames wherein the rate at which the fuel and oxidizer diffuse into the reaction zone is what primarily controls the combustion rate [127]. The combustion rate at the flame is known to increase with an increase in diffusion rate. With an increase in flow rate (strain-rate) of the reactants, the residence time and the characteristic diffusion time become shorter. At high enough flow velocities, these characteristic diffusion time and residence times may become comparable to the reaction time between the fuel and oxidizer. If the flow of the reactants is now increased further, the chemical reaction can no longer keep pace with the flow-rate of the reactants. The reaction thus abruptly ceases and the diffusion flame is now seen to extinguish. This is due to the reaction being controlled by the high activation energy of the reactions. In the microreactor experiments, the activation energy of the condensed phase reactions is very low and thus an abrupt extinguishment of the reaction is not observed. This can be explained by looking at the dependence of the reaction rates on temperature given by the Arrhenius equation as:

$$k = Ae^{-E_a/RT}$$

where, k is the reaction rate for the system, A is the pre-exponential factor, E_a is the activation energy, R is the gas constant and T is the temperature of the system. Thus from the equation it is clear that if the activation energy (E_a) is very large, then even a small reduction in the reaction rate will result in a large reduction in the values of the temperature and thus lead to the extinguishing of the reaction. On the other hand, in the case of the hypergols, with very low or negligible activation energies, the reduction in reaction rates will not result in drastic reduction of temperatures. As the inverse of the strain rate is a natural time scale for the flow in a counter-flow configuration, using various assumptions, the strain-rate at extinction of the diffusion flame has been shown to be proportional to the global reaction rate [128], [129]. Similarly, in the case of the microreactors, the critical flow rate (when the reaction mechanism seems to shift from a diffusion or heat loss controlled system to a kinetically controlled system), can be used to measure reaction rates for the condensed phase between the two reactants.

The hypergol pair which shows the peak at higher flow rates than a pair which has the peak at a lower flow rate will have a faster reaction occurring at the interface. Thus the temperature trends from the microreactor experiments can also give an idea on which hypergolic pair will have a faster heat release. This difference in condensed phase reaction rates can also be seen from the images of the reactions between the various fuels and WFNA in the micro reactor (Figure 6-10). The reaction interface between TMEDA and WFNA is very thin and grows wider when moving downstream, while the reaction interface between indene and WFNA starts out quite wide at the stagnation point itself. This can be explained by the fact that the reaction between liquid TMEDA and WFNA is very quick and the Damkohler similarity group (D_1) is very high leading to a very thin reaction front where the reactants do not have a large time to diffuse across the interface. In the case of Indene and WFNA on the other hand the reaction between the two liquids is comparatively very slow and thus D_1 is much lower in value allowing for a larger time for the reactants to diffuse across the interface and in turn leading to an optically thick reaction zone.

The ignition delay times for hypergols, apart from being dependent on how quickly the heat is released, are also largely dependent upon the quantity of the heat released by the reaction between the two hypergols. Thus if a pair of hypergols can release a large amount of heat in a quick enough time, the ignition delay for this pair would be expected to be the least. The microreactors clearly show a trend in the amount of heat released by the early liquid phase reactions. And most noticeably the fuels with the higher heat release (TMEDA and triethylamine) showed by a larger temperature rise at the exit of the microreactor, result in the combination having the lowest ignition delay times amongst the group of fuels tested. This was also closely seen in the case of mixing DMAZ and TMEDA to form a blend which showed the highest heat release when the composition of the blend was similar to the one which had the shortest ignition delay times.

From the experiments (refer to summary provided in Table 6-1) it can be clearly seen that TMEDA, amongst all the fuels tested, has the highest heat release as well as has temperature trend in which no peak was noticed to occur within the range of flow rates used in the present study. On the other hand, it is also easy to see that the fuel with the lowest heat release and also with the lowest flow rate at which the peak temperature occurs is indene. These two trends showed that TMEDA would have a much shorter ignition delay time than indene and the drop tests showed similar results. In fact the heat release values and the flow rates at which the peak temperatures occurred had a trend which showed exactly what the trend for ignition delay times of the various fuels would be like. These experimental results with the microreactor prove the relative importance of the early liquid phase reactions to the overall ignition process. A faster liquid phase reaction with a higher heat release also implies a shorter ignition delay thus implying that the gas phase reactions that occur later on between the hypergols are intrinsically linked to the early liquid phase chemistry.

Table 6-1: Summary of Ignition Delay times for various fuels with WFNA as well as flow rates at which peak temperatures occur in the microreactor.

Fuel	Ignition Delay (ms)	Flow rate at which peak temperature occurs (µl/min)
TMEDA	19	N/A
DMAZ	99	750
Triethylamine	45	1500
Dicyclopentadiene	No ignition but noticeable vigorous reaction at ~ 65 ms	500
Indene	No ignition but noticeable vigorous reaction at ~ 300 ms	400

Chapter 7

Numerical Simulation of Reactive Flow in the Microreactors

The stagnation flow microreactors used to study the fast condensed phase reactions occurring between hypergols can be compared to an opposed-flow or counter-flow diffusion flame system. Like in the counter-flow diffusion flame the reactions at the interface of the liquids in the microreactor are dependent both on the diffusion of the reagents across the interface as well as the reaction rate of the reactions in the chemical mechanism. This chapter details the numerical analysis of the stagnation reaction zone in the microreactor based on numerical methods used to solve counter-flow diffusion flames. Described in detail are the governing equations for a reactive counter-flow system as well as differences between the numerical simulations that involve reactive gas-phase and reactive liquid-phase flows. Numerical simulations of flow in the microreactor while varying the flow rate of the reagents as well as the reaction rates used in the chemical mechanism are discussed. And finally changes to the model are suggested so as to better match the numerical temperature trends with the trends observed from the experiments.

7.1 The Counter-Flow Diffusion Flame

In a diffusion flame, unlike a premixed flame, the fuel and the oxidizer are initially separated and are only mixed in the same region in which the reactions between the various reagents take place. The combustion thus takes place at the interface of the incoming fuel and oxidizer streams. The combustion rate in the diffusion flame is thus dependent both on the mixing (or diffusion) rate between the fuel and the oxidizer as well as the reaction rate between the reagents. In most diffusion

flames, the reaction rate can be safely assumed to be much higher than the diffusion rate (hence, the flame is diffusion-controlled) and thus the reaction between the fuel and the oxidizer takes place in a very narrow region between the fuel and oxidizer flow streams. Also, the rate of combustion can be controlled by changing the rate at which the fuel and oxidizer are fed into the reaction zone [127]. In limiting cases, when the reaction rate is assumed to be infinitely fast, the reaction zone can be considered to be infinitesimally thin and is referred to as a flame-sheet. Also, in this case, there is no diffusion of species across the fuel-oxidizer interface and thus the concentrations of the fuel and oxidizer become zero at the location of the flame sheet, with no fuel being present on the oxidizer side and no oxidizer being present on the fuel side.

The counter-flow diffusion flame is a diffusion flame formed between two opposing jets of fuel and oxidizer. These flames have become important for research purposes [128], [130]–[134] as they approximate a one-dimensional character and because the residence times of the reagents in the reaction zone can be varied with ease [135]. The one-dimensional nature of the counter-flow diffusion flame makes numerical calculations as well as experiments much easier than the two-dimensional flames seen in axisymmetric jet setups [135].

7.2 Governing Equations for the Counter-Flow Diffusion Flame

A typical experimental setup for a counterflow diffusion flame is shown in Figure 7-1 where the fuel and oxidizer are impinged on each other from two opposing inlet nozzles. The opposing flow from the nozzles creates a stagnation plane between the nozzles (shown in the figure by the dashed line). The location of the stagnation plane depends on the relative magnitudes of the initial momentum fluxes of the fuel and oxidizer jets. When the momentum fluxes from both the fuel and oxidizer nozzles are equal, the stagnation plane is located at the midpoint between the nozzles. When the fluxes are unequal, the stagnation plane moves towards the nozzle which has the lower

momentum flux. The diffusion flame formed between the opposing jets is formed at a location where the mixture fraction is nominally stoichiometric. As for most hydrocarbon fuels, the stoichiometric conditions require more air than fuel, thus the diffusion flame is often located on the oxidizer side. In this case, the fuel needs to diffuse across the stagnation plane to the flame location.

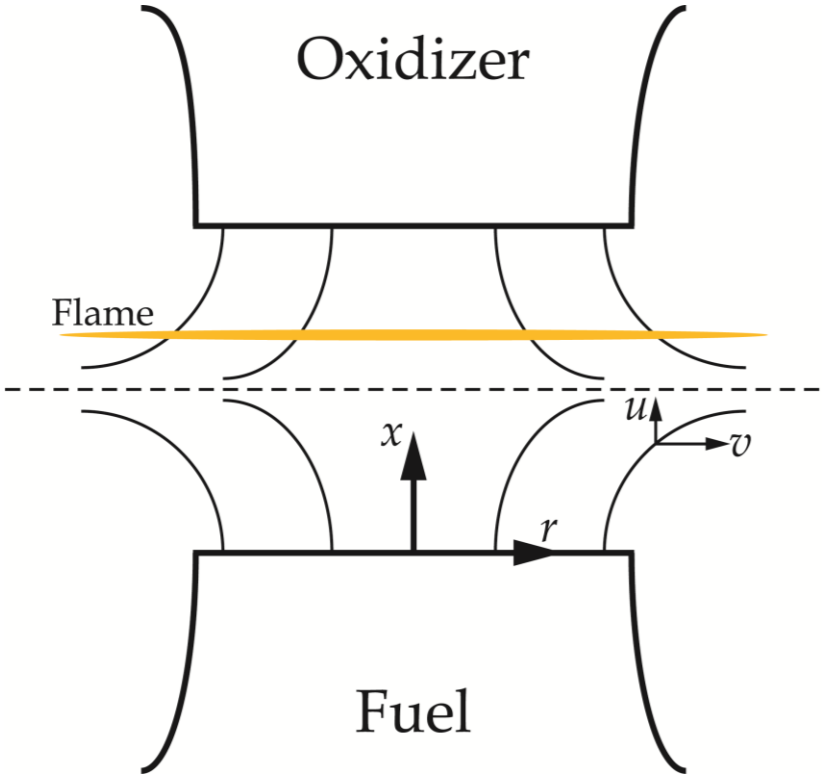

Figure 7-1: Schematic of a counter-flow diffusion flame (adapted from [136]**).**

To model the counterflow diffusion flame, solutions concentrate on the centerline fluid mechanics by using a similarity solution. Two different approaches are generally used with the first one coupling a stagnation-point potential flow from a point source at infinity with a boundary layer analysis. This approach is not able to take into account the separation between the nozzles and thus a second approach has been developed to specifically account for the separation distance between the nozzles. This approach was originally developed to model counter-flow premixed flames [137] but the method has been extended for opposed-flow diffusion flames [136] as well. The two dimensional

nature of the setup is reduced to one dimension by assuming that the radial velocity varies linearly with distance in the radial direction. This assumption makes it possible to assume that the fluid properties are dependent only on the axial distance.

The governing equations for the counter-flow diffusion flame formed between the opposing circular jets can be represented by starting out with the Navier-Stokes equations in cylindrical coordinates and using a stream function which satisfies the continuity equation. The continuity equation in cylindrical coordinates can be represented as:

$$\frac{\partial}{\partial x}(r\rho u) + \frac{\partial}{\partial r}(r\rho v) = 0$$

while the stream function can be expressed as:

$$\psi(x,r) \equiv r^2 U(x)$$

thus,

$$\frac{\partial \psi}{\partial r} = r\rho u = 2rU$$

$$-\frac{\partial \psi}{\partial x} = r\rho v = -r^2 \frac{dU}{dx}$$

Thus the axial velocity u depends only on x, while the radial velocity v varies linearly with r. We also assume that the temperature T and the species mass fractions Y_k are functions of x alone while buoyancy effects are neglected. Thus the partial differential momentum equations now reduce to third order ordinary differential equations which can be expressed as:

$$\frac{\partial p}{\partial x} = -4U\frac{d}{dx}\left(\frac{U}{\rho}\right) - 2\mu\frac{d}{dx}\left(\frac{1}{\rho}\frac{dU}{dx}\right) + \frac{4}{3}\frac{d}{dx}\left[2\mu\frac{d}{dx}\left(\frac{U}{\rho}\right) + \vartheta\frac{dU}{dx}\right]$$

$$\frac{1}{r}\frac{\partial p}{\partial r} = \frac{d}{dx}\left(\frac{2U}{\rho}\frac{dU}{dx}\right) - \frac{3}{\rho}\left(\frac{dU}{dx}\right)^2 - \frac{d}{dx}\left[\mu\frac{d}{dx}\left(\frac{1}{\rho}\frac{dU}{dx}\right)\right]$$

Thus both $\frac{1}{r}\frac{\partial p}{\partial r}$ and $\frac{\partial p}{\partial x}$ are functions of x alone and $\frac{1}{r}\frac{\partial p}{\partial r}$ is a constant as:

$$\frac{\partial}{\partial x}\left(\frac{1}{r}\frac{\partial p}{\partial r}\right) = \frac{1}{r}\frac{\partial}{\partial r}\left(\frac{\partial p}{\partial x}\right) = 0$$

Thus the radial momentum equation is satisfied by the radial pressure dependent eigen value:

$$H = \frac{1}{r}\frac{\partial p}{\partial r}$$

For numerical implementation, a new variable is introduced such that:

$$G(x) \equiv \frac{dU}{dx} = -\frac{\rho v}{r}$$

Thus the radial momentum equation can now be represented as:

$$H + \frac{d}{dx}\left[\mu\frac{d}{dx}\left(\frac{G}{\rho}\right)\right] - 2\frac{d}{dx}\left(\frac{UG}{\rho}\right) + \frac{3}{\rho}G^2 = 0$$

while the energy equation and the species equation for *K* species are expressed as:

$$2U\frac{dT}{dx} - \frac{1}{c_p}\frac{d}{dx}\left(\lambda\frac{dT}{dx}\right) + \frac{\rho}{c_p}\sum_{k=1}^{K} Y_k c_{pk} V_k \frac{dT}{dx} + \frac{1}{c_p}\sum_{k=1}^{K} h_k \dot{\omega}_k = 0$$

$$2U\frac{dY_k}{dx} + \frac{d}{dx}(\rho Y_k V_k) - W_k \dot{\omega}_k = 0 \quad (k = 1, K)$$

where, c_p is the specific heat, h_k are the molar enthalpies, $\dot{\omega}_k$ are the chemical production rates of the species due to reaction, W_k are the molecular weights of the species, μ is the viscosity while λ is the thermal conductivity. The diffusion velocities (V_k) are expressed using the mixture averaged formulation as:

$$V_k = -\frac{1}{X_k} D_{km} \frac{dX_k}{dx} - \frac{D_k^T}{\rho Y_k}\frac{1}{T}\frac{dT}{dx}$$

where X_k are the mole fraction in the given mixture, D_k^T are the thermal diffusion coefficients and D_{km} are the ordinary mixture-averaged diffusion coefficients that can be expressed as:

$$D_{km} = \frac{1 - Y_k}{\sum_{j \neq k}^{K} \frac{X_j}{D_{jk}}}$$

The boundary conditions for the fuel (F) and oxidizer (O) streams in the model can be expressed as:

$$x = 0: \; u = u_F, \; G = 0, \; T = T_F, \; \rho u Y_k + \rho Y_k V_k = (\rho u Y_k)_F$$

$$x = L: \; u = u_O, \; G = 0, \; T = T_O, \; \rho u Y_k + \rho Y_k V_k = (\rho u Y_k)_O$$

7.3 Analysis of the Stagnation-Flow Microreactor

The reactive flow in the stagnation-flow microreactor was analyzed with liquid flows using the same set of governing equations as described in the previous section. The governing equations for the counter-flow diffusion flame were solved using a FORTRAN code developed by the Sandia National Laboratories – Oppdif [136]. The original code for the numerical simulations of a counter-flow diffusion flame was written for gas-phase chemistry and thus uses the ideal gas law to calculate mass density values. As the flow in the microreactor is in the liquid phase, the fluids are incompressible in nature and all the mass density values were set to be constant in the governing equations.

Viscosity, thermal conductivity and mass diffusivity values for each of the fluids are required for the numerical simulation of the reactive flow. The values for these properties for the various species involved in the simulation are listed in Table 7-1. As the binary molecular diffusion coefficients (mass diffusivities) for the various chemical species were not known, the values for the numerical simulations were estimated using the Wilke-Chang estimation [138]. The estimation can be expressed as:

$$D = 7.4 \times 10^{-8} \frac{(xM)^{1/2} \cdot T}{\eta V^{0.6}}$$

where, D is the binary molecular diffusion coefficient, x is the association parameter which is 2.6 for water and 1 for non-associated solvents, M is the molecular weight of the solvent, T is the temperature, η is the viscosity of the solvent and V is the molal volume of the solute at the boiling point. Calculated diffusivity values for the various molecule pairs used in the numerical simulations are listed in Table 7-2.

Table 7-1: Thermal conductivity and viscosity values for the various species used in the numerical simulation of reactive flow in the microreactor.

Species	Thermal Conductivity (W/m-K)	Viscosity (kg/m-s)
TMEDA	0.45	0.001
Nitric Acid	0.28	0.0009
Water	0.56	0.001
TMEDADN	0.337	0.0093

The numerical simulations were performed for a variety of inlet flow rates for the TMEDA – nitric acid system. The concentration of the nitric acid was kept at 20% by diluting the oxidizer inlet with liquid water (similar to the experiments carried out with the microreactor). The inlet temperature for both the fuel and oxidizer was kept at 300 K. A single step reaction suggested by Wang et al. [53] was used as the reaction mechanism for the system with the heat of the reaction being - 45 kcal/mol as suggested by Liu et al. [54]. This mechanism involves the reaction of one molecule of TMEDA with two molecules of nitric acid to form a di-nitrate salt (TMEDADN) along with the evolution of heat:

$$TMEDA + 2HNO_3 \rightarrow TMEDADN$$

No activation energy was used for the one-step reaction and thus the reaction was assumed to be temperature independent. The rate of the reaction for the single step in the reaction mechanism was varied so as to provide information on the effect of reaction rates on the temperature profiles.

Table 7-2: Bimolecular diffusion coefficients for the various molecule pairs used in the numerical simulation of reactive flow in the microreactor.

Molecule Pair	**Bimolecular Diffusion Coefficient (m^2/s)**
TMEDA – TMEDA	1.1890×10^{-9}
Nitric Acid – TMEDA	2.5405×10^{-9}
Nitric Acid – Nitric Acid	2.0819×10^{-9}
Water – TMEDA	4.221×10^{-9}
Water – Nitric Acid	3.259×10^{-9}
Water – Water	1.6628×10^{-9}
TMEDADN – TMEDA	1.7280×10^{-9}
TMEDADN – Nitric Acid	3.6709×10^{-9}
TMEDADN – Water	6.0993×10^{-9}
TMEDADN – TMEDADN	1.1046×10^{-9}

The numerical model uses the Chemkin package [139] to calculate reaction rates for the given reaction mechanism as well as thermodynamic and transport properties [140]. The Twopnt [141] boundary value solver is used to solve the discretized governing differential equations. Twopnt is a computer program that solves for steady state solutions for a system of differential equations (usually in one dimension). The computation begins with making second-order, conservative finite-difference approximations so as to reduce the boundary value problem to a system of algebraic equations.

The Twopnt solver uses the Newton's method [142] to make successive approximations and iterate towards a steady state solution of the governing equations and it uses time integration when the solution cannot be converged using Newton's method. The time integration provides a new starting point for the Newton's method that is closer to the solution and is hence more likely to lead to a converged solution. Thus Newton's method and time marching is used in tandem to converge to a steady state solution. A more detailed description of the solution method followed by Twopnt is provided by J. F. Gcar [141].

If needed Twopnt is able to refine the mesh by adding in grid points to the region under study. These points are added to regions where the solution changes rapidly and the addition of points can be controlled using parameters specified as inputs to the numerical code. It is usually recommended that one starts a simulation with a coarse mesh and allows the program to add the required grid points to the region. The solution for one mesh and boundary conditions can be reused as a starting point while changing boundary conditions. The restart option helps in more efficiently solving flame conditions which do not yield a converged solution with a simple fresh start.

7.4 Typical Structure of Reaction Zone in a Counter-Flow Setup

Figure 7-2 shows the profiles for both mass fractions of the various species, as well as the temperature in a counter-flow hydrogen-air diffusion flame. The flame was numerically solved at a pressure of 1 atm while using a reduced chemical mechanism having 8 species and 23 reactions [136]. The thermodynamic and transport properties of the species in the chemical mechanism for the hydrogen-air diffusion flame were calculated using the CHEMKIN thermodynamic and transport databases. The separation between the opposing jets was kept at 2cm and the inlet flow velocities for both the fuel and the oxidizer was 200 cm/s. The inlet fuel and oxidizer streams were kept at a constant temperature of 300 K.

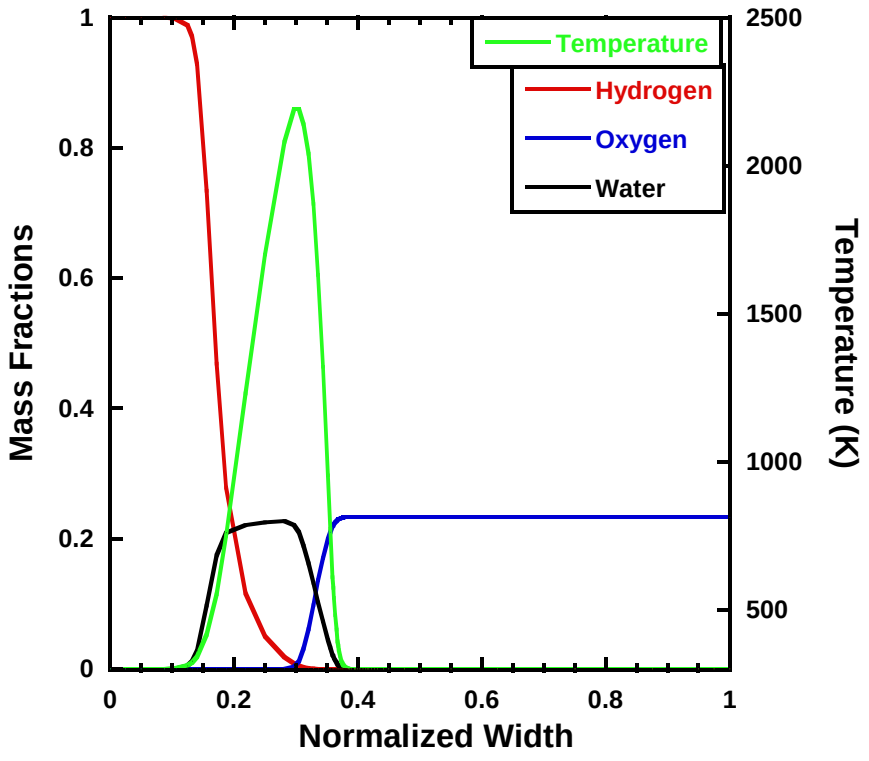

Figure 7-2: Species mass fraction and temperature profiles for a hydrogen-air counter-flow diffusion flame run at 1 atm with inlet velocity of fuel and oxidizer being 200 cm/s each.

As can be seen from the profiles, the diffusion for temperature and mass are on similar orders. This is because the thermal diffusivities for the various species are on the order of 10^{-5} m^2/s, while the mass diffusivities for the species-pairs are on the order of 10^{-5} m^2/s as well. This allows the Lewis numbers for gas-phase simulations of the counter-flow diffusion flame to be approximated as unity. The Lewis number is a dimensionless quantity which is defined as the ratio of thermal diffusivity to mass diffusivity. The number is thus used to characterize fluid flows wherein there is simultaneous heat and mass transfer. The fact that the mass and thermal diffusion are on the same order helps in making approximations and reducing the complexities while solving the energy and species equations as now the energy and species equations can be considered to be similar in nature.

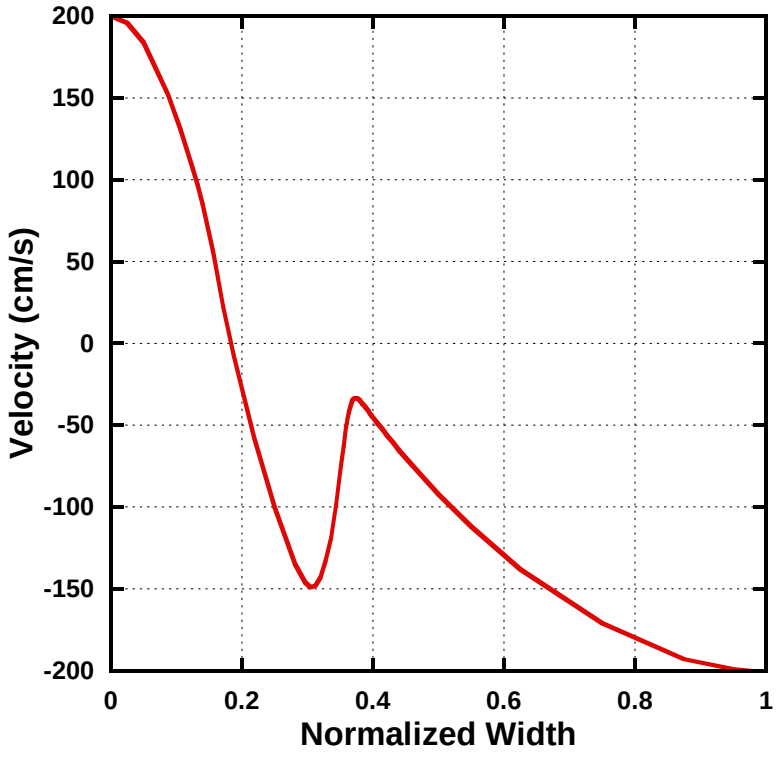

Figure 7-3: Velocity profile at the stagnation zone of the hydrogen-air diffusion flame.

Figure 7-3 provides the velocity profile at the stagnation zone for the hydrogen-air diffusion flame. Unlike the velocity profile for the microreactor, the velocity profile for the hydrogen-air flame

shows clear differences to what is expected from a stagnation flow. Here the high heat release from the reactions causes a large change in temperature. The large change in temperature in turn changes the densities of the fluids in the stagnation zone which has a clear effect on the flow profiles.

In contrast to a gas-phase counter-flow diffusion flame, Figure 7-4 shows the mass fraction and temperature profiles for the numerical simulation of reactive flow in the microreactor. Here the inlet velocities of TMEDA and diluted nitric acid are kept at 2.5 cm/s (so as to match the global strain rate for the hydrogen-air diffusion flame) while the separation between the opposing inlets is 250 microns. These inlet velocities correspond to a flow rate of 21.6 µl/min for each of the reactants. The temperature of the inlet TMEDA and nitric acid streams was a constant 300 K.

As can be seen from the temperature and the species profiles for the simulation of reactive flow in the microreactor, the thermal diffusion and the mass diffusions are no longer on the same order as they were for the hydrogen-air diffusion flame. This is because as seen in values listed in Table 7-2, the mass diffusivity values are on the order of 10^{-9} m^2/s. These low mass diffusivity values give rise to the steep concentration gradients on both the fuel and the oxidizer side of the reaction zone. On the other hand the thermal diffusivity values are only on the order of 10^{-7} m^2/s, thus leading to Lewis numbers that can be approximated to be on the order of 10^2.

Given the large Lewis numbers, the approximations that could be used to solve gas-phase equations for energy and species can no longer be used for reactive flow in the liquid phase. The energy and species equations can no longer be treated as similar to one another. The difference in scales in the diffusion terms in the species and energy equations causes the governing equations to become very difficult to numerically solve – a case which is referred to as having ‘stiff equations’. The solution of stiff equations becomes computationally expensive and often a large number of grid points are required to accurately solve the governing equations at and near the stagnation zone.

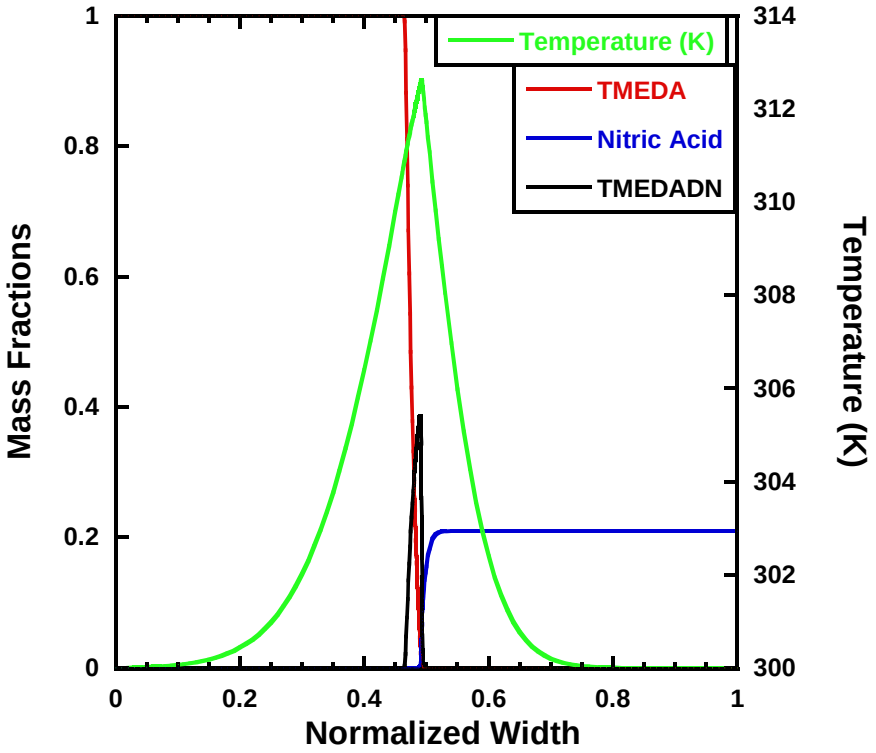

Figure 7-4: Species mass fractions and temperature profiles for a sample simulation of reactive flow in the microreactor. Inlet flow velocities of the fuel and the oxidizer are 2.5 cm/s.

The corresponding velocity profile at the stagnation zone for the flow in the microreactor is shown in Figure 7-5. As can be seen from the velocity profile, the reaction occurring at the interface has no perceptible effect on the velocity profile. This is due to the incompressible nature of the liquids used in the simulation for the microreactor and thus the change in temperature having no effect on the densities of the fluids in the stagnation zone. As the position of the stagnation plane is dependent on the momentum flux of the respective inlet jet, the velocity profile is not perfectly symmetrical about the midpoint between the two inlets. This can be seen more clearly in Figure 7-6 where the velocity profile from a numerical simulation of the flow in the microreactor is generated while keeping the mass density of both the fuel and the oxidizer stream to be that of water. Also plotted in Figure 7-6 is the velocity profile generated from a PIV experiment. The PIV run was selected such that the velocity at the inlets to the stagnation zone was close to 2.5 cm/s.

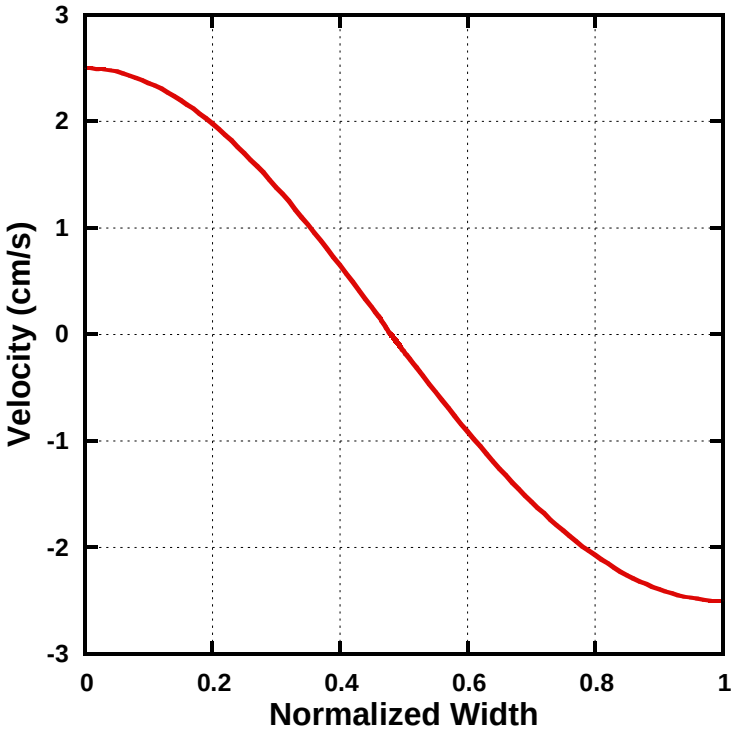

Figure 7-5: Velocity profile at the stagnation zone in the microreactor from the numerical simulation.

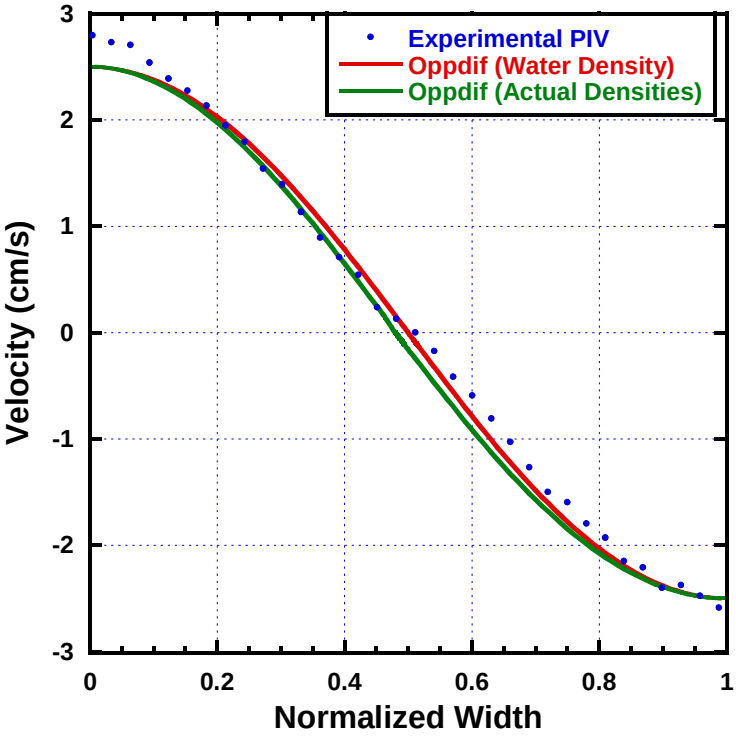

Figure 7-6: Comparison between velocity profiles generated using numerical simulations and PIV experiments at the stagnation zone

7.5 Results and Discussion of Numerical Simulations of Reactive Flow

7.5.1 Temperature Trends in the Microreactor for Varying Inlet Velocities and Reaction Rates

The numerical simulations were first carried out by keeping the reaction rate for the single step reaction constant and varying the inlet flow velocities for both the fuel and the oxidizer into the microreactor. The temperature for the inlet TMEDA and nitric acid streams for all the simulations was kept at a constant 300 K. The fuel inlet velocity was kept the same as the oxidizer inlet velocity for all the numerical simulations. To start the simulations with a relatively slow reaction rate, a reaction rate constant (K) of $2\times10^{6}\ l^{2}\cdot mol^{-2}\cdot s^{-1}$ was chosen.

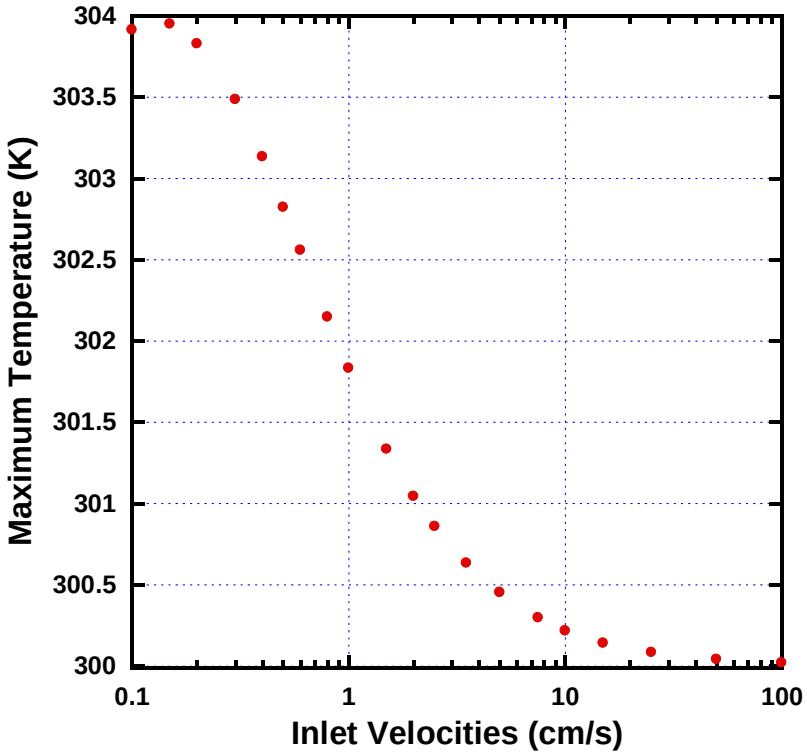

Figure 7-7: Maximum temperature profile at the stagnation zone from numerical simulations of flow in the microreactor with reaction rate constant $K = 2\times10^{6}\ l^{2}\cdot mol^{-2}\cdot s^{-1}$.

Figure 7-7 shows the temperature trends for the peak temperature as the inlet velocities for the fuel and oxidizer were varied. The inlet velocities on the x-axis are plotted on the log scale so as to clearly represent the trends for a large change in inlet velocities. As can be seen from the plot, the temperature is seen to rise very slightly when the flow rate of the reagents in the stagnation zone is increased from 0.1 cm/s to 0.15 cm/s. Any further increase in inlet flow velocities of the reagents into the microreactor stagnation zone sees the temperatures reduce severely. When the inlet flow velocities of the reagents reaches a value of 100 cm/s then there is hardly any noticeable change in temperature when compared to the inlet temperatures of the fuel and oxidizer streams.

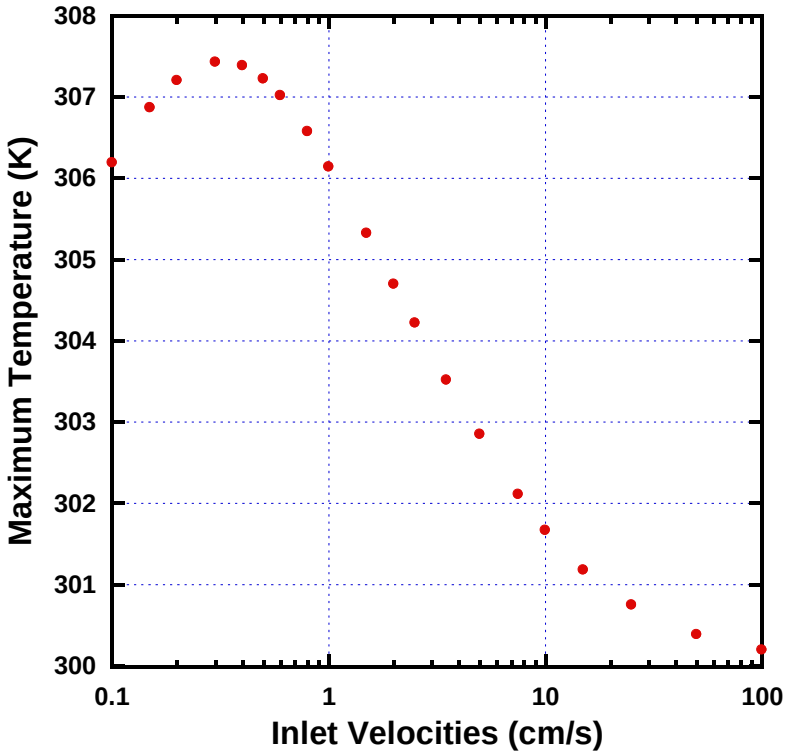

Figure 7-8: Maximum temperature profile at the stagnation zone from numerical simulations of flow in the microreactor with reaction rate constant $K = 2\times10^{7}\ l^{2}\cdot mol^{-2}\cdot s^{-1}$.

The value of the reaction rate constant was then increased so as to observe the effect on the temperature trends in the stagnation zone of the microreactor. As seen from the plot in Figure 7-8,

where the reaction rate constant has been raised to 2×10^{7} $l^{2}\cdot mol^{-2}\cdot s^{-1}$, the temperature trends at the stagnation zone in the microreactor remain similar to those seen with the reaction rate constant set at 2×10^{6} $l^{2}\cdot mol^{-2}\cdot s^{-1}$.The temperatures first rise with an increase in flow velocities of the reagents, then peak and continue to decrease with a further increase in inlet flow velocities. But now the peak in the temperature trend occurs at a higher inlet flow velocity (0.3 cm/s) than that observed when the reaction rate constant was 2×10^{6} $l^{2}\cdot mol^{-2}\cdot s^{-1}$ (Figure 7-7). Also noticeable is the fact that the temperatures are now higher for each inlet velocity than with the lower reaction rate constant.

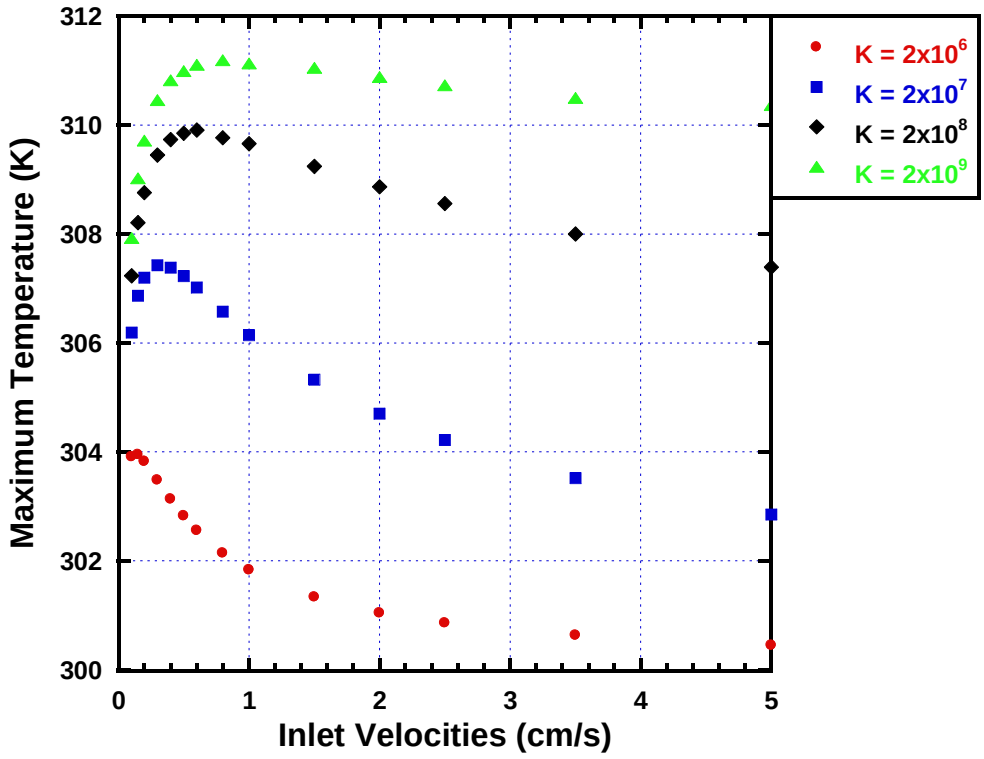

Figure 7-9: Maximum temperature profiles in the stagnation zone from numerical simulation of flow in the microreactor while varying reaction rate constant (*K*).

With a further increase in the reaction rate constant, the peak in the temperature trends can be made to shift to even higher inlet flow velocities. This is easily noticeable in Figure 7-9, where the temperature trends are shown for varying reaction rate constant. Here the value of ***K*** is varied

between 2×10^{6} $l^{2}\cdot mol^{-2}\cdot s^{-1}$ and 2×10^{9} $l^{2}\cdot mol^{-2}\cdot s^{-1}$. The peak for $\boldsymbol{K} = 2\times10^{9}$ $l^{2}\cdot mol^{-2}\cdot s^{-1}$ occurs at a flow rate close to 0.6 cm/s. Also noticeable is the fact that the drop in temperatures after the peak temperature becomes less severe with an increase in reaction rate constant. But the temperature trends before the peak remain similar for the different reaction rates. The slope of the rise in temperatures when the reaction rate is varied between 2×10^{7} $l^{2}\cdot mol^{-2}\cdot s^{-1}$ and 2×10^{9} $l^{2}\cdot mol^{-2}\cdot s^{-1}$ can be said to be almost the same.

The temperature trends observed from the numerical simulations of the flow in the microreactor can be explained by reasoning used to explain trends in the counter-flow diffusion flame. In a diffusion flame, the combustion rate can be controlled by controlling the diffusion rate of reactants into the reaction zone. With an increase in diffusion rate, the combustion rate of the flame can be increased. Thus an increase of flow of the fuel and oxidizer to the reaction zone will cause an increase in the combustion rate at the flame. If the flow rates of the fuel and oxidizer are further increased, and are able to exceed a critical value, then the reaction between the fuel and oxidizer will not be able to keep up with the flow of reagents into the reaction zone, and the reaction rate will abruptly decrease.

Similarly, as the inlet flow velocities of TMEDA and nitric acid into the microreactor are increased, the residence time at the stagnation point becomes shorter. At a critical flow rate, the residence time of the reagents becomes shorter than the time required for reaction. At this critical flow rate, the temperature in the simulations starts decreasing with any further increase in inlet flow velocities of the fuel and oxidizer. As the reaction rate constant was initially chosen to reflect a relatively slow reaction between the reagents, the peak in temperature occurs at very low inlet velocities for the reagents as the time required for the reaction to occur with a rate constant of 2×10^{6} $l^{2}\cdot mol^{-2}\cdot s^{-1}$ is long.

When the reaction rate constant is increased, then the reaction occurs at a quicker pace and thus the time required for the reaction to occur is lesser than before. For the system to switch from a

mixing controlled regime, to a kinetically controlled regime, the residence times have to be much shorter than in the case when the reaction rate constant is assumed to be $2\times10^{6}\ l^{2}\cdot mol^{-2}\cdot s^{-1}$. Thus, when the reaction rate constant is increased, the peak in the temperature trends occurs at a higher inlet flow velocity than in the case with the lower reaction rate constant. Thus for the case when the reaction rate constant is $2\times10^{9}\ l^{2}\cdot mol^{-2}\cdot s^{-1}$, the peak in temperatures occurs at an inlet flow velocity of 0.6 cm/s.

Given that the slopes of the temperature trends after the peak change with the value of reaction rate constant, the regime after the temperature peak can be said to be dependent on the reaction rate. This regime at the flow velocities beyond the peak in temperature is kinetically controlled. On the other hand, the slopes of the temperature trends before the peak in temperature are seen to be independent of the value of the reaction rate constant. The regime for the flow velocities before the peak in temperature can be said to be influenced by the diffusional mixing between the reagents and can thus be termed as diffusion controlled.

7.5.2 Comparing the Relative Importance of Terms in the Energy Equation

The increase in reaction rate made it possible to shift the peak in the temperature trends to higher inlet flow velocities but the shift was limited in nature and the inlet flow velocities at which the peaks occurred were low when compared to the experimental data in the microreactors. To better understand the heat released at the reaction zone between the fuel and the oxidizer, the individual terms in the energy equation were analyzed. The energy equation for *K* species interacting at the reaction zone can be expressed as:

$$2U\frac{dT}{dx} - \frac{1}{c_p}\frac{d}{dx}\left(\lambda\frac{dT}{dx}\right) + \frac{\rho}{c_p}\sum_{k=1}^{K} Y_k c_{pk} V_k \frac{dT}{dx} + \frac{1}{c_p}\sum_{k=1}^{K} h_k \dot{\omega}_k = 0$$

where, c_p is the specific heat, h_k are the molar enthalpies, $\dot{\omega}_k$ are the chemical production rates of the species due to reaction, W_k are the molecular weights of the species, μ is the viscosity while λ is the thermal conductivity. Thus each individual term in the energy equation can be defined as follows : $2Uc_p\frac{dT}{dx}$ is the term that causes the convection of heat due to fluid flow, $\frac{d}{dx}\left(\lambda\frac{dT}{dx}\right)$ is the term that is responsible for the heat transfer through the fluid due to conduction, $\rho\sum_{k=1}^{K}Y_k c_{pk}V_k\frac{dT}{dx}$ represents the heat transfer due to the mass diffusion of species and $\sum_{k=1}^{K}h_k\dot{\omega}_k$ signifies the energy transfer due to the production or destruction of species due to the reaction.

Figure 7-10 provides a plot of these individual terms in the energy equation against the normalized width of the stagnation zone. This plot is able to explain where in the stagnation zone, the various terms from the energy equation have an effect. The inlet velocity for the simulation that was used for Figure 7-10 was set at 0.1 cm/s for both the fuel and the oxidizer while the reaction rate was 2×10^7 $l^2\cdot mol^{-2}\cdot s^{-1}$. As can be seen from the plot, the heat produced by the reaction is confined to a very small portion of the stagnation zone, signifying that the heat release and thus the reaction between the reagents occurs in a very thin region in the microreactor. Also observed in the plot is that the heat transfer due to conduction seems to balance the heat produced by the reaction at the reaction zone. The terms which cause changes in the energy equation due to convection and mass diffusion are relatively small when compared to the reaction and heat conduction term. Also noticed is the fact that the convection term only seems to appear away from the reaction zone. Thus it can now be said that the convective forces will act only away from the reaction zone while the heat produced at the reaction zone due to the reaction will be conducted away from the zone through conduction. The effect of mass diffusion on the rate at which heat is produced or extracted from the system will be negligibly small. More generally, the heating rate caused by the reaction will be balanced by the conduction at the reaction zone, meanwhile, away from the reaction zone, there will be a balance between the conduction and convection of heat due to the fluid flow.

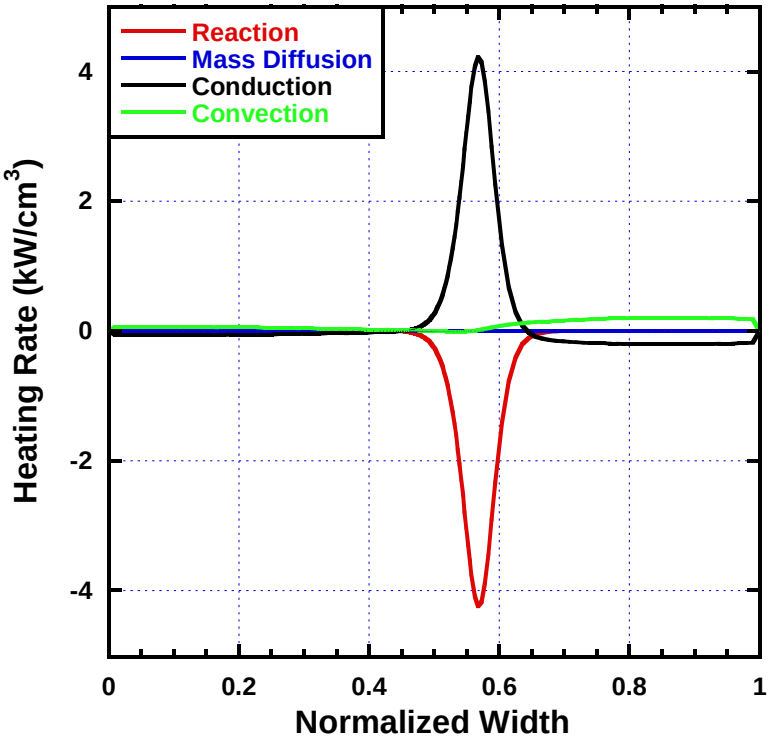

Figure 7-10: Heating rate along the stagnation centerline. Inlet velocity for both fuel and oxidizer is 0.1 cm/s while the reaction rate constant = 2×10^{7} $l^{2}\cdot mol^{-2}\cdot s^{-1}$.

The inlet velocities for both the fuel and oxidizer were then increased to see the effect on the heat release rates from the various terms in the energy equation. For this purpose the inlet velocities of both the reagents were raised first to 1 cm/s and then to 50 cm/s. The reaction rate for these simulations was kept the same at 2×10^{7} $l^{2}\cdot mol^{-2}\cdot s^{-1}$. The plots for the heat release rates for an inlet velocity of 1 cm/s and 50 cm/s are provided in Figure 7-11 and Figure 7-12 respectively. It is easy to see that the heat release rates increased with an increase in inlet velocities and that the spread of heat becomes lesser with an increase in flow rates. This decrease in the spread of heat can be linked to the lesser time scales at higher inlet flow velocities. This is because the heat release rate is an intensive property and will depend on the flow rate of reagents into the reaction zone. Also noticeable is that the convective effect for heat transfer is still away from the reaction zone but becomes more pronounced with an increase in inlet velocities.

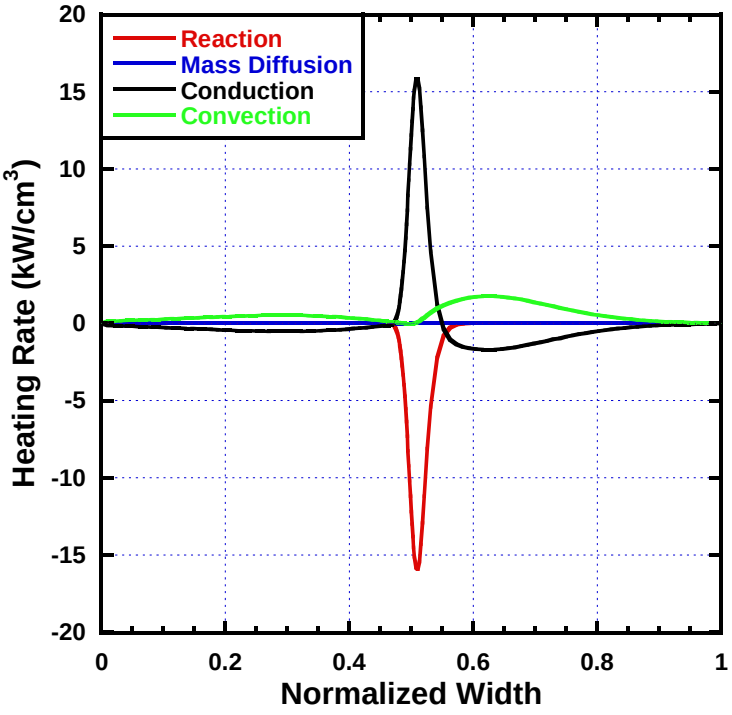

Figure 7-11: Heating rate along the stagnation centerline. Inlet velocity for both fuel and oxidizer is 1 cm/s while the reaction rate constant = 2×10^{7} $l^{2}\cdot mol^{-2}\cdot s^{-}$.

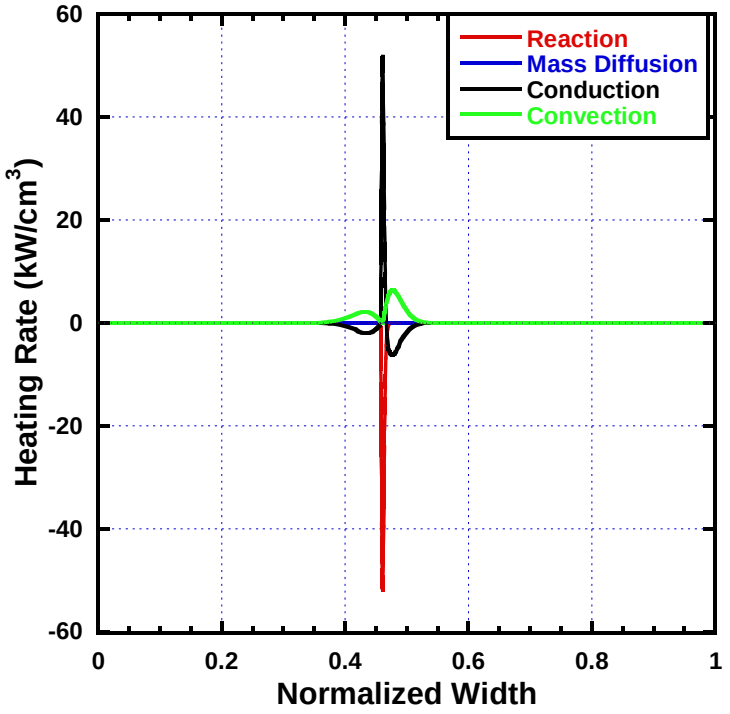

Figure 7-12: Heating rate along the stagnation centerline. Inlet velocity for both fuel and oxidizer is 50 cm/s while the reaction rate constant = 2×10^{7} $l^{2}\cdot mol^{-2}\cdot s^{-1}$.

To observe the effect of the reaction rate on the heating profiles of the various terms in the energy equation the simulations were repeated for a reaction rate of $2\times10^{9}\ l^{2}\cdot mol^{-2}\cdot s^{-1}$. Again terms were plotted along the stagnation centerline for inlet velocities of 0.1cm/s, 1 cm/s and 50 cm/s. The plots for these inlet velocities are shows in Figure 7-13, Figure 7-14 and Figure 7-15 respectively. Although the trends remain similar to those seen for a reaction rate of $2\times10^{7}\ l^{2}\cdot mol^{-2}\cdot s^{-1}$, the magnitudes of the heating rates are much higher than those seen at the lower reaction rate. A possible explanation for this is that due to the increase in reaction rate, more reaction occurs at the interface between the reagents thus resulting in an increase in heating rate magnitudes. Also noticeable is that the reaction zone is thinner when the reaction rates are increased. This is due to the faster consumption of species at the interface with an increase in reaction rates for the reaction.

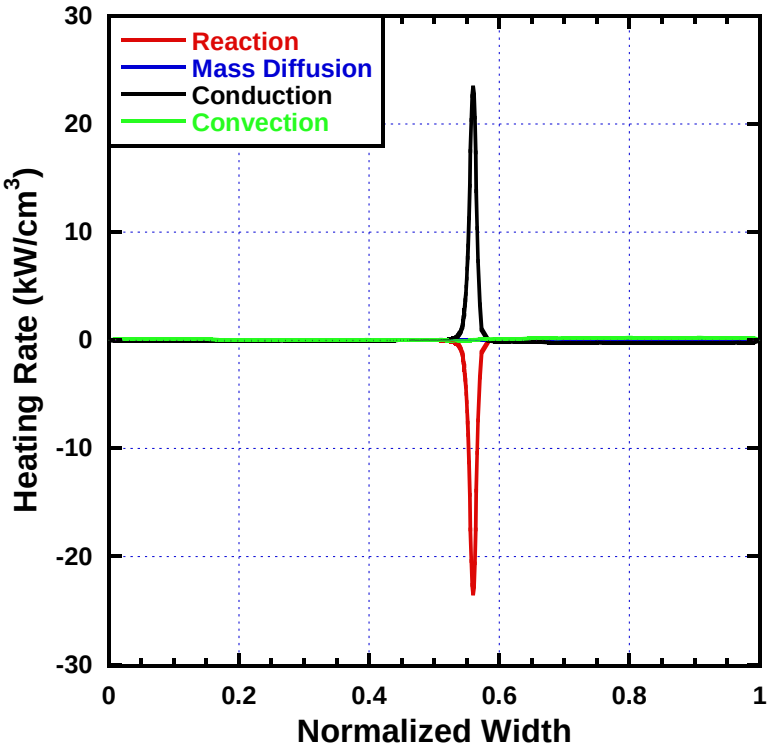

Figure 7-13: Heating rate along the stagnation centerline. Inlet velocity for both fuel and oxidizer is 0.1 cm/s while the reaction rate constant = $2\times10^{9}\ l^{2}\cdot mol^{-2}\cdot s^{-1}$.

But like previously, at the reaction zone, the heat produced by the reaction is balanced by the heat conducted away through the fluids with there being very low convection present at the reaction zone. Away from the reaction zone, there is a balance between the conduction through the fluids and the convection forces caused by the fluid flow. The convective effect on the heating rate in the energy effect becomes more pronounced at higher inlet velocities of the reagents with it being negligibly small when the inlet velocity for the reagents is 0.1 cm/s. In all regions and for all the values of the inlet flow velocities, the change in energy due to the mass diffusion stays negligibly small.

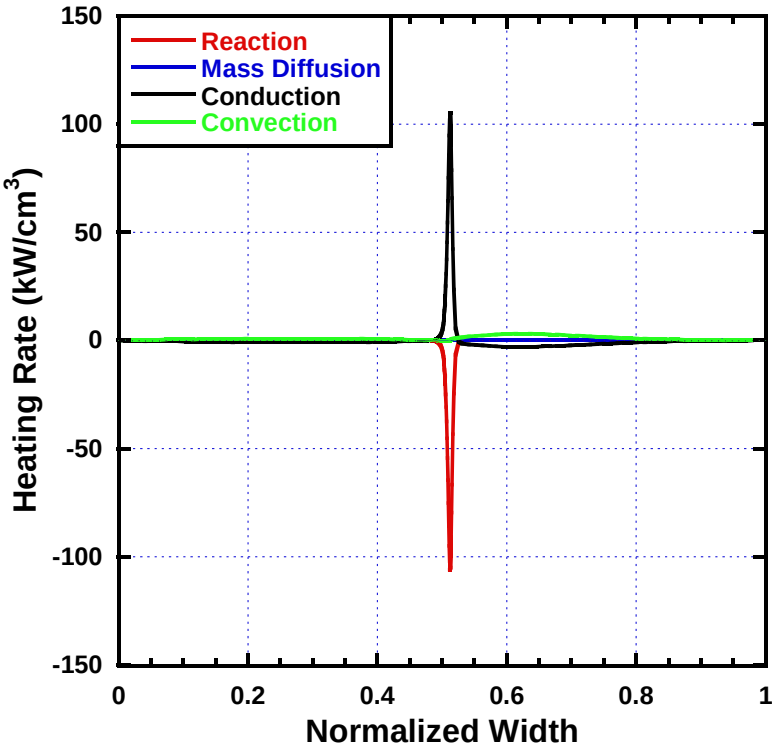

Figure 7-14: Heating rate along the stagnation centerline. Inlet velocity for both fuel and oxidizer is 1 cm/s while the reaction rate constant = 2×10^{9} $l^{2}\cdot mol^{-2}\cdot s^{-1}$.

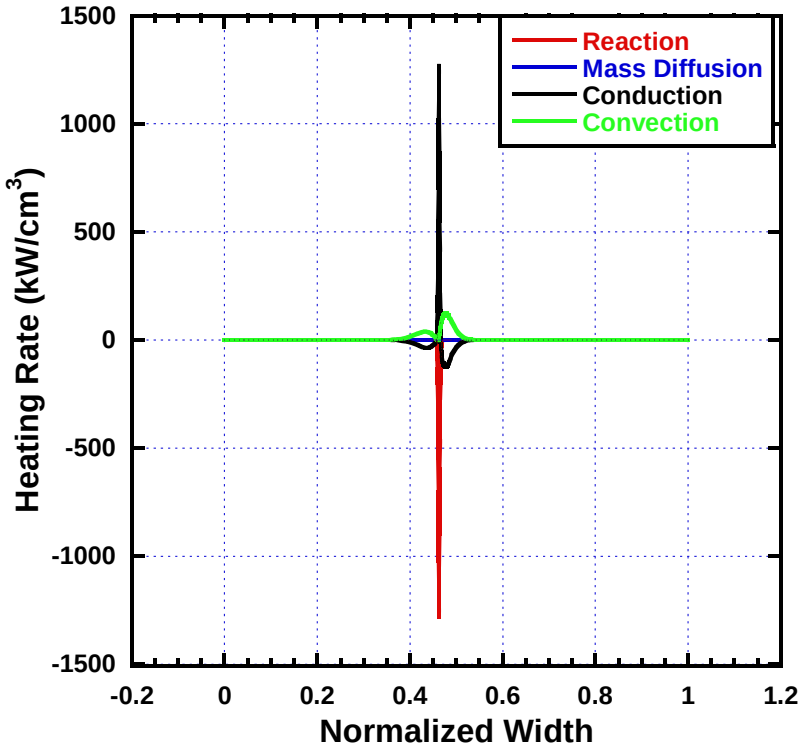

Figure 7-15: Heating rate along the stagnation centerline. Inlet velocity for both fuel and oxidizer is 50 cm/s while the reaction rate constant = 2×10^{9} $l^{2}\cdot mol^{-2}\cdot s^{-1}$.

As can be seen in the temperature trends in Figure 7-9, the inlet velocity at which the peak in temperature occurs could not be shifted to higher values by simply increasing the reaction rate constant. The inlet flow velocities at which the temperature peaks occurred in the simulation (ranging between 0.1 cm/s and 0.6 cm/s) were much lower than the inlet velocities at which the peak occurred in the actual microreactor experiments (ranging between 4 cm/s and 200 cm/s for the various fuels). Thus changes were needed in the system to account for the increase in temperatures with an increase in the flow rates, as seen in the experiments.

7.5.3 Heat Loss Effect at the Reaction Zone

Heat transfer plays a critical role in microfluidic devices. As heat transfer coefficients are inversely proportional to the hydraulic diameter of a channel, thus the small dimensions of a microfluidic device will imply a large increase in heat transfer coefficients. Heat transfer on the micron-scale has been extensively studied over the past two decades and behavior of heat and mass transfer in the fluid on the micron-scale has been compared to the behavior observed on the macro-scale. Different experimental studies have shown widely disparate results, with some studies showing heat transfer coefficients that have been far lower [143], [144] or far greater [145] than those observed for macro-scale flow. More recent studies [146], [147], on the other hand, have suggested that heat transfer behavior on the micro-scale is similar to that seen in macro-scale setups and the same set of correlations as used for conventional channels, can be used for microchannel. It is believed that errors in measurements led to the previously held discrepancies in heat transfer at the micron-scale and in actuality, the heat transfer behavior at the small scale was not very different from conventional channels [146].

To approximate the heat transfer coefficients in the present microreactor, conventional relationships developed for the macro-scale flow are used. The Nusselt number, a dimensionless quantity, is often used to compare the convective and conductive heat transfer processes. The Nusselt number can be defined as:

$$Nusselt\ Number = Nu = \frac{Convective\ Heat\ Transfer}{Conductive\ Heat\ Transfer} = \frac{h \cdot L}{K_f}$$

where, h is the convective heat transfer coefficient of the fluid, L is the characteristic length of the channel and K_f is the thermal conductivity of the fluid. If a fully developed flow is assumed to occur in the microchannel with constant wall temperature, then for a rectangular cross-section with

aspect ratio of 1:4 (height : width), the Nusselt number has a value of 4.44 [148]. The hydraulic diameter of a channel can be considered as the characteristic length for a channel with a rectangular cross-section. For the microreactor used in the reactive flow studies the hydraulic diameter can be approximated to be 100 μm. The thermal conductivity of the fluids can be approximated as 0.5 W/m-K and thus the convective heat transfer coefficient for the microreactor can be approximated to be 22,200 W/m^2-K. This high convective heat transfer coefficient (when compared to values in macro-scale flow where the coefficient usually scales on the order of 100) is due to the small length scales of the fluid flow in the microchannel. Due to such high values of heat transfer that are possible from a microfluidic device, there is a need for the heat loss from the microreactor to be accounted for.

The current reactive flow simulation of the microreactor ignores heat loss from the top and bottom areas of the stagnation zone. A method for accounting for the heat loss from the reaction zone would be to introduce a heat loss term in the energy equation. This heat loss term could be coupled with the diffusion of the temperature profile along the width of the stagnation zone, thus making akin to a heat loss mechanism from the top and bottom of the reaction zone. The addition of a constant heat loss (coupled with the temperature diffusion profile) through the top and bottom of the reaction zone would make the simulation more physically realistic.

For the purpose of the heat loss, the simulations for the various reaction rates and the various inlet flow velocities were rerun. For each reaction rate a heat loss rate was added to the governing energy equation. This heat loss term had a constant heat loss coefficient multiplied by the change in temperature profile along the stagnation centerline. To establish the initial effects of the heat loss process on the temperatures observed in the stagnation zone, this constant heat loss coefficient was assumed to be a set percentage of the maximum heat produced by the reaction at an inlet flow velocity of 0.1 cm/s. The percentage that was used as the heat loss coefficient was varied to see what effect the heat loss mechanism introduced in the energy equation had on the temperature trends.

The simulations were first run with a reaction rate constant of at 2×10^{7} $l^{2}\cdot mol^{-2}\cdot s^{-1}$. As can be seen from Figure 7-10, the maximum value of the heating rate due to the reaction is approximately 5 kW/cm^3. The heat loss coefficient ($\dot{q}_l$) was first assumed to be 20% of the maximum heating rate due to the reaction and was thus approximated to be 1 kW/cm^3-K. The heat loss coefficient was then coupled to the temperature profile along the stagnation centerline so to give the heat loss term used in the energy equation. This heat loss term can be represented as:

$$Heat\ Loss\ Term = \dot{q}_l[T(x) - T_o]$$

where, $T(x)$ provides the temperature at each point along the stagnation centerline while T_o is the temperature of the incoming fuel and oxidizer streams.

Figure 7-16 shows the profiles for the various terms in the energy equation as well as the temperature profiles along the stagnation centerline in the case of an added heat loss term into the energy equation ($\dot{q}_l$ = 1 kW/cm^3-K). Also from the plot, the profile of the heat loss term in the energy equation can be seen to scale similarly to the profile of the temperature along the stagnation centerline. Given that the magnitude of $\dot{q}_l$ was chosen to represent 20% of the maximum value of the heating rate produced by the reaction, the heat loss term has a significant role to play at an inlet flow velocity of 0.1 cm/s.

Again, at the reaction zone, the energy change due to conduction through the liquid (in addition to the heat loss term) is balanced by the heat generated due to the reaction at the interface between the reagents. Very little effect of either convection of the heat due the fluid flow or energy change due to the mass diffusion of the species is observed in the simulation result. This is because at such low inlet velocities, the major changes in the energy equation are not affected by the convective forces of the fluid flow but rather by the reaction at the interface of the reagents.

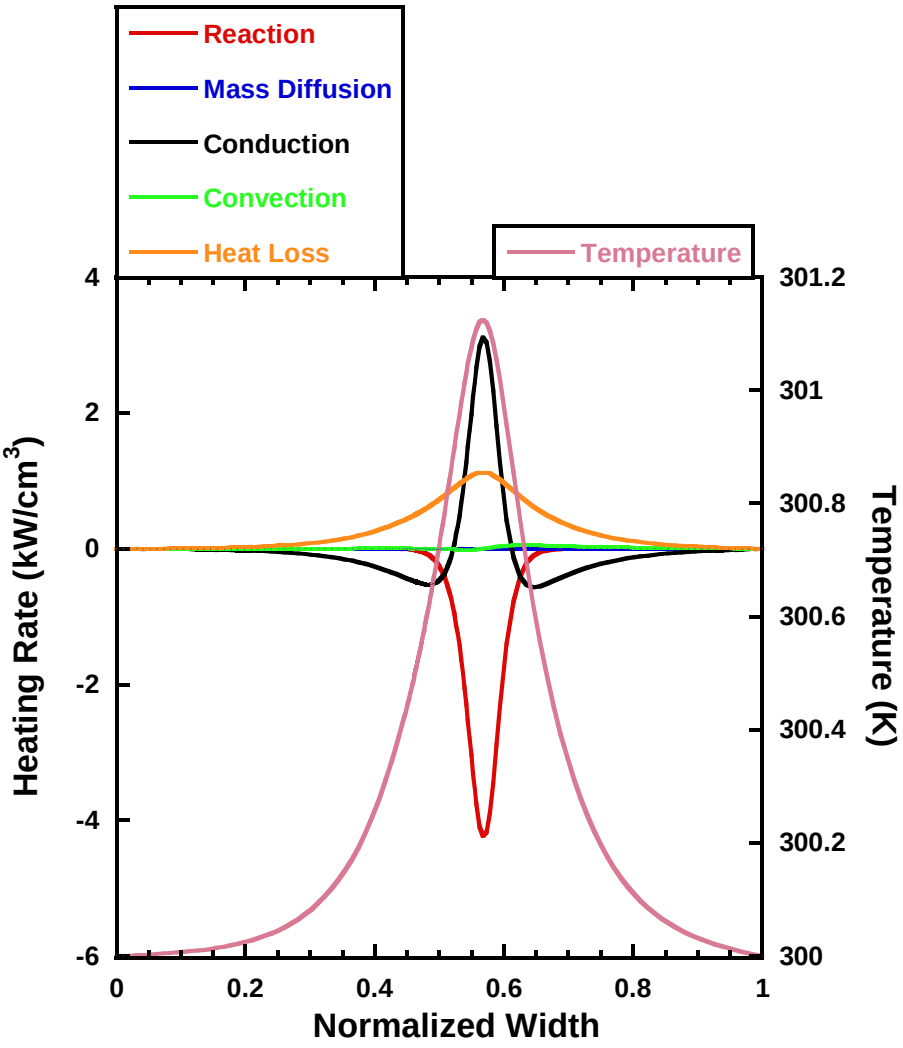

Figure 7-16: Heating rate and temperature profile along the stagnation centerline. Inlet velocity for both fuel and oxidizer is 0.1 cm/s while the reaction rate constant = 2×10^7 l^2·mol^{-2}·s^{-1}. $\dot{q}_l$ = 1 kW/cm^3-K.

With an increase in inlet velocities, it is expected that the heat loss term in the energy equation will have lesser and lesser effect on the energy equation. This is because the heat loss term has been assumed to have a constant heat loss coefficient ($\dot{q}_l$) which will not change with flow rates of the reagents unlike the other terms in the energy equation which are seen to increase with an increase in flow velocities. This is seen Figure 7-17 where the inlet velocities are 1 cm/s and the heat loss term is seen to be lesser in magnitude when compared to the maximum values of the energy change due to heat conduction and the energy change due to the reaction. This effect is more

pronounced when the inlet velocities are raised even further. Figure 7-18 provides the profiles for a case where the inlet velocities are 50 cm/s. Here the heat loss term is seen to be almost negligibly small when compared to the heating rates due to the reaction and the conduction through the fluid.

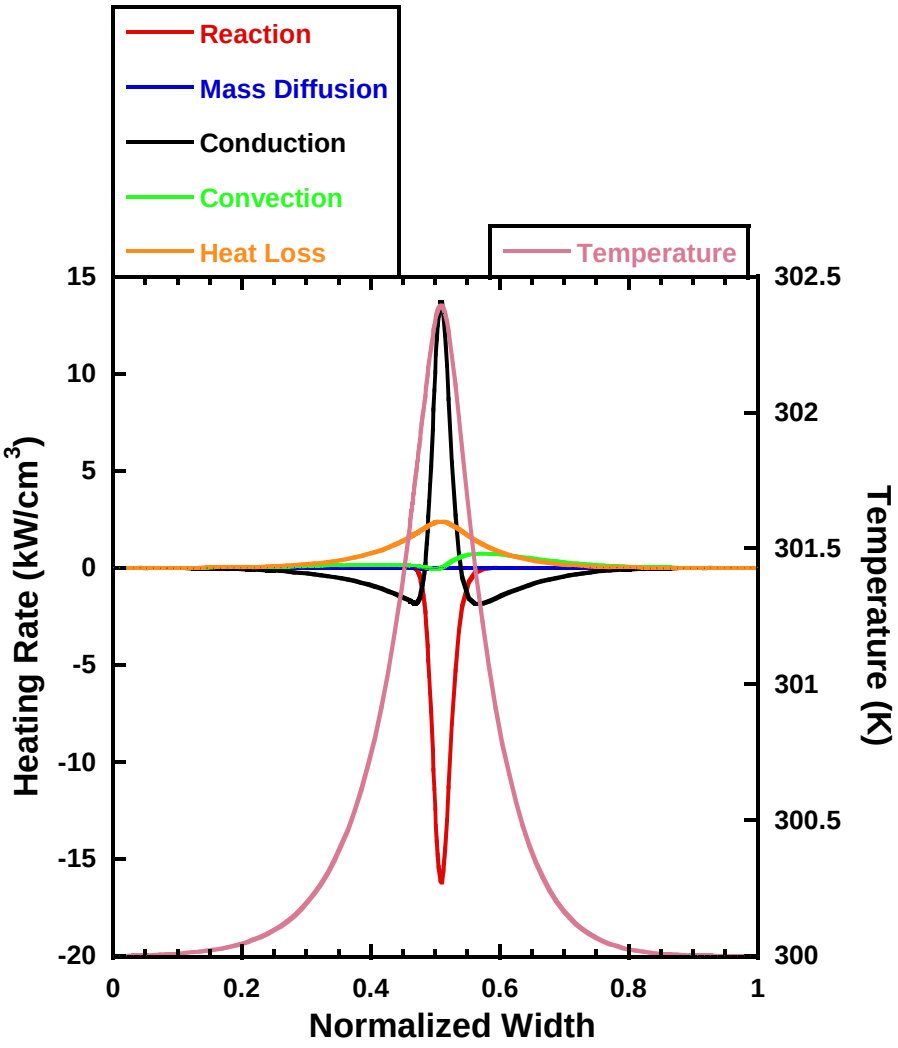

Figure 7-17: Heating rate and temperature profile along the stagnation centerline. Inlet velocity for both fuel and oxidizer is 1 cm/s while the reaction rate constant = 2×10^{7} $l^{2}\cdot mol^{-2}\cdot s^{-1}$. $\dot{q}_l$ = 1 kW/cm^{3}-K.

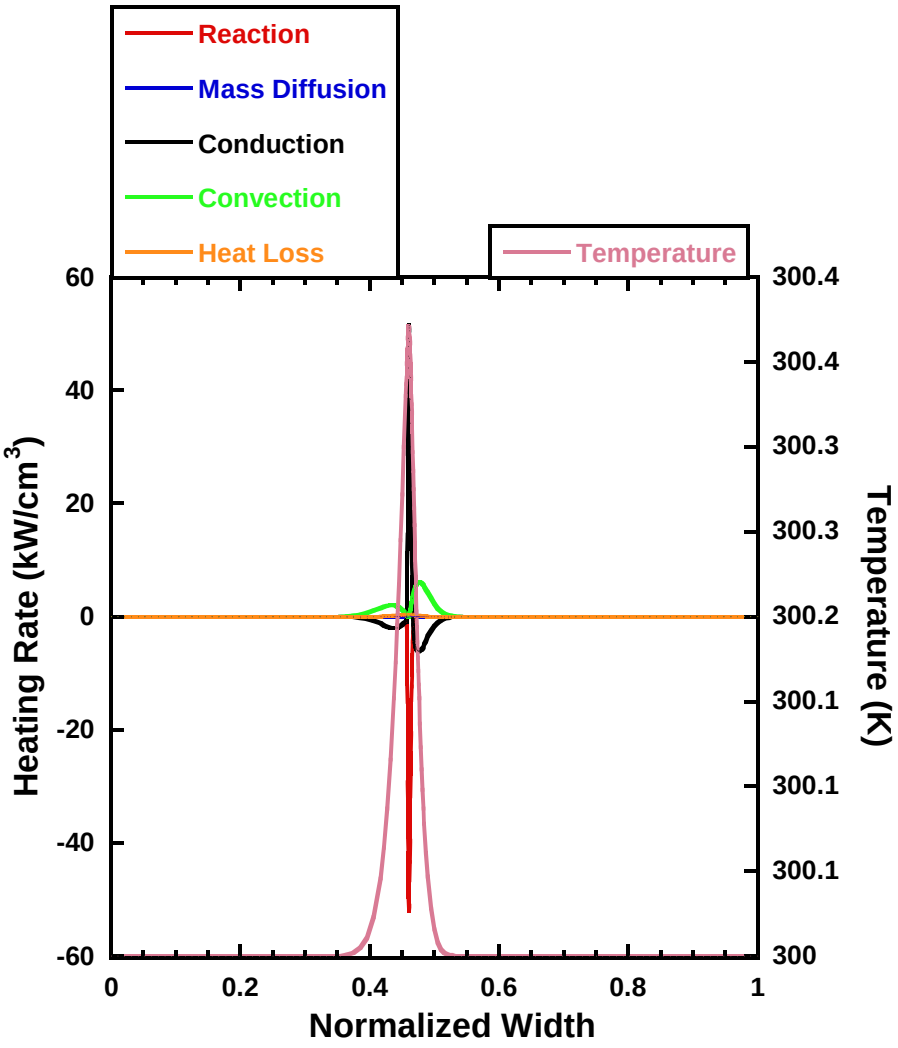

Figure 7-18: Heating rate and temperature profile along the stagnation centerline. Inlet velocity for both fuel and oxidizer is 50 cm/s while the reaction rate constant = 2×10^7 $l^2\cdot mol^{-2}\cdot s^{-1}$. $\dot{q}_l$ = 1 kW/cm^3-K.

The fact that the heat loss will have a large effect at a low inlet velocity while the effect of the heat loss term will become negligible at higher velocities means that it can expected that there will be a rise in temperature when the inlet flow velocities are increased. This is seen in the plot shown in Figure 7-19 . In the figure, the maximum temperature observed in the stagnation zone for each flow rate is plotted against the inlet flow velocities. Results in the plotted figure are for when there is no added heat loss term, for when the heat loss coefficient ($\dot{q}_l$) is 1 kW/cm^3-K and also for a case in which the value of the heat loss coefficient ($\dot{q}_l$) was increased to 2.5 kW/cm^3-K.

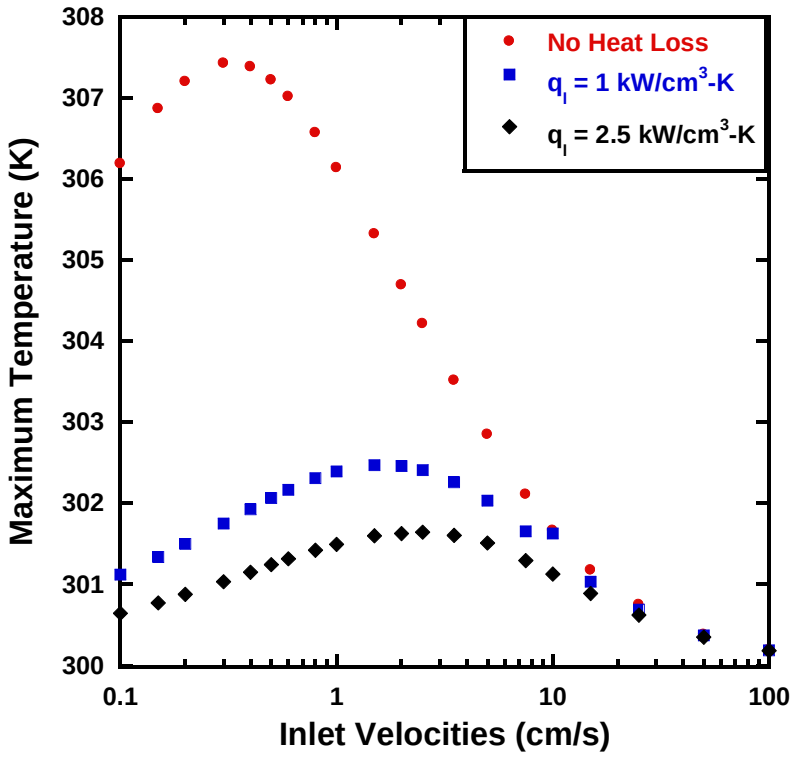

Figure 7-19: Maximum temperature profile at the stagnation zone from numerical simulations of flow in the microreactor with reaction rate constant $K = 2\times10^{7}\ l^{2}\cdot mol^{-2}\cdot s^{-1}$. In addition to the temperature trends from the original simulation, temperature trends with the added heat loss term in the energy equation are also shown.

With the addition of the heat loss term in the energy equation, the peak in the temperature in the stagnation zone now occurs at a higher inlet flow velocity (1.5 cm/s) of the reagents than when there was no heat loss term in the equation (0.3 cm/s). In fact, when the heat loss coefficient is increased from 1 kW/cm^3-K to 2.5 kW/cm^3-K, the peak in temperatures occurs at an even higher inlet flow velocity (2.5 cm/s). Thus with the addition of heat loss terms in the energy equations, the rise of the temperatures with an increase in flow velocities could be easily affected. But because of the addition of the heat loss terms, there was an obvious reduction in the magnitude of the temperatures observed in the stagnation zone of the microreactor.

The reaction rate constant was then increased to a value of 2×10^{9} $l^{2}\cdot mol^{-2}\cdot s^{-1}$, to observe the impact on the temperature profiles in the stagnation zone and to see if the inlet velocity at which the peak in temperatures occurred could be raised further from 2.5 cm/s. For this reaction rate, the maximum heating rate due to the reaction at an inlet velocity of 0.1 cm/s could be approximated as 25 kW/cm^{3} (Figure 7-13). Thus the value of the heat loss coefficients for the simulations with a reaction rate of 2×10^{9} $l^{2}\cdot mol^{-2}\cdot s^{-1}$ were chosen to be 5 kW/cm^{3}-K and 12.5 kW/cm^{3}-K (again, 20% and 50% of the maximum heating rate due to reaction). For these simulations as well, the heat loss term had a large effect at the low velocities but had lesser of an effect when the inlet velocities of the fuel and oxidizer stream were increased.

Figure 7-20 shows the maximum temperatures in the stagnation zone of the microreactor from numerical simulations run at a reaction rate constant of 2×10^{9} $l^{2}\cdot mol^{-2}\cdot s^{-1}$. Along with the temperatures for the case in which there was no heat loss term added to the energy equation, temperature trends are also shown for heat loss coefficients equaling 5 kW/cm^{3}-K and 12.5 kW/cm^{3}-K. The added heat loss term reduces the overall temperature of the fluids in the microreactor (as now energy that was earlier used to heat the fluids is now lost) but also aids in shifting the peak in temperatures to a higher inlet velocity. For a heat loss coefficient of 5 kW/cm^{3}-K the temperatures peaked at a flow rate of 25 cm/s which was a large change from the inlet velocity where the peak happened (0.6 cm/s) when no heat loss term was used in the energy equation. Again, just like in the case with the reaction rate constant being 2×10^{7} $l^{2}\cdot mol^{-2}\cdot s^{-1}$, a higher heat loss coefficient helped in the temperature peaking at an even higher inlet flow velocity. For a heat loss coefficient of 12.5 kW/cm^{3}-K, the temperatures are seen to peak at a flow velocity of 50 cm/s.

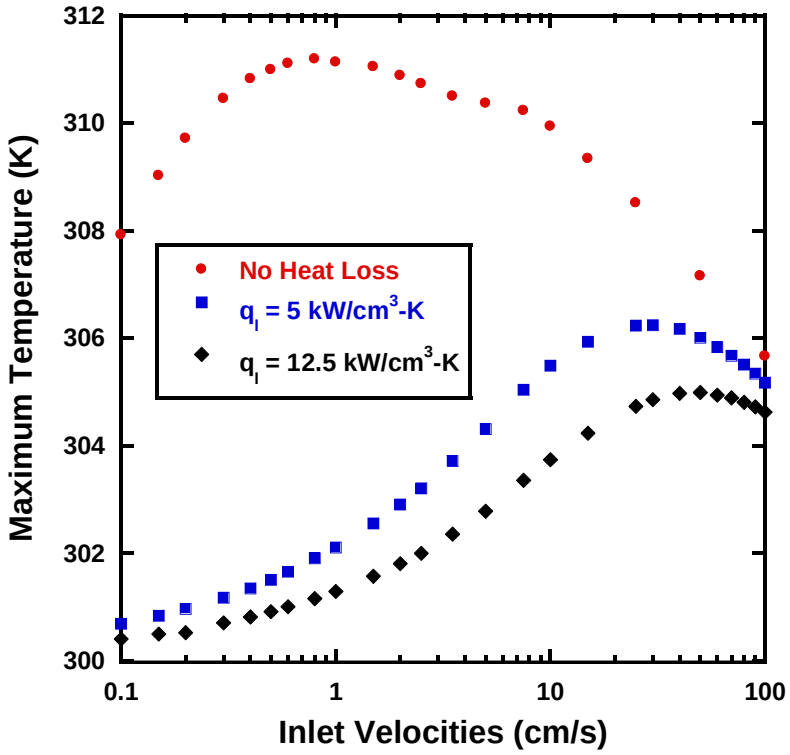

Figure 7-20: Maximum temperature profile at the stagnation zone from numerical simulations of flow in the microreactor with reaction rate constant $K = 2\times10^{9}$ l$^2 \cdot$ mol$^{-2} \cdot$ s^{-1}. In addition to the temperature trends from the original simulation, temperature trends with the added heat loss term in the energy equation are also shown.

Simulations for the various reaction rate constants (***K***) were also run while keeping the heat loss coefficient ($\dot{q}_l$) at a constant value. For this purpose, the lowest of the $\dot{q}_l$ values (1 kW/cm^3-K) was chosen and the values for the reaction rate constants were varied between 2×10^{7} l$^2\cdot$mol$^{-2}\cdot$s^{-1} and 2×10^{11} l$^2\cdot$mol$^{-2}\cdot$s^{-1}. Figure 7-21 shows the trends for the maximum temperature observed in the stagnation zone as the inlet velocities were varied for each of the simulations at a particular reaction rate constant. The temperatures can be seen to rise initially with a rise in inlet velocities, hit a peak and then decrease with a further rise in inlet velocities. It should be noted that much like the case with the no-heat loss term added to the energy equation, the peaks in temperature occur at a higher inlet velocity for as the reaction rate constant is increased. The peak for the reaction rate of 2×10^{7} l$^2\cdot$mol$^{-2}\cdot$s^{-1} occurs at an inlet velocity of 1.5 cm/s while the peak for a reaction rate constant of 2×10^{11} l$^2\cdot$mol^{-}

$^{2}\cdot s^{-1}$ occurs at an inlet velocity of 40 cm/s. This implied, once again, that the temperature trend after the peak in temperature is residence time controlled and is dependent only on the reaction rate of the chemical reaction at the interface.

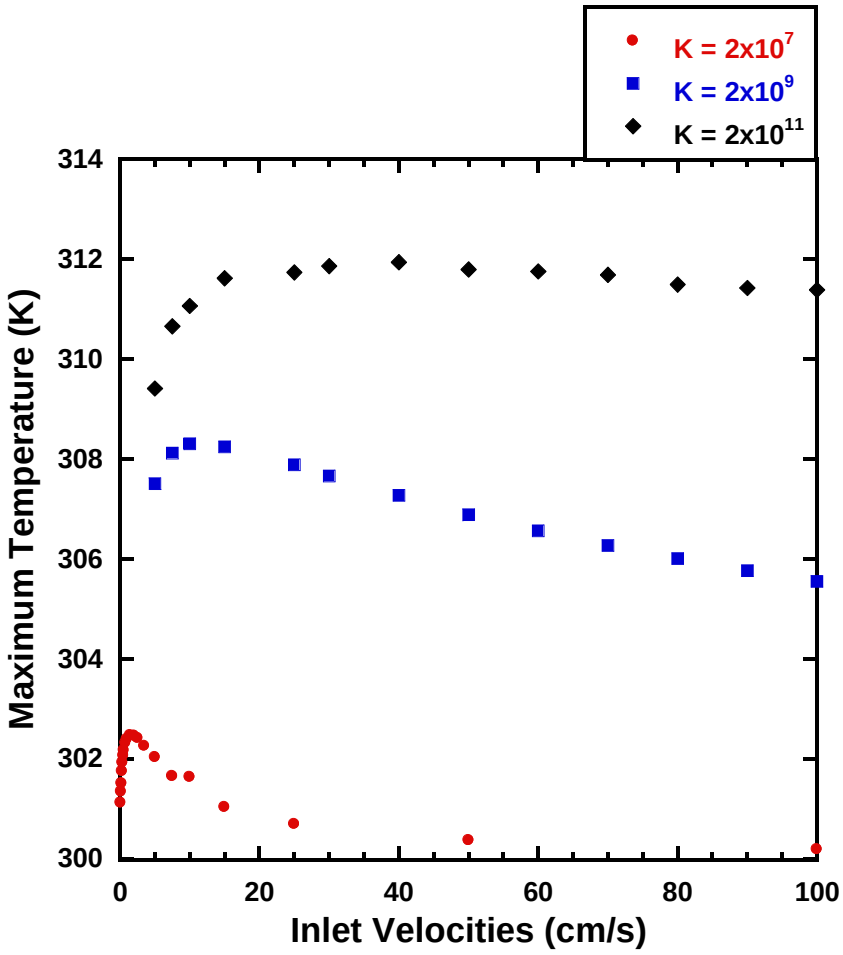

Figure 7-21: Maximum temperature profiles in the stagnation zone from numerical simulation of flow in the microreactor while varying reaction rate constant (K). $\dot{q}_l$ = 1 kW/cm^3-K.

A similar simulation was also run with the heat loss coefficient set at 5 kW/cm3-K and the reaction rate constant being varied along with the inlet velocities. Figure 7-22 shows the plot for the maximum temperature for the two reaction rate constants as the inlet velocities are varied and it can be seen that the peak for $K = 2\times10^{9}$ $l^{2}\cdot mol^{-2}\cdot s^{-1}$ now occurs at an inlet velocity of almost 80cm/s. Thus

the inlet velocity at which the peak occurs can be affected by using both the reaction rate constant and an appropriate value of the heat loss term in the energy equation.

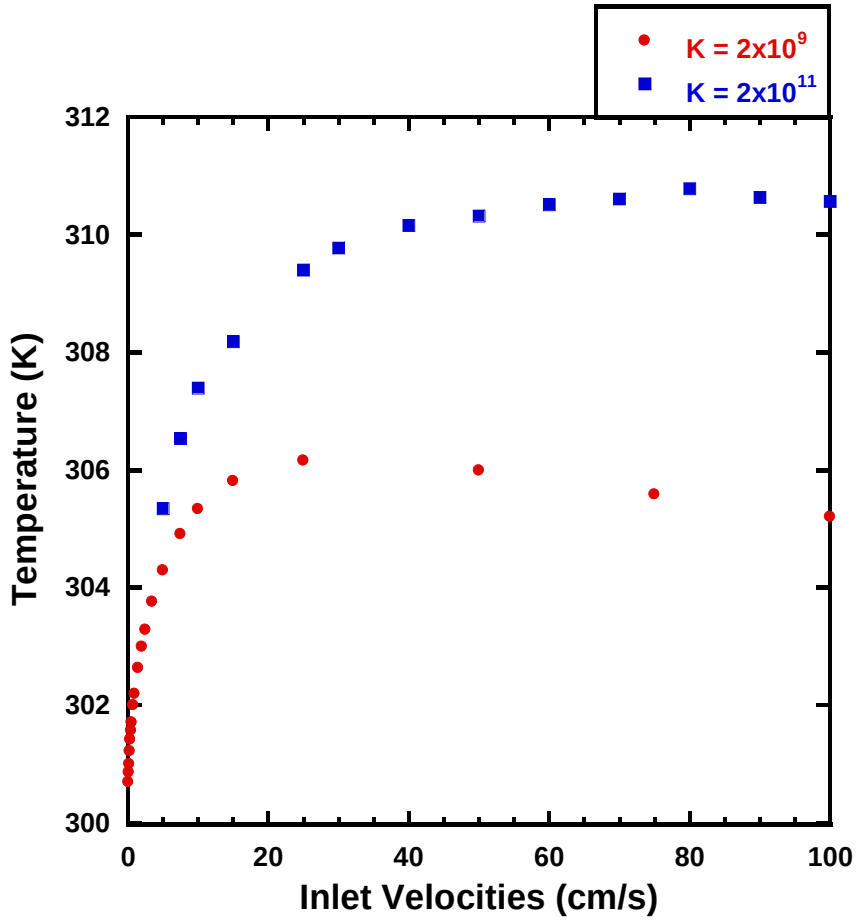

Figure 7-22: Maximum temperature profiles in the stagnation zone from numerical simulation of flow in the microreactor while varying reaction rate constant (*K*). $\dot{q}_l$ = 5 kW/cm^3-K.

It should be noted that for a heat loss coefficient of 1 kW/cm^3-K, with a hydraulic diameter of 100 µm, the equivalent convective heat transfer coefficient (h) is 100,000 W/m^2-K. An increase of the heat loss coefficient in turn implies an increase in the equivalent convective heat transfer coefficient and thus for a heat loss coefficient ($\dot{q}_l$) of 12.5 kW/cm^3-K, h can be approximated as 125,000 W/m^2-K. The large values for the convective heat transfer coefficient, when compared to the theoretical value as derived earlier for the microreactor (22,200 W/m^2-K) can be attributed to the fact that as the

flow approaches the stagnation zone, it is decelerating and not fully developed. Figure 7-23 shows the Z-component of the velocity (i.e. the velocity in the vertical direction) along the height of the microreactor from a 3D simulation of non-reactive flow in the microreactor as the fluid approaches the stagnation point. Thus distances mentioned in the legend of the plot are distances from the stagnation point. It can be clearly seen from the plot that as the flow approaches the stagnation point, a higher portion of the flow is in the vertical direction. This is because the flow is retarding in the Y-direction and due to the incompressible nature has to flow along the height of the microreactor. This situation of the flow field changing in the Z-direction is similar to the case of developing flow and the flow in the stagnation zone, due to the changes in the flow field cannot be considered to be fully developed. It should be noted that the width of the microreactor channel is 240 μm and thus the reactor side walls are at distance of 120 μm away from the stagnation point.

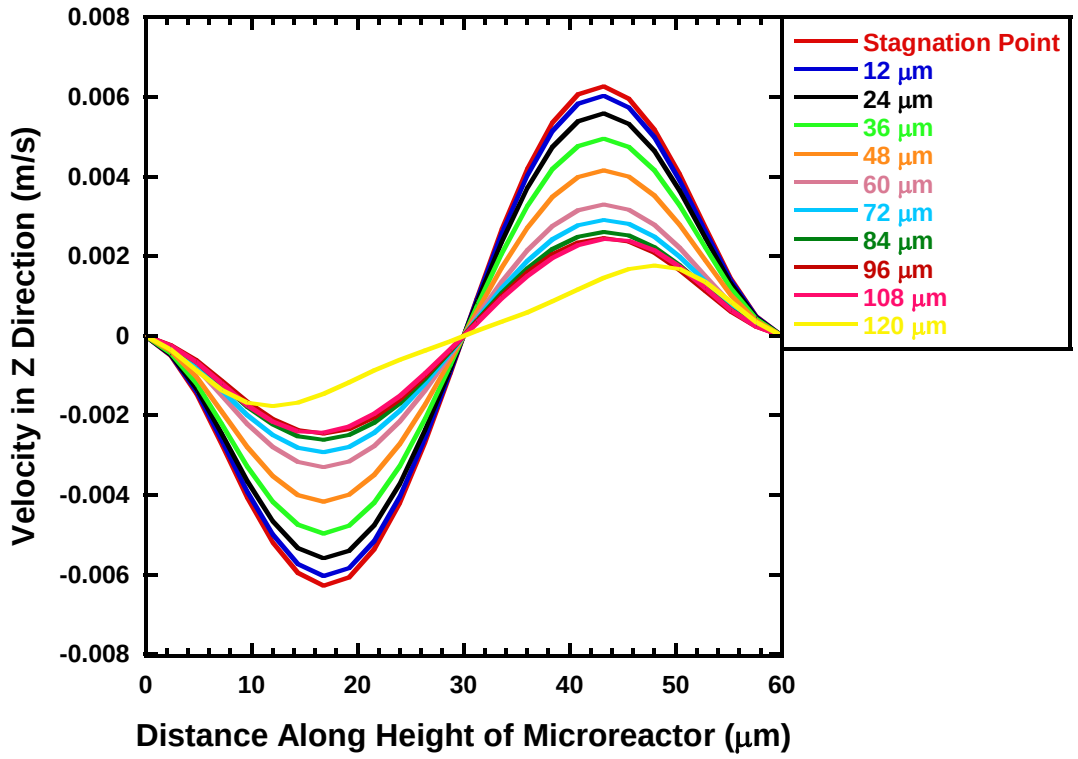

Figure 7-23: Velocity profiles for the Z-component of the Velocity along the height of the microreactor from 3D FLUENT simulation of non-reactive flow in the microreactor. The profiles are shown at various distances away from the stagnation point as the flow approaches the stagnation point.

Thus the flow moving towards and away from the stagnation zone will be influenced by effects similar to the entry-effects seen in macro-scale channels and thus will see an increase in the convective heat transfer coefficient [149] which will be dependent on the flow velocities of the fluid. It is noticed in flows that are not fully developed that the Nusselt number is higher at the entrance to the channel and it then decreases asymptotically as the flow develops [150]. Studies have shown that the average Nusselt numbers in the entrance region can be as high as 40 times the value of the Nusselt number for fully developed flow [151]. The convective heat transfer coefficient will thus have a value higher than the value derived earlier using the theoretical expression for fully developed flow.

7.5.4 Conclusion

The numerical simulations carried out for this work thus show that the temperature trends in the stagnation zone are similar to the trends observed in the microreactor experiments. An initial increase in observed in the temperature when the flow velocities are increased, but then the temperature is seen to hit a peak and any further increase in the flow velocities causes a decrease in temperatures. It was noticed that the flow velocities at which this peak in temperatures occurs could be affected by the reaction rate of the reaction occurring at the interface between the hypergols. A higher reaction rate pushed the peak towards higher inlet velocities and also resulted in higher overall temperatures in the stagnation zone. Also noticed was the fact that adding a heat loss term to the energy equation (to account for the heat loss from the top and bottom areas of the stagnation zone) was able to push the peaks in temperatures to still higher inlet flow velocities. As the simulations in their original form neglect heat loss from the top and bottom areas of the stagnation zone, the addition of such a heat loss term makes the simulation more physically realistic and can provide for a far truer picture of the reaction zone in the microreactor. The occurrence of the peak in temperatures at closer

values to the experiments with the added heat loss term in the energy equation showed that heat loss could have a role to play in the initial rise in temperatures that were observed in the microreactor experiments. The numerical simulations, though, were not able to accurately predict the velocities at which the peaks occurred in the experiments, with the peaks occurring at higher velocities in the experiments than seen in the numerical simulations. A more detailed analysis of the heat transfer characteristics of the microreactor and the diffusion of heat away from the reaction zone is thus needed to accurately model the reactive flow at the stagnation zone and match the temperature trends seen in the microreactor experiments. By matching the numerical simulations with the experimental results, the previously unknown reaction rates for the condensed phase hypergolic reactions can be estimated.

Chapter 8

Conclusion

8.1 Summary of Research

Novel stagnation flow microreactors have been fabricated to study the reactions occurring between extremely corrosive hypergolic propellants. Scaling down the dimensions of the reactor to micron-scale provides for a laminar flow of reagents in the microreactor and results in minimal mixing of the reagents as they flow. Due to the low mixing between the reagents the system is prevented from transitioning to an ignition event and the early condensed phase chemistry can be isolated between hypergols that exhibit fast liquid phase reactions.

To characterize the flow-field in the microreactors and in-depth particle image velocimetry (PIV) study with non-reactive fluids was carried out. This PIV study concentrated on the stagnation zone of the microreactors as this was the region which showed a high degree of change in the velocity flow-field. For the present study a variety of flow rates in the microreactor were used so as to change the strain rate occurring at the stagnations point. The experimental PIV measurements were compared to numerical simulations of the fluid flow carried out using the commercially available software FLUENT. Excellent overlap was seen between the experimental measurements and the numerical calculations thus proving that the flow-field in the microreactor was laminar and could be easily calculated using numerical simulations. Although the flow in the microreactor was observed to be stratified at lower flow rates, when the flow rates of the fluids in the microreactor was increased over a critical flow rate, a transition occurred and the flow was observed to be more engulfed – with the two fluid streams not flowing alongside one another. The transition from the stratified flow regime

was found to not only depend on the flow rate (Reynolds number) of the reagents but also on the geometry of the microreactor.

Reactive flow studies in the microreactor were carried out with a variety of fuels and nitric acid as the oxidizer. Steady flow was observed in the microreactors with no perturbation of the interface between the reactants. Thus laminar flow was observed in the microreactors even with reactions occurring at the interface of the reagents. Temperature measurements at the stagnation zone, exhaust ports and along the length of the microreactor were used to quantify the reaction occurring at the interface between the two hypergolic reagents. The temperature at the exhaust ports was seen to increase with a flow rate, hit a peak value and then decrease with a further increase in flow rates. This peak in temperature trend followed by a decrease in temperature with an increase in flow rates is attributed to the flow regime now being kinetically controlled and thus the reaction occurring at the interface is determined by the residence time of the reagents in the microreactor. Thus the flow rate at which this peak in temperature occurs can be related to the rate of the reaction between the hypergolic reactants. Temperature trends at various points along the length of the channel of the microreactor revealed that the temperature increased as the flow progressed down the channel. Also, temperature trends at the stagnation zone, as well as along the length of the reactor, were similar to those observed at the exhaust ports. Thus it can be concluded that the measurements of temperature at the exhaust port are affected by the conditions upstream and in fact depend on the conditions that occur at the stagnation zone.

Conventional drop test experiments with the hypergolic reagents were also carried out as part of the present study. These experiments were conducted to quantify the reactivity of the various fuels with nitric acid. The various fuels provided a range of ignition delay times with white fuming nitric acid and thus the various fuels could now be ranked on the basis of their reactivity. The fuels with the lowest ignition delay times were quantified as the fuels with the fastest reaction rate while the fuels which did not ignite were quantified as the fuels with the slowest reaction rate. The reactive flow

experiments in the microreactor were compared to these drop test experiments and a correlation was found between the heat releases in the microreactor as well as the flow rate at which the peak temperature occurred with the ignition delay times. The fuel with the shortest ignition delay time produced the highest heat release in the microreactor experiments as well as had the temperature peak at the highest flow rate. On the other hand, the fuels with the longest ignition delay time produced the lowest heat release in the microreactor as well as had the temperature peak at the lowest flow rate. Thus the overall ignition delay times can be related to the heat released by the liquid phase reactions as well as how quickly this heat is released. This indicates that liquid phase reactions are very important in the overall performance of hypergolic propellants.

The studies using both the drop tests and the condensed phase interactions in the microreactor have shown that reactivity order for the various fuels studied in the present study is TMEDA > Triethylamine > DMAZ > Dicyclopentadiene > Indene. A recent study [15] has argued that the amine group has a higher heat release than the azide group when the molecules interact with nitric acid because of the higher basicity of the amine molecule. The microreactor experiments have similarly shown that the heat release from the condensed phase reactions for both TMEDA and triethylamine with nitric acid result in a higher temperature than what is observed for the interaction between nitric acid and DMAZ. Combined with the fact that the peak in temperatures for the interaction with nitric acid occurs at a higher flow rate for both TMEDA and triethylamine than for DMAZ, it can also be stated that the two amine based fuels also have a higher reaction rate (as proved by the numerical simulations of the reactive flow in the stagnation zone of the microreactor). The temperature trends from the microreactor experiments can thus be used to gauge the relative heat release and reactivity of the different fuels when they are each reacted with nitric acid.

Recent studies [15] have shown that blends of TMEDA and DMAZ exhibit ignition delay times shorter than either pure TMEDA or DMAZ when reacted with nitric acid. This reduction in ignition delay time was attributed to a relative increase in heat release caused by the addition of

TMEDA to DMAZ while the DMAZ in the blend results in the reduction in ignition temperature with respect to TMEDA. Microreactor experiments were carried out with blends of TMEDA and DMAZ as the fuel and nitric acid as the oxidizer. Higher exit temperatures were noticed for the blends than for pure TMEDA or pure DMAZ. This increase in temperature implies a higher heat release for the blended fuel. The higher heat release can be then related to shorter ignition delay times. Once again the early condensed phase reactions were shown to play a large role in the ignition characteristics of hypergols. Other recent studies have also supported the fact that early liquid phase reactions contribute to the ignition delay times for the TMEDA and DMAZ blend [124].

To numerically model the reactive flow in the microreactor, the reactive was treated similar to the reaction zone in a counter-flow diffusion flame and numerical simulations of the reactive flow were carried out along the centerline of the stagnation zone. These simulations were carried out using a FORTRAN code that accounted for changes between a gas-phase counter-flow diffusion flame and the liquid phase flow in the microreactor. Temperature trends similar to the experiments were seen in the numerical simulation with the temperature first increasing with increasing flow velocities, then hitting a peak and then decreasing with a further increase in flow velocities. The flow velocities at which this peak in temperature occurred could be varied by varying the reaction rate of the reaction between the hypergols. Although the temperature trends in the simulations were similar to those seen in the experiments, the flow velocities at which the peaks occurred in the simulation were much smaller than those observed in the experiments. To account for this discrepancy an additional convective heat loss term was introduced in the energy equation to account for heat loss from the top and bottom areas of the stagnation zone. The addition of the additional heat loss term was able to achieve peak temperatures at inlet velocities closer to those seen in the microreactor experiments but also led to overall reduction in temperatures seen in the stagnation zone. Thus using appropriate heat loss terms and reaction rates for the chemical mechanism will lead to more accurate simulations of the reactive flow at the stagnation zone of the microreactor. With more accurate simulations of the

reactive zone, it will be possible to match the temperature trends of the various fuels in the microreactor experiments with corresponding simulations to estimate reaction rate constants for the various hypergol pairs.

8.2 Recommendations for Future Work

The present study proves that using microfluidics is a viable method to study fast reactions that occur at the interface of liquid hypergols. Microreactors can be used to contribute further to the knowledge with regards to early chemistry that occurs in hypergols and in turn provide information on choosing replacement hypergolic fuels. It is believed that the present study can be continued further in a number of ways and some of them are enumerated below.

8.2.1 Developing Microreactors with Deposited Temperature Sensors

The current study has used thermocouples at the exit and along the length of the reactor channel to measure temperature trends for reactive flow in the microreactor. Owing to the large sizes of the thermocouples used in the present study it has not been possible to accurately measure the thermal diffusion away from the reaction zone and across the width of the reactor channel. Also, as the thermocouples along the length could only be inserted at limited positions, it has not been possible to measure the development of the temperature profile along the length of the channel in an accurate and quantitative manner. Infrared cameras could be used to measure the temperature of the material that is contact with the reacting fluids. The use of infrared cameras for temperature measurements is able to provide for a temperature map of the entire microreactor but the studies usually involve tedious pyrometer calibrations [152]. For further studies with reactive flow using microreactors it is recommended that microfabrication techniques are used so as to fabricate

microreactors which have thermocouple deposited along the bottom of the reactor channel. These deposited thermocouples usually are in the form of thin-film resistance sensors and can be used to accurately measure temperatures in regions with dimensions as small as 50 microns [153]. Thin film sensors can thus be used to provide a more accurate temperature measurement at the stagnation zone as well as other point in the microreactor and can be used to help with the analysis of thermal diffusion in the fluids. As shown by the numerical simulations of the reactive flow in the microreactor, the reaction term in the energy equation is balanced by the thermal conduction term. Thus a more accurate profile of the thermal diffusion across the cross-sections of the microreactor will help in more accurately estimating the reaction rate term in the energy equation. Once the reaction rate term in the energy equation is determined, then the overall reaction rate of the single step reaction in the chemical mechanism can be determined.

8.2.2 Analysis of Products of Early Condensed Phase Reactions

Given that the condensed phase reactions between hypergols occur very quickly, sampling of products for analysis has been difficult. The reactions cannot be quenched by passing the reagents from the microreactor through an ice bath. And thus the reagents continue to react even after exiting the microreactor and no analysis of the intermediates formed during early condensed phase reactions can be carried out. Attempts have been made to flash evaporate the reagents in the microreactor downstream of the stagnation zone but this was not successful owing to the low vapor pressure of the reagents used. A possible method for analyzing the products formed by early condensed phase reactions could be coherent anti-Stokes spectroscopy (CARS). CARS, like Raman spectroscopy, is sensitive to the vibrational signature of molecules. But the signal to noise ratio for the CARS system is much better than what can be achieved with using Raman spectroscopy as the signal obtained from CARS is much stronger. CARS is a third order non-linear optical process and uses three laser beams

(a pump beam, a Stokes beam and a probe beam) for analyzing molecules. Dudovich et al. [154] have devised a novel way of using a single pulse to carry out vibrational spectroscopy. Both the excitation and the readout processes were carried out using the same pulse and thus it was possible to construct a CARS microscope using just one laser. The one laser CARS technique can be used to probe the stagnation zone of the microreactor to carry out selective species microscopy of combustion products formed at the interface of the hypergols. As this technique requires optical access from both sides of the microchannel thus microreactors fabricated from either etched silicon bonded on both sides to glass or LTCC with sapphire windows need to be used. The LTCC fabrication process is much quicker and cheaper than the micro-fabrication process followed for silicon and thus a number of reactor designs can be tried and perfected with a relatively short turnaround time. But as the sheets used for fabricating the LTCC reactors shrink on sintering, care must be taken with tolerances when fabricating with designs that include windows.

8.2.3 Development of a Simple Condensed Phase Chemistry Model

Current studies on hypergolic fuels are focused on better understanding the reactions that occur between hypergols so as to create a better reaction mechanism. Most of the research work for reaction mechanisms has concentrated on gas-phase chemistry between the hypergols [50], [52] and a more robust mechanism for condensed phase reactions is still needed. The present study has used microreactors to isolate early condensed-phase reactions that occur between hypergols and limits the transition of the system to the gas-phase. Attempts have also been made to use a simple one-step model to numerically simulate the reactive flow in the microreactors but these attempts have not been able to provide a complete picture of what occurs at the interface between the hypergols with the temperature trends observed in the microreactor experiments being different from those seen in the numerical simulation with the one step chemical mechanism. Chemical species data collected from

the microreactor using CARS can be combined with the improved temperature measurements from the microreactor to formulate a better condensed phase chemistry model for the hypergols. A simple model such as this would be a significant improvement in the condensed phase models currently used in multi-dimensional motor calculations

.

References

[1] G. P. Sutton, *Rocket propulsion elements - An introduction to the engineering of rockets*, 6th ed. New York: Wiley-Interscience, 1992.

[2] G. P. Sutton, *History of liquid propellant rocket engines*. AIAA, 2006.

[3] G. P. Sutton, "History of liquid propellant rocket engines in the United States," *J. Propuls. power*, vol. 19, no. 6, pp. 978–1007, 2003.

[4] A. Davenas, "Development of modern solid propellants," *J. Propuls. power*, vol. 19, no. 6, pp. 1108–1128, 2003.

[5] D. Altman, "Hybrid rocket development history," in *AIAA paper 91-2515, 27th AIAA/SAE/ASME/ ASEE Joint Propulsion Conference*, 1991.

[6] G. A. Risha, "Enhancement of hybrid rocket combustion performance using nano-sized energetic particles," The Pennsylvania State University, 2003.

[7] P. Estey, D. Altman, and J. McFarlane, "An evaluation of scaling effects for hybrid rocket motors," in *AIAA paper 91-2517, 27th AIAA/SAE/ASME/ ASEE Joint Propulsion Conference*, 1991.

[8] J. D. Clark, *Ignition! An Informal History of Liquid Rocket Propellants*. New Brunswick, NJ: Rutgers University Press, 1972.

[9] B. Nufer, "A Summary of NASA and USAF Hypergolic Propellant Related Spills and Fires," in *SpaceOps 2010 Conference Delivering on the Dream Hosted by NASA Marshall Space Flight Center and Organized by AIAA*, 2009.

[10] T. Kubal and E. Dambach, "Aspects of monomethylhydrazine and red fuming nitric acid ignition," in *46th AIAA/ASME/SAE/ASEE Joint Propulsion Conference & Exhibit*, 2010.

[11] D. M. Thompson, "Amine azides used as monopropellants," US. Patent No. 6,299,654.2001.

[12] D. M. Thompson, "Tertiary amine azides in hypergolic liquid or gel fuels propellant systems," U.S. Patent No. 6,013,143.2000.

[13] D. M. Thompson, "Tertiary amine azides in liquid or gel fuels in gas generator systems," U.S. Patent No. 6,210,504.2001.

[14] D. M. Thompson, B. F. Wilson, and W. H. Stevenson, "Hypergolic Azide Liquid Fuels," in *Proceedings of the 1998 JANNAF Propulsion Meeting*, 1998, pp. 515–523.

[15] W. H. Stevenson III, L. S. D. Felton, and Z. Slocum-Wang, "Hypergolic Liquid Or Gel Fuel Mixtures," U.S. Patent No. 8,435,364.2013.

[16] M. J. McQuaid, K. L. McNesby, B. M. Rice, and C. F. Chabalowsk, "Density functional theory characterization of the structure and gas-phase, mid-infrared absorption spectrum of 2-azido-N, N-dimethylethanamine (DMAZ)," *J. Mol. Struct. THEOCHEM*, vol. 587, no. 1–3, pp. 199–218, 2002.

[17] M. J. McQuaid, W. H. Stevenson, and D. M. Thompson, "Computationally Based Design and Screening of Hypergolic Multiamines," DTIC Document, Aberdeen, MD, 2004.

[18] M. J. McQuaid, "Amine azide propellant," U.S. Patent No. 6,962,633.2005.

[19] M. J. McQuaid, "The Estimation of Properties Employed to Predict the Environmental Fate and Transport of Hydrazine-Alternative Hypergols," DTIC Document, Aberdeen, MD, 2006.

[20] B. Mellor and M. Ford, "Investigation of Ignition Delay with DMAZ Fuel and MON Oxidiser," in *42nd AIAA/ASME/SAE/ASEE Joint Propulsion Conference & Exibit, AIAA 2006-5215*, 2006, no. July.

[21] D. Sengupta and S. Raman, "Theoretical Investigation of Some High Performance Novel Amine Azide Propellants," *Propellants, Explos. Pyrotech.*, vol. 32, no. 4, pp. 338–347, 2007.

[22] K. W. Richman, K. N. Griffith, C. L. Liotta, and P. Pollet, "Investigation of Ignition Delay: Novel Beta-Substituted Ethylazide Derivatives as Potential New Liquid Propellant Fuels (Preprint)," DTIC Document, Cedar City, UT, 2007.

[23] M. J. McQuaid, "Henry's Law Constants for 2-Azidoethanamine Hypergols: Estimates From a Density Functional Theory/Polarizable Continuum Model," DTIC Document, Aberdeen, MD, 2009.

[24] G. Reddy, J. Song, M. S. Mecchi, and M. S. Johnson, "Genotoxicity assessment of two hypergolic energetic propellant compounds," *Mutat. Res. Toxicol. Environ. Mutagen.*, vol. 700, no. 1, pp. 26–31, 2010.

[25] C. S. Hampton, K. K. Ramesh, and J. E. Smith, "Importance of chemical delay time in understanding hypergolic ignition behaviors," in *AIAA 41st Aerospace Sciences Meeting and Exhibit*, 2003, pp. 6–9.

[26] E. A. Hurlbert, R. J. Moreland, and S. Candel, "Propellant Ignition and Flame Propagation," in in *Liquid rocket thrust chambers: aspects of modeling, analysis, and design*, vol. 200, AIAA, Inc., 2004, pp. 405–435.

[27] J. D. Broatch, "An apparatus for the measurement of ignition delays of self-igniting fuels," *Fuel*, vol. 29, 1950.

[28] S. V Gunn, "The Effects of Several Variables Upon the Ignition Lag of Hypergolic Fuels Oxidized by Nitric Acid," *J. Am. Rocket Soc.*, vol. 22, no. 1, pp. 33–38, 1952.

[29] A. J. Alfano, J. D. Mills, and G. L. Vaghjiani, "Highly accurate ignition delay apparatus for hypergolic fuel research," *Rev. Sci. Instrum.*, vol. 77, p. 45109, 2006.

[30] M. A. Pino, “A Versatile Ignition Delay Tester for Self Igniting Rocket Propellants,” *J. Jet Propuls.*, vol. 25, no. 9, pp. 463–467, 1955.

[31] M. Kilpatrick and L. L. Baker Jr, “Fifth Symposium (International) on Combustion.” Reinhold Publishing Corp., New York, 1955.

[32] D. J. Ladanyi and R. O. Miller, “Two Methods for Measuring Ignition Delay of Self-Igniting Rocket Propellant Combinations,” *J. Jet Propuls.*, vol. 26, no. 3, pp. 157–163, 1956.

[33] M. A. Saad and S. R. Goldwasser, “Role of pressure in spontaneous ignition,” *AIAA J.*, vol. 7, no. 8, pp. 1574–1581, 1969.

[34] G. Spengler and J. Bauer, “Ignition delay of hypergolic rocket propellants,” *Tech. Transl. 16-US Army*, 1966.

[35] V. Agosta, T. Seamans, and M. Vanpee, “Development of a fundamental model of hypergolic ignition in space-ambient engines.,” *AIAA J.*, vol. 5, no. 9, pp. 1616–1624, 1967.

[36] G. Choudhary and H. Hansen, “Human health perspective on environmental exposure to hydrazines: a review.,” *Chemosphere*, vol. 37, no. 5, pp. 801–43, 1998.

[37] D. M. Golden, R. K. Solly, N. A. Gac, and S. W. Benson, “Very low-pressure pyrolysis. VII. The decomposition of methylhydrazine, 1, 1-dimethylhydrazine, 1, 2-dimethylhydrazine, and tetramethylhydrazine. Concerted deamination and dehydrogenation of methylhydrazine,” *Int. J. Chem. Kinet.*, vol. 4, no. 4, pp. 433–448, 1972.

[38] I. J. Eberstein and I. Glassman, “The gas-phase decomposition of hydrazine and its methyl derivatives,” in *Symposium (International) on Combustion*, 1965, vol. 10, no. 1, pp. 365–374.

[39] H. Sun, L. Catoire, and C. K. Law, “Thermal decomposition of monomethylhydrazine: Shock tube experiments and kinetic modeling,” *nternational J. Chem. Kinet.*, vol. 41, no. 3, pp. 176–186, 2009.

[40] R. D. Cook, S. H. Pyun, J. Cho, D. F. Davidson, and R. K. Hanson, “Shock tube measurements of species time-histories in monomethyl hydrazine pyrolysis,” *Combust. Flame*, vol. 158, no. 4, pp. 790–795, 2011.

[41] S. Li, D. F. Davidson, and R. K. Hanson, “Shock tube study of the pressure dependence of monomethylhydrazine pyrolysis,” *Combust. Flame*, vol. 161, no. 1, pp. 16–22, 2014.

[42] H. Sun and C. K. Law, “Thermochemical and kinetic analysis of the thermal decomposition of monomethylhydrazine: An elementary reaction mechanism,” *J. Phys. Chem. A*, vol. 111, no. 19, pp. 3748–3760, 2007.

[43] S. W. Mayer, D. Taylor, and L. Schieler, “Preignition products from storable propellants at simulated high-altitude conditions,” 1967.

[44] W. Daimon, Y. Gotoh, and I. Kimura, “Mechanism of explosion induced by contact of hypergolic liquids,” *J. Propuls.*, vol. 7, pp. 946–952, 1991.

[45] A. E. Axworthy and S. E. Rodriguez, "Liquid phase reactions of hypergolic propellants. Final Report (Measuring heat and gas release rates for initial reaction of liquid nitrogen tetroxide with hydrazine, monomethyl hydrazine, and unsymmetric dimethyl hydrazine)," 1970.

[46] M. A. Saad, M. B. Detweiler, and M. A. Sweeney, "Analysis of Reaction Products of Nitrogen Tetroxide with Hydrazines under Nonignition Conditions," *AIAA J.*, vol. 10, pp. 1073–1078, 1972.

[47] L. Catoire, N. Chaumeix, and C. Paillard, "Chemical kinetic model for monomethylhydrazine/nitrogen tetroxide gas-phase combustion and hypergolic ignition," *J. Propuls. power*, vol. 20, no. 1, pp. 87–92, 2004.

[48] M. J. Nusca, "Utility of Computational Modeling for the Study of Combustion Instability in Small MMH-NTO Liquid Rocket Engines," *43rd AIAA/ASME/SAE/ASEE/ Jt. Propuls. Conf. Exhib. AIAA 2007-5562*, 2007.

[49] Z. Slocum-Wang, L. D. Felton, T. W. Turner, and W. H. Stevenson Iii, "Ignition Delay Screening Techniques: Drop Testing vs. Engine Testing," in *42nd AIAA/ASME/SAE/ASEE/ Joint Propulsion Conference & Exhibit, AIAA 2006-4543*, 2006.

[50] W. R. Anderson, M. J. McQuaid, M. J. Nusca, and A. J. Kotlar, "A Detailed, Finite-Rate, Chemical Kinetics Mechanism for Monomethylhydrazine-Red Fuming Nitric Acid Systems," US Army Research Laboratory, Aberdeen, MD, 2010.

[51] S. Wang and S. T. Thynell, "An experimental study on the hypergolic interaction between monomethylhydrazine and nitric acid," *Combust. Flame*, vol. 159, no. 1, pp. 438–447, 2011.

[52] C.-C. Chen, M. J. Nusca, and M. J. McQuaid, "Modeling Combustion Chamber Dynamics of Impinging Stream Vortex Engines Fueled with Hydrazine-Alternative Hypergols," DTIC Document, Aberdeen, MD, 2008.

[53] S. Wang, S. T. Thynell, and A. Chowdhury, "Experimental Study on Hypergolic Interaction between N, N, N', N'-Tetramethylethylenediamine and Nitric Acid," *Energy & Fuels*, vol. 24, no. 10, pp. 5320–5330, 2010.

[54] W.-G. Liu, S. Dasgupta, S. V Zybin, and W. a Goddard, "First principles study of the ignition mechanism for hypergolic bipropellants: N,N,N',N'-tetramethylethylenediamine (TMEDA) and N,N,N',N'-tetramethylmethylenediamine (TMMDA) with nitric acid.," *J. Phys. Chem. A*, vol. 115, no. 20, pp. 5221–9, 2011.

[55] C.-C. Chen and M. J. McQuaid, "Mechanisms and Kinetics for the Thermal Decomposition of 2-Azido-N, N-dimethylethanamine (DMAZ)," *J. Phys. Chem. A*, vol. 116, no. 14, pp. 3561–3576, 2012.

[56] C.-C. Chen and M. McQuaid, "Thermochemical and kinetics modeling of 2-azido-N,N-dimethylethanamine-red fuming nitric acid (DMAZ-RFNA) systems," in *The 6th Liquid Propulsion Subcommittee Meeting*, 2011.

[57] M. J. McQuaid, C.-C. Chen, A. J. Kotlar, W. R. Anderson, and M. J. Nusca, “Computationally Based Development of Chemical Kinetics Mechanisms for Modeling the Combustion Chamber Dynamics of Rocket Propulsion Systems,” *Int. J. Energ. Mater. Chem. Propuls.*, vol. 12, no. 1, pp. 27–40, 2013.

[58] P. Zhang and C. K. Law, “Density Functional Theory Study of the Ignition Mechanism of 2-Azido- N , N -Dimethylethanamine (DMAZ),” in *Fall Technical Meeting of the Eastern States Section of the Combustion Institute*, 2011.

[59] W. B. J. Zimmerman, *Microfluidics: history, theory and applications*, vol. 466. Springer Verlag, 2006.

[60] G. M. Whitesides, “The origins and the future of microfluidics.,” *Nature*, vol. 442, no. 7101, pp. 368–373, 2006.

[61] R. P. Feynman, “There’s plenty of room at the bottom,” *Eng. Sci.*, vol. 23, no. 5, pp. 22–36, 1960.

[62] Y. Bar-Cohen, “Electroactive polymers as artificial muscles-reality and challenges,” *Structure*, 2001.

[63] K. Mateti, “Flapping Wing Mechanisms for Pico Air Vehicles Using Piezoelectric Actuators,” The Pennsylvania State University, 2012.

[64] A. Manz, N. Graber, and H. M. Widmer, “Miniaturized total chemical analysis systems: a novel concept for chemical sensing,” *Sensors actuators B Chem.*, vol. 1, no. 1–6, pp. 244–248, 1990.

[65] D. Erickson and D. Li, “Integrated microfluidic devices,” *Anal. Chim. Acta*, vol. 507, no. 1, pp. 11–26, 2004.

[66] J. R. Webster, M. A. Burns, D. T. Burke, and C. H. Mastrangelo, “Monolithic capillary electrophoresis device with integrated fluorescence detector.,” *Anal. Chem.*, vol. 73, no. 7, pp. 1622–6, 2001.

[67] H. Yin, K. Killeen, R. Brennen, D. Sobek, M. Werlich, and T. van de Goor, “Microfluidic chip for peptide analysis with an integrated HPLC column, sample enrichment column, and nanoelectrospray tip.,” *Anal. Chem.*, vol. 77, no. 2, pp. 527–33, 2005.

[68] J. Khandurina and A. Guttman, “Bioanalysis in microfluidic devices.,” *J. Chromatogr. A*, vol. 943, no. 2, pp. 159–83, 2002.

[69] C. a Emrich, H. Tian, I. L. Medintz, and R. a Mathies, “Microfabricated 384-lane capillary array electrophoresis bioanalyzer for ultrahigh-throughput genetic analysis.,” *Anal. Chem.*, vol. 74, no. 19, pp. 5076–83, 2002.

[70] J. Gao, J. Xu, L. E. Locascio, and C. S. Lee, “Integrated microfluidic system enabling protein digestion, peptide separation, and protein identification.,” *Anal. Chem.*, vol. 73, no. 11, pp. 2648–55, 2001.

[71] H. Andersson and A. Van den Berg, “Microfluidic devices for cellomics: a review,” *Sensors Actuators B Chem.*, vol. 92, no. 3, pp. 315–325, 2003.

[72] R. M. Guijt, E. Baltussen, and G. W. K. Van Dedem, “Use of bioaffinity interactions in electrokinetically controlled assays on microfabricated devices,” *Electrophoresis*, vol. 23, no. 6, pp. 823–835, 2002.

[73] L. Zhang, J. M. Koo, L. Jiang, M. Asheghi, K. E. Goodson, J. G. Santiago, and T. W. Kenny, “Measurements and modeling of two-phase flow in microchannels with nearly constant heat flux boundary conditions,” *Microelectromechanical Syst. J.*, vol. 11, no. 1, pp. 12–19, 2002.

[74] R. A. Hayes and B. J. Feenstra, “Video-speed electronic paper based on electrowetting,” *Nature*, vol. 425, no. 6956, pp. 383–385, 2003.

[75] R. Ferrigno, A. D. Stroock, T. D. Clark, M. Mayer, and G. M. Whitesides, “Membraneless vanadium redox fuel cell using laminar flow,” *J. Am. Chem. Soc.*, vol. 124, no. 44, pp. 12930–12931, 2002.

[76] E. Choban, “Microfluidic fuel cell based on laminar flow,” *J. Power Sources*, vol. 128, no. 1, pp. 54–60, 2004.

[77] T. M. Squires and S. R. Quake, “Microfluidics: Fluid physics at the nanoliter scale,” *Rev. Mod. Phys.*, vol. 77, no. 3, pp. 977–1026, 2005.

[78] R. F. Ismagilov, A. D. Stroock, P. J. a. Kenis, G. Whitesides, and H. a. Stone, “Experimental and theoretical scaling laws for transverse diffusive broadening in two-phase laminar flows in microchannels,” *Appl. Phys. Lett.*, vol. 76, no. 17, p. 2376, 2000.

[79] A. E. Kamholz, B. H. Weigl, B. A. Finlayson, and P. Yager, “Quantitative analysis of molecular interaction in a microfluidic channel: the T-sensor,” *Anal. Chem.*, vol. 71, no. 23, pp. 5340–5347, 1999.

[80] N. T. Nguyen and Z. Wu, “Micromixers - A Review,” *J. Micromechanics Microengineering*, vol. 15, pp. R1–R16, 2005.

[81] J. Atencia and D. J. Beebe, “Controlled microfluidic interfaces,” *Nature*, vol. 437, no. 7059, pp. 648–655, 2004.

[82] M. J. Madou, *Fundamentals of microfabrication: the science of miniaturization*. CRC Press, 2002.

[83] G. M. Whitesides and A. D. Stroock, “Flexible methods for microfluidics,” *Phys. Today*, vol. 54, no. 6, p. 42, 2001.

[84] D. C. Duffy, J. C. McDonald, O. J. A. Schueller, and G. M. Whitesides, “Rapid prototyping of microfluidic systems in poly (dimethylsiloxane),” *Anal. Chem.*, vol. 70, no. 23, pp. 4974–4984, 1998.

[85] M. Alonso-Amigo, “Polymer Microfabrication for Microarrays, Microreactors and Microfluidics,” *J. Assoc. Lab. Autom.*, vol. 5, no. 6, pp. 96–101, Dec. 2000.

[86] K. J. Regehr, M. Domenech, J. T. Koepsel, K. C. Carver, S. J. Ellison-Zelski, W. L. Murphy, L. a Schuler, E. T. Alarid, and D. J. Beebe, “Biological implications of polydimethylsiloxane-based microfluidic cell culture.,” *Lab Chip*, vol. 9, no. 15, pp. 2132–9, 2009.

[87] J. D. Plummer, M. D. Deal, and P. B. Griffin, *Silicon VLSI technology: fundamentals, practice and modeling*, vol. 4. Upper Saddle River, NJ: Prentice Hall Inc., 2000.

[88] N. T. Nguyen and S. T. Wereley, *Fundamentals and applications of microfluidics*. Artech House Publishers, 2002.

[89] F. Laermer and A. Schilp, “Method of anisotropically etching silicon,” U.S. Patent No. 5,501,893.1996.

[90] M. R. Gongora-Rubio, P. Espinoza-Vallejos, L. Sola-Laguna, and J. J. Santiago-Aviles, “Overview of low temperature co-fired ceramics tape technology for meso-system technology (MsST),” *Sensors Actuators A Phys.*, vol. 89, no. 3, pp. 222–241, 2001.

[91] L. J. Golonka, T. Zawada, J. Radojewski, H. Roguszczak, and M. Stefanow, “LTCC Microfluidic System,” *Int. J. Appl. Ceram. Technol.*, vol. 3, no. 2, p. 150, 2006.

[92] L. J. Golonka, H. Roguszczak, T. Zawada, J. Radojewski, I. Grabowska, M. Chudy, A. Dybko, Z. Brzozka, and D. Stadnik, “LTCC based microfluidic system with optical detection,” *Sensors Actuators B Chem.*, vol. 111–112, pp. 396–402, 2005.

[93] IMST GmbH, “LTCC Process.” 2010.

[94] “ANSYS® FLUENT Academic Research, Release 14.0.0.” ANSYS Inc.

[95] M. Raffel, C. Willert, and J. Kompenhans, “Particle Image Volocimetry, a practical guide.” Springer Verlag, 2001.

[96] J. G. Santiago, S. T. Wereley, C. D. Meinhart, D. J. Beebe, and R. J. Adrian, “A particle image velocimetry system for microfluidics,” *Exp. Fluids*, vol. 25, no. 4, pp. 316–319, 1998.

[97] R. J. Adrian and J. Westerweel, *Particle image velocimetry*, vol. 30. Cambridge University Press, 2010.

[98] S. Wereley, L. Gui, and C. Meinhart, “Advanced algorithms for microscale particle image velocimetry,” *AIAA J.*, vol. 40, no. 6, pp. 1047–1055, 2002.

[99] R. D. Keane and R. J. Adrian, “Theory of cross-correlation analysis of PIV images,” *Appl. Sci. Res.*, vol. 49, no. 3, pp. 191–215, 1992.

[100] S. M. Soloff, R. J. Adrian, and Z.-C. Liu, “Distortion compensation for generalized stereoscopic particle image velocimetry,” *Meas. Sci. Technol.*, vol. 8, no. 12, p. 1441, 1997.

[101] C. D. Meinhart, S. T. Wereley, and M. H. B. Gray, “Volume illumination for two-dimensional particle image velocimetry,” *Meas. Sci. Technol.*, vol. 11, no. 6, pp. 809–814, 2000.

[102] M. G. Olsen and R. J. Adrian, “Out-of-focus effects on particle image visibility and correlation in microscopic particle image velocimetry,” *Exp. Fluids*, vol. 29, no. 1, pp. S166–S174, 2000.

[103] M. Gad-el-Hak, “Differences between liquid and gas transport at the microscale,” *Tech. Sci.*, vol. 53, no. 4, 2005.

[104] S. Janson, H. Helvajian, and K. Breuer, “MEMS, microengineering and aerospace systems,” *AIAA Pap. 99-3802*, 1999.

[105] P. Bridgman, “The thermal conductivity of liquids under pressure,” *Proc. Am. Acad. Arts Sci. Am. Acad. Arts Sci.*, vol. 59, no. 7, pp. 141–169, 1923.

[106] M. J. Lighthill, “Introduction. Real and ideal fluids.,” in in *Laminar Boundary Layers*, L. Rosenhead, Ed. Oxford: Clarendon Press, 1963, pp. 1–45.

[107] S. Chapman and T. G. Cowling, *The Mathematical Theory of Non-Uniform Gases*, Third edit. London: Cambridge University Press, 1970.

[108] M. Gal-el-Hak, “The Fluid Mechanics of Microdevices-The Freeman Scholar Lecture,” *J. Fluids Eng.*, vol. 121, no. 1, pp. 5–33, 1999.

[109] K. V. Sharp, “Experimental Investigation of Liquid and Particle-Laden Flows in Microtubes,” University of Illinois at Urbana-Champaign, 2001.

[110] K. V. Sharp, R. J. Adrian, J. G. Santiago, and J. I. Molho, “Liquid Flow in Microchannels,” in in *The Handbook of MEMS*, M. Gad-el-Hak, Ed. CRC Press, 2005.

[111] “FLUENT User Guide.” ANSYS Inc., 2008.

[112] A. E. Kamholz and P. Yager, “Theoretical Analysis of Molecular Diffusion in Pressure-Driven Laminar Flow in Microfluidic Channels,” *Biophys. J.*, vol. 80, no. 1, p. 155, 2001.

[113] A. Ciani, W. Kreutner, C. E. Frouzakis, and K. Lust, “An experimental and numerical study of the structure and stability of laminar opposed-jet flows,” *Comput. Fluids*, vol. 39, no. 1, pp. 124–114, 2010.

[114] M. Engler, N. Kockmann, T. Kiefer, and P. Woias, “Numerical and experimental investigations on liquid mixing in static micromixers,” *Chem. Eng. J.*, vol. 101, no. 1–3, pp. 315–322, 2004.

[115] D. Bothe, C. Stemich, and H.-J. Warnecke, “Fluid mixing in a T-shaped micro-mixer,” *Chem. Eng. Sci.*, vol. 61, no. 9, pp. 2950–2958, 2006.

[116] M. Hoffmann, M. Schlüter, and N. Räbiger, “Experimental investigation of liquid–liquid mixing in T-shaped micro-mixers using -LIF and -PIV,” *Chem. Eng. Sci.*, vol. 61, no. 9, pp. 2968–2976, 2006.

[117] A. Soleymani, E. Kolehmainen, and I. Turunen, “Numerical and experimental investigations of liquid mixing in T-type micromixers,” *Chem. Eng. J.*, vol. 135, pp. S219–S228, 2008.

[118] D. Bothe, C. Stemich, and H.-J. Warnecke, “Computation of scales and quality of mixing in a T-shaped microreactor,” *Comput. Chem. Eng.*, vol. 32, no. 1–2, pp. 108–114, 2008.

[119] M. A. Sultan, C. Fonte, and M. Dias, “Experimental study of flow regime and mixing in T-jets mixers,” *Chem. Eng. Sci.*, vol. 73, pp. 388–399, 2012.

[120] R. J. Santos and M. A. Sultan, “State of the Art of Mini/Micro Jet Reactors,” *Chem. Eng. Technol.*, vol. 36, no. 6, pp. 937–949, 2013.

[121] A. Soleymani, H. Yousefi, and I. Turunen, “Dimensionless number for identification of flow patterns inside a T-micromixer,” *Chem. Eng. Sci.*, vol. 63, no. 21, pp. 5291–5297, 2008.

[122] R. Schalla and E. Pletcher, “The behavior of the system triethylamine—White fuming nitric acid under conditions of rapid mixing,” *Symp. Combust.*, vol. 6, no. 1, pp. 911–917, 1957.

[123] C. Trent and M. Zucrow, “Behavior of Liquid Hydrocarbons with White Fuming Nitric Acid,” *Ind. Eng. Chem.*, vol. 44, no. 11, pp. 2668–2673, 1952.

[124] S. Wang and S. T. Thynell, “Experimental Investigation of Pressure Effect on Ignition Delay of Monomethylhydrazine, 1, 1-Dimethylhydrazine, Tetramethylethylenediamine and 2-Dimethylaminoethylazide with Nitric,” in *8th U. S. National Combustion Meeting, Organized by the Western States Section of the Combustion Institute and hosted by the University of Utah*, 2013, pp. 1–6.

[125] R. B. Bird, W. E. Stewart, and E. N. Lightfoot, *Transport Phenomena*. New York: Wiley, 1960.

[126] M.-H. Wu and R. A. Yetter, “Development and analysis of a LTCC micro stagnation-point flow combustor,” *J. Micromechanics Microengineering*, vol. 18, no. 12, p. 125016, 2008.

[127] H. Tsuji, “Counterflow diffusion flames,” *Prog. Energy Combust. Sci.*, vol. 8, pp. 93–119, 1982.

[128] Potter Jr A. E., Heimal S., and Butler H. S., “Apparent flame strength: A measure of maximum reaction rate in diffusion flames,” *Symp. Combust.*, vol. 8, no. 1, pp. 1027–1034, 1961.

[129] A. Liñán, “The asymptotic structure of counterflow diffusion flames for large activation energies,” *Acta Astronaut.*, vol. 1, pp. 1007–1039, 1974.

[130] Y. Otsuka and T. Niioka, “On the deviation of the flame from the stagnation point in opposed-jet diffusion flames,” *Combust. Flame*, vol. 19, no. 2, pp. 171–179, 1972.

[131] T. P. Pandya and F. J. Weinberg, “The structure of flat, counter-flow diffusion flames,” *Proc. R. Soc. London. Ser. A. Math. Phys. Sci.*, vol. 279, no. 1379, pp. 544–561, 1964.

[132] D. B. Spalding, “Experiments on the burning and extinction of liquid fuel spheres,” *Fuel*, vol. 32, pp. 169–185, 1953.

[133] R. F. Simmons and H. G. Wolfhard, “Some limiting oxygen concentrations for diffusion flames in air diluted with nitrogen,” *Combust. Flame*, vol. 1, no. 2, pp. 155–161, Jun. 1957.

[134] H. Tsuji and I. Yamaoka, “The counterflow diffusion flame in the forward stagnation region of a porous cylinder,” *Symp. Combust.*, vol. 11, no. 1, pp. 979–984, 1967.

[135] S. R. Turns, *An Introduction To Combustion*, 2nd ed. New York: McGraw-Hill, 2000.

[136] A. E. Lutz, R. J. Kee, J. F. Grcar, and F. M. Rupley, “OPPDIF: A Fortran program for computing opposed-flow diffusion flames,” *Sandia Natl. Lab. Report, SAND96-8243*, 1997.

[137] R. J. Kee, J. A. Miller, G. H. Evans, and G. Dixon-Lewis, “A computational model of the structure and extinction of strained, opposed flow, premixed methane-air flames,” *Symp. Combust.*, vol. 22, no. 1, pp. 1479–1494, 1989.

[138] C. R. Wilke and P. Chang, “Correlation of diffusion coefficients in dilute solutions,” *AIChE J.*, vol. 1, no. 2, p. 264, 1955.

[139] R. J. Kee, J. A. Miller, and T. H. Jefferson, “CHEMKIN: A general-purpose, problem-independent, transportable, FORTRAN chemical kinetics code package.,” *Sandia Natl. Lab. Report, SAND80-8003*, 1980.

[140] R. J. Kee, G. Dixon-lewis, and J. A. Miller, “A Fortran Computer Code Package for the Evaluation of Gas-Phase Multicomponent Transport Properties,” *Sandia Natl. Lab. Report, SAND86-8246*, 1998.

[141] J. F. Grcar, “The Twopnt program for boundary value problems,” *Sandia Natl. Lab. Report, SAND91-8230*, 1992.

[142] J. H. Ferziger, *Numerical methods for engineering application*. Wiley, 1998.

[143] B. Wang and X. Peng, “Experimental investigation on liquid forced-convection heat transfer through microchannels,” *Int. J. Heat Mass Transf.*, vol. 37, pp. 73–82, 1994.

[144] X. F. Peng and G. P. Peterson, “Convective heat transfer and flow friction for water flow in microchannel structures,” *Int. J. Heat Mass Transf.*, vol. 39, no. 12, pp. 2599–2608, 1996.

[145] S. B. Choi, R. F. Barron, and R. O. Warrington, “Fluid flow and heat transfer in microtubes,” *Micromechanical Sensors, Actuators, Syst. ASME DSC*, vol. 32, pp. 123–134, 1991.

[146] B. Xu, K. T. Ooti, N. T. Wong, and W. K. Choi, “Experimental investigation of flow friction for liquid flow in microchannels,” *Int. Commun. Heat Mass Transf.*, vol. 27, no. 8, pp. 1165–1176, 2000.

[147] D. Liu and S. V. Garimella, “Investigation of Liquid Flow in Microchannels,” *J. Thermophys. Heat Transf.*, vol. 18, no. 1, pp. 65–72, 2004.

[148] F. P. Incropera, A. S. Lavine, and D. P. DeWitt, *Fundamentals of heat and mass transfer*. John Wiley & Sons, 2011.

[149] G. Gamrat, M. Favre-Marinet, and D. Asendrych, “Conduction and entrance effects on laminar liquid flow and heat transfer in rectangular microchannels,” *Int. J. Heat Mass Transf.*, vol. 48, no. 14, pp. 2943–2954, 2005.

[150] D. Haller, P. Woias, and N. Kockmann, “Simulation and experimental investigation of pressure loss and heat transfer in microchannel networks containing bends and T-junctions,” *Int. J. Heat Mass Transf.*, vol. 52, no. 11–12, pp. 2678–2689, 2009.

[151] W. M. Kays and M. E. Crawford, *Convective Heat and Mass Transfer*, 3rd ed. New York: McGraw-Hill, 1993.

[152] G. Hetsroni, A. Mosyak, E. Pogrebnyak, and R. Rozenblit, “Infrared temperature measurements in micro-channels and micro-fluid systems,” *Int. J. Therm. Sci.*, vol. 50, no. 6, pp. 853–868, 2011.

[153] P. B. Allen, I. Rodriguez, C. L. Kuyper, R. M. Lorenz, P. Spicar-Mihalic, J. S. Kuo, and D. T. Chiu, “Selective electroless and electrolytic deposition of metal for applications in microfluidics: fabrication of a microthermocouple.,” *Anal. Chem.*, vol. 75, no. 7, pp. 1578–83, Apr. 2003.

[154] N. Dudovich, D. Oron, and Y. Silberberg, “Single-pulse coherently controlled nonlinear Raman spectroscopy and microscopy,” *Nature*, vol. 418, no. 6897, pp. 512–514, 2002.

Appendix A

Standard Operating Procedure for PIV System

1. Turning on the PIV Laser
    a. Turn the AC power on from the back of the power source
    b. On the front, turn the key to the on position
    c. Press the stand by button to get the machine ready
    d. Set both lasers to external control
    e. Press the power button to high
    f. Turn the Rep Rate knob to max
    g. Turn the Energy up to ~950
    h. When ready to perform the experiment press both lasers on

2. Turning on the PIV Camera
    a. Turn the power on from the back of the Laser Pulse Synchronizer
    b. Turn on the PIV camera with the switch in the back
    c. Observe the Light on the back of the camera:
        i. Steady Red means there is a connection problem
        ii. Flashing Green/Red means the camera is warming up
        iii. Steady Green means the camera is ready to go

3. Preparing the PIV particle solution
    a. Mix one part of the 2 μm fluorescent particle solution (Thermo Scientific Fluoro-Max Red Aqueous Fluorescent Particles) with nine parts of distilled water
    b. Concentration can be changed so as to affect the number of particles observed in the microreactor
    c. Sonicate the mixture using the sonicating horn. Usually done for three cycles which are of 30 seconds duration each
    d. Allow sonicated solution to cool and then fill into appropriate syringes
    e. Set up the syringes in the syringe pump and connect the syringes to the microreactor manifold assembly

f. Make sure all the lines and connections are free of leaks

4. Setting up the Optical Microscope
    a. Turn on the microscope lamp
        i. Using the bottom Nikon power box, switch the power on
        ii. Turn the knob all the way to maximum
        iii. Make sure the lever on the microscope directs the lamp light in (the lever will be pointed off to the right)
    b. On the right side of the microscope, turn the Port to 2
    c. Select filter
        i. Position 1 – Orange image (used while recording images using the PIV camera)
        ii. Position 2 – White image (used while setting up the system and aligning the microreactor and optics before running of the experiment)
        iii. Position 3-6 – No Image
    d. Focus in on the area of interest in the microreactor
        i. The large focusing knob on the microscope provides for coarse tune while the smaller knob is for fine tune
        ii. The hanging knob on the right side of the microscope can be used to adjust the position of the microreactor in the X-Y plane

5. Setting up the PIV Imaging Software (Insight)
    a. Double click the Insight icon on the desktop
    b. Click on new experiment and then name your experiment
    c. Set the following conditions in the upper right hand corner:
        i. Date Source – Camera
        ii. Exposure Mode – Free (allows for continuous exposure)
        iii. Capture Mode – Continuous
    d. Click View > LUT > Linear and set it in between 8 & 15
    e. Calibrate the length scaling
        i. Adjust the microscope in the X-Y plane such that the image of the microreactor can be seen on the computer screen

ii. Adjust the positioning of the microreactor to focus on the part of the microreactor which has a known dimension
iii. Focus on the top of the microreactor channel so that the side walls are in focus
iv. Click on the Calibration tab and select 2D Velocity Calibration
v. Under Measurement choose Velocity
vi. Under Measure mm/pixel click on the measure button
vii. Draw a line from wall to wall on the image that was taken and insert the object size in millimeters in the blank box
viii. Click Recalculate and Ok

f. Adjust microscope in the Z direction so as to fix the depth at which the measurements will be made
    i. Start by focusing the microscope on the top of the channel
    ii. Focus the microscope in until the bottom of the channel is well defined noting how much you turned the tuning knob
    iii. The positions of the top and bottom of the reactor channel provide for tatal depth and a depth can be chosen in the middle for taking the measurements.
g. Once image is in focus, lower the lamp intensity to minimum, switch the lever at the back of the microscope over to the laser (the lever will be pointing straight at the microscope) and shift the filter to position 1.
h. Begin flow of the solutions into the microreactor by turning on the flow using the syringe pumps
i. Turn on laser
    i. First manually press in both laser buttons on the power source (This is also step 2h so do not repeat if already done!)
    ii. Then click on the green icon in the lower left hand corner on the computer screen which allows for external control of the laser
j. Once laser is running, click on the Begin Image Capture icon
k. Check if the fluorescent particles are visible on the computer screen as bright spheres
l. If the particles appear to be oversaturated on the computer screen the LUT values can be lowered, while if they are not bright enough, LUT values should be raised.
m. Click on the Stop button on the top to end the image capture and the Stop button on the bottom to turn off the lasers

6. Recording Data using Insight
    a. Set the following conditions in the upper right hand corner
        i. Data – Camera
        ii. Exposure – Frame Straddle (allows two frames to be captures in quick succession)
        iii. Capture Mode - Sequence
        iv. Click on the box next to the sequence tab and set the number of captures (typically number of captures for every experiment range between 100 and 200)
        v. Choose save to disk option to save all recorded images from the run
    b. Set the time between successive laser pulses (Δt) for the flow rate at which the test is supposed to be run
        i. Calculate the average velocity expected in the microreactor channel based on the area of cross-section and the flow rate
        ii. Δt is calculated for each experimental run such that the average displacement of each particle is between 8 and 12 pixels.
        iii. The calibration step provides for a measure of how a μm length in the microchannel relates to the number of pixels.
        iv. Δt is thus calculated by dividing the appropriate length for 8 – 12 pixels by the average velocity
    c. Begin to run the PIV solution through the microreactor, at the predetermined flow rate, using the syringe pump
    d. Once there is a steady flow inside the channel, click the “Begin Image Capture” icon (the camera at the top of the screen)
    e. Click on the save icon to store the newly obtained images

7. Processing Data in Insight
    a. Removing background images
        i. Click on Process > Background Setup
        ii. Under “Background Processor” choose average background image processor and click “Start Background Processing”
        iii. Click on Process > Setup

iv. Under Image Conditioner choose Background Image Conditioner and click on the Conditioner Settings button
v. Click Frame A > Browse > Choose the background image that ends in “a”
vi. Click Frame B > Browse > Choose the background image that ends in “b”
vii. Click on the “Whole Field” icon and then click on the “Begin Image Processing” icon to start the background image removal process
viii. If you want to use a new background image removal or just want the original images:
    1. Go to Data Source and select Archive
    2. Click on Raw under the Image Data Type
    3. Select the images desired

b. Creating Vectors
    i. Click on Process > Setup
    ii. From the drop down menus select “Ensemble Average Correlation Processor” as the PIV processor
    iii. Under PIV Process select “Processor Settings”
        1. Grid Engine – Nyquist Grid
        2. Spot Mask Engine – ZeroPadMask
        3. Correlation Engine – FFT Correlator
        4. Peak Engine – Gaussian Peak
        5. Size of Spot A and B – 48 pixels × 48 pixels
        6. Maximum Displacement – 18 pixels
    iv. Select the whole field icon or the area of interest icon (if the latter is selected draw a box on the image where you want to analyze)
    v. Click the Begin Image Processing icon (green arrow) (This will give you the vectors for the particle flow and can take a few minutes to generate.
    vi. Under the vector tab one can change the vector color, size, and width to better see the direction of the flow

8. Plotting Vector Data using Tecplot
    a. Tecplot can be accessed through Insight using an icon on the GUI
    b. Select the vector files from a particular run using the dialog box that opens while initializing Tecplot

c. Tecplot displays each vector file along with a measure of each particle velocity and *x* and *y* dimensions
d. Average the vector files from a particular run to obtain an averaged vector field
e. The vector field can be displayed by changing the scaling for the velocity vectors

Appendix B

Sample Input for Simulation of Microreactor Flow

```
/RSTR
MIX
PCAD 0.7
RGTC 1.0
ENRG
PLAT
AFUE 0
AOXI 0
VFUE 5
VOXI 5
TFUE 300
TOXI 300
TMAX 1000
GRID 0.00000
GRID 0.00100
GRID 0.00200
GRID 0.00300
GRID 0.00400
GRID 0.00500
GRID 0.00600
GRID 0.00700
GRID 0.00800
GRID 0.00900
GRID 0.01000
GRID 0.01100
GRID 0.01200
GRID 0.01300
GRID 0.01400
GRID 0.01500
GRID 0.01600
GRID 0.01700
GRID 0.01800
GRID 0.01900
GRID 0.02000
GRID 0.02100
GRID 0.02200
GRID 0.02300
GRID 0.02400
XEND 0.024
XCEN 0.012
WMIX 0.012
PRES 1.0
IRET 20
```

```
UFAC 2.
SFLR -1.E-4
PRNT 11
TIME 200 1.E-3
TIM2 200 1.E-3
GRAD 0.1
CURV 0.5
FUEL TMEDA 1.0
OXID NA 0.07053
OXID WATER 0.92947
PROD TMEDADN 0.03655
PROD WATER 0.96345
KOUT TMEDA NA WATER TMEDADN
RTOL 1.E-3
ATOL 1.E-6
ATIM 1.E-6
RTIM 1.E-3
END
```

For all the numerical simulations, the reaction in the microreactor was first solved for inlet velocity equaling 5cm/s for both the fuel and the oxidizer. Once a converged solution was obtained for this inlet velocity case, then the boundary conditions were changed in incremental steps to run the numerical simulations at different inlet velocities with the output profiles from the 5 cm/s case used as the input profiles. This use of previously converged solutions to simulate the other boundary conditions helped in reaching the converged steady solutions in a quicker, less computationally demanding manner. This method of restarting a simulation by using previously converged solutions was also used while changing the reaction rate of the single step reaction in the chemical mechanism. To make modifications to the boundary conditions and use a previously converged solution as the initial condition for the system, the CNTN command can be used in the input file. A sample of such an input file is:

```
RSTR
MIX
PCAD 0.7
RGTC 1.0
ENRG
PLAT
```

```
AFUE 0
AOXI 0
VFUE 5
VOXI 5
TFUE 300
TOXI 300
TMAX 1000
GRID 0.00000
GRID 0.00100
GRID 0.00200
GRID 0.00300
GRID 0.00400
GRID 0.00500
GRID 0.00600
GRID 0.00700
GRID 0.00800
GRID 0.00900
GRID 0.01000
GRID 0.01100
GRID 0.01200
GRID 0.01300
GRID 0.01400
GRID 0.01500
GRID 0.01600
GRID 0.01700
GRID 0.01800
GRID 0.01900
GRID 0.02000
GRID 0.02100
GRID 0.02200
GRID 0.02300
GRID 0.02400
XEND 0.024
XCEN 0.012
WMIX 0.012
PRES 1.0
IRET 20
UFAC 2.
SFLR -1.E-4
PRNT 11
TIME 200 1.E-3
TIM2 200 1.E-3
GRAD 0.1
CURV 0.5
FUEL TMEDA 1.0
OXID NA 0.07053
OXID WATER 0.92947
PROD TMEDADN 0.03655
PROD WATER 0.96345
KOUT TMEDA NA WATER TMEDADN
RTOL 1.E-3
```

```
ATOL 1.E-6
ATIM 1.E-6
RTIM 1.E-3
CNTN
VFUE 5.1
VOXI 5.1
CNTN
END
VFUE 5.2
VOXI 5.2
CNTN
END
VFUE 5.3
VOXI 5.3
END
```

Appendix C

Modified Subroutines for Microreactor Flow Simulation

The original Oppdif code was meant to solve a gas-phase counter-flow diffusion flame. Thus the mass densities for the fluids were calculated using the ideal gas law. As the flow in the microreactor is in the liquid-phase, thus the subroutines that calculate mass densities for the various species were modified such that the liquid-phase mass densities could be hard-coded into the subroutines. The subroutines that calculate production rate of the species due to the reactions ($\dot{\omega}_k$) were also modified so as to calculate mass densities according to the input values rather than use the ideal gas law. As all the simulations were carried out at standard atmospheric conditions, thus no change was made to the subroutine that accounts for the change in mass diffusivities due to change in pressure. Modifications were also made to the subroutines used to calculate the transport properties for the various fluids. This included hard-coding the viscosity, conductivity and mass-diffusivity values for each species into the original code. These properties were assumed to be independent of temperature.

```
C-----------------------------------------------------------------C
C
      SUBROUTINE CKRHOY (P, T, Y, ICKWRK, RCKWRK, RHO)
C
C  START PROLOGUE
C
C  SUBROUTINE CKRHOY (P, T, Y, ICKWRK, RCKWRK, RHO)
C     Returns the mass density of the gas mixture given the
pressure,
C     temperature and mass fractions;  see Eq. (2).
C
C  INPUT
C     P      - Pressure.
C                    cgs units - dynes/cm**2
C                    Data type - real scalar
C     T      - Temperature.
C                    cgs units - K
```

```
C                   Data type - real scalar
C     Y      - Mass fractions of the species.
C                   cgs units - none
C                   Data type - real array
C                   Dimension Y(*) at least KK, the total number of
C                   species.
C     ICKWRK - Array of integer workspace.
C                   Data type - integer array
C                   Dimension ICKWRK(*) at least LENIWK.
C     RCKWRK - Array of real work space.
C                   Data type - real array
C                   Dimension RCKWRK(*) at least LENRWK.
C
C  OUTPUT
C     RHO    - Mass density.
C                   cgs units - gm/cm**3
C                   Data type - real scalar
C
C  END PROLOGUE
C
C*****precision > double
        IMPLICIT DOUBLE PRECISION (A-H, O-Z), INTEGER (I-N)
C*****END precision > double
C*****precision > single
C        IMPLICIT REAL (A-H, O-Z), INTEGER (I-N)
C*****END precision > single
C
      DIMENSION ICKWRK(*), RCKWRK(*), Y(*), DENSITY(4)
      COMMON /CKSTRT/ NMM , NKK , NII , MXSP, MXTB, MXTP, NCP ,
NCP1,
     1           NCP2, NCP2T,NPAR, NLAR, NFAR, NLAN, NFAL, NREV,
     2           NTHB, NRLT, NWL,  IcMM, IcKK, IcNC, IcPH, IcCH,
     3           IcNT, IcNU, IcNK, IcNS, IcNR, IcLT, IcRL, IcRV,
     4           IcWL, IcFL, IcFO, IcKF, IcTB, IcKN, IcKT, NcAW,
     5           NcWT, NcTT, NcAA, NcCO, NcRV, NcLT, NcRL, NcFL,
     6           NcKT, NcWL, NcRU, NcRC, NcPA, NcKF, NcKR, NcK1,
     7           NcK2, NcK3, NcK4, NcI1, NcI2, NcI3, NcI4
C
C     ORIGINAL CODE:
C
C       SUMYOW = 0.0
C       DO 150 K = 1, NKK
C          SUMYOW = SUMYOW + Y(K)/RCKWRK(NcWT + K - 1)
C150    CONTINUE
C       RHO = P/(SUMYOW*T*RCKWRK(NcRU))
C       RETURN
C       END
C
C     Hard-Coding Mass Density Values:
C
C
```

```
      DENSITY(1) = 0.780
      DENSITY(2) = 1.504
      DENSITY(3) = 1.000
      DENSITY(4) = 1.263
C
C
      RHO = 0.0
C
C
      DO K = 1, NKK
      RHO = RHO + Y(K)*DENSITY(K)
      END DO
      RETURN
      END
C



C-----------------------------------------------------------------------C
C
      SUBROUTINE CKYTCP (P, T, Y, ICKWRK, RCKWRK, C)
C
C  START PROLOGUE
C
C  SUBROUTINE CKYTCP (P, T, Y, ICKWRK, RCKWRK, C)
C     Returns the molar concentrations given the pressure,
C     temperature and mass fractions;  see Eq. (7).
C
C  INPUT
C     P      - Pressure.
C                   cgs units - dynes/cm**2
C                   Data type - real scalar
C     T      - Temperature.
C                   cgs units - K
C                   Data type - real scalar
C     Y      - Mass fractions of the species.
C                   cgs units - none
C                   Data type - real array
C                   Dimension Y(*) at least KK, the total number of
C                   species.
C     ICKWRK - Array of integer workspace.
C                   Data type - integer array
C                   Dimension ICKWRK(*) at least LENIWK.
C     RCKWRK - Array of real work space.
C                   Data type - real array
C                   Dimension RCKWRK(*) at least LENRWK.
C
C  OUTPUT
C     C      - Molar concentrations of the species.
C                   cgs units - mole/cm**3
```

```
C                   Data type - real array
C                   Dimension C(*) at least KK, the total number of
C                   species.
C
C  END PROLOGUE
C
C*****precision > double
      IMPLICIT DOUBLE PRECISION (A-H, O-Z), INTEGER (I-N)
C*****END precision > double
C*****precision > single
C      IMPLICIT REAL (A-H, O-Z), INTEGER (I-N)
C*****END precision > single
C
      DIMENSION ICKWRK(*), RCKWRK(*), Y(*), C(*), DENSITY(4)
      COMMON /CKSTRT/ NMM , NKK , NII , MXSP, MXTB, MXTP, NCP ,
NCP1,
     1           NCP2, NCP2T,NPAR, NLAR, NFAR, NLAN, NFAL, NREV,
     2           NTHB, NRLT, NWL,  IcMM, IcKK, IcNC, IcPH, IcCH,
     3           IcNT, IcNU, IcNK, IcNS, IcNR, IcLT, IcRL, IcRV,
     4           IcWL, IcFL, IcFO, IcKF, IcTB, IcKN, IcKT, NcAW,
     5           NcWT, NcTT, NcAA, NcCO, NcRV, NcLT, NcRL, NcFL,
     6           NcKT, NcWL, NcRU, NcRC, NcPA, NcKF, NcKR, NcK1,
     7           NcK2, NcK3, NcK4, NcI1, NcI2, NcI3, NcI4
C
C
C     Hard-Coding Mass Density Values for Concentration Calculation
C
C
      DENSITY(1) = 0.780
      DENSITY(2) = 1.504
      DENSITY(3) = 1.000
      DENSITY(4) = 1.263
C
C
      RHO = 0.0
C
C
      DO K = 1, NKK
      RHO = RHO + Y(K)*DENSITY(K)
      END DO
C
C     ORIGINAL CODE:
C
C      SUMYOW = 0.0
C      DO 150 K = 1, NKK
C         SUMYOW = SUMYOW + Y(K)/RCKWRK(NcWT + K - 1)
C150   CONTINUE
C      SUMYOW = SUMYOW*T*RCKWRK(NcRU)
C
      DO 200 K = 1, NKK
C         C(K) = P*Y(K)/(SUMYOW*RCKWRK(NcWT + K - 1))
```

```
C
C
      C(K) = RHO*Y(K)/(RCKWRK(NcWT + K - 1))
200   CONTINUE
      RETURN
      END
C
```

Changes made to tranfit.f to assign transport properties for the species.

```
C
      IF (.NOT. KERR) THEN
C
C        FIT THE CONDUCTIVITIES AND VISCOSITIES
C
         CALL LAMFIT (KK, NT, NO, NFDIM, LOUT, WT, SIG, EPS, DIP,
     1               ZROT, NLIN, P, TLOW, DT, ALOGT, FITRES, FITWT,
     2               FITWRK, XLA, XETA, CV, ICKWRK, RCKWRK, COFLAM,
     3               COFETA, EMAXL, EMAXE)
C
C        FIT THE DIFFUSION COEFFICIENTS
C
         CALL DIFFIT (KK, NT, NO, NFDIM, KDIM, LOUT, WT, SIG, EPS,
     1               DIP, POL, P, TLOW, DT, ALOGT, FITRES, FITWT,
     2               FITWRK, XD, COFD, EMAXD)
C
C        FIT THE THERMAL DIFFUSION RATIOS
C
         CALL THMFIT (KK, NT, NO, KDIM, LOUT, WT, SIG, EPS, DIP,
     1               POL, TLOW, DT, ALOGT, FITRES, FITWT, FITWRK,
     2               XD, NLITE, KTDIF, COFTD, EMAXTD)
C
C
C     Hard-Coding the Transport Coefficients
C
C
      do k=1,kk
        do j=1,kk
          do n=2,NO
            COFLAM(N,K) = 0d0
            COFETA(N,K) = 0d0
            COFD(N,J,K) = 0d0  ! Sets coefficient to 0 when N/=1
(Taylor expansion coefficients for first, second and third order
terms)
          end do
        end do
```

```
      end do
      COFLAM(1,1) = 10.714418 !Coef numbering according to numbering
      COFLAM(1,2) = 10.239960 !in thermdat file
      COFLAM(1,3) = 10.933107
      COFLAM(1,4) = 10.425252
C
C
      COFETA(1,1) = -4.6051702
      COFETA(1,2) = -4.7105307
      COFETA(1,3) = -4.6051702
      COFETA(1,4) = -4.6777409
C
C
      COFD(1, 1, 1) = -11.339813
      COFD(1, 2, 1) = -10.580565
      COFD(1, 2, 2) = -10.779653
      COFD(1, 3, 1) = -10.072853
      COFD(1, 3, 2) = -10.271946
      COFD(1, 3, 3) = -11.004456
      COFD(1, 4, 1) = -10.971771
      COFD(1, 4, 2) = -10.212489
      COFD(1, 4, 3) = -9.7047597
      COFD(1, 4, 4) = -11.413472
C
C        PRINT THE FITS
C
         WRITE (LOUT, 7030)
         WRITE (LOUT, 7035) EMAXL
         WRITE (LOUT, 8200)
         WRITE (LOUT, 8100) (KSYM(K), (COFLAM(N,K),N=1,NO), K=1,KK)
C
         WRITE (LOUT, 7050)
         WRITE (LOUT, 7035) EMAXE
         WRITE (LOUT, 8200)
         WRITE (LOUT, 8100) (KSYM(K), (COFETA(N,K),N=1,NO), K=1,KK)
C
         WRITE (LOUT, 7060)
         WRITE (LOUT, 7035) EMAXD
         DO 2300 J = 1, KK
            WRITE (LOUT, 8200)
            WRITE (LOUT, 8110)
     1           (KSYM(J), KSYM(K), (COFD(N,J,K),N=1,NO), K=1,J)
 2300    CONTINUE
C
         WRITE (LOUT, 7070)
         WRITE (LOUT, 7035) EMAXTD
         DO 2400 M = 1, NLITE
            K = KTDIF(M)
            WRITE (LOUT, 8200)
            WRITE (LOUT, 8110)
     1           (KSYM(K), KSYM(J), (COFTD(N,J,M),N=1,NO), J=1,KK)
```

```
 2400    CONTINUE
      ELSE
         WRITE (LOUT, '(/A)')
     1   ' WARNING...THERE IS AN ERROR IN THE TRANSPORT LINKING
FILE'
      ENDIF
```

VITA

Pulkit Saksena

Education

THE PENNSYLVANIA STATE UNIVERSITY — **University Park, PA**
Doctor of Philosophy, Mechanical Engineering, August 2008 – August 2014
Master of Science, Mechanical Engineering, August 2008 – May 2012

MANIPAL UNIVERSITY, Manipal Institute of Technology — **Manipal, India**
Bachelor of Engineering, Mechanical Engineering, August 2002 - May 2006